NASA Conference Publication 2483

Theoretical Problems in High Resolution Solar Physics II

Edited by
G. Athay
High Altitude Observatory/National
Center for Atmospheric Research
Boulder, Colorado

D. S. Spicer
NASA Goddard Space Flight Center
Greenbelt, Maryland

Proceedings of a workshop held in
Boulder, Colorado
September 15–17, 1986

NASA
National Aeronautics
and Space Administration

Scientific and Technical
Information Office

1987

FOREWORD

The Science Working Group for the High Resolution Solar Observatory (HRSO) (and its predecessor, the Solar Optical Telescope) laid plans beginning in 1984 for a series of workshops designed to stimulate a broad-based input from the scientific community to the HRSO mission. These workshops have the dual objectives of encouraging an early start on the difficult theoretical problems in radiative transfer, magnetohydrodynamics, and plasma physics that will be posed by the HRSO data, and maintaining current discussions of results in high resolution solar studies. The Boulder, Colorado workshop was the second of the series, following the initial workshop held a year earlier in Munich, W. Germany. Subsequent workshops will be held periodically as deemed appropriate by the Science Working Group.

The format at the Boulder workshop continued the pattern set in Munich with invited review papers during the formal sessions and contributed poster papers for discussions during open periods. The Boulder meeting was timed to capitalize on the exciting new results emerging from the earlier Space Lab II mission. Results from the HRTS experiment were reviewed by G. Brueckner, J. Cook, and K. Dere and those from the SOUP experiment by A. Title. Following the reviews A. Title and H. Zirin described the two principal experiments planned for HRSO. A. Van Ballegooijen then reviewed the HRSO science objectives and the observing programs.

Discussion on the second day of the workshop shifted to observation and modeling of solar magnetic features and their associated velocity profiles. Invited reviews were presented by C. Zwaan, S. Martin, R. Moore and D. Rabin, V. Pizzo and P. Foukal. G. Doschek concluded the day with an important review of the need for high resolution data in the UV and EUV spectral regions.

A highlight of the meeting was the third-day reviews on magnetic diffusion by R. Rosner, MHD turbulence by D. Montgomery, and small scale energy storage and release by E. Parker. Additionally, many new and exciting results were presented in the 25 contributed poster papers.

The editors wish to express their thanks to other members of the organizing committee including: R. Fisher, H. Schmidt, A. Title, H. Zirin, and C. Zwaan. Additional thanks are due the High Altitude Observatory which hosted the meeting and especially K. Drake for making all necessary arrangements and handling all correspondence.

G. Athay
D. Spicer

PRECEDING PAGE BLANK NOT FILMED

CONTENTS

Invited Papers: Page

Contributed Papers:

N88-11610

MAGNETIC FIELD MORPHOLOGY IN THE UPPER LAYERS

V. J. Pizzo
High Altitude Observatory
National Center for Atmospheric Research[1]

ABSTRACT

We examine some basic properties of emerged magnetic flux concentrations, with emphasis on the interplay between the magnetic and thermodynamic structure in the region between the photosphere and the transition zone. The discussion is limited to the gross behavior of those phenomena that may be reasonably regarded as quasi-static, such as the longer-lived sunspots, pores, and some smaller magnetic flux tubes. Substructure and dynamic phenomena are not considered.

I. INTRODUCTION

In most regions of the solar surface, only a small fraction of the total area at deep photospheric levels is thought to be pierced by magnetic flux concentrations, yet the field is known to be essentially ubiquitous at coronal levels. In the important intervening region of the upper photosphere, chromosphere, and transition zone, then, the magnetic field evidently undergoes a rather drastic spreading with height. The physical factors which govern the magnetic topology of emerged flux concentrations are therefore of both theoretical and observational interest. In particular, the upper layers of emerged magnetic structures may be heated by both acoustic and magnetic waves, and the relative proportion of heating stemming from these and other sources is related to the fraction of the atmosphere threaded by magnetic fields at the relevant height. Theoretical models of the heating processes thus depend upon the assumed background magnetic structure, as does our interpretation of observations of solar and stellar emission from the upper layers.

Our discussion of the field morphology in the upper layers stresses two main points. First, understanding of the magnetostatic structure of solar flux concentrations stems from the relation among three factors: force balance, energy balance, and the way in which the observations are interpreted. The balance of gas pressure, magnetic, and gravitational forces directly determines the equilibrium geometry (or shape) of the magnetic configuration. However, the energy balance regulates the thermodynamic properties, which in turn influence the force balance. The energy transfer processes, of course, depend upon the geometric and magnetic properties of the structure. Thus in a real solar feature, force balance and energy balance cannot in general be legitimately discussed separately. Similarly, the observational properties of such structures are in most cases intimately related to their presumed thermodynamic and magnetic properties, i.e., the interpretation of the measurements are highly model-dependent, except in certain circumstances.

Second, we emphasize the importance of scale size -- the physical dimensions of the flux concentration -- on all three factors. At least in some aspects, the larger features (e.g. the centers of large, homogeneous sunspots) are simpler to understand on a theoretical basis and offer the best opportunities for making unambiguous observations on the sun. Small features like network elements, on the other hand, are inherently more complicated: the energy and force balance is strongly coupled and the observational inferences are closely tied to operational assumptions regarding the structure of the feature.

---

[1] The National Center for Atmospheric Research is sponsored by the National Science Foundation.

Finally, much of the emerged magnetic flux on the sun is manifestly bipolar in nature, i.e., the flux elements connect to some nearby point on the solar surface. Such structures are inherently three-dimensional (3-D) and hence pose a tough theoretical challenge. Nevertheless, because the bipolarity should have perceptible impact upon the the field morphology in the upper layers, techniques for generating truly 3-D magnetostatic models suitable for quantitative analysis are of obvious importance. We briefly touch upon relevant developments in this direction at the end of the paper.

II. THE SPREADING OF EMERGED FLUX -- GENERAL PRINCIPLES

Magnetic flux evidently erupts from the interior of the sun because the buoyancy associated with the reduced gas densities inside a submerged flux rope eventually forces it to the surface. At photospheric levels, the buoyancy is thought to be strong enough to cause the footpoints of the erupted flux concentration to be nearly vertical. The structure spreads with height because the overall gas pressure falls off more rapidly than does the field. However, the flux tube interior and the surrounding exterior fluid are subject to different heating mechanisms and the resulting lateral gas pressure gradients may alter the rate and extent of the expansion. In sunspots and pores, for example, the cool interior is at lower pressure than the exterior gas at the same height (the Wilson depression), causing the exterior gas to squeeze in and oppose the spreading described above. A similar sort of confinement occurs in smaller flux tubes, though they are evidently at more nearly the same temperature as the undisturbed photosphere. In groups of spots and pores, however, where the flux ropes reconnect to the surface in a compact and complex pattern, the individual strands may deviate strongly from the vertical. Nevertheless, the basic rationale that there must be spreading with height still holds, even if the expansion is modified by strong tension forces.

To illustrate the general principles involved in the spreading of emerged magnetic flux, let us consider the theoretical idealization depicted in Figure 1a (top). Here we view a vertically-oriented, cylindrically symmetric bundle of field lines that are fanning out with height about the axis. We assume the field lines are fixed (rooted) in place at some level $z = 0$ in the atmosphere and that the gas pressure at any given height z along the axis differs from that at the same height far from the axis. Let us also stipulate that the structure is magnetostatic (no flows) and twist-free. That is, gas pressure forces balance the Lorentz force in the horizontal direction, hydrostatic equilibrium obtains along field lines, and there are no field-aligned currents. Hence the field lines lie entirely in the plane of the Figure.

Let us now define some basic parameters governing the expansion. As measured at the base, we have

$\Delta P \equiv$ net horizontal gas pressure differential

$B^2/8\pi \equiv$ magnetic field pressure on the axis

$R \equiv$ horizontal scale (radius) of flux concentration

$H \equiv$ vertical scale of atmospheric ΔP variation.

By averaging the equation of horizontal force balance over a cylindrical volume of radius and height R about the axis and above the base ($z = 0$), it can be shown (Pizzo, 1986) that when

$$\frac{\Delta P}{B^2/8\pi} \lesssim \frac{R}{H} , \qquad (1)$$

the spreading of the field lines does not deviate significantly from a free, potential expansion, i.e., the solution to the boundary problem is little affected by the gas pressure forces. (By free, potential expansion we mean one in which there are no currents above the $z = 0$ surface.) Conversely, where the above

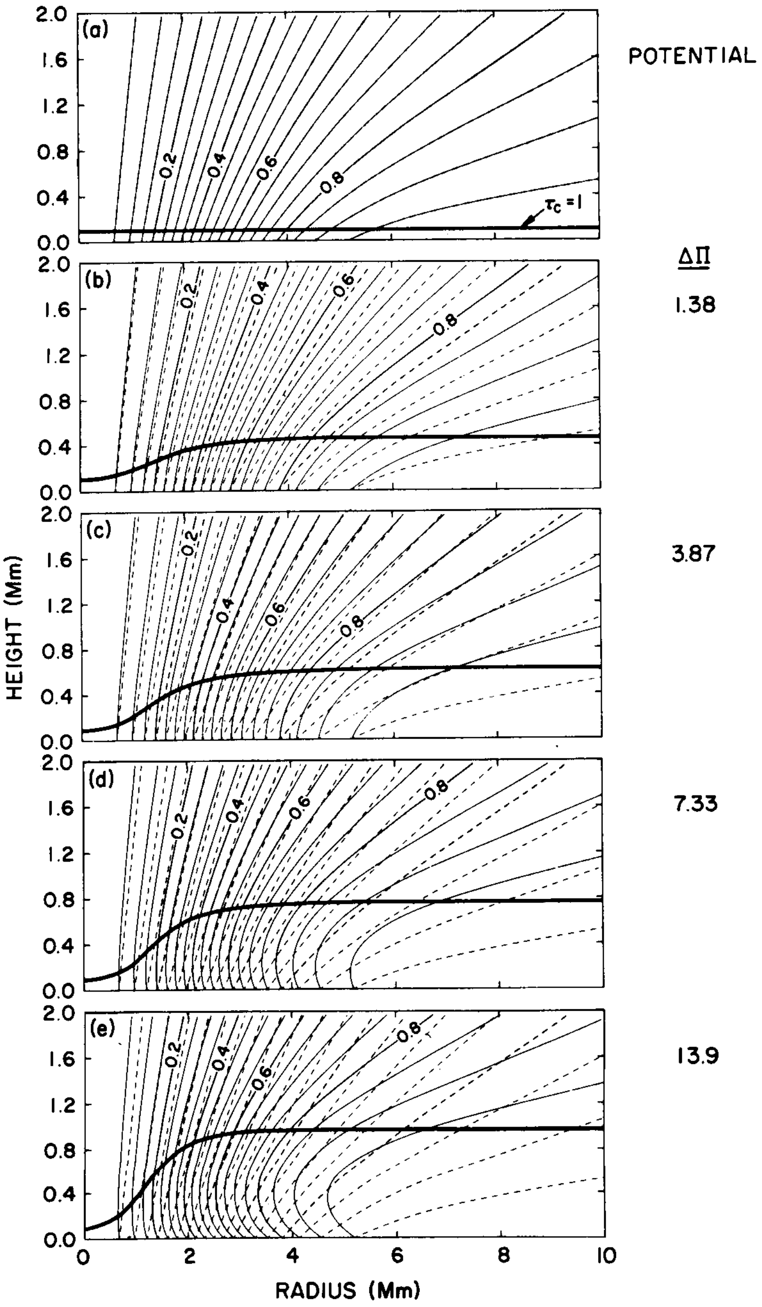

Fig. 1 -- Series of equilibria for a smoothly varying magnetic flux concentration in which the normalized horizontal gas pressure differential $[\Delta\Pi \equiv \Delta P/(B^2/8\pi)]$ increases from (a) to (e). Topmost panel (a) shows field lines for a purely potential ($\Delta P = 0$) solution which appears in each of the subsequent plots as dashed lines. The ΔP variation is generated by vertical displacement of an umbral model atmosphere (Avrett, 1981), which is presumed to obtain along the axis, against a quiet photosphere atmosphere (Spruit, 1977), which is presumed to obtain at large horizontal distances. The $\tau_c = 1$ surface is denoted by the heavy horizontal line to aid in visualizing the Wilson depression. Base axial field strength in all cases is held constant at B = 2.2 kG, and the size of the tube is fixed at R = 3.0 Mm. Labels on field lines indicate fraction of total flux interior to each line. (From Pizzo, 1986.)

condition is violated, the interior-exterior pressure differential will play a significant role in confining the flux tube in the atmosphere.

The physical basis for relation (1) can be traced in Figures 1 and 2. In each panel, the vertical coordinate (z) records height above the lower boundary (z = 0), which is set at some arbitrary level in the atmosphere just below the $\tau_c = 1$ visible surface (indicated by the heavy horizontal line); the horizontal coordinate (r) denotes distance from the symmetry axis (r = 0). Both are given in units of 1000 km. The lines fanning out portray the field lines for a magnetic flux concentration in which the normal component of the magnetic field along the lower boundary is given by a gaussian with an e-folding scale of R = 3000 km. (The lateral and top boundaries of the computational regime used to generate the solutions in Figs. 1 and 2 have been removed to very large distances to approximate a free expansion.)

The top panel of Figure 1 shows a purely potential solution, i.e., there are no horizontal pressure gradients ($\Delta P = 0$) and the magnetic field is force-free. The succeeding panels in Figure 1 demonstrate the effects of progressively increasing interior-exterior gas pressure differential on the equilibrium. As ΔP increases relative to the nominal base magnetic pressure, the field lines are squeezed in towards the axis more and more. Eventually (bottom panels), the constriction is so great that the field lines are bent into an hourglass shape. In these cases, equilibrium is rather graphically provided by the tension forces associated with the curving field lines acting in opposition to the encroachment of the external gas; but it is of paramount importance to recognize that throughout the Figure -- including the potential solution at the top -- magnetic tension plays a major role and lateral total pressure balance is not a prerequisite for equilibrium.

While this behavior is fairly straightforward, the effects of horizontal scale size are more subtle. In Figure 2, the interior-exterior pressure differential is held constant, while only the horizontal scale of the field R is varied. Scanning up from the bottom, we see that flux concentrations of the largest scale are the least affected by a given gas pressure deficit, while those of the smallest scale are most affected. What is happening here is that in the absence of gas pressure gradients, the magnetic field falls off vertically with a natural scale of order R. Hence the vertical distance over which the field pressure remains substantial is also of order R. The gas pressure differential, meanwhile, is falling off with a characteristic scale commensurate (in this particular case) with that of the exterior atmosphere, or H $\approx$ 350 km. For the examples towards the bottom of Figure 2, where R greatly exceeds H, the layer in which the gas pressure forces are significant is so shallow that only minor deviation from a potential solution results (note, the field responds globally to an external force, so the stress across the thin layer is distributed in varying measure to the whole configuration). In the panels towards the top, where R approaches H, the layer is relatively thick and the interaction correspondingly strong. Ultimately, in the limit where the field is of such small scale that R $<<$ H, the field wants to fan out so rapidly with height that the presence of even weak gas pressure differentials is going to have major effects, particularly in the upper levels of the configuration.

Although relation (1) is to be viewed as primarily functional in nature and is of limited quantitative value, it nonetheless offers some important insights, which can be summarized as follows:

1. Big structures, such as the larger leader and follower spots, require gas pressure differentials of enormous magnitude and depth to have much effect on the spreading above the photosphere; for credible solar values (e.g. Maltby, 1977), we might expect to find direct manifestation of the gas pressure confinement only near the edges of the structure (e.g., in the penumbra). Hence, with regard to establishing the overall shape of the structure, the thermodynamic properties in the region in and above the photosphere (where we can measure them) are relatively unimportant.
2. Small structures, in contrast, are inherently sensitive to gas pressure differentials and therefore to the details of the energy balance. In this case, the thermodynamic properties of

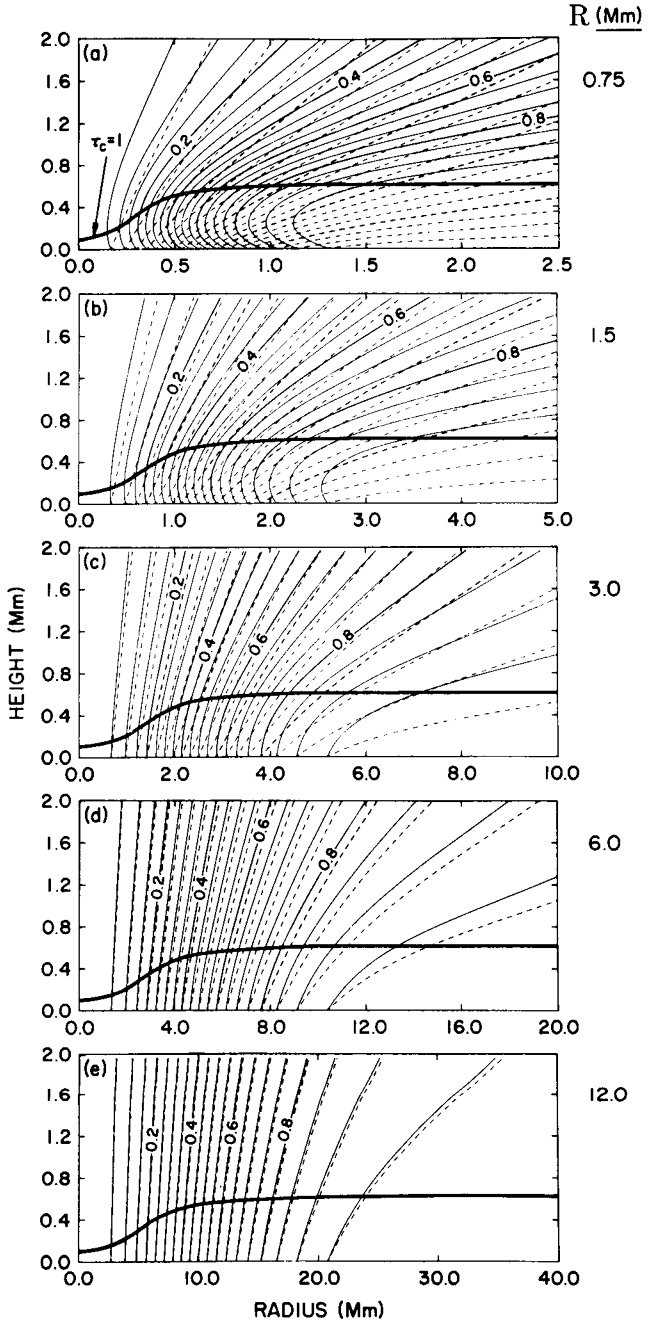

Fig. 2 -- Series of equilibria in which the tube radius R is varied between 0.75 Mm (a) and 12.0 Mm (e), while all else is held fixed. The vertical scale is the same as in Fig. 1, but the horizontal scale in each plot is proportional to R. (From Pizzo, 1986.)

both exterior and interior gas largely determine the expansion of the flux tube into the atmosphere.

Finally, it is to be emphasized that this dependence on scale size is a geometric property of the equilibrium and does not hinge upon details of the energy transfer or fine structure of the magnetic configuration. Although the behavior implicit in (1) was derived on the basis of smooth distributions of magnetic flux and gas pressure, as were the examples illustrating that relationship, the fundamental principles are not vitiated by the presence of current sheets or thermodynamic discontinuities. Such complexities will only wreak quantitative changes in the relationship and result in local modifications of the equilibrium structure.

III. PRACTICAL APPLICATION TO SUNSPOTS

The functional relationship (1) suggests a simple but telling test of the theoretical concepts sketched out above. Namely, it says that the centers of large sunspots (R $>$ several thousand km) ought to be thoroughly insulated from the crush of the surrounding atmosphere and therefore only the most minor deviations from free, potential expansion are to be anticipated. Accordingly, the observed magnetic field structure in the upper layers of a large spot should compare favorably with the predictions of a potential calculation based on the observed normal photospheric field. Though simple in the extreme, the importance of conducting such an experiment cannot be overstated: there is no place on the entire sun where physical conditions conform so neatly with the assumptions implicit in the analysis of magnetic spectral data and where we have greater confidence in our ability to accurately predict the magnetic structure. Indeed, if we cannot confirm theoretical expectations in so straightforward a test case, one must seriously question how much progress we can expect to make in divining the small scale structures that are the object of this conference.

The general idea of comparing observations of the magnetic field in spots with model calculations has been around for some time. These attempts have taken two tacks: measurements of the longitudinal field in several lines at different presumed heights to obtain an estimate of the vertical variation of the magnetic field (Beckers and Schroter, 1969; Abdussamatov, 1971; Wittman, 1974; Henze *et al.*, 1982); and, measurements of the vector magnetic field, from which the vertical gradient may be deduced via the divergence-free condition (Denisenko *et al.*, 1982). The most comprehensive of these studies (Hagyard *et al.*, 1983), combining both techniques, indicates that the field probably does not deviate significantly from potential between the photosphere and transition zone.

The problem with these studies, however, is that they are based upon one or a few spots and suffer from uncertainties introduced by the lack of an absolute reference frame for the height of line formation. In addition, all are done at fairly marginal resolution, so that only the vertical gradient near the axis can be estimated with any degree of confidence. The end result is a large scatter in published estimates of the axial vertical gradient and only the most rudimentary data on the evolution of the overall structure with height.

The scaling relation (1) suggests a procedure whereby many of these difficulties could be circumvented. Specifically, because the centers of large, symmetric, isolated spots should have a nearly potential structure, it follows that measurement of the vertical gradient of the axial field $(\partial B_z / \partial z)/B_z$ in a sequence of sunspots of varying horizontal dimension R should show a 1/R trend. There are at least two ways to implement this strategy. The simplest approach parallels earlier studies, in that one would measure B_z in several spectral lines formed at different (and unknown) heights. If the field is really potential, then the 1/R scaling should be evident, *so long* as each spectral line giving rise to the magnetograph signal is formed at the same respective height in the atmospheres of the different spots in the sequence. (For sufficiently large, uniform spots this should be a less risky proposition than deriving the actual heights of line formation from some generic umbral model.) Thus, even without direct knowledge of the line formation heights, one should be able to test convincingly whether the basic geometric properties of the expansion embodied in (1) are indeed valid.

A more complicated experiment, also drawing upon previous efforts, would be to use the observed line-of-sight field in the photosphere to generate a potential model prediction for the overlying magnetic structure and to compare the predicted structure with the observed 2-D distribution in the upper layers. By again assuming that a given line is formed at the same height in all spots of sufficient size, it would be possible to obtain an estimate for that height by seeking consistency of the fit between the model and the observations. A meaningful fit would simultaneously show low variance in the inferred heights of line formation and would exhibit the 1/R scaling in the vertical field gradient.

In either case, the advantage over previous attempts comes from the added constraint afforded by the 1/R scaling of a sequence of spots, as opposed to singular observations of random examples. The scaling may be anticipated to break down systematically in smaller spots and pores, where gas pressure forces become strong enough to affect the entire magnetic structure. It is at this juncture that it becomes possible -- in principle -- to use spectral observations in the upper layers to obtain information on the vertical run of gas pressure below $\tau_c = 1$ in the surrounding photosphere. Provided accurate, high-quality observations can be secured across the entire feature, there is the hope that iteration between the observed spectra and magnetostatic model predictions should converge to a self-consistent structure. Pores may offer the most lucrative return in this regard because they are of sufficiently small scale so as to ensure a strong interaction between the field and the confining gas, yet they are large enough to permit detailed, localized observations if high-resolution instrumentation is employed. Though pores may be construed as unlikely targets for the sort of hardware discussed in this conference, it is to be stressed that the essential information for our purposes resides in the field distribution. If the iterative process envisioned above is to converge uniquely, many data points across the structure -- and therefore quite high resolution -- are required to make the project feasible. For this reason, structures much smaller than pores are inappropriate.

IV. FIELD SPREADING IN THE UPPER LAYERS OF SMALL STRUCTURES

The field expansion in the upper layers of smaller structures, like magnetic elements, is far more complicated than in spots. This is because the energy transport mechanisms are more diverse and that the thermodynamic properties couple into the force balance more directly. Radiation, for example, plays an increasingly important role in establishing the equilibrium thermodynamic structure at and above the photosphere as the scale size of the feature decreases (Spruit, 1976; Kalkofen *et al.*, 1986): radiation from the hot surrounding walls, which penetrate only a short distance horizontally into the umbra of a large spot at photospheric levels, can instead pass entirely across the Wilson depression of a network element. Thus, while the cool lower portions of a spot are effectively insulated from the hotter gases in which they are embedded, the interior of a small flux tube is openly bathed in the external radiation field and should not depart too far from thermal equilibrium with it. Other mechanisms, such as the dissipation of mechanical energy by waves (Spruit, 1982; Ulmschneider and Stein, 1982) and compressive downdrafts (Ribes and Unno, 1976; Hasan and Schussler, 1985), may also contribute to the heating of the upper layers of flux tubes.

The spreading of the magnetic structure is linked to the energy balance via the gas pressure forces. Relation (1) tells us that the smaller the scale size, the greater the effect a given gas pressure differential will have on the magnetic structure. For features at the small end of the horizontal scale spectrum, then, internal-external thermodynamic differences essentially dictate the expansion of the field, at least in the photosphere.

If internal and external temperatures at and above the surface of small structures are roughly equal, then the classic thin flux tube approximation for the field expansion may pertain. For tubes whose horizontal dimension R is less than four times the external atmospheric scale height, it can be shown (Parker, 1955; Roberts and Webb, 1978) that the magnetic field spreads at a very slow rate: the field lines at photospheric levels are nearly straight and vertical, magnetic tension forces are negligible, and the field strength is almost uniform across the tube (see Figure 3). The spreading increases in the upper layers, so that, for typical fill factors, the height at which neighboring tubes begin to merge together is well up into the chromosphere. Twisting the fieldlines in the flux tube has only minor effect upon the merging height (Pneuman, Solanki, and Stenflo, 1986; Steiner, Pneuman, and Stenflo, 1976).

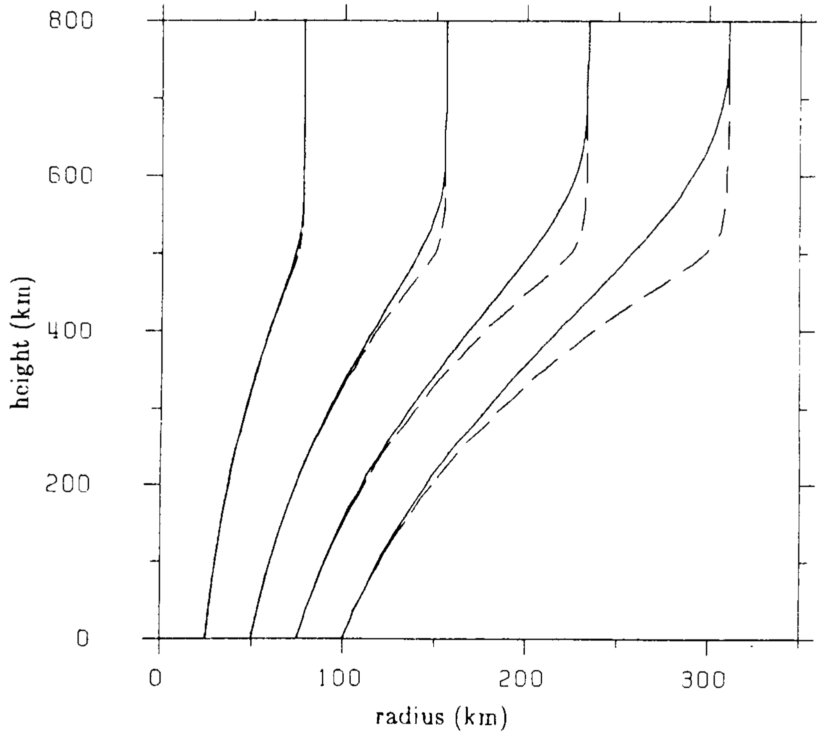

Fig. 3 -- Shape of flux tubes of several different radii as computed from thin flux tube approximation (dashed) and an expansion technique involving second-order corrections in the tube radius (solid). Note that the larger tubes spread out flatter. (From Pneuman, Solanki, and Stenflo, 1986.)

In terms of the scaling relation (1), the thin flux tube approximation represents a particular realization of the regime wherein the gas pressure differential is large enough to distort the magnetic structure far from a free, potential expansion. Note, however, that its applicability hinges upon the assumption that the temperature differences are small and that total pressure balance really does apply at the level in the atmosphere at which the flux tube is presumed to be rooted (which depends, in part, upon the scale size R). Under these conditions, the gas pressure differential falls off with height with the same scale as the external atmosphere, and the flux tube experiences significant constriction for a considerable vertical distance. (Recall that as R approaches H, the natural scale of the vertical magnetic field decline shrinks proportionately, enhancing the effects of the gas pressure differential.)

Unfortunately, the available observations provide little insight as to the details of the thermodynamic state of small scale structures. Numerous attempts have been made to infer the temperature and pressure profiles for small flux tubes (e.g. Foukal and Duvall, 1985; Solanki and Stenflo, 1985; Foing, Bonnet, and Bruner, 1986), but the observational difficulties are severe. Not only does the spatial resolution of the instrument impose serious limitations, but so also does the inherent vertical averaging of the magnetograph signal in structures which may well be significantly inhomogeneous over the height of line formation. Perhaps the best that can be stated at present is that there is some evidence for heating within small flux concentrations and that they are probably bright in the continuum, rather than cool and dark like spots (Spruit and Zwaan, 1981). On the other hand, the magnitude and spatial distribution of this heating is not known with any confidence and it is therefore impossible to assess whether the thermodynamic state is generally consistent with the simple radiatively dominated picture outlined above or to identify with any precision where additional heating may become important.

Therefore, until the advent of high resolution instruments of the type advocated in this conference series, progress on understanding the physics of the smaller magnetic concentrations depends heavily on theoretical advances. Two of the most important questions remaining to be answered are:

1. How does heating take place in a spreading magnetic field?
2. How does this heating affect the magnetic topography and its observational properties?

We shall offer some ideas on the second question first, as recent developments allow us to draw a qualitative picture with some confidence. To begin, let us consider a vertically-oriented flux tube in which the internal and external temperatures are equal at any given geometric height in the atmosphere. Let us further stipulate that the tube is of sufficiently small horizontal scale to justify application of the thin flux tube approximation. Thus, the field lines are nearly straight and spread out substantially only at great heights. Suppose the flux tube is now subjected to some heating, which, for the sake of argument, is uniform across the tube and varies only with height along it. The effects of heating upon the force balance may then be summarized as follows:

1. If the temperature enhancement is significant and the structure may be viewed as magnetostatic, then the internal-external pressure differential profile must be affected. For heating, the internal pressure is increased and ΔP must be accordingly reduced.
2. A reduced ΔP causes the tube to spread more than before, since the internal total pressure is increased.
3. If the heating occurs low enough and is of sufficient magnitude, the force balance will be seriously affected and the shape of the flux tube changed. However, if it is confined to the uppermost reaches of the structure, the effects on the spreading will be minimal, as the absolute magnitude of the gas pressure there is so low that the equilibrium state is essentially force-free. Hence even moderate heating at photospheric levels is of greater consequence than vigorous heating in the chromosphere.

Two recent studies directly address the question of flux tube spreading with height in response to an imposed internal temperature enhancement. In one, Pneuman, Solanki, and Stenflo (1986) considered flux tubes wherein the internal temperature was held at some fixed fraction of the local exterior temperature all along the tube. (Such a scenario is physically unrealistic, but it does illustrate the basic principles.) The results for three model tubes are shown in Figure 4, where the merging height serves as a measure of the spreading rate. The tubes with cool interiors ($T_e > T_i$) exhibit little dependence upon the temperature ratio because the lower internal temperatures cause such a rapid fall-off in density with height that the interior is essentially evacuated. As progressively warmer internal temperatures are considered, however, the internal gas pressure becomes significant, forcing the tube to spread more rapidly and thus to reduce the merging height.

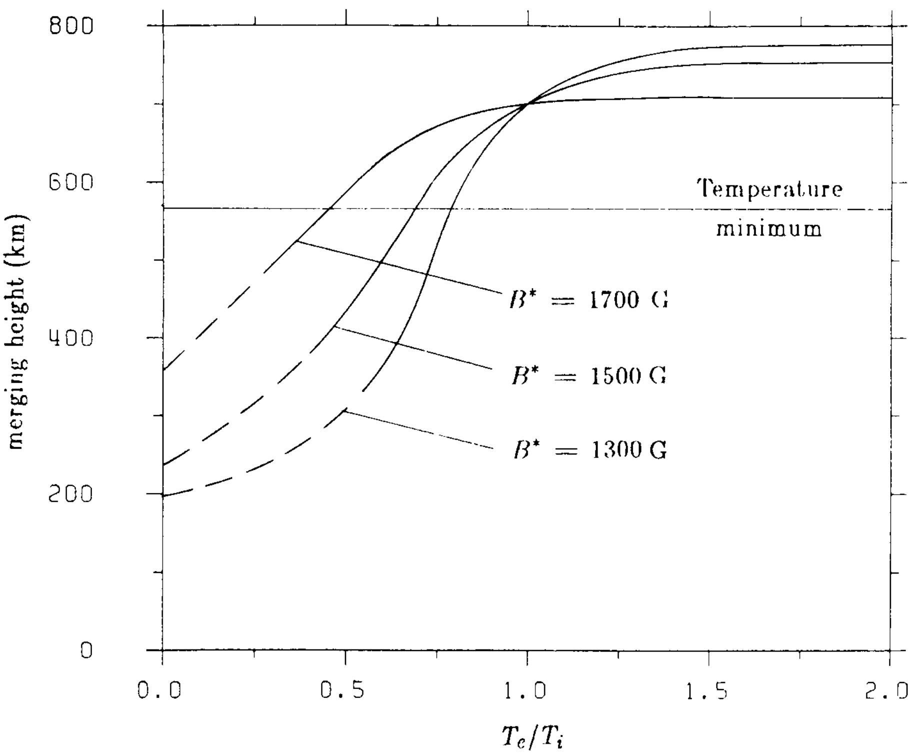

Fig. 4 -- Dependence of merging height upon ratio of external (T_e) to internal (T_i) temperature for different base magnetic field strengths. At $T_e/T_i = 1$, the merging height is independent of the field strength. For $T_e/T_i > 1$ the height decreases with increasing field strength and for $T_e/T_i < 1$ the reverse is true. (From Pneuman, Solanki, and Stenflo, 1986.)

Figure 4 also points up a subtlety of parametric modeling. Note that the tube with the greatest field strength shows the least spreading, in apparent contravention of relation (1). The resolution of the problem lies in recognizing what is held constant in the parametric series. Since it is desired to enforce horizontal total pressure balance at the base across the entire parameter range, it becomes necessary to reduce the base density (a free parameter of the calculation) to compensate for the higher field strengths and for the increase in the internal temperature due to the applied heating. The density profile at all higher levels is therefore affected, and the net internal gas pressure enhancement is accordingly diminished. In short, increasing the temperature in a sequence of models need not increase the internal pressure to the degree one might first suppose, depending upon what else is held constant.

A second parametric study aimed at elucidating heating effects utilizes a numerical technique (Steiner, Pneuman, and Stenflo, 1986) to obtain full magnetostatic solutions for flux tubes bounded by a current sheet (Steiner and Pizzo, in progress). A horizontally uniform temperature increase of arbitrary magnitude and vertical scale is introduced above some $z = z_c$ in the model tubes to simulate the effects of heating in the upper layers. Preliminary results indicate that temperature enhancements of several thousand degrees occurring within several hundred kilometers of the $\tau_c = 1$ level in the undisturbed photosphere are needed to produce a major change in the spreading rate. It is not at all clear that heating of this magnitude can be supported by the observations. The models suggest, however, that the optical and magnetic signatures may still be seriously affected even if heating does not change the overall shape of the tube very much. What happens is that the increase in opacity stemming from the elevated temperatures and densities shifts the surfaces of constant τ higher up in the tube, where the magnetic field begins to fan out. Hence, the observed properties may be altered perceptibly, leading to erroneous interpretations.

Parametric studies such as these are illuminating and instructive, but their many simplifications restrict their utility. Most onerous are those associated with the neglect of energy balance. It is to be expected that radiation, conduction, and wave transport effects should impose limits on the amount and location of heating, and they must therefore be included in any realistic physical model. Further progress in this area thus awaits the application of more sophisticated treatments that take the energy transport and force balance into account self-consistently (e.g., Deinzer *et al.*, 1984a,b).

In this context, we return to the question concerning wave heating in a spreading magnetic field. Owing to formidable computational problems, theoretical efforts to date (see the review by Thomas, 1985, and the references therein) have included the influence of the magnetic field upon the propagation and dissipation of waves in only the simplest ways. Allowance is made for the variation of field strength along the tube, but the curvature in the field lines is neglected. This is perhaps justifiable in the deep photosphere but clearly breaks down in the upper layers. Neglect of the field spreading eliminates an important mode-coupling mechanism and may result in serious underestimation of the role played by fast-mode waves.

In a similar vein, we note that spreading is an inherently differential effect and that wave heating effects might be quite inhomogeneous. Typically, the field intensity along the axis exceeds that at the edges in the upper layers of the flux tube models, the difference increasing with the spreading. If the density is relatively stratified, lower field intensity at the edge implies a lower alfven speed there. This raises the possibility of differential heating, as waves may be refracted into regions of low relative alfven speed under certain conditions (e.g. Habbal, Leer, and Holzer, 1979). Furthermore, the low field strengths at the edges of flaring structures make them locally more susceptible to the effects of gas pressure forces due to any such heating. Therefore, it is conceivable that a highly inhomogeneous structure could exist in the upper layers -- a cool, concentrated, nearly vertical core surrounded by a warm, diffuse, predominantly horizontal fringe. Such a structure would only be revealed by high resolution observations, and, even then, proper analysis of the spectroscopic data might be complicated by the line-of-sight inhomogeneities.

Thus, the feedback between heating, field spreading, and observational properties virtually guarantees that improved understanding of the wave processes occurring in rapidly flaring flux tubes will lead to interesting new perspectives on the state of small scale erupted flux on the solar surface.

V. THREE-DIMENSIONAL MAGNETIC STRUCTURE

Thus far, we have been treating emerged magnetic flux concentrations as isolated phenomena, i.e. with little regard for their interaction with the surrounding magnetic medium. For many solar features, particularly sunspot groups, this conceptualization is overly simplistic and obviously inadequate. While some 3-D aspects of the network structure, for example, may be approximated with a 2-D arcade configuration (e.g. Gabriel, 1976; Deinzer *et al.*, 1984a,b; Jones, 1985), it is to be expected that tension forces should play an important role in the equilibrium force balance of 3-D structures down into the photosphere and that this modified state should be reflected in the thermodynamic properties. Unfortunately, computational difficulties have long stood in the way of quantitative magnetostatic models of collections of flux tubes in realistic 3-D geometries, and only purely potential models have been available to study more complex and therefore more interesting structures (e.g. Anzer and Galloway, 1983). While such models may, in some instances, provide a reasonable approximation to the magnetic structure of the nearly force-free upper layers, on a practical basis they incorporate into their boundary conditions information taken from deeper layers, where thermodynamic effects are non-negligible. Furthermore, even in the upper layers, potential models neglect tension forces associated with field-aligned currents stemming from footprint displacements, for example.

Recently, a methodology has been worked out making it feasible to obtain 3-D magnetostatic solutions with surprising ease (Low, 1985). The power of the technique lies in its mathematical proximity to standard boundary value problems and in the computational tractability accruing from longstanding practical experience with these methods. It is able to include simultaneously the effects of both field-aligned and drift currents in a realistic, though not completely general way. The weakness in the approach is that it hinges upon an assumption that is of dubious validity in the real solar atmosphere and that the parameterization used to construct the individual examples is convolved and obscure. (Explication of the technique is beyond the scope of this review, and the reader is referred to the original work for full details.) What is important for our purposes, however, is that the formulation -- despite its shortcomings -- provides an avenue for tackling for the first time some intriguing questions concerning the influence of bipolarity on flux tube structure. Is, for example, the spreading of flux tubes with height changed in any substantial way when they are in the form of loops tightly connected to the solar surface? What is the nature of the magnetic field topology in the upper layers of a complex spot group? What are the properties of the associated magnetograph signal, especially for structures at and below the resolution limit? All these questions and more could be addressed if the requisite modeling were pursued vigorously; it is virgin territory waiting to be explored.

SUMMARY

We have considered how the interplay between magnetic and gas pressure forces regulates the spreading of simple magnetic flux concentrations with height above the solar surface. We have suggested that the magnetic structure in the center of large sunspots provides a simple observational test of the basic physical concepts and have discussed some theoretical and observational intricacies associated with small magnetic features. In addition, we have identified theoretical questions concerning wave heating in flux tubes and 3-D effects in erupted active region groups that need to be addressed if proper advantage is to be taken of the high resolution observations hopefully to be obtained in the future.

ACKNOWLEDGMENTS

The author wishes to thank T. J. Bogdan for reading the manuscript and L. Croom for her assistance in its preparation.

REFERENCES

Abdussamatov, H. I., 1971, Solar Phys., 16, 384.

Anzer, U., and Galloway, D. J., 1983, M.N.R.A.S., 203, 637.

Avrett, E. H., 1981, in The Physics of Sunspots, ed. L. E. Cram and J. H. Thomas (Sunspot: Sacramento Peak Observatory), p. 235.

Beckers, J. M., and Schroter, E. H., 1969, Solar Phys., 10, 384.

Deinzer, W., Hensler, G., Schussler, M., Weisshaar, E., 1984, Astr. Ap., 139, 426.

________, 1984, Astr. Ap., 139, 435.

Denisenko, V. V., Kotov, V. A., Romanov, V. A., and Sokolov, V. S., 1982, Solar Phys., 81, 217.

Foing, B., Bonnet, R.-M., and Bruner, M., 1986, Astr. Ap., 162, 292.

Foukal, P. and Duvall, T. Jr., 1985, Ap. J., 296, 739.

Gabriel, A. H., 1976, Phil. Trans. R. Soc. Lond. A, 281, 339.

Habbal, S. R., Leer, E., and Holzer, T. E., 1979, Solar Phys., 64, 287.

Hagyard, M. J., Teuber, D., West, E. A., Tandberg-Hanssen, E., Henze, W. Jr., Beckers, J. M., Bruner, M., Hyder, C. L., and Woodgate, B. E., 1983, Solar Phys., 84, 13.

Hasan, S. S., and Schussler, M., 1985, Astr. Ap., 151, 69.

Henze, W. Jr., Tandberg-Hanssen, E., Hagyard, M. J., Woodgate, B. E., Shine, R. A., Beckers, J. M., Bruner, M., Gurman, J. B., Hyder, C. L., and West, E. A., 1982, Solar Phys., 81, 231.

Jones, H. P., 1985, Aust. J. Phys., 38, 919.

Kalkofen, W., Rosner, R., Ferrari, A., and Massaglia, S., 1986, Ap.J., 304, 519.

Low, B. C., 1985, Ap. J. 293, 31.

Maltby, P., 1977, Solar Phys., 55, 335.

Parker, E. N., 1955, Ap. J., 121, 491.

Pizzo, V. J., 1986, Ap. J., 302, 785.

Pneuman, G. W., Solanki, S. K., Stenflo, J. O., 1986, Astr. Ap., 154, 231.

Ribes, E., and Unno, W., 1976, Astr. Ap., 53, 197.

Roberts, B., and Webb, A. R., 1978, Solar Phys., 56, 5.

Solanki, S. K. and J. O. Stenflo, 1985, Astr. Ap., 148, 123.

Spruit, H. C., 1976, Solar Phys., 50, 269.

________, 1977, Ph.D. thesis, University of Utrecht.

________, and Zwaan, C., 1981, Solar Phys., 70, 207.

Steiner, O., Pneuman, G. W., and Stenflo, J. O., 1986, submitted to Astr. Ap.

Thomas, J. H., 1985, in Theoretical Problems in Astrophysics, ed. H. U.Schmidt (Munich: MPA 212), p. 126.

Ulmschneider, P., and Stein, R. F., 1982, Astr. Ap., 106, 9.

Wittman, A., 1974, Solar Phys., 36, 29.

N88-11611

ACTIVE REGION FLOWS

Peter Foukal
Cambridge Research and Instrumentation, Inc.
Cambridge, Massachusetts

Abstract

A wide range of observations has shown that active region phenomena in the photospheric, chromospheric and coronal temperature regimes are dynamical in nature. We focus here on three topics where substantial developments have occurred in the past few years. At the photosphere, recent observations of full line profiles place an upper limit of about ±20 msec^{-1} on any downflows at supergranule cell edges. Observations of the full Stokes V profiles in the network show no evidence for downflows in magnetic flux tubes either, although the errors here are still an order of magnitude larger. Velocity observations such as those planned with HRSO can be designed to avoid the spurious signals generated by line profile changes.

In the area of chromospheric dynamics, several models have been put forward recently to reproduce the observed behavior of spicules. However, we point out that these adiabatic models do not include the powerful radiative dissipation which tend to damp out the large-amplitude disturbances that produce the spicular acceleration in the models. HRSO observations would be helpful in tracing spicule development from the triggering process through evolution of the structure, and thus help to decide whether much longer-period photospheric disturbances or spicule triggering at much higher altitudes might avoid the dissipation and produce more promising results.

In the corona, loop flows along field lines clearly transport mass and energy at rates important for the dynamics of these structures. However, advances in understanding the heating and mass balance of the loop structures seem to require new kinds of observations. We present some results using a remote sensing diagnostic of the intensity and orientation of macroscopic plasma electric fields predicted by models of reconnective heating and also wave heating. Use of this diagnostic should be possible from HRSO with significantly higher spatial resolution and sensitivity than is possible from the ground.

PRECEDING PAGE BLANK NOT FILMED

I. Introduction

We have seen many fine space- and ground-based observations presented at this meeting. It is probably useful to show an old observation to remind us that the subject of flows in active regions, and their control by electromagnetic forces, is quite venerable. Figure 1 is a drawing made of an active region at the limb in H_α by A. Secchi on October 5, 1871. This drawing, made from visual observations through a spectrohelioscope, shows most of the basic structures we are still seeking to understand--a well-defined loop system, coronal rain, spicules and some surging activity. This illustrates a point which has been made also in several of the preceeding papers, that interpretation is lagging rather far behind observations.

The remedy is of course not to stop observing--understanding can come only from much better data of the kind that we expect from HRSO. But we do perhaps need to think more clearly about the specific observations that are required to answer some rather long-standing and relatively well-posed problems.

II. Overview of Active Region Flows

Figure 2 shows schematically some of the basic types of flows that have been identified in active regions (see, e.g., review by Athay 1981). Associated with spots we find the strong Evershed flows of the penumbra, and in the H_α superpenumbra that overlies it, a predominant inflow. Evidence on the Evershed outflow indicates it is confined to dark penumbral filaments of relatively low magnetic field strength (see review by Moore 1981). It is not yet clear whether it represents a steady outward flow or whether it reverses within individual filaments on time scales comparable to the penumbral crossing time and returns along less visible paths. Within spots, one finds a relatively static atmosphere, with no detectable large-scale flow (Beckers 1977). In the corona above the spot we observe predominantly downflowing material, "coronal rain," not only in H_α, but also in the EUV radiations (Foukal 1978, Brueckner 1981).

The excellent HRTS rocket and Spacelab data also give us our best look at flows in coronal radiations, which consist of up and downflows over spots and plages at velocities around 30 km $\sec^{-1}$ (Brueckner 1981). Analysis of the Skylab EUV data showed rapid variations in the intensities of plasma radiations, which have been interpreted as explosive bursts (Emslie and Noyes 1978). In the chromosphere we have many observations of spicules and fibrils in visible radiations (see review by Beckers 1972) and now also in the ultraviolet (Cook 1985).

Lower in the atmosphere, there has been much work on flows in and around magnetic flux tubes ever since the report of systematic redshifts in network boundaries by Simon and Leighton (1964), and the later report of strong downdrafts within the small network flux tubes by Giovanelli and Slaughter (1978). The relative motions of photospheric flux tubes are in themselves tracers of velocity fields at deeper layers (see, e.g., review by Gilman and Foukal 1979).

Since there isn´t time to discuss all of the above flow phenomena, I would like to concentrate on three topics where interesting progress has been made in observations and theory. One area is the observational evidence on photospheric flows inside and around flux tubes, and their relation to the supergranulation. Another is the dynamics of spicules and fibrils. Finally, I would like to present some new observational evidence with a direct bearing on the dynamics of coronal flows in magnetic loops.

III. Photospheric Flows at Supergranule Boundaries and Within Flux Tubes

The observations of the supergranular flow pattern obtained by Simon and Leighton (1964) led to the concept of an overturning supergranular convective cell. Strong horizontal flows $v_h \sim 0.5$ km sec^{-1} are observed to diverge from the cell center. No good evidence has ever been given for any significant upflow velocity $v_u \gtrsim 10$ msec^{-1} (Giovanelli 1980). However, relatively strong redshifts near the flow edges were interpreted as downflows of amplitude 100-200 msec^{-1}. The correlation between network (marked by excess brightness in Fraunhofer lines) and redshifts is well illustrated by Tanenbaum et al. (1969).

Observations by Howard (1972) and others showed that systematic redshifts over network and faculae were observed whenever a magnetograph Doppler servo was used to measure photospheric velocities. The large areas covered by these apparent downdrafts and the absence of any detectable compensating blue-shifted material led to the increasing suspicion that at least a large part of the redshift was generated by magnetic suppression of the blue-shift of Fraunhofer lines. This blue-shift near disc center is known to be caused by the intensity-velocity correlation of granules (see review by Dravins, Lindegren and Nordlund 1981). Somewhat surprisingly, the observations of full line profiles at cell centers and boundaries needed to resolve this question were not obtained until quite recently (Miller, Foukal and Keil 1984, Cavallini, Ceppatelli and Righini 1985).

Our line profile results for the two g = 0 FeI lines λ 5434 and λ 4065 are shown in Figure 3a. The two left panels show the line profiles observed in cell centers and in the network. The right two panels show the bisectors of the cell and network profiles at a scale expanded 40 times. All the bisectors show the characteristic "C" curvature (Dravins, Lindegren and Nordlund 1981), but the network bisector curvature is less than that of the cell bisector. Both the absolute curvature and the cell-network curvature are larger for λ 5434 than for λ 4065, which is formed over a narrower height (and velocity) interval.

We can see that if the relative position of the cell and network λ 5434 profiles were measured with a line-wing sensor such as a magnetograph, the network profile would appear shifted to the red by 100-200 msec^{-1}. But the cell and network bisectors coincide in the line core for both the lines shown here. This indicates that no relative velocity between cell and network is measured in that part of the line profile formed highest and thus least affected by the granulation I-V correlation.

Figure 3b from Miller, Foukal and Keil (1984) shows how the observed decrease of network line curvature can be simulated for atmospheres in which the effect of granular convection is decreased by specified amounts. The observed decrease can be produced, for instance, by a model in which roughly 20% of the network area is covered with flux tubes that completely inhibit granular convection. Figure 3c from Cavallini, Ceppatelli and Righini (1986) shows how closely the observed bisectors can be simulated with a more sophisticated model.

The close coincidence of the cell and network bisectors in the line cores shows that any general downflows present in the network must lie below the noise level of ±20 msec^{-1} of our study. This limit on downflow velocity at supergranule cell edges is not low enough to rule out supergranulation as an overturning cell pattern. The continuity equation can still be satisfied (at least kinematically) if we suppose that the horizontal flow at v_h ~ 0.5 km sec^{-1} is confined to a thin layer comparable to the depth of photospheric line formation, with up- and downflows over large areas. However, it is questionable whether such a pattern would be dynamically realistic and stable. Unfortunately, there are no good dynamical models of supergranulation to use for guidance.

The ±20 msec^{-1} limit we have placed on v_d is based on about 5 arc sec spatial resolution, so it does not rule out the possible existence of much larger downdrafts inside flux tubes occupying only a small fraction of the network area. Giovanelli and Slaughter (1978) were the first to use the technique of observing the position of the V Stokes profile which measures the degree of circular polarization, and thus is indicative of flows inside the flux tube. They found a red-shift indicating downflow of 0.6 kms^{-1}

More recently, Stenflo et al. (1984) have observed the full Stokes V profile of network structures using the Fourier Transform Spectrometer at Kitt Peak. They find no evidence for a downflow, but they do note a pronounced asymmetry of the red and blue V profile intensities (Fig. 4), which could explain how the observations of Giovanelli and Slaughter (made by setting on the line wings with a magnetograph) might have indicated an apparent redshift. More recent observations by S. Solanki and E. Wiehr indicate that a discrepancy between the results of Stenflo et al. and later observations of Wiehr (1985) have been resolved in favor of the observation of no downflows exceeding ±0.25 km sec^{-1}. The relatively large error on these observations is due to the large uncertainty in the absolute rest wavelength of the lines used, which is required as a reference for the zero-level crossing of the V Stokes profile.

The above discussion indicates that there is presently no direct observational evidence for downflows at supergranule edges, nor inside magnetic flux tubes. Another conclusion is that line-wing comparisons such as used in magnetographs are not well suited to measurement of small velocities of order 10 msec^{-1} in solar plasmas where line profile asymmetries can account for apparent shifts of several hundred meters sec^{-1}. It is helpful to use lines known to be relatively less susceptible to the I-V correlation, such as λ 4065. Alternatively, velocities can be measured through shifts in the line core (e.g., Kuhn 1983). Studies of line profiles with a spectrograph are required to check results.

IV. Dynamics of Spicules and Fibrils

Observations of spicules at the limb and their Hα disc analogues seen as network rosettes and fibrils indicate that these structures are ubiquitous in solar magnetic regions, and their propulsion must be due to a rather general mechanism. The observations (see, e.g., Beckers 1972) indicate that we have a relatively cool (~ 10^4K), dense ($\rho \sim 10^{-13} g\,cm^{3}$) plasma column propelled to a height of 7-10x10^3 km over 5-10 mins at a velocity of about 10-20 km sec^{-1}. It turns out that these deceptively simple requirements pose a dynamical problem which is not yet solved.

Following the work of Osterbrock (1961) most models have considered the spicule to be the more or less direct result of a pressure disturbance originating in the photosphere and propagating outward along the magnetic field lines. Since these field lines become force-free in the chromosphere, the problem reduces essentially to that of a shock tube at these altitudes. The most basic difficulty facing dynamical models is how to account for the rather high density at heights of up to 10^4 km, without producing high temperatures and flow velocities far in excess of the observed values. Since adiabatic shocks produce only modest compression, the density requirement at $h \sim 10^4$ km seems to require that the plasma of $\rho \sim 10^{-13}$ g/cm^3 that is found at $h \sim 2000$ km in quiet sun models be propelled upwards by about 8000 km.

This problem has been studied in most detail by Suematsu et al. (1982) and Hollweg (1982). Their results are similar, and we describe them using figures from Suematsu et al. Figure 5a shows a 3-D representation of the upward propagation of the disturbance, and the response of the transition region. We see that as the disturbance moves through the transition region and on outwards into the corona, the cool material is propelled outward along ballistic trajectories (see also Fig. 5b), and eventually begins to fall back. A feature of these models are the rebound shocks that continue to be generated from the base of the atmosphere in response to the original disturbance. These successive shocks continue to lift the cool material to spicular heights.

The flaw in these interesting models is their adiabatic nature, which does not take into account the powerful dissipation that must decrease the amplitude of non-linear waves and shocks propagating through the upper photosphere and chromosphere. The importance of this dissipation is illustrated in Fig. 6a (from Ulmschneider 1971) for simple waves of flux density similar to that required for spicule excitation. We see that compressional waves of period below 50 secs used by Hollweg (1982) and by Suematsu et al. (1982) lose all but a tiny fraction of their flux by the time they have travelled to h = 2000 km.

We have calculated (Foukal and Smart 1981) the dissipation suffered by such shocks propagating along diverging field lines which will tend to decrease the losses, since the increasing area of the shock front reduces its energy flux density and thus its strength, which sensitively determines its dissipation rate. Our results are illustrated in Fig. 6b, and they show that although inclusion of this effect helps, the losses still remain very high.

The effect of including such radiative losses in the development of the specific disturbances responsible for the spicules of Hollweg (1982) and Suematsu et al. (1982) has recently been studied by Mariska and Hollweg (1986). The results of their adiabatic and non-adiabatic calculations are given for comparison in Fig. 7. We see that the adiabatic disturbance propagates with increasing amplitude past $h \doteq 2000$ km, while in the non-adiabatic calculation, radiative losses rapidly damp the wave, so that essentially nothing remains at the transition region altitude. These results show the difficulty of attempting to explain spicules as the result of single or recurrent disturbances of high frequency propagating up from the photosphere.

The difficulty persists even if we consider isothermal shocks; i.e., associate the spicule with rapid cooling and condensation of thermally unstable coronal material behind a pressure disturbance. The problem then is to cause sufficiently rapid radiative cooling behind the shock and produce upward propagation of the $T \sim 10^4$ K isotherm at $v \sim$ 10-20 km sec^{-1}. In unpublished calculations we have carried out, the medium was initially taken to be in energy equilibrium between inflow of heat by conduction from the corona above, and local radiative losses. The passage of a shock disturbs this balance by increasing the density and thus the radiative losses, and also by somewhat smoothing the temperature gradient. Both effects promote thermal instability, leading to upward propagation of the chromospheric isotherms, although actual mass motions are modest. We found that isotherm propagation speeds in the range 10-15 km sec^{-1} may be achieved behind a strong $M_s = 4$ shock, but this shock is so highly dissipative that one must face the question of how a disturbance of that strength could ever have reached $h = 2000$ km from the photosphere.

In summary, we see that the highly dissipative nature of the upper photosphere and chromosphere make it difficult to understand how disturbances of sufficient amplitude to drive spicules and fibrils can reach the required heights. This is true whether we envisage the spicule to be caused by the quasi-adiabatic upward propulsion of the chromospheric isotherms, as did Osterbrock (1961) and most recently Hollweg (1982) and Suematsu et al. (1982), or whether we identify spicules with the upward propagation of a thermal instability into the corona, as is implicit in the isothermal shock case calculated by Wentzel and Solinger (1967) and was more explicitly studied in our calculation described above.

The main conclusion from the studies of spicule dynamics so far seems to be that some means of obviating the dissipation must be found, if the attractive concept of driving spicules directly by photospheric motion is to be preserved. One possibility is to consider disturbances of long period, so that energy can continue to be supplied to the "piston" to balance the large losses at the shock front that it is driving. A model in which the whole atmosphere is slowly lifted by deformation of the flux tube may be viable, but a consistent model needs to be constructed. Another approach is to simply trigger the spicule disturbance and supply the energy higher up, where radiative dissipation is less effective. A logical energy source might be reconnection, as suggested by Uchida (1969) and Pikelner (1969).

HRSO observations will no doubt contribute to resolution of these questions. The work of Dunn and Zirker (1973) on the photospheric sites of spicule and fibril formation is a good guide. Much might be done with continuous 0.1 arc second resolution in tracing spicule development through the atmosphere with filtergrams and spectra to study the morphology and kinematics of these fascinating and fundamental structures.

V. Coronal Loop Flows

Figure 11b shows an image of a post-flare loop observed at Big Bear on December 19, 1982. It clearly consists of many fine thin filaments, and analysis of its structure offers some test of the fundamental plasma scales that one might expect to resolve with a space telescope such as HRSO. Microdensitometric tracings we performed across the loop legs show $H\alpha$ structures as thin as about 0.4". We have found that these are consistent with the scales and cross-sectional area filling factors derived from comparison in this same loop of various diagnostics of local density n_e and mean column density $n_e \ell$ obtained from line ratios, Stark effect and Thomson scattering

(Foukal, Hoyt and Gilliam 1986). Smaller scales down to the proton gyroradius of a few cm might well exist, but they are not demanded by these observations.

Time-lapse films show the development of cool condensations in this loop, and their proper motion down the field lines, on time scales of tens of minutes. There is no doubt that these proper motions in H_α represent flows, since we see clearly in Fig. 8 how a slit placed at a similar loop apex shows little relative Doppler shift of the condensations (seen here in H_γ), and increasing shift up to about 50 km sec^{-1} as the condensation picks up speed moving down the loop legs, when the slit is moved lower (Foukal 1978). Observations of this kind of flows in visible and UV radiations certainly convince us that the solar atmosphere is dynamical, and that advective transports probably dominate the energy balance equation. But attempts to construct models of these loop structures have not made much progress in answering the key questions--namely what process heats coronal loops, and what is the source of the mass excess that illuminates one set of field lines more than another?

To make faster progress, one might do better to confront the possible mechanisms with direct observational tests rather than proceeding by the circuitous route of constructing ever more complicated (and not very unique) atmospheric models. As an example of such an approach I would like to show some results obtained recently in a study of possible macroscopic electric fields in coronal loops. The presence (or absence) of detectable electric fields in post-flare loops bears directly upon both the energy balance and mass balance problems. Reconnection models used to explain dissipation of magnetic energy require the existence of an intense macroscopic E-field to allow relative motion of field lines and plasma at a slip rate given by $v_s = E \times B/B^2$. Intensities of order $E \sim 10\text{-}10^2$ volt/cm are quite likely. The reconnection also provides one mechanism by which plasma can cross magnetic field lines at the high rate v_s, a process of relevance in the mass balance problem along a given flux tube. Clearly then, inability to detect fields of this magnitude with a suitable diagnostic could directly test the importance of reconnection and at least one kind of cross-field plasma flow. On the other hand, measurement of the magnitude, orientation, etc., of E would be extremely helpful in improving our ideas of how this process operates in the corona.

Figure 9 shows the high Balmer lines in a bright post-flare loop, and a plot of their halfwidth against Balmer number. The rapid increase in width shows clear Stark effect corresponding to an electric field of order 10^2 volt/cm. This sort of broadening has been known for decades in flares and has been used as a diagnostic of high local plasma densities $n_e \sim 10^{12}$ cm^{-3}. The question is whether at least a good fraction of this total electric field might be due to macroscopic electric fields associated with reconnection or perhaps with waves.

To answer this question we need a remote sensing technique that will enable us to distinguish between macroscopic, ordered electric fields and the microscopic, disordered fields of pressure broadening. A new diagnostic for this purpose was recently described by Foukal, Hoyt and Gilliam (1986). As shown in Fig. 10a, the transverse Stark effect is very similar to the transverse Zeeman effect, except that the π components (polarized linearly along the E-field) now lie in the wings, and the σ (polarized linearly transverse to E) lie closer to the unshifted wavelength. This is the opposite of the Zeeman effect. By placing a polarizing prism before the spectrograph, we thus see the maximum Stark broadening at the position θ_{max} when its transmission axis is aligned with the π vibration direction, and a minimum broadening at the angle θ_{min} at 90° to θ_{max}. We expect then that if we take successive Balmer line spectra at different polarizer angles θ of a loop in which a uniform E-field is present with a substantial component in the sky-plane, the plots of $\Delta\lambda_{1/2}$ vs. n for the separate spectra should reveal a maximum broadening in the spectra taken at θ_{max}, and a minimum at θ_{min} (Fig. 10b).

Results of observations carried out so far on a bright post-flare loop using this method are shown in Fig. 11a. It can be seen that the curves for $0 \leq \theta \leq 45$ exhibit significantly larger slope for $n > 15$ than do the curves for $90 \leq \theta \leq 135$. This leads us to associate θ_{max} (and thus the E-field direction) with an orientation corresponding to roughly radial in Fig. 11b. The field intensity required is approximately 10^2 volts cm^{-1}. The scale over which the field is detected is $L \sim 10^4$ km, but it might occupy only a small fraction of the volume, provided the emission measure is sufficient in the electrified plasma to dominate the Balmer line emission passed through the slit. The E-field observed must be uniform in space over a time scale of at least 10^3 secs.

The observed E-field direction is compatible with reconnection occurring either near the top or side of the loop, since $E = v_s \times B$. The magnitude of the field is about an order of magnitude larger than conventional models of flare loop reconnection (e.g., Somov and Titov 1985) would suggest. However, the fields could easily be much higher, since v_s is quite dependent on the local Alfvèn speed and thus on the local density in the small reconnecting region.

For reasons given by Foukal, Hoyt and Gilliam, this result is unlikely to be caused by instrumental effects since three active prominences showed none of the ordering effect with θ seen in Fig. 11a. The result could be a statistical fluke, however, and more observations of this kind are needed. Observations of the high Balmer lines with a linear polarizer before the spectrograph slit might be profitably tried with the HRSO. The ability to resolve and track very small plasma elements might significantly increase the sensitivity to the electric fields of waves and reconnection, and study their spatial distribution and time dependence.

This work was supported under NSF grant ATM 8519121 and NASA contract NAS 5-29349.

References

Athay, G. 1981, in "Solar Active Regions," F. Orrall, ed. Colorado Univ. Press, p. 83.

Beckers, J. 1972, Ann. Rev. Astr. Ap. 10, 73.

Beckers, J. 1977, Ap. J. 213, 900.

Brueckner, G. 1981, in "Solar Active Regions," F. Orrall, ed. Colorado Univ. Press, p. 113.

Cavallini, F., Ceppatelli, G., and Righini, A. 1985, Astron. Ap. 143, 116.

Cavallini, F., Ceppatelli, G., and Righini, A. 1986, Astron. Ap. in press.

Cook, J. 1985, in "Theoretical Problems in High Resolution Solar Physics," H. Schmidt, ed. Max Planck Institute Publication MPA 212, p. 308.

Dravins, D., Lindegren, L., and Nordlund, A. 1981, Astron. Ap. 96, 345.

Dunn, R. and Zirker, J. 1973, Solar Phys. 33, 259.

Emslie, G. and Noyes, R. 1978, Solar Phys. 57, 373.

Foukal, P. 1978, Ap. J. 223, 1046.

Foukal, P., and Smart, M. 1981, Solar Phys. 69, 15.

Foukal, P., Hoyt, C., and Gilliam, L. 1986, Ap. J. 303, 861.

Gilman, P., and Foukal, P. 1979, Ap. J. 229, 1179.

Giovanelli, R., and Slaughter, C. 1978, Solar Phys. 57, 255.

Giovanelli, R. 1980, Solar Phys. 67, 211.

Hollweg, J. 1982, Ap. J. 257, 345.

Howard, R. 1972, Solar Phys. 24, 123.

Kuhn, J. 1983, Ap. J. 264, 689.

Mariska, J., and Hollweg, J. 1986, Ap. J. in press.

Miller, P., Foukal, P., and Keil, S. 1984, Solar Phys. 92, 33.

Moore, R. 1981, in "The Physics of Sunspots," L. Cram and J. Thomas, eds., Sac Peak Publication, p. 259.

Osterbrock, D. 1961, Ap. J. 134, 347.

Pikelner, S. 1969, Astron. Zhurnal 13, 259.

Simon, G. and Leighton, R. 1964, Ap. J. 140, 1120.

Somov, B., and Titov, V. 1985, Solar Phys. 95, 141.

Stenflo, J., Harvey, J., Brault, J., and Solanki, S. 1984, Astron. Ap. 131, 333.

Suematsu, Y., Shibata, K., Nishikawa, T., and Kitai, R. 1982, Solar Phys. 75, 99.

Tanenbaum, A., Wilcox, J., Frazier, E., and Howard, R. 1969, Solar Phys. 9, 329.

Uchida, Y. 1969, Publ. Astr. Soc. Japan 21, 128.

Wentzel, D., and Solinger, A. 1967, Ap. J. 148, 877.

Wiehr, E. 1985, Astron. Ap. 149, 217.

Ulmschneider, P. 1971, Astron. Ap. 14, 275.

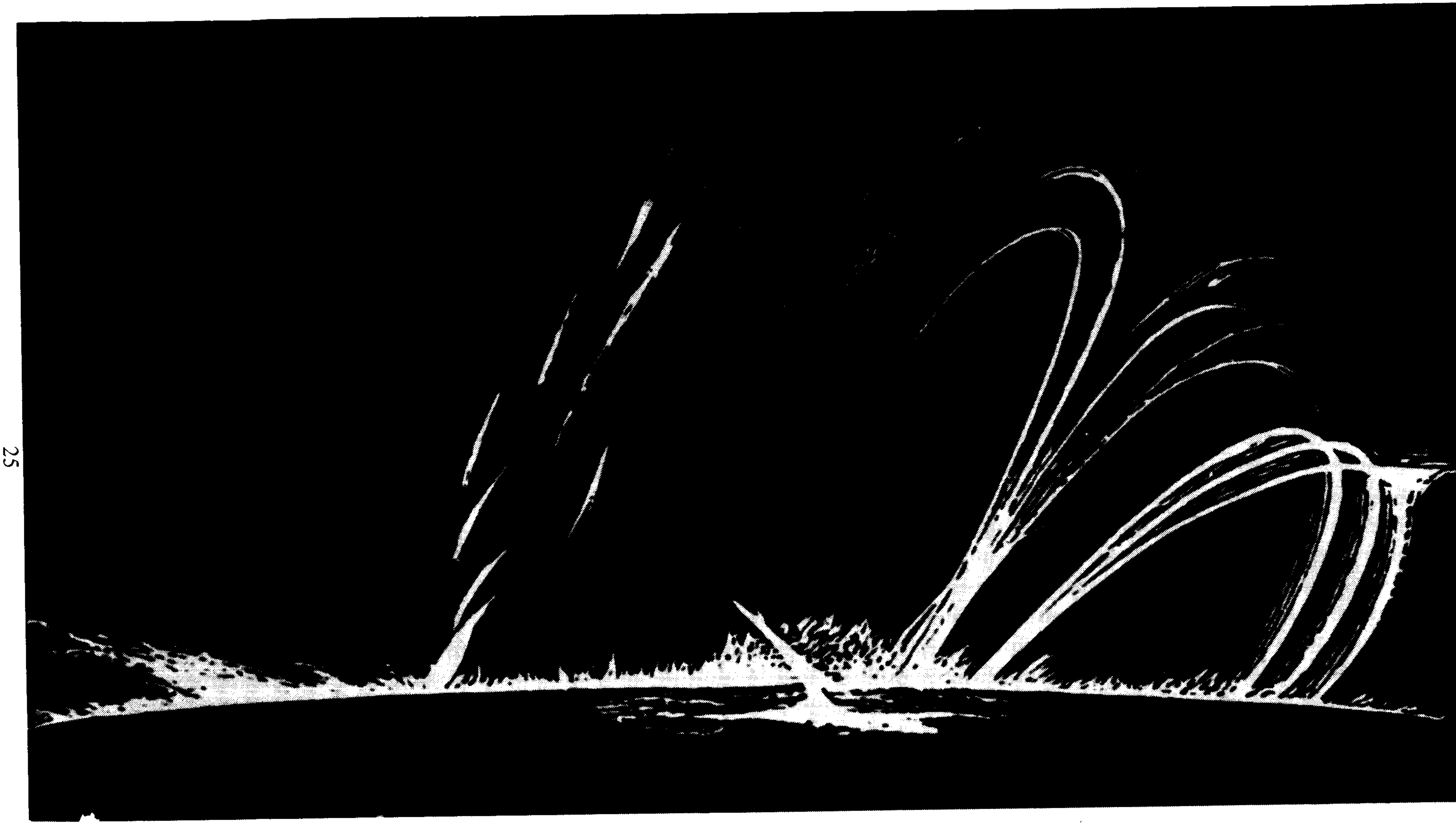

Fig. 1 Drawing of an active region made on October 5, 1871, from spectroheliescope observations in H_α by A. Secchi.

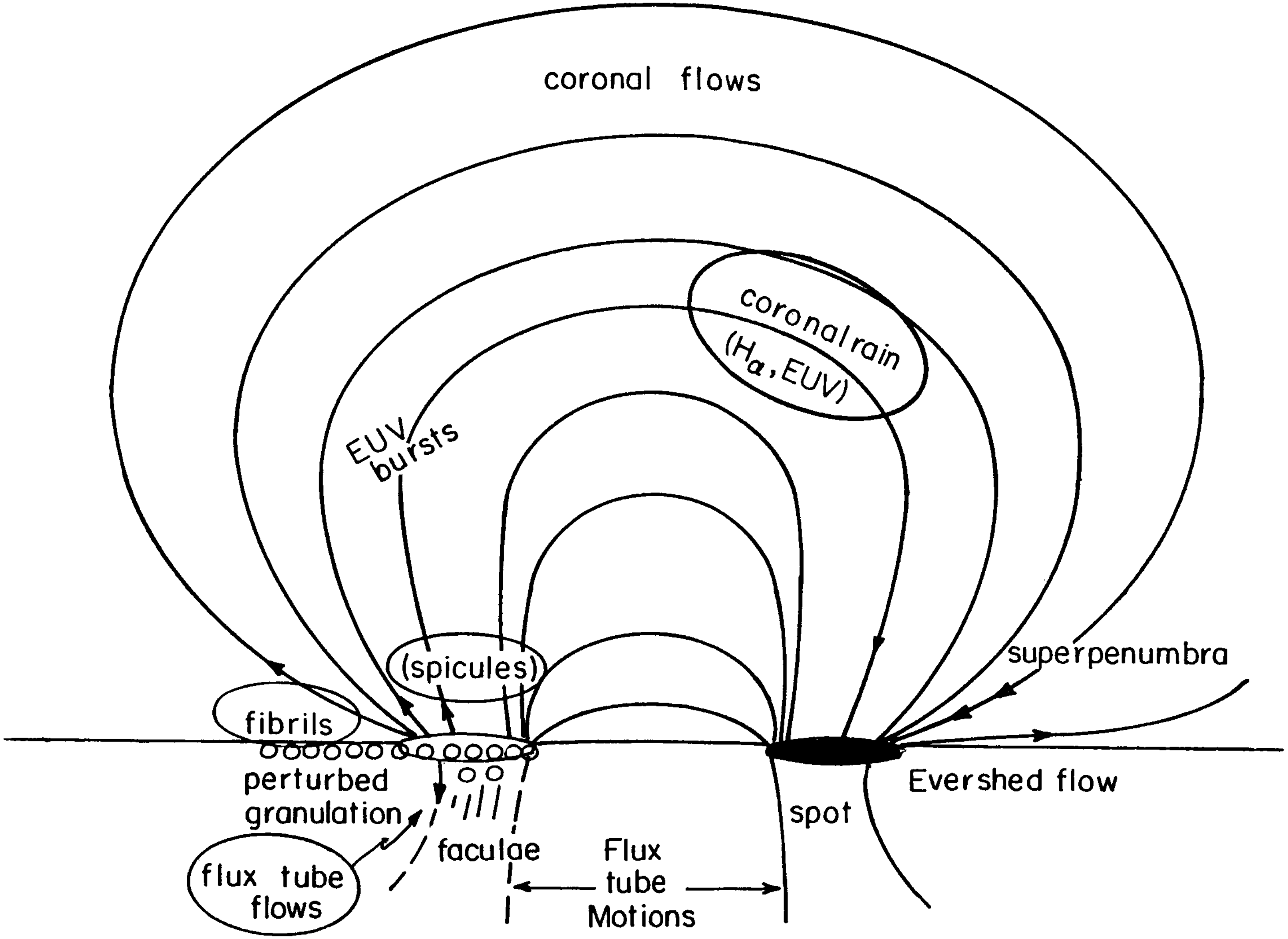

Fig. 2 Schematic representation of active region flows at photospheric, chromospheric and coronal levels.

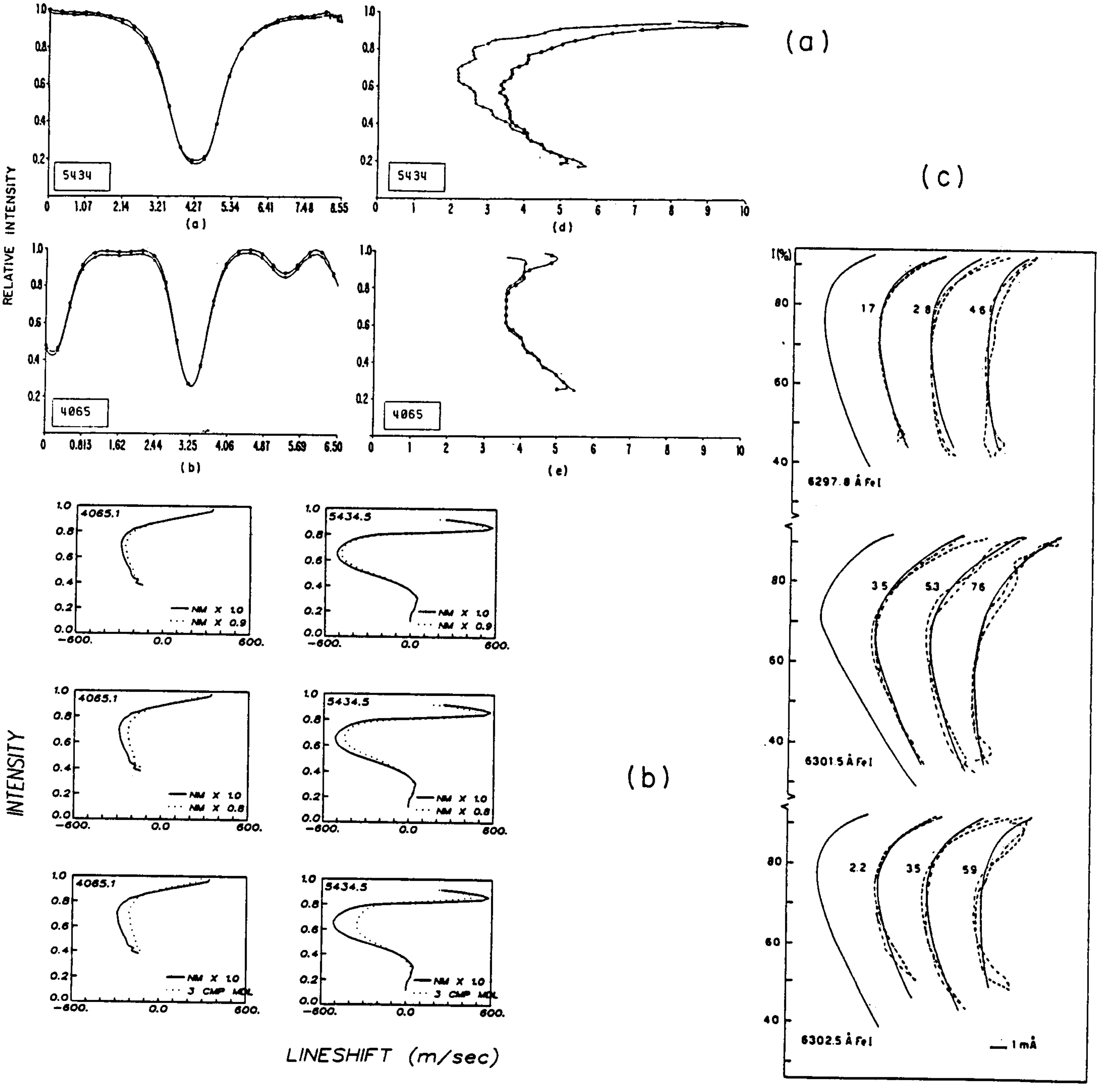

Fig. 3(a) Line profiles and bisectors for λ4065, λ5434 in cells (triangles) and network (circles). The abscissae are mÅ x 10^2 for the profiles and msec^{-1} x 10^2 for bisectors. The zeros are arbitrary.

(b) Line bisectors for λ4065, λ5434 computed for the Nelson-Musman (NM) granulation model (solid line), and for various degrees of convective inhibition.

(c) Observed (solid, left-hand line) and calculated bisectors for various scenarios using a three-component model consisting of normal granules, magnetic flux tubes, and non-convective atmosphere.

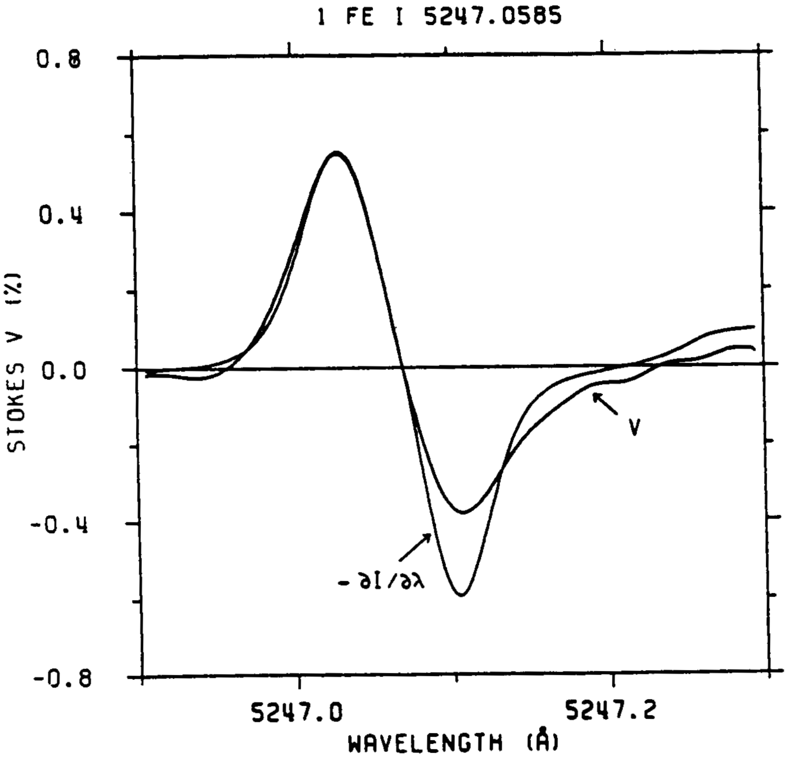

Fig. 4 Plot of the Stokes V profile (and also $dI/d\lambda$) for the FeI line 5247, showing the asymmetry of the blue and red V-profiles.

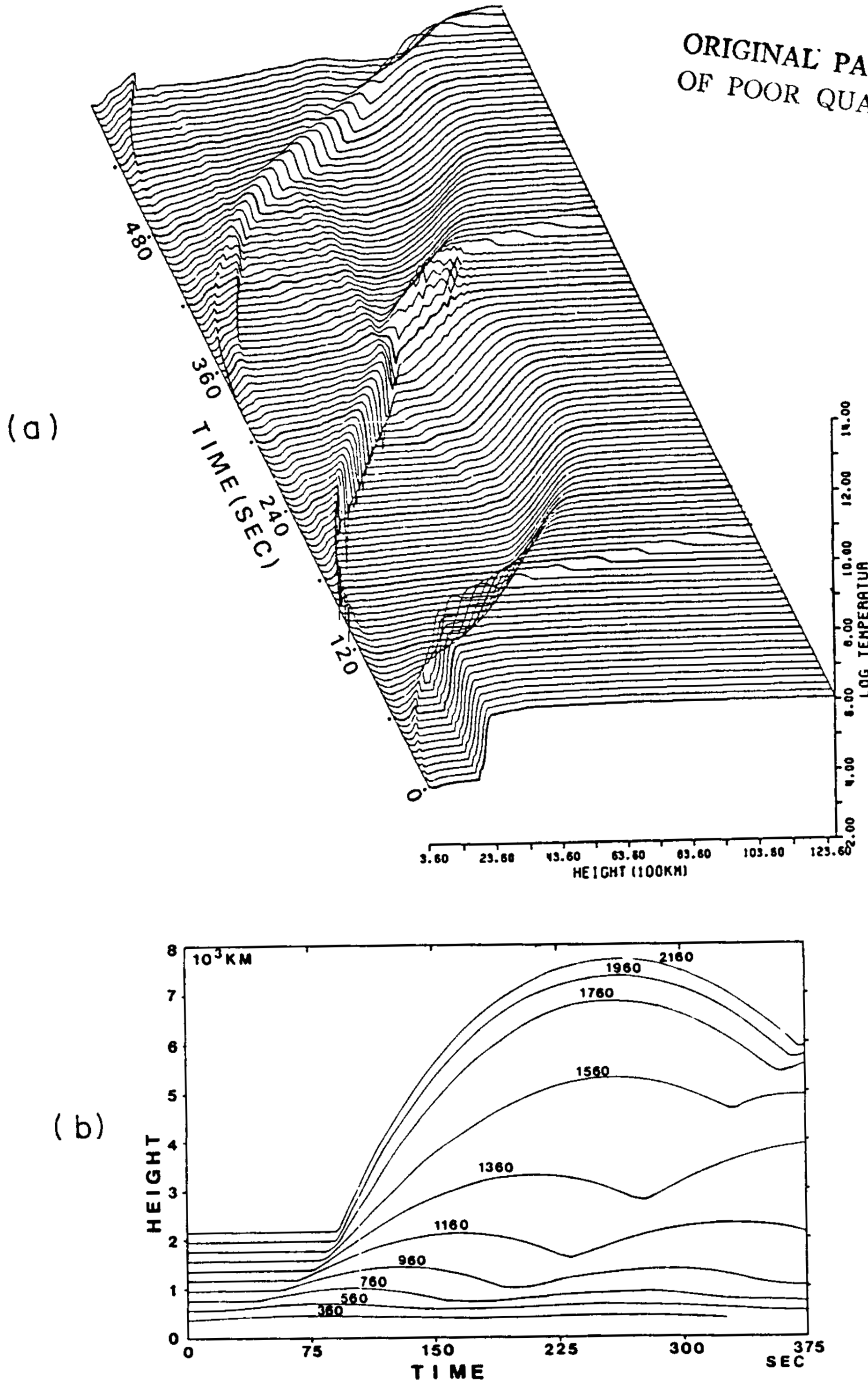

Fig. 5(a) Three-dimensional representation of upward propagating disturbances in the model of Suematsu at al. 1982. Coordinates are time (left), height (bottom) and log temperature (right). Successive traces are separated by ten seconds.

(b) Ballistic curves showing profiles of height with time, of material originating at heights marked (in km) on each curve.

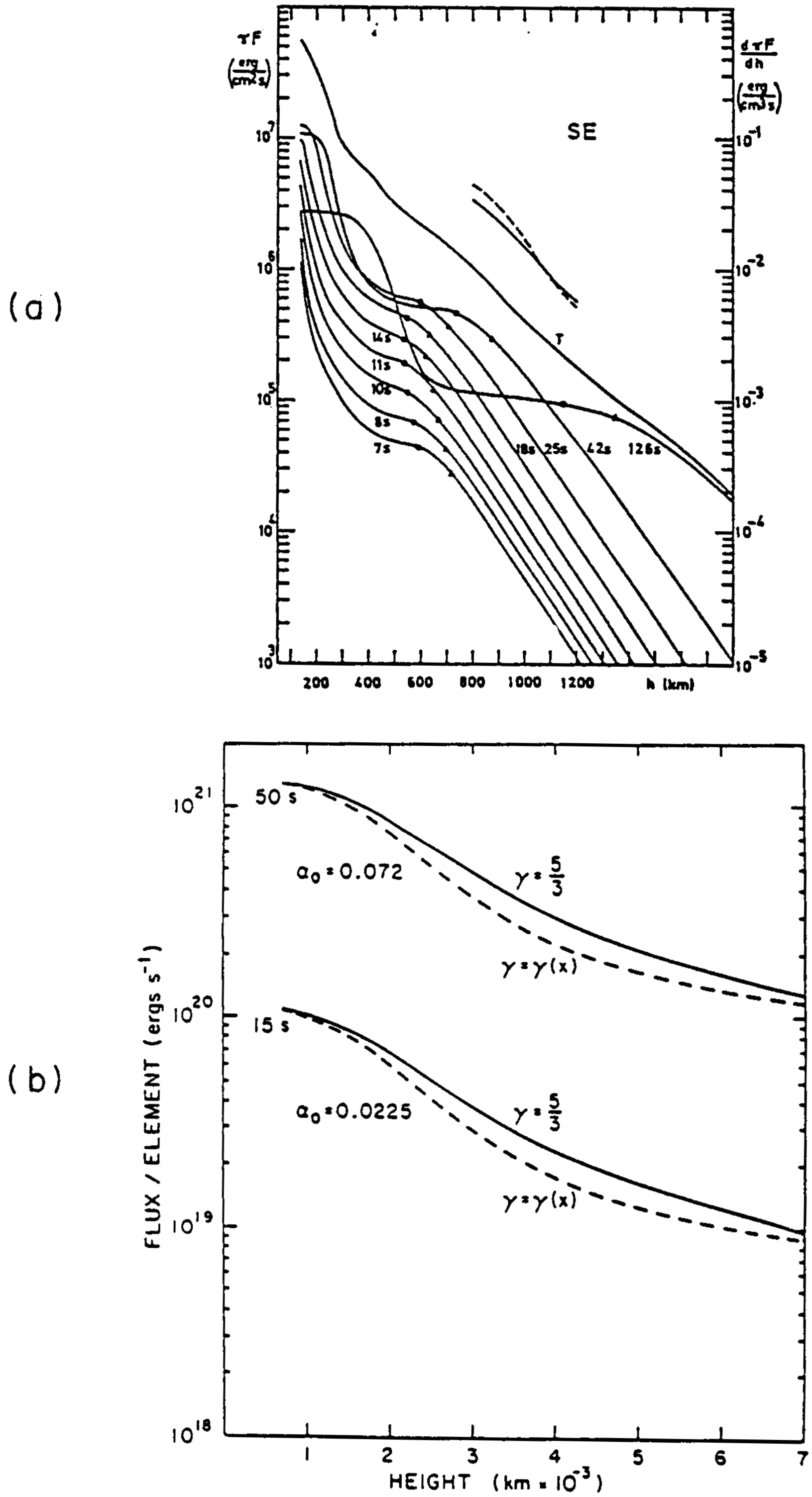

Fig. 6(a) Curves showing dissipation of flux in simple waves originating in the photosphere, between periods of 7 and 126s, for a plane-parallel atmosphere.

(b) Dissipation of flux for weak shocks in the upper photosphere and chromosphere, propagating along diverging field lines, for different γ, and for two values of shock strength $\alpha = M_S-1$.

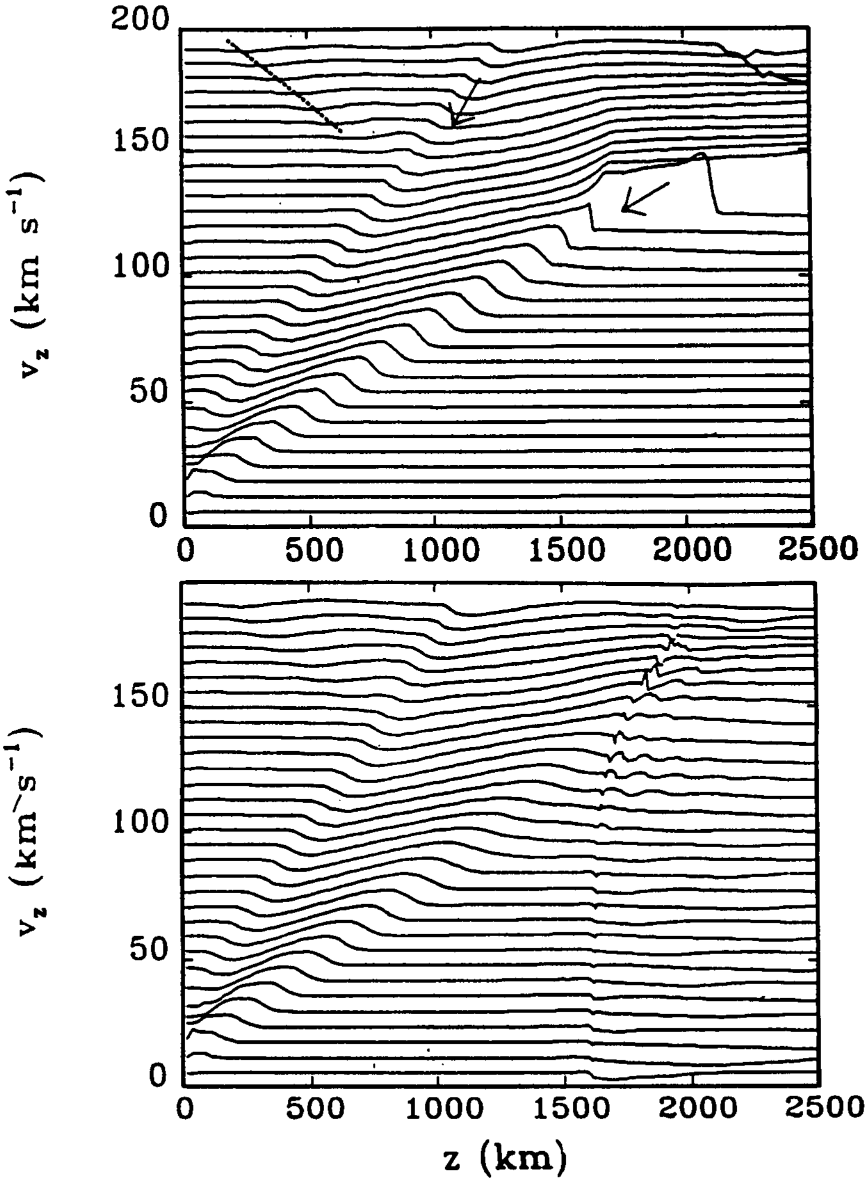

Fig. 7 Comparison of adiabatic (above) and non-adiabatic (below) calculations for the vertical velocity field v_Z excited by successive compressional disturbances of identical initial amplitude and period. The glitches in the right-hand side of the lower frame are numerical errors.

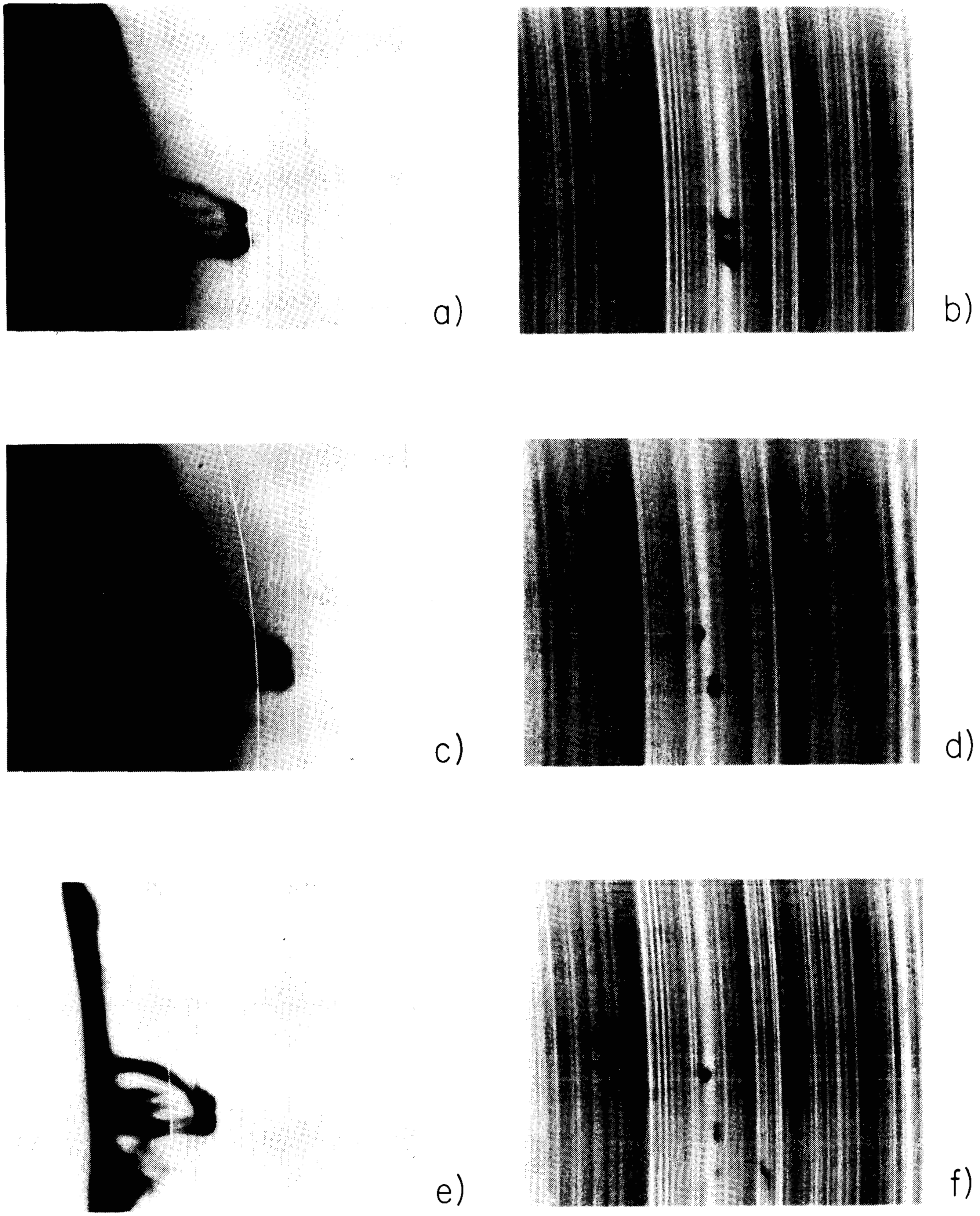

Fig. 8 Slit jaw pictures in H_α and spectra of H_γ for a post-flare loop. Note how the H_γ emission is increasingly Doppler separated as the slit is moved downward in the loop in frames a, c, e and (correspondingly) in spectra b, d, f.

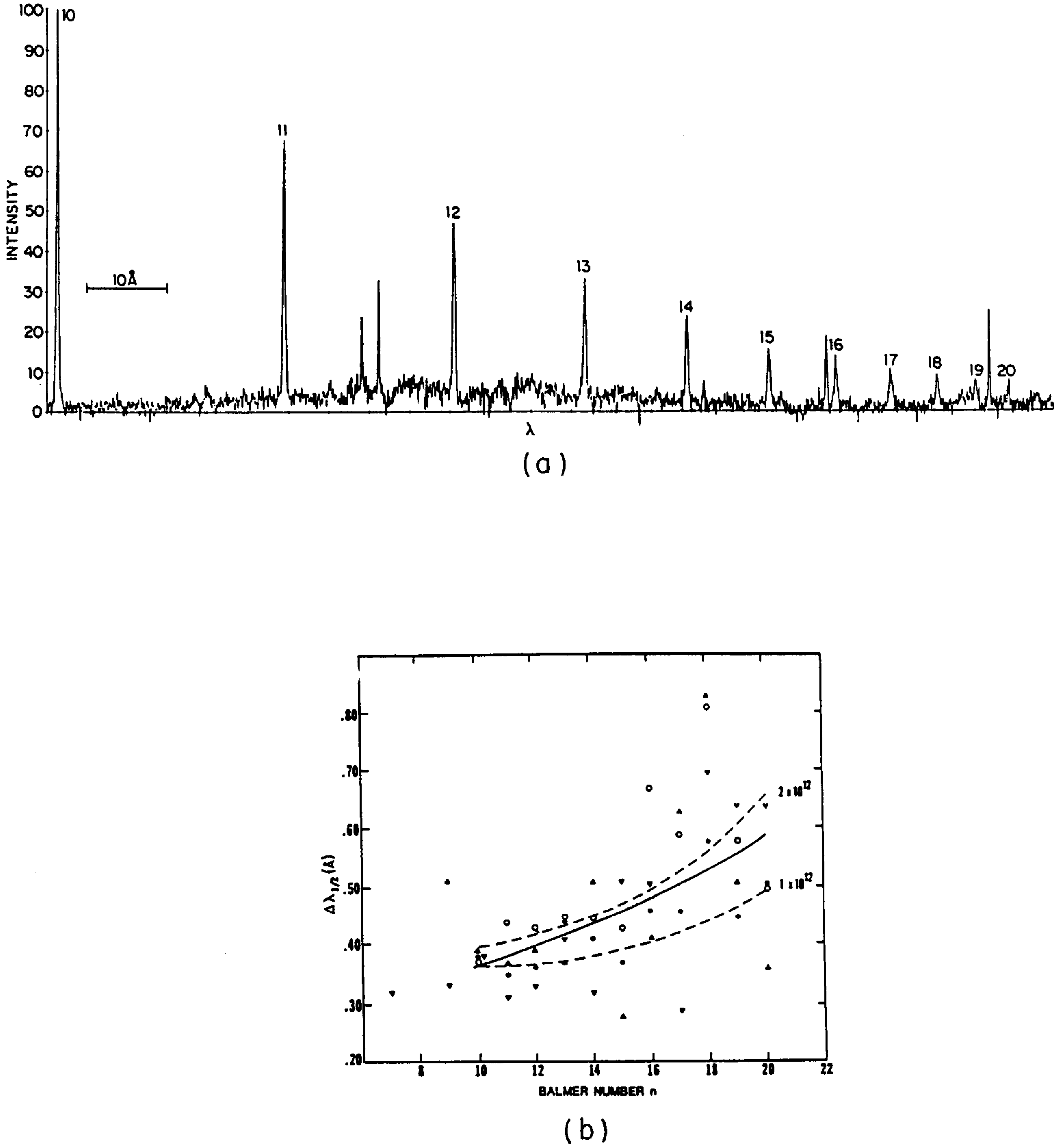

Fig. 9 The high Balmer lines in a post-flare loop (a) and (b) a typical plot of their half-width against Balmer number (from Foukal, Hoyt and Gilliam 1986).

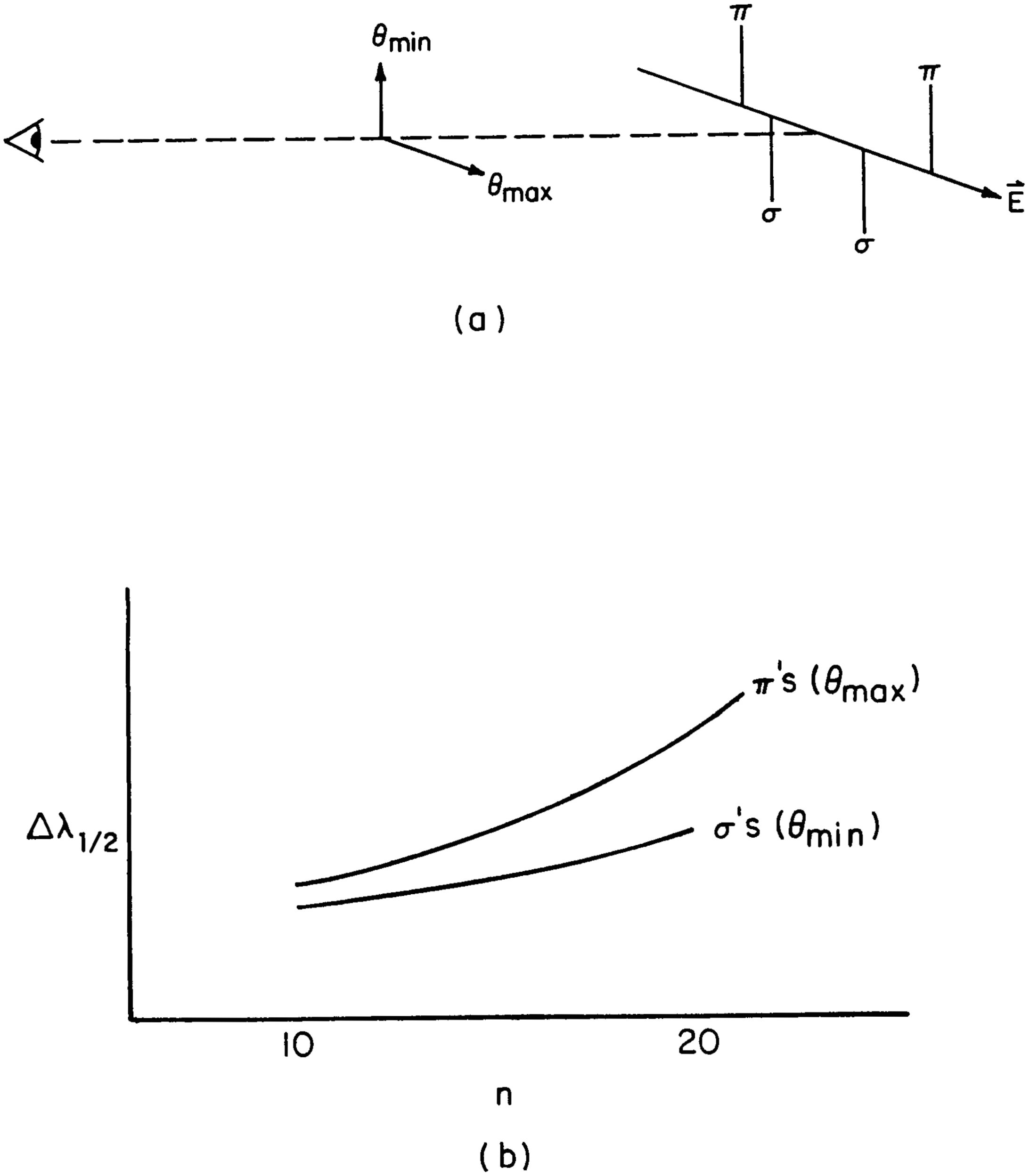

Fig. 10 Schematic diagram of the polarization structure of Balmer line Stark broadening (a) and the expected behavior of halfwidth plotted against Balmer number for π and σ components separately.

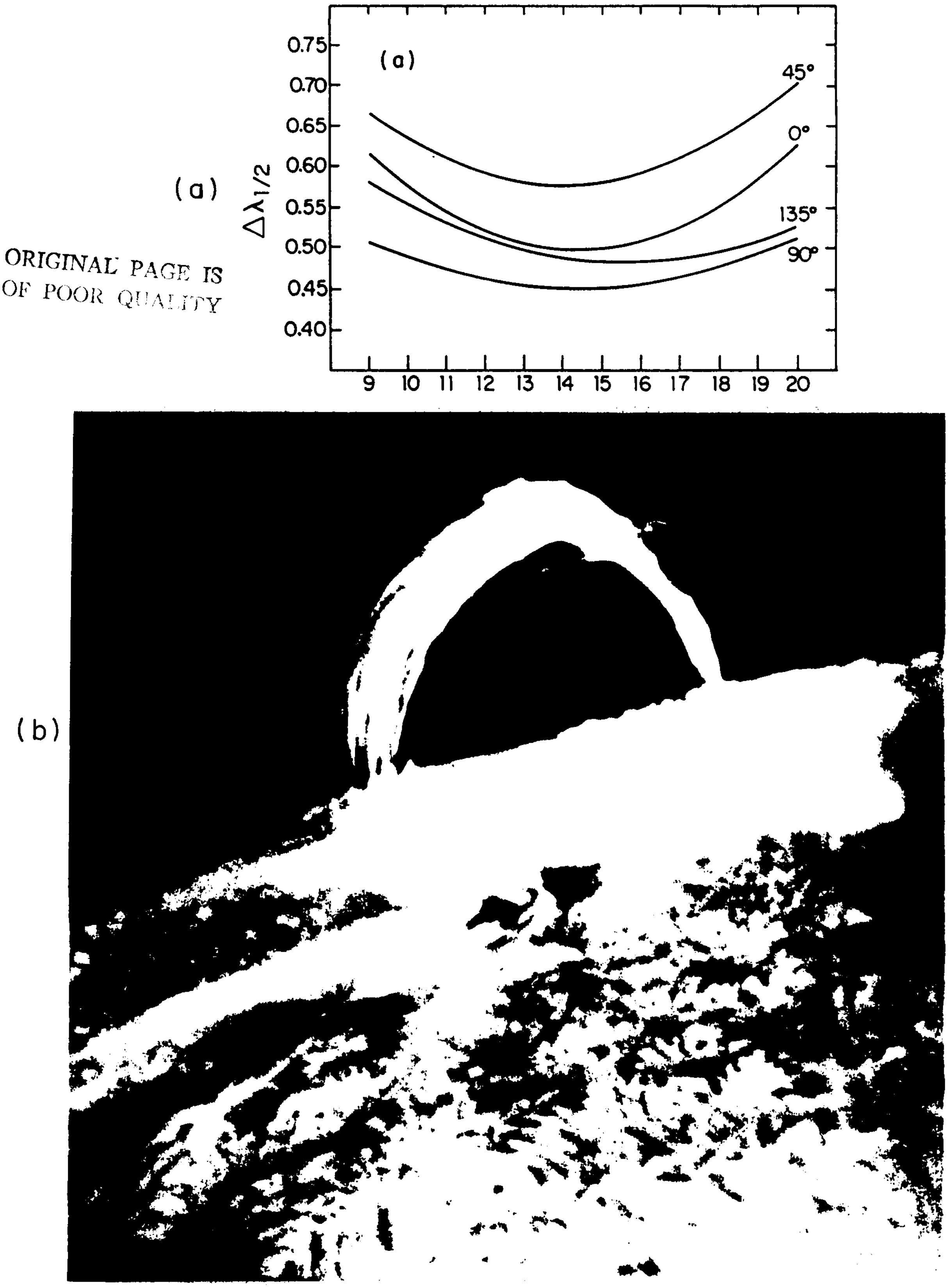

Fig. 11 Plots (a) of observed halfwidth against Balmer number for four different polarizer orientations, for the December 19, 1982, loop, shown in (b). The angle $\theta = 45$ corresponds roughly to E-field transverse to B-field at the loop apex.

N88-11612

WHAT'S NEEDED IN THE UV AND EUV

by

G.A. Doschek
E.O. Hulburt Center for Space Research
Naval Research Laboratory

ABSTRACT

High spectral and spatial resolution UV and EUV spectroscopy is discussed with emphasis on the spectroscopic observations that are required in order to increase our understanding of the physics of the lower transition region. The properties of the lower transition region are reviewed, and the available lower transition region plasma diagnostics are reviewed for the wavelength range between about 1150 and 2000 Å. One important conclusion is that comprehensive spectroscopic coverage over a rather broad temperature range is necessary in order to observe satisfactorily small transition region structures. This is illustrated by two examples from the recent NRL Spacelab 2 HRTS experiment.

I. INTRODUCTION

The hotter layers of the Sun's atmosphere, the transition region and corona, can only be satisfactorily studied in the UV, EUV, and X-ray spectral regions. The lower transition region may be defined as the atmospheric region at temperatures roughly between 10^4 and 10^5 K. The upper transition region contains plasma between about 10^5 and 10^6 K. Regions between about 10^6 K and 3 x 10^6 K are defined as the solar corona. Plasma hotter than 3 x 10^6 K is associated with transient energetic events such as surges, eruptive prominences, and of course flares. In this paper I will emphasize what can be learned about the hotter regions of the Sun's atmosphere from high resolution spectroscopy and imaging in the UV and EUV. Although not impossible in principle, it is highly unlikely that an X-ray telescope and/or X-ray spectrometer will accompany the HRSO on its first flight.

I will emphasize in particular what can be learned about the transition region, and possibly the corona, since these are areas of particular interest to me. However, regarding the chromosphere I would like to point out that in addition to the well-known diagnostic lines of Mg II near 2800 Å, the UV and EUV contain very rich and complete emission line spectra of C I, S I, Fe II, Si I and Si II, as well as important continuum emission. Very little work on the diagnostic potential of these spectra has been done so far, and the analysis of these spectra is a promising research topic.

The question posed as the title of this paper, "What's Needed in the UV and EUV", can only be answered by considering the known properties of the atmospheric regions we wish to study, and by reflecting on our ideas concerning the physics of these regions. In addition, instrumental limitations and atomic spectroscopy play an important role in answering this question. In the first High Resolution Solar Physics Workshop, Athay (1985) outlined some of the properties and physics of the chromosphere and transition region. In this paper I will also undertake such a review, but with emphasis on how the atmospheric characteristics and physics affect the UV and EUV spectrum.

Before proceeding further, however, I will give a somewhat utopian answer to the question of what's needed in the UV and EUV. If funding, flight opportunities, and instrumental limitations did not present the severe problems that they do, it would be desirable to obtain high resolution spectra, with spectral resolution of about 1/3 the Doppler width of chromospheric and transition region lines, between about 400 and 4000 Å, with accompanying high spatial resolution images, about 0.1", in selected spectral lines formed between 10^4 and 10^6 K. Of course all this is also desired with high time resolution, on the order of a few seconds. As will be seen below, it is not realistic to obtain this type of information for the first flight of HRSO. However, a great deal can be accomplished even with considerably "descoped" instrumentation.

II. INSTRUMENTAL AND SPECTROSCOPIC LIMITATIONS

The region from about 1150 to 4000 Å can be well-observed using optics coated with aluminum and a protective coating of MgF_2. The normal incidence reflectivity of aluminum at these wavelengths is about 80% or better. Below about 1150 Å, however, the reflectivity of aluminum decreases rapidly and it becomes necessary to use other coatings in order to achieve normal incidence reflectances of not more than about 20%. It is possible to achieve much higher reflectances than 20% by using grazing incidence optics, but then spatial imaging becomes a severe problem. Multilayer optics is a promising technology for some solar spectroscopic applications, but the current spectral resolution is very bad for wavelengths greater than 400 Å ($\Delta\lambda/\lambda \approx 0.07$). Because of the properties of aluminum mentioned above, there are few high spectral resolution UV solar observations at wavelengths much shorter than 1150 Å. The IUE wavelength cutoff is around 1150 Å for the same reason. In addition, for astronomical spectrometers the hydrogen continuum edge at 912 Å can cause severe absorption for wavelengths less than 912 Å in even relatively nearby sources, depending on the direction of the source in the sky. This continuum absorption is also important in the solar atmosphere (e.g., Schmahl and Orrall 1979, Doschek and Feldman 1982).

Because of the above limitations, there is an instrumental dividing line at around 1150 Å. If one wishes to observe both below and above this wavelength, more than one instrument is needed, and the instruments will be significantly different in design. This fact has important consequences for the study of the transition region and corona, when atomic spectroscopy is considered.

The lower transition region can be observed through spectral lines of ions such as C II, C III, C IV, O III, O IV, O V, N III, N IV, N V, Si III, Si IV, S III, and S IV. Many of the resonance and/or allowed (by pure electric dipole spontaneous decay) lines of these ions fall at wavelengths less than 1150 Å. However, diagnostically important intersystem lines fall at longer wavelengths. As examples, allowed lines of O III fall near 526, 703, and 835 Å, and strong intersystem lines fall at 1660 and 1666 Å. Allowed lines of O IV fall near 554 and 790 Å and strong intersystem lines fall near 1402 Å. It is of course desirable to observe both the allowed and intersystem lines simultaneously, because of the temperature sensitivity of line ratios and the information the ratios provide concerning the Lyman continuum absorption, but it is also impractical with a single instrument.

By considering the spectroscopy in detail, we reach the conclusion that only one strong line formed at temperatures above about 2 x 10^5 K can be observed at wavelengths longer than 1150 Å. This is the Fe XXI line at 1354 Å and it can only be observed during flares. However, there are a number of weak coronal and upper transition region lines from ions such as Si VIII, Fe IX - Fe XII that appear at longer wavelengths, but a very sensitive instrument with large dynamic range is required to observe these lines against the solar disk. For example, the Fe XII line at 1242.0 Å is only 1/80 the strength of the neighboring N V line at 1242.8 Å at $4''$ above the white light limb (Doschek et al. 1976). Lists of these forbidden coronal lines are given by Feldman and Doschek (1977) and Sandlin, Brueckner, and Tousey (1977).

Although only a handful of intersystem lines of transition region ions fall at wavelengths longer than 1150 Å, their diagnostic potential is enormous for deducing properties of the transition region. I shall devote most of the following discussion to the 1150 - 2000 Å region, with emphasis on the lower transition region.

III. THE TRANSITION REGION AND UV - EUV OBSERVATIONS

a) Physical Structure

The physical structure of the transition region is presently unknown. About ten years ago the transition region was viewed solely as an interface between chromospheric and coronal plasma. The chromospheric and coronal plasma was assumed to be confined by some type of magnetic structure, such as a closed flux tube, spicule, or field lines compressed over supergranule cell boundaries, such as in the Gabriel (1976) model. There is no way that the coronal and chromospheric plasma can be in contact without generating plasma at intermediate temperatures. In models without flow, where classical thermal conduction is the dominant energy transport mechanism, the transition region is very thin in height, of the order of 100 km. It turns out that the transition region is also very thin in models that encorporate flow, e.g., Mariska (1984). In fact it seems perfectly reasonable to believe that hot coronal loops, such as observed by X-ray telescopes, interface with the chromosphere and contain this type of transition region. This is so because the physical characteristics of such loops appear to obey scaling laws based on physics that produce such transition regions (Rosner, Tucker, and Vaiana 1978).

However, there are observations indicating that the actual situation is far more complicated (e.g., Feldman 1983). Perhaps the most outstanding observations are images of extended structures in transition region lines such as C IV and Ne VII, and the fact that none of the classical transition region models, with or without flow, can produce the observed chromospheric-transition-region emission measure distribution (Athay 1982). It appears that cool transition region structures may exist that are separated by magnetic fields from at least the coronal plasma. Since heat conduction across magnetic fields is very small, it is no longer obvious that plasma at transition region temperatures must occur in very thin layers, although the structures containing transition region plasma are undoubtedly quite small. Thus the observed transition region emission is composed of two types of emission: emission from "classical" transition regions and emission from structures with properties that are largely unknown. A central problem to be answered from HRSO UV instrumentation is the nature of these unknown structures. Thus the HRSO UV instrumentation should be able to obtain high spatial resolution transition region images that can be located with respect to chromospheric and photospheric features.

There are three current theories regarding what these structures might be, proposed by Antiochos and Noci (1986), Rabin and Moore (1984), and Athay (1984).

I will not discuss the details of these models here, but only emphasize that the models provide, or can be developed to provide, predictions regarding the physical properties of the transition region. For example, in the model of Antiochos and Noci (1986) the transition region structures are cool loops. This model predicts that the pressure in a loop varies inversely as a high power of the maximum loop temperature. In the model of Moore and Rabin (1984) the pressure is the same for all temperatures. In the model of Athay (1984) the pressure is time dependent, but on average, should increase with temperature. In order to determine the validity of these and other models it is clearly desirable to derive densities as a function of temperature from UV and EUV observations.

The sizes of transition region structures are known to be very small. Direct imagery from HRTS (by building up spectroheliograms) shows structures with sizes down to the HRTS spatial resolution (0.8" for HRTS 1). From a flare observed from Skylab, Doschek, Feldman, and Rosenberg (1977) concluded that a surge observed at lower transition region temperatures during flare onset had a characteristic length of about 60 km, or < 0.1". This result was based on obtaining a density N_e from intersystem lines and a volume emission measure N_e^2V from allowed lines. Most density-emission measure analyses indicate very small filling factors for transition region plasma, 0.1 - 0.001. Thus UV, EUV instrumentation should have as high a spatial resolution as possible, at least 0.5".

The location of transition region structures is well-known. From limb observations, peak emission from lower transition region structures occurs at 2" - 4" above the white light limb. However, emission extends to heights of at least 10" in the quiet Sun and extends to 20" or more in coronal holes. Figure 1 shows the source functions obtained from Abel inversions of limb brightening curves obtained from Skylab data (see Feldman, Doschek, and Mariska 1979). The full width at half maximum FWHW of the functions in Figure 1 is about 5". As an example of the small filling factor of transition region plasma, if this region were uniformly filled with plasma, the path length L through this plasma above the limb would be $L = \sqrt{2RH}$, where R is the solar radius and H is the 5" layer thickness, and L equals about 7×10^4 km. The actual path length may be obtained from the ratios of doublet lines from Al III, Si IV, C IV, and N V, obtained from Skylab spectra, as described by Doschek, Mariska, and Feldman (1981). Figure 2 shows that above the limb the peak intensities of these lines depart from the optically thin ratio, 2:1. From these observations path lengths can be derived and these are given in Table 1. The path lengths for Al III, Si IV, and N V indicate filling factors of 6%; for C IV the filling factor is 1.1%. The difference between the C IV and other path lengths is probably significant. C IV is formed at about 10^5 K, where the differential emission measure is at its smallest value.

b) Plasma Diagnostics

The discussion so far indicates the importance of density and temperature, or pressure measurements. There are several excellent density diagnostics for the lower transition region, based on the intersystem lines that arise from metastable levels. These levels can be depopulated by collisions as well as radiative decay when densities are high, which provides a density diagnostic. The densities above which several prominent transition region lines become affected by collisional depopulation are shown in Figure 3. Plotted is the ratio of the population of the metastable level to the product of the electron density and the density of the ion in which the line arises, as a function of electron density. For a line unaffected by collisional depopulation and/or formed at very low densities this

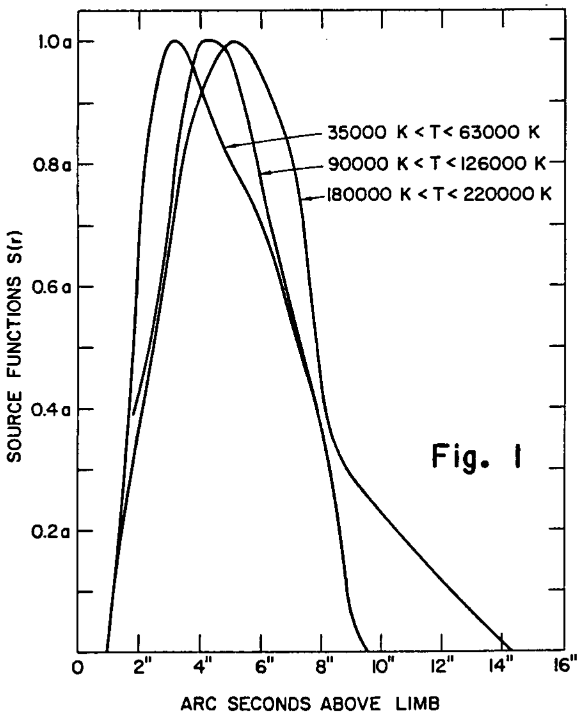

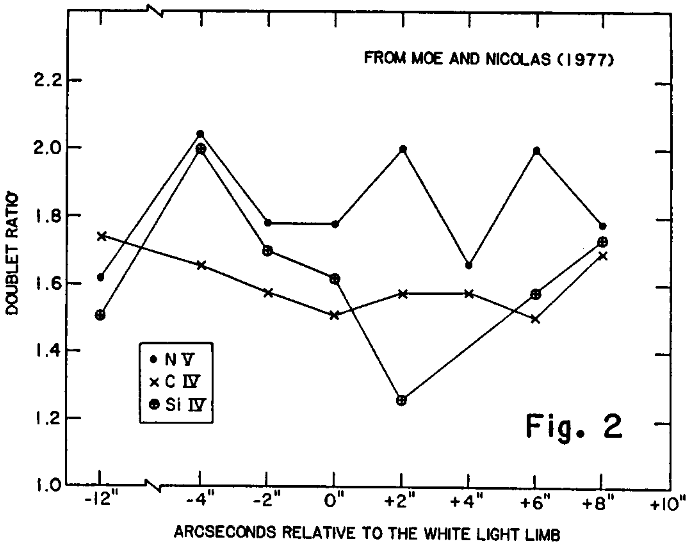

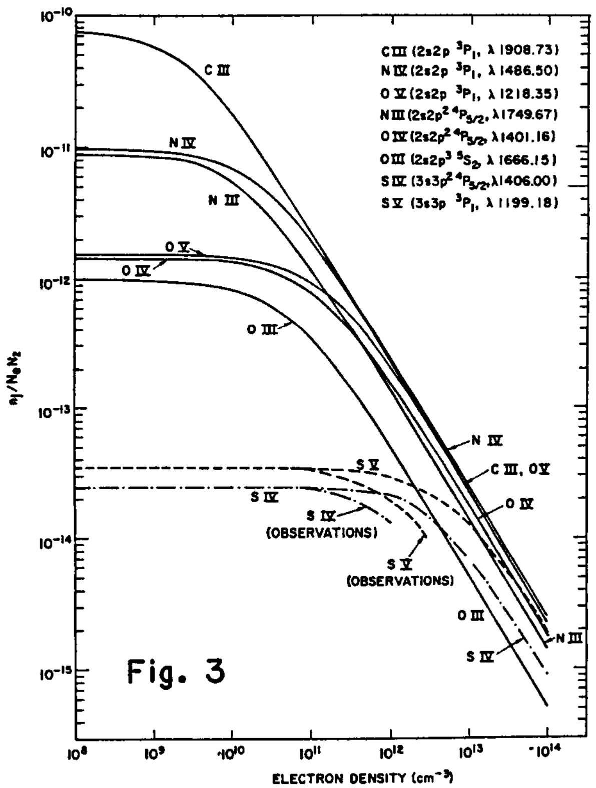

Fig. 1 - The distribution of lower transition region plasma with height above the limb (Feldman, Doschek, and Mariska 1979).

Fig. 2 - Intensity ratio of indicated doublets above the limb. The optically thin ratio is 2:1 (Doschek, Mariska, and Feldman 1981).

Fig. 3 - Populations of levels and ions indicated as a function of electron density (Doschek 1985).

TABLE 1

Opacity and Path Lengths at 2" - 4" Above the Limb

T_e(K)	L(km)[a]
4×10^4	3,500
7×10^4	4,500
10^5	800
1.8×10^5	4,800

[a] The path lengths can be uncertain by factors of about 2 .

TABLE 2

Electron Pressures

Region	Log($N_e T_e$)
Quiet Sun (Chromosphere)	15.2
Quiet Sun (Transition Region)	15.1
Quiet Sun (Corona)	15.0 (h > 20")
Coronal Hole (Transition Region)	15.1 (14.8)
Active Region (Chromosphere)	15.2
Active Region (Transition Region)	15.9
Active Region (Corona)	15.2 - 16.0
Prominence (Transition Region)	14.9
Sunspot (Transition Region)	15.0
Surges (Flare-related Activity)	
(Transition Region)	15.0 - 16.2
Flares (Transition Region)	16.0 - 18.0
Flares (Corona, 10^6 K < T_e < 6×10^6 K)	16.8 - 18.7

ratio is a horizontal line as a function of density. However, when the density is high enough to produce collisional depopulation, the ratio begins to fall and eventually falls linearly on a logarithmic scale. In this region the ratio of the intersystem lines to allowed lines unaffected by density and formed at the same temperature is a very sensitive function of density. The good news is that many lines are available for density diagnostics; the bad news is that most lines are not sensitive for densities below 10^{10} cm^{-3}. The canonical quiet Sun transition region pressure is 10^{15} cm^{-3} K, so for O IV at 1.3 x 10^{5} K the average density is about 8 x 10^{9} cm^{-3}, where the O IV lines are not sensitive. Only C III provides a line that is fairly sensitive in the important regime between 10^{9} and 10^{10} cm^{-3}. However, this line is rather weak against the solar disk and must be observed over a strong continuum background. The situation is much improved for active regions and explosive events, where typical pressures are around 10^{16} cm^{-3} K. In this case many of the lines in Figure 3 provide good diagnostics.

There are two types of density sensitive line ratio available. One involves the ratio of two intersystem lines. Examples occur for N III, O IV, Si III, and S IV lines between 1150 and 2000 Å. A typical result for O IV lines is shown in Figure 4, and the O IV lines from Skylab spectra for three different solar regions are shown in Figure 5. The left most panel in Figure 5 shows the quiet Sun limb spectrum. The 1407 Å/1405 Å ratio is in the low density limit. The other two spectra are from energetic events and indicate densities of about 5 x 10^{10} cm^{-3}. The problem with these ratios is that they become insensitive at very high densities or at very low densities. However, the O IV ratio in Figure 4 may be sufficiently sensitive to work in the 10^{9} - 10^{10} cm^{-3} region, if measurements are good and the atomic data are as good as claimed. A partial test of the atomic data can be found by observing the O IV lines in stellar spectra of stars with atmospheres of very low density. The ratios should then be in the low density limit predicted by theory. High resolution IUE spectra are perfectly adequate for such a test. The O IV line ratios in the star RR Tel (Penston *et al.* 1983) are very close to the low density limits computed by Nussbaumer and Storey (1982). This example demonstrates the interplay between solar and stellar spectra in the area of plasma diagnostics, a topic often overlooked in discussions of the solar-stellar connection.

The other type of density diagnostic is the ratio of an intersystem line to an allowed line of a different ion, but an ion formed at the same temperature as the intersystem line ion. There are several pitfalls to this technique, but it is very useful for high density structures (10^{11} - 10^{13} cm^{-3}, see Figure 3). Because the differential emission measure can vary in different solar regions, it is necessary that the intersystem and allowed line are formed at the same temperature, or if not that the emission measure at the temperature of the intersystem line can be interpolated from the emission measures of allowed lines. This can be accomplished by constructing plots such as shown in Figure 6. In Figure 6 line intensities are plotted normalized to the C IV intensity in the quiet Sun. Crosses mark allowed lines and solid dots refer to intersystem lines. If the differential emission measure (DEM) of the region in question has the same shape as the quiet Sun DEM, then the crosses should define a horizontal line in the plot, as is the case for the particular active region chosen. However, for the active region the intersystem line intensities fall substantially below the intensities predicted for allowed lines, because the active region densities are higher than the quiet Sun densities. The vertical lines connecting the intersystem line dots to the horizontal line segments define the decrements that can be used to directly infer electron densities using Figure 3. Note that the shape of the surge DEM departs from the quiet Sun shape, but that electron

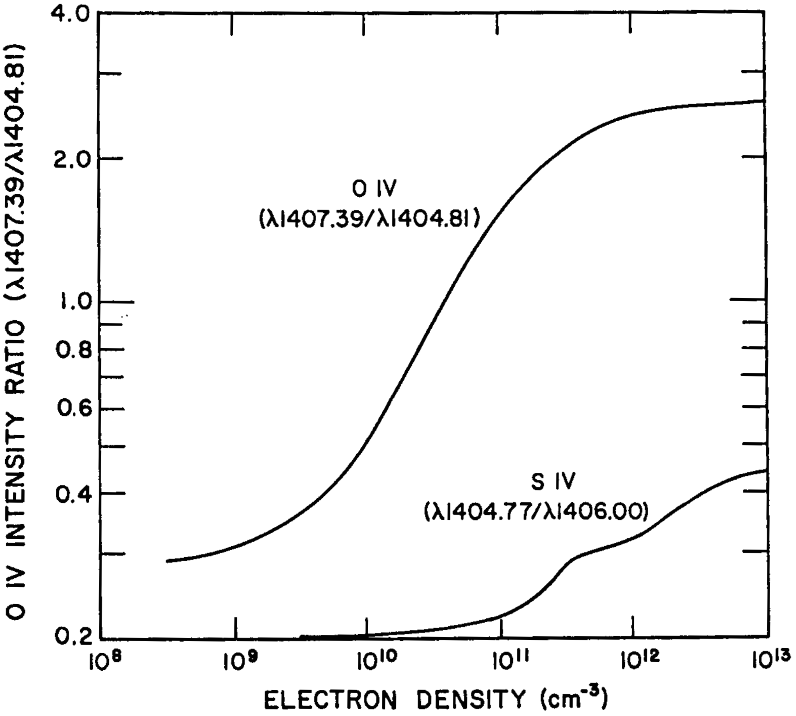

Fig. 4 - A density sensitive O IV line ratio. The S IV line ratio can be used to correct the λ1405 line for blending. See Doschek (1984) for sources of atomic data.

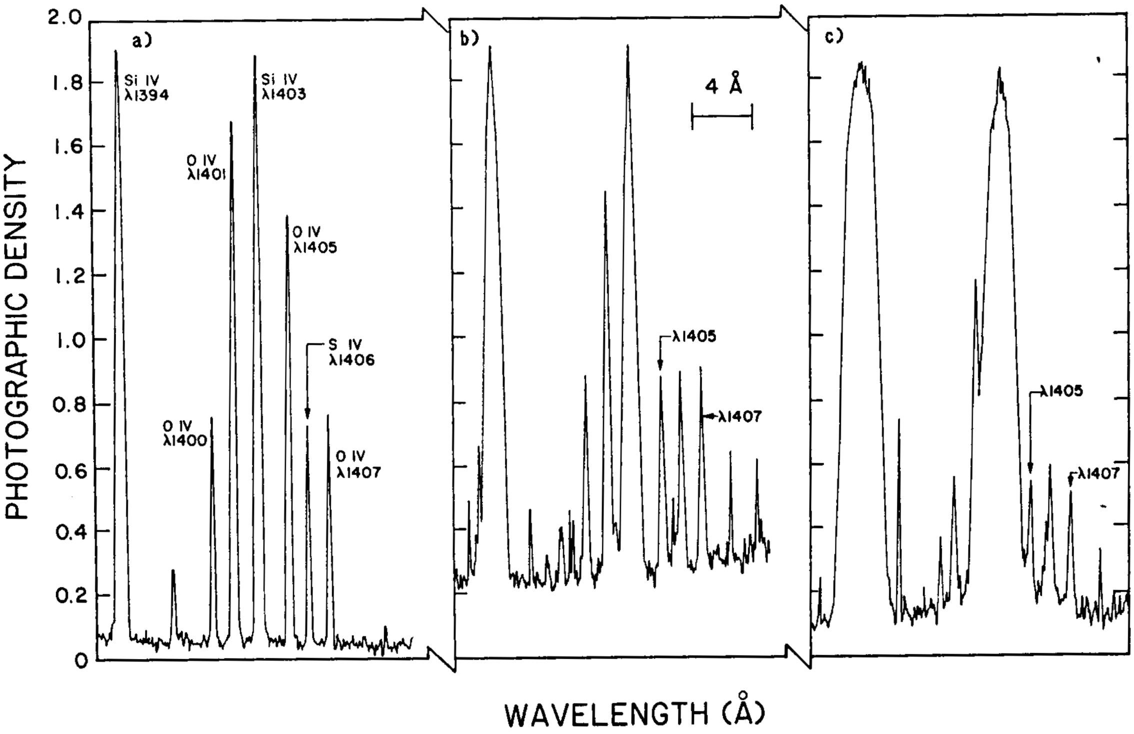

Fig. 5 - The O IV multiplet from Skylab S082-B spectra (Doschek 1984).

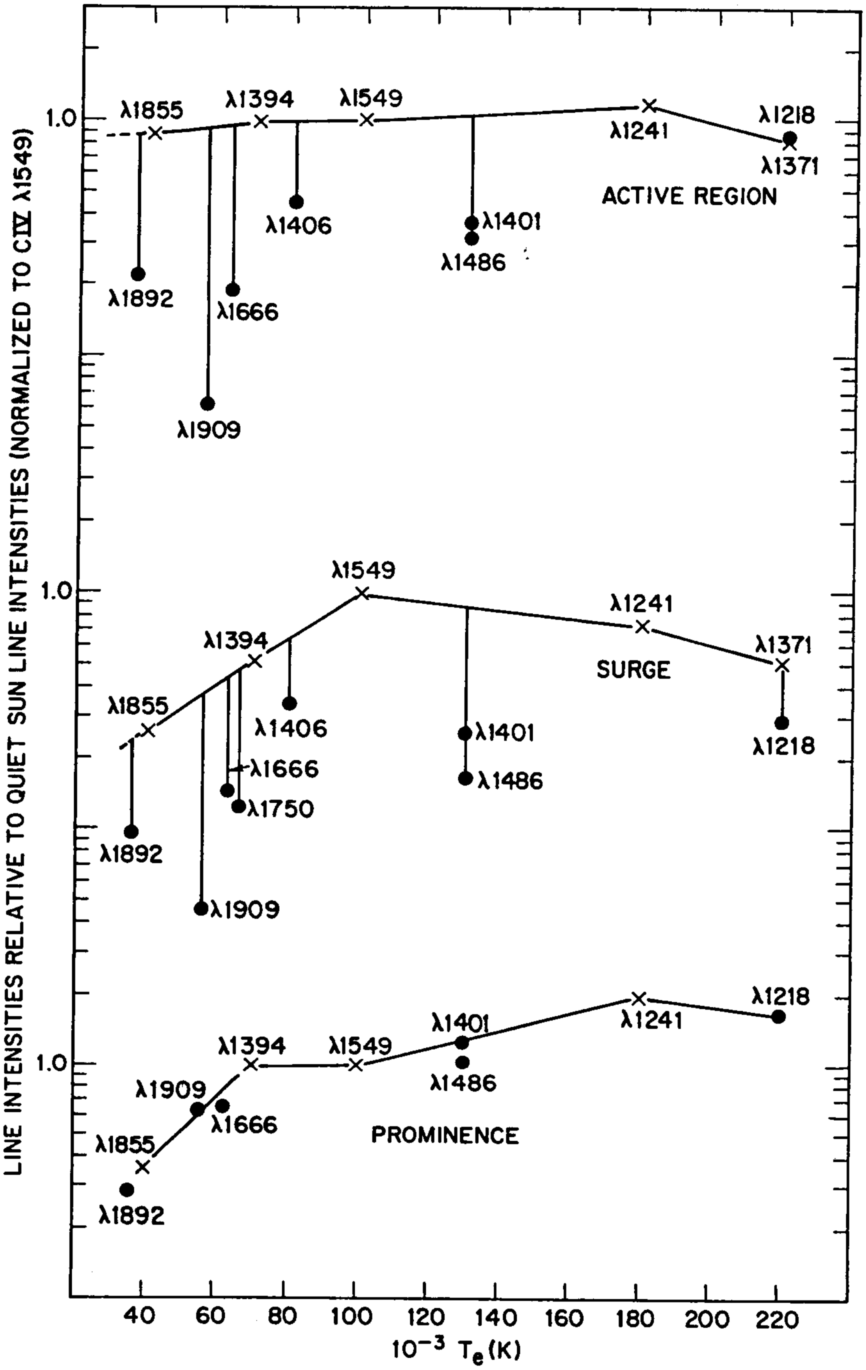

Fig. 6 - Skylab solar spectra of an active region, surge, and prominence compared to the quiet Sun spectrum (Doschek 1985).

densities are still high. The shape of the prominence DEM also departs from the quiet Sun shape, but the densities are the same as in the quiet Sun. A summary of electron pressures in different solar regions is given in Table 2.

Figure 6 shows that the shape of the DEM in different regions can depart from quiet Sun values. Inspection of the HRTS data indicates that on the scale of fine structures there is no "canonical" DEM distribution, although if many different structures in a region are averaged together, the shape of the DEM appears in many cases to be similar to the quiet Sun DEM over limited temperature ranges.

Examples of how different the shape of the DEM can be in different regions are found in the HRTS Spacelab 2 data. Figure 7 shows what Brueckner and Bartoe (1983) define as a turbulent event, i.e., an event exhibiting large, nearly symmetrically broadened line profiles. The event is well-observed in lines of low temperature ions such as C II, Si III, and Si IV, but is weaker in C IV lines, much weaker in O IV lines, and not seen at all in lines of N V. This implies that the DEM begins to decrease rapidly above 7 x 10^4 K, the temperature at which Si IV is formed. If only the O IV and Si IV lines were observed, and the small O IV/Si IV ratio were interpreted as due to a high density, then a spuriously high density would be obtained. The problem is that the O IV lines are formed at a temperature almost twice as high as the temperature at which Si IV is formed. Nevertheless, a density can be inferred for this event, by using density sensitive line ratios of Si III that are analogous to the O IV lines in their density sensitivity. The density is about 10^{11} cm^{-3} at the temperature of formation of Si III, about 3 x 10^4 K.

Another interesting example of how unpredictable the shape of the DEM can be in energetic events is shown in Figure 8. The event in question is a strong downflowing region as evidenced by the predominant redshifted structures in the line profiles. Note that this event can be easily seen in high temperature lines, such as N V formed at about 1.8 x 10^5 K, but is completely absent in lines of lower temperature ions such as C II and Si III. The O IV line ratios can be used to obtain densities at a temperature of about 1.3 x 10^5 K.

The above examples illustrate the unpredictability of the shape of the DEM when fine structures are resolved or partially resolved. The conclusion is that UV instrumentation should be able to observe a large number of lines, that, if possible, do not leave gaps in temperature. That is, for the region above 1150 Å, lines from cold ions ranging from S I and Si I up through N V should be observed. The Si I and S I lines are not only good chromospheric diagnostics, but the very narrow lines allow quite accurate wavelength measurements that in turn enable velocities relative to the chromosphere to be measured with an accuracy that can be as high as 1-2 km s^{-1} (Dere, Bartoe, and Brueckner 1986).

b) Transition Region Dynamics

Up to now the discussion has centered on the sizes, densities, and the DEM of transition region structures. However, one of the most outstanding characteristics of the transition region is its highly dynamic character. Random or turbulent, as well as anisotropic flows, are a common characteristic of at least the lower transition region. The motions can be divided into two distinct classes: those associated with apparently typical quiescent regions, and those associated with transient events. The motions associated with transient events are subdivided into the so-called "turbulent" events or into the category of "jets" (Dere, Bartoe, and Brueckner 1983, 1984, 1986). The "jets" appear in emission lines of chromospheric (C I) and transition region (C IV) ions.

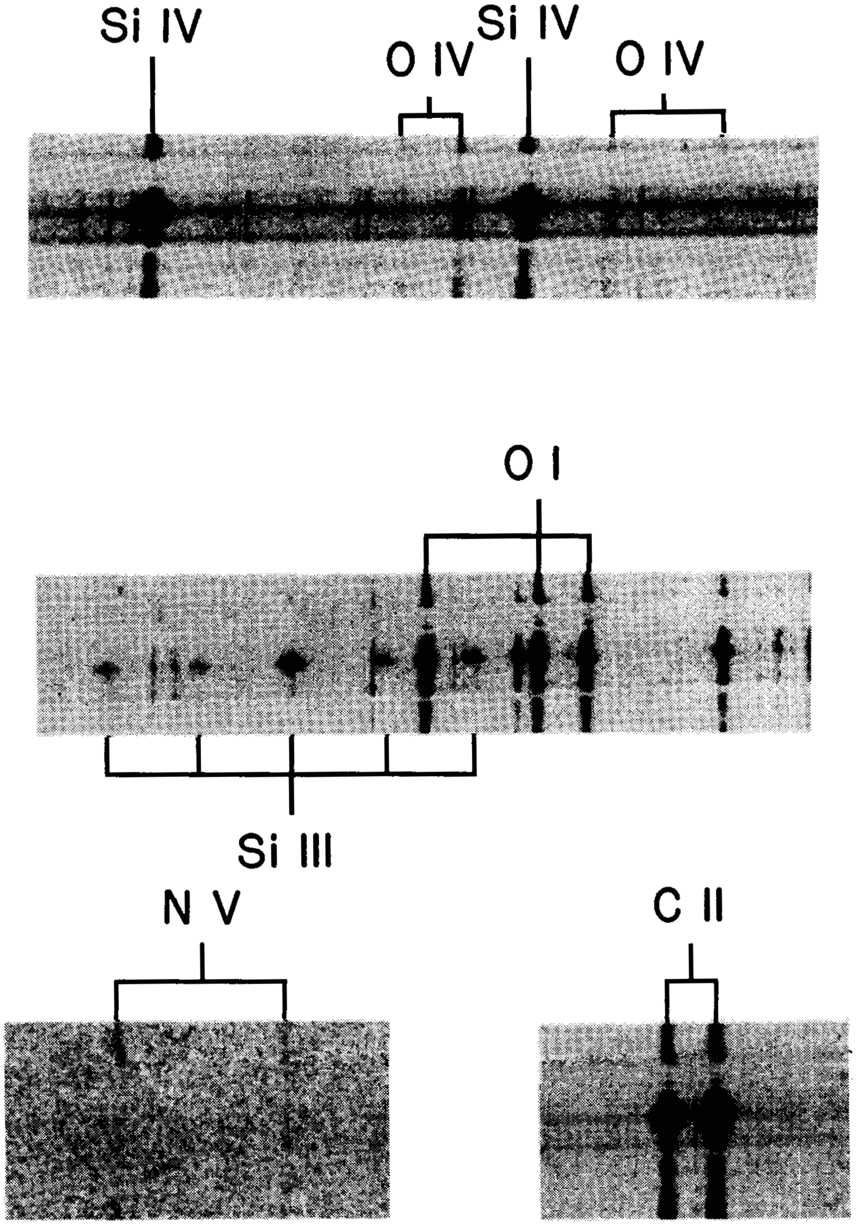

Fig. 7 - A "turbulent" transition region event recorded by the HRTS Spacelab 2 instrument. The event is seen at temperatures characteristic of C II($\approx 2 \times 10^4$ K), Si III(≈ 2-4×10^4 K), and Si IV(7×10^4 K). It is not seen at temperatures characteristic of O IV(1.3×10^5 K) and N V(1.8×10^5 K). Approximate wavelengths are: C II(1335 A), Si III (1300 A), Si IV(1400 A), O IV(1400 A), N V(1240 A).

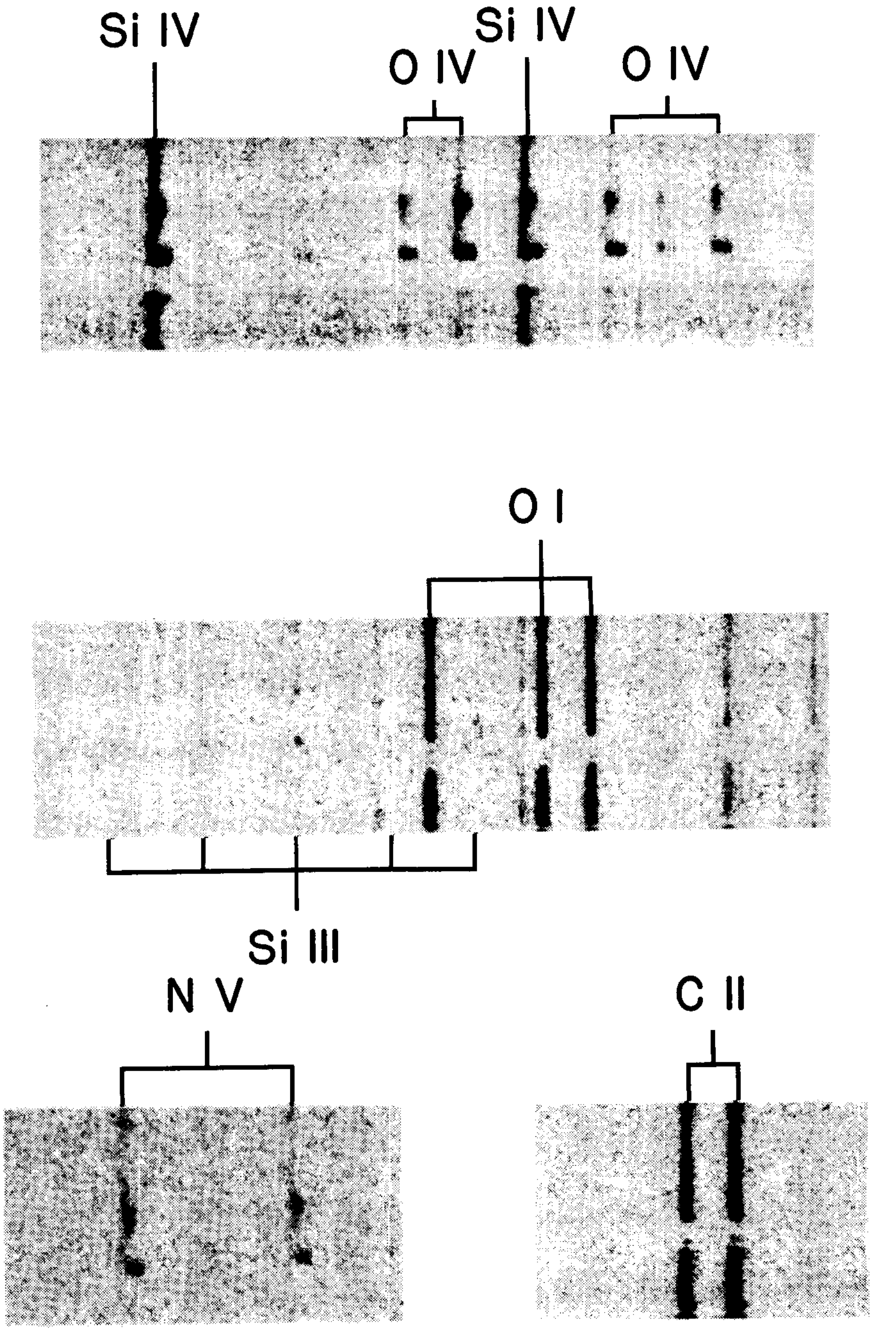

Fig. 8 - An event exhibiting large downflows recorded by the HRTS Spacelab 2 instrument. The event is seen in higher temperature lines such as Si IV, O IV, and N V, but is not seen in lower temperature lines of C II and Si III.

Turbulent events appear as both blue- and redshifted emission with velocites of about 100 km s^{-1}. Note that the transient events we are discussing are not flares, surges, or sprays. They are relatively new phenomena discovered with the HRTS. Of course larger events such as flares and surges also appear in transition region lines, but we confine our attention here to events not obviously associated with solar flares.

The motions associated with quiescent regions are also of two types. There is a random mass motion or perhaps turbulence associated with chromospheric and transition region lines. Lower transition region line widths are dominated by this motion, and not by their intrinsic Doppler widths. The average motions (averaged over many fine structures) range from about 8 km s^{-1} for upper chromospheric temperatures up to about 25 km s^{-1} at temperatures of 2 x 10^5 K. The increase in average motion appears to be monotonic with temperature (Figure 9), but there is considerable scatter in the results, principally because when viewed on a fine scale, such as with HRTS, the motions vary considerably from one individual structure to another. Nevertheless, the average values, as obtained from Skylab, OSO-8, SMM, and HRTS data are well-represented by the data in Figure 9.

Most of the lower transition region line width measurements have been obtained from the intersystem and allowed lines we have been discussing. An enlarged and more detailed portion of Figure 9 is shown in Figure 10. The data in Figure 10 are obtained from Skylab and are discussed in Doschek, Mariska, and Feldman (1981). The values shown by the circles enclosing dots are from data obtained above the limb. Above the limb the allowed lines are broadened by opacity, as discussed previously.

Above 3 x 10^5 K there is a gap in our knowledge concerning the motions up to about 8 x 10^5 K. Above this temperature, we again have measurements. These data come from the weak forbidden coronal lines at wavelengths greater than 1150 Å mentioned in Section II. The gap arises because of the difficulty of observing below 1150 Å with both high spectral resolution and high sensitivity.

Inspection of Figure 9 indicates that the motions peak around log $T_e \simeq 5.4$, but this is uncertain because of the gap. We also know that the motions at any given temperature appear to increase with height above the limb. Finally, the mass motions either disappear or are very small in quiescent prominences. They are also less in sunspot spectra and can be narrow at times during flares.

The origin of these motions is unclear and represents one of the outstanding problems in the UV to be addressed by HRSO UV instrumentation. They may arise because different unresolved fine structures have nonzero motions relative to each other, or they may be truly turbulent in nature. Recent HRTS Spacelab 2 results (Brueckner et al. 1986) indicate that both line broadening mechanisms may be present.

The other pervasive and interesting quiescent motion is the tendency for most lower transition region lines to be redshifted relative to chromospheric lines from ions such as Si I and S I (Doschek, Feldman, and Bohlin 1976). The redshift generally indicates motions of about 6-10 km s^{-1} and SMM observations have shown that these motions can persist for long time intervals over certain regions. The redshifts can also vary considerably from point to point on the Sun. Detailed studies of these redshifts, commonly interpreted as due to a net downflow of material, have been carried out with the SMM data (e.g., Gebbie et al. 1981, Klimchuk 1986). The velocity patterns appear to be organized over large regions of the solar surface (Athay 1985). One point to keep in mind concerning the redshifts is that they are smaller than the random motions on the average. That is, the net Doppler shift of the line centroid is less than the line width. The

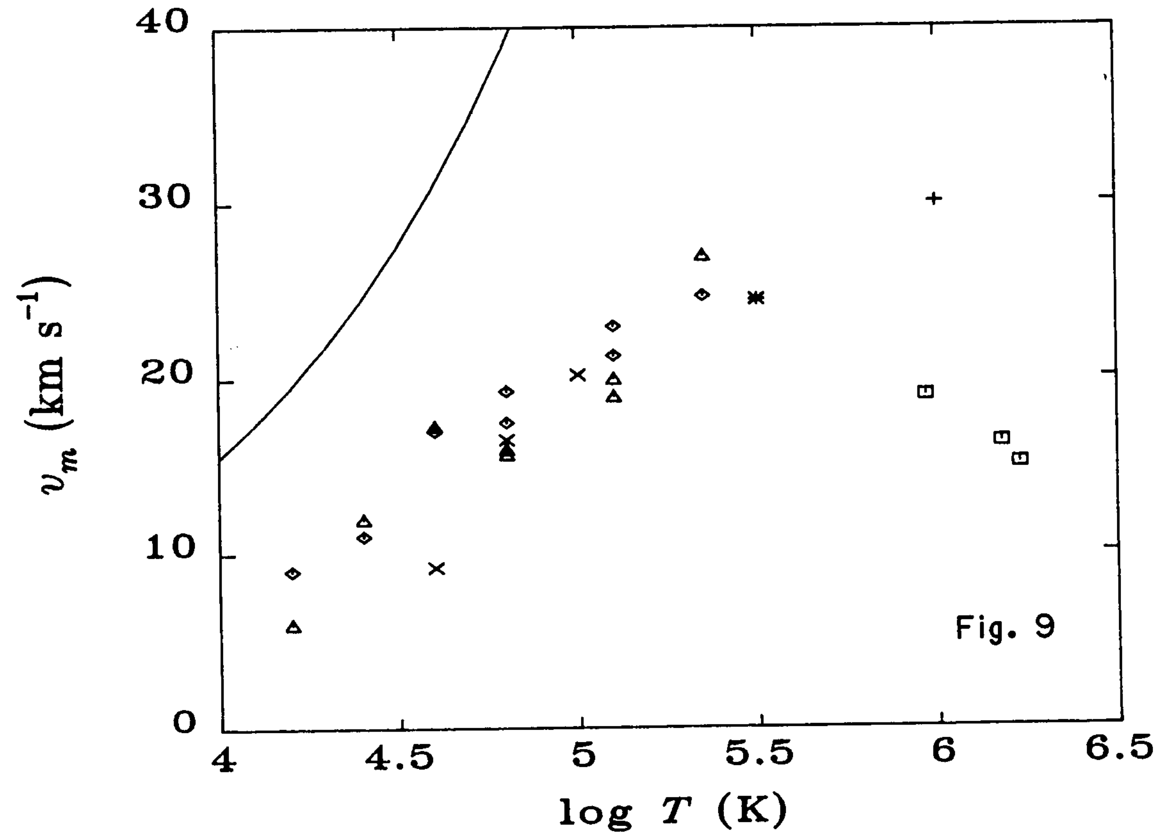

Fig. 9

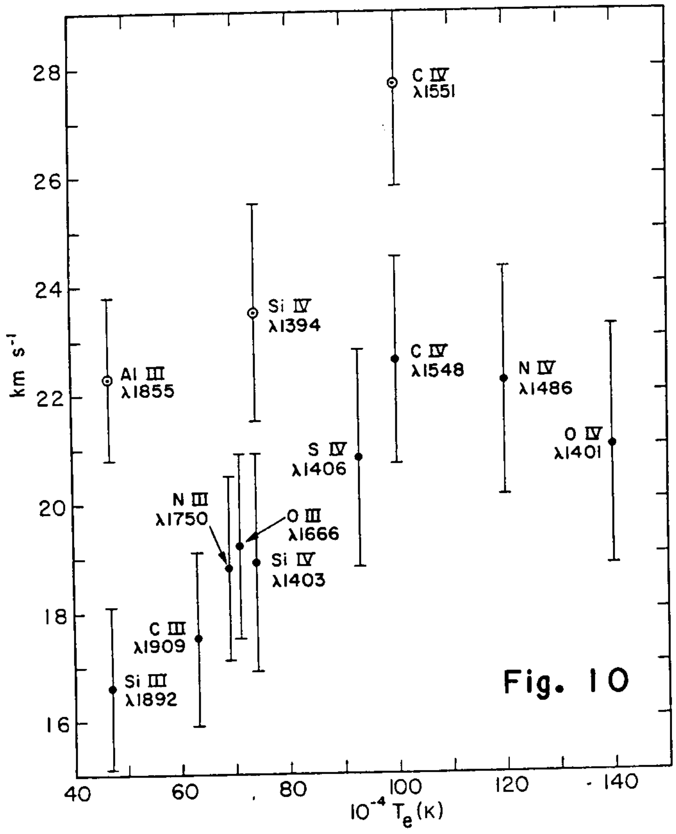

Fig. 10

Fig. 9 - Nonthermal broadening as a function of temperature. The solid line is the sound speed. See Mariska (1986) for details.

Fig. 10 - A detailed view of nonthermal motions in the lower transition region. The error bars are due to measurement statistics and real variations from region to region. Open circles are for lines measured above the limb and broadened by opacity.

implication is that there are unresolved structures, exhibiting both upflows and downflows, but that either more plasma is moving downward, or the plasma moving downward has a larger emission measure than the upward flowing plasma. A second strange point about the redshifts is that they do not appear to vanish at the limb (Feldman, Cohen, and Doschek 1982). The reason for this is unclear. And a third interesting point is that the redshifts are also seen in the spectra of other stars (e.g., Ayres et al. 1983). Whatever the cause of the redshifts, it is clear that these motions are closely linked with the origin and structure of the lower transition region, and it is important to study the dynamics of the transition region at a spatial resolution of about 0.1". Therefore, UV instrumentation should have sufficient spectral resolution to adequately measure chromospheric and lower transition region line profiles. A resolution of 0.03 Å between 1150 and 2000 Å would be adequate.

d) Some Non-equilibrium Effects

The turbulent events and their short lifetimes indicate that the plasma associated with these events may not be in ionization equilibrium. If the plasma is not in ionization equilibrium, then interpretation of the UV emission lines is complicated since ionization fractions and temperatures of ion formation can no longer be taken as known quantities. Several workers have considered possible scenarios in which ionization equilibrium might not be valid. Mariska (1984) considered the case of a flux tube in which a steady flow is established by asymmetric heating. He examined the effect of this flow on UV and XUV lines of O III, O IV, O V, and O VI. In his cases, the transition region is "classical", i.e., a thin layer separating the chromosphere from a hotter, nearly coronal plasma. Mariska (1984) found departures of about a factor of 4 or so between emission measures derived under the assumption of ionization equilibrium and the actual emission measures. However, the departures in the upflowing portion of the loop differed in sign from those in the downflowing leg, and if the results are averaged, as would occur with a low spatial resolution instrument, no substantial disagreement in emission measure was obtained. Similarly, for the ions he chose, temperature sensitive line ratios did not yield temperatures much different than expected assuming ionization equilibrium.

Dere et al. (1981) have also considered transient transition region plasmas. They adopted a non-"classical" transition region model in which hot coronal plasma cools rapidly to chromospheric temperatures and conduction is unimportant. An interesting result of their calculation is that pulses of emission are generated in UV emission lines at times differing by a few tens of seconds (Figure 11). Broad spectral line coverage, along with time resolution of a few seconds, would be able to detect such cooling plasma and would provide an unambiguous signature of transient ionization in the plasma. Therefore, UV instrumentation should have time resolution no worse than about 20s.

Another non-equilibrium process that might affect UV line intensities is the existence of non-Maxwellian electron velocity distributions. Such distributions might be maintained in a quasi-stationary state because of steep temperature gradients that produce appreciable temperature variations over the mean free path of an electron (e.g., Schoub 1983). Such non-Maxwellian distributions can alter the ionization balance and the excitation rates of spectral lines. In particular, precipitations of such particles into relatively cool regions (about 3-4 x 10^4 K) can affect high excitation emission lines from ions such as Si III by a factor of 2 or so (Dufton, Kingston, and Keenan 1984). Dufton, Kingston, and Keenan (1984) were able to explain the intensity of a high excitation Si III line by invoking a

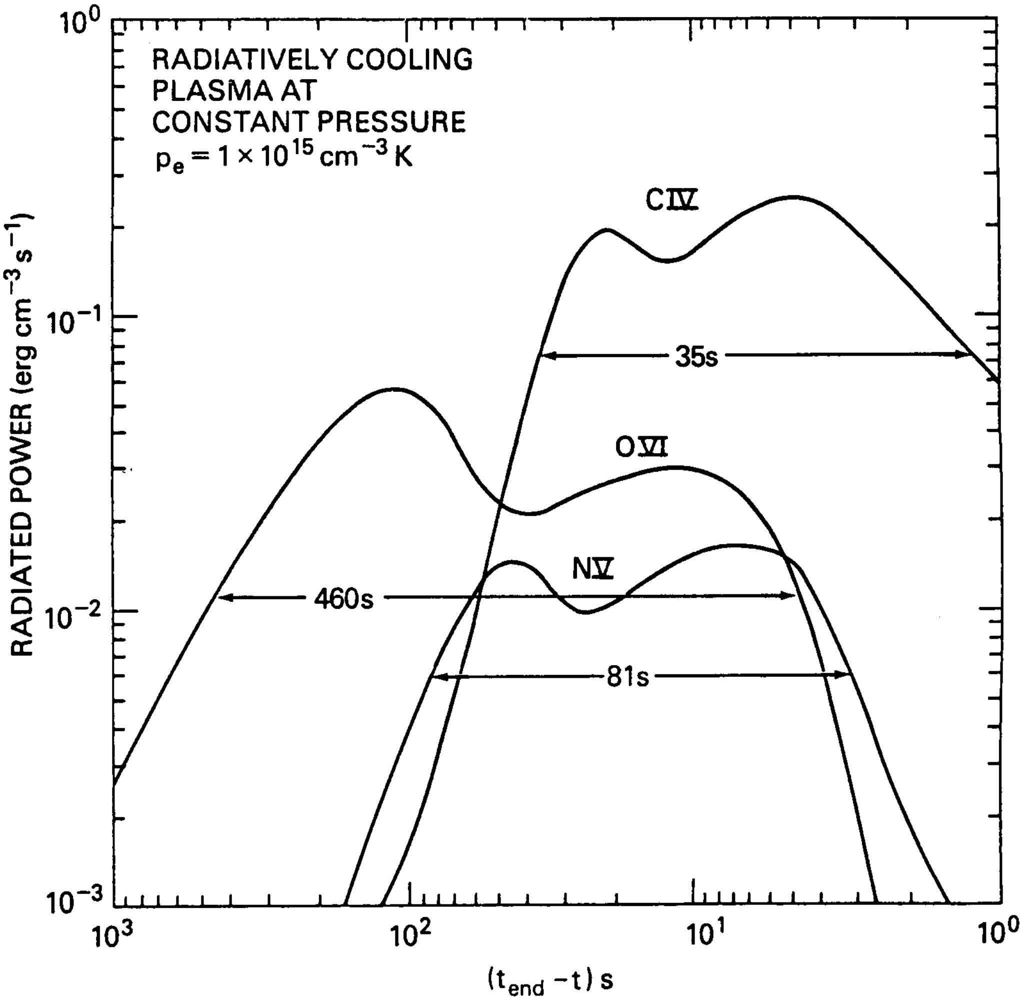

Fig. 11 - Time histories of emission from lithiumlike ions from a radiatively cooling plasma. The elapsed time t_{end} corresponds to $T_e = 10^4$K (Dere et al. 1981).

non-Maxwellian distribution, but Doschek and Feldman (1986) did not find such an effect for a similar line of Aℓ III. It is desirable to measure temperatures, if possible, for transition region ions, in order to investigate such effects. Transport of ions into higher temperature regions, such as discussed by Jordan (1975) for He II, would similarly enhance high excitation lines. Unfortunately, the high excitation lines that appear longward of 1150 Å are weak, and the resonance lines fall shortward of the 1150 Å cutoff. The Si IV 3d --> 3p lines, which are really excited from the 3s $^2S_{1/2}$ ground state, fall near 1128 Å. Other candidates for temperature measurement are the same transitions in Mg II and Aℓ III, and the line of Si III mentioned above. Another possible candidate, mentioned in Doschek and Feldman (1986), is a ratio involving S III lines. However, all of the high excitation lines are weak and therefore a sensitive spectrograph is required. It would be interesting to see if such weak lines might be detected by the Space Telescope in certain stellar objects that have strong UV emission line spectra such as RR Tel.

A final point should be made concerning UV spectra. Frequently the most interesting lines are the intercombination lines. For these lines resonances in the excitation cross sections and precise values of radiative decay rates are very important. It is therefore necessary for the support of HRSO to *maintain strong support for theoretical atomic physics calculations of highly ionized atoms, and also to support laboratory measurements of radiative decay rates and excitation processes for such ions*.

I thank Guenter Brueckner and the NRL Spacelab 2 team for providing access to the HRTS Spacelab 2 data. I thank Spiro Antiochos, Kenneth Dere, and Uri Feldman for useful comments on the manuscript.

REFERENCES

Antiochos, S.K., and Noci, G. 1986 *Ap. J.*, 301, 440.

Athay, R.G. 1982, *Ap. J.*, 263, 982.

Athay, R.G. 1984, *Ap. J.*, 287, 412.

Athay, R.G. 1985, in Proceedings of the MPA/LPARL Workshop on *Theoretical Problems in High Resolution Solar Physics*, 16-18 September 1985, page 205.

Ayres, T.R., Stencel, R.E., Linsky, J.L., Simon, T., Jordan, C., Brown, A., and Engvold, O. 1983, *Ap. J.*, 274, 801.

Brueckner, G.E., and Bartoe, J.-D.F. 1983, *Ap. J.*, 272, 329.

Brueckner, G.E., Bartoe, J.-D.F., Cook, J.W., Dere, K.P., and Socker, D.G. 1986, COSPAR *Topical Meeting on Solar Investigations from Spacelab 2*, July 1986, to appear in *Advances in Space Research*.

Dere, K.P., Bartoe, J.-D.F., and Brueckner, G.E. 1983, *Ap. J. (Letters)*, 267, L65.

Dere, K.P., Bartoe, J.-D.F., and Brueckner, G.E. 1984, *Ap. J.*, 281, 870.

Dere, K.P., Bartoe, J.-D.F., and Brueckner, G.E. 1986, *Ap. J.*, 305, 947.

Dere, K.P., Bartoe, J.-D.F., Brueckner, G.E., Dykton, M.D., and Van Hoosier, M.E. 1981, *Ap. J.*, 249, 333.

Doschek, G.A. 1984, *Ap. J.*, 279, 446.

Doschek, G.A. 1985, in *Autoionization*, edited by A. Temkin (Plenum Press Corp., New York), Chapter 6.

Doschek, G.A., and Feldman, U. 1982, *Ap. J.*, 254, 371.

Doschek, G.A., and Feldman, U. 1986, *Ap. J. (Letters)*, to be submitted.

Doschek, G.A., Feldman, U., and Bohlin, J.D. 1976, *Ap. J. (Letters)*, 205, L177.

Doschek, G.A., Feldman, U., and Rosenberg, F.D. 1977, *Ap. J.*, 215, 329.

Doschek, G.A., Feldman, U., Van Hoosier, M.E., and Bartoe, J.-D.F. 1976, *Ap. J.*

Suppl., 31, 417.

Doschek, G.A., Mariska, J.T., and Feldman, U. 1981, *M.N.R.A.S.*, 195, 107.

Dufton, P.L., Kingston, A.E., and Keenan, F.P. 1984, *Ap. J. (Letters)*, 280, L35.

Feldman, U. 1983, *Ap. J.*, 275, 367.

Feldman, U., Cohen, L., and Doschek, G.A. 1982, *Ap. J.*, 255, 325.

Feldman, U., and Doschek, G.A. 1977, *J. Opt. Soc. Am.*, 67, 726.

Feldman, U., Doschek, G.A., and Mariska, J.T. 1979, *Ap. J.*, 229, 369.

Gabriel, A.H. 1976, *Phil. Trans. Roy. Soc. of London A*, 281, 339.

Gebbie, K.B. *et al.* 1981, *Ap. J. (Letters)*, 251, L115.

Jordan, C. 1975, *M.N.R.A.S.*, 170, 429.

Kjeldseth Moe, O., and Nicolas, K.R. 1977, *Ap. J.*, 211, 579.

Klimchuk, J.A. 1986, *Ph.D. Thesis*, University of Colorado and National Center for Atmospheric Research, NCAR/CT-96.

Mariska, J.T. 1984, *Ap. J.*, 281, 435.

Mariska, J.T. 1986, *Ann. Rev. Astron. Astrophys.*, 24, 23.

Nussbaumer, H., and Storey, P.J. 1982, *Astr. Ap.*, 115, 205.

Penston, M.V., *et al.* 1983, *M.N.R.A.S.*, 202, 833.

Rabin, D., and Moore, R. 1984, *Ap. J.*, 285, 359.

Rosner, R., Tucker, W.H., and Vaiana, G.S. 1978, *Ap. J.*, 220, 643.

Sandlin, G.D., Brueckner, G.E., and Tousey, R. 1977, *Ap. J.*, 214, 898.

Schmahl, E.J., and Orrall, F.Q. 1979, *Ap. J. (Letters)*, 231, L41.

Schoub, E.C. 1983, *Ap. J.*, 266, 339.

N88-11613

FIRST RESULTS ON QUIET AND MAGNETIC GRANULATION FROM SOUP

A. Title, T. Tarbell (Lockheed PARL), and the SOUP Team

(L. Acton[1], D. Duncan[1], S. Ferguson[1], M. Finch[1], Z. Frank[1], G. Kelly[1], R. Lindgren[1], M. Morrill[1], T. Pope[1], R. Reeves[1], R. Rehse[1], R. Shine[1], K. Topka[1], G. Simon[2], J. Harvey[3] J. Leibacher[3], W. Livingston[3], L. November[4], J. Zirker[4])

[1]*Lockheed Palo Alto Research Laboratory, Dept. 91-30,*
Bldg. 256, 3251 Hanover Street, Palo Alto, CA 94304, U.S.A.
[2]*Air Force Geophysics Laboratory, Sunspot, NM 88349, U.S.A.*
[3]*National Solar Observatory, Tucson, AZ 85718 U.S.A.*
[4]*National Solar Observatory, Sunspot, NM 88349, U.S.A.*

ABSTRACT

The flight of SOUP on Spacelab 2 allowed the collection of time sequences of diffraction limited (0.5 arc second) granulation images with excellent pointing (0.003 arc seconds) and completely free of the distortion that plagues groundbased images. The p-mode oscillations are clearly seen in the data. Using fourier transforms in the temporal and spatial domain we have shown that the p-modes dominate the autocorrelation lifetime in magnetic regions. When these oscillations are removed the autocorrelation lifetime is found to be 500 seconds in quiet and 950 seconds in magnetic regions. In quiet areas exploding granules are seen to be common. It is hard to find a granule that does not explode or is not affected by an explosion. We speculate that a significant fraction of granule lifetimes are terminated by nearby explosions. Using local correlation tracking techniques we have been able to measure horizontal displacements, and thus transverse velocities, in the intensity field. In quiet sun it is possible to detect both super- and mesogranulation. Horizontal velocities are as great as 1000 m/s and the average velocity is 400 m/s. In magnetic regions horizontal velocities are much less, about 100 m/s.

I. Introduction

In the traditional model solar granulation is considered to be convective overshoot, in which the convective cells have a center to center distance of about 2 arc seconds and a lifetime of 4 to 16 minutes. In previous studies the lifetime has been highly dependent on whether the measurement technique averaged over ensembles of granules or isolated individual features. There have been some indications that granulation is slightly different in magnetic field regions and near sunspots, but there is still controversy on this point. On average the picture is that a granule is a bright central region of upflow, with a diameter of 1.5 arc seconds, surrounded by a darker region of downflow. The picture of granulation before the flight of SOUP has been excellently reviewed in "Solar Granulation" by Bray, Loughhead, and Durrant (1984).

The picture emerging from the analysis of the SOUP data is qualitatively different from the traditional model. However, at this point in time we cannot define granule evolution. The definition of granular evolution is complex because there exists in the solar surface a hierarchy of intensity fluctuations, from the p-mode oscillations with scales of many tens of arc seconds and large phase velocities to apparent surface waves with scales at or below the resolution limit and low or zero phase velocities. There are also local phenomena, which involve areas with radii of a few to ten arc seconds, such as the well-known exploding granules (Namba, 1986) which seem to be much more pervasive in the SOUP data than previously noted. It is difficult to find a point in the movies that does not "explode" or is clearly not affected by a nearby event. Other time evolving patterns exist that probably have a different physical origin than exploders. All of the wave fields and the local phenomena, of course, coexist in the intensity field we have called granulation. A single image does not begin to reveal the richness in the solar surface.

The granulation pattern is embedded in systematic flows with spatial scales from ten to at least forty arc seconds, and lifetimes long compared to a single thirty minute orbital observing period. Some of the flow fields probably are the meso and supergranulation, but other patterns may also exist.

In regions with significant magnetic field the surface flow patterns are considerably less vigorous, but not significantly less complex. The granulation pattern is statistically more stable, there is lower modulation in the intensity field, the wave patterns are diminished in amplitude as are the velocities of the steady flows, and exploding granules are much less common; but most of the phenomena seen in quiet sun can also be found in the magnetic regions.

The SOUP instrument on Spacelab 2 (SL 2) collected granulation data spanning a period of about 16 hours. The images are very uniform in quality and are distortion free. Using the ESA Instrument Pointing System (IPS) and an internal fast guider, image stability of 0.003 arc seconds RMS was achieved. An ideal data set was collected for movie analysis. We have created about 100 processed movies (15,000 processed frames) from three original digital image sequences. Image processing techniques have included spatial smoothing, running averages, median filtering, spatial and spatial-temporal fourier filtering, blink comparison, color overlays, and differencing. The processed images are recorded permanently on optical disks. The optical disks can be studied using a normal video monitor and a computer controlled video disk player.

We have spent many hours viewing the various movies. It is extremely unfortunate that there is not a convenient method for publishing them. Most of the topics reported here are based upon impressions gained from the movies. The eye-brain system is a subtle tool for acquiring information from movie presentations. However, developing quantitative procedures to describe some of these impressions is difficult and requires extensive calculations.

At the current stage of the data analysis, we are still sorting out what we have observed in movies, and analyzing the results of numerical processes we have applied. So far no combination of algorithms has produced a convincing definition of a granule or the process of granule evolution. However, some of the investigations have been sufficiently quantitative to provide useful measures of the phenomena we observe in the solar surface. In the sections below we will report on the state of the analysis of granulation in quiet and magnetic sun as inferred from different analysis techniques.

II. Observations

The data used for this report were all collected on film using the Solar Optical Universal Polarimeter (SOUP) which operated on the flight of Spacelab 2 (Title *et al.* , 1986). The original images are 140 × 250 arc seconds and are taken in a thousand angstrom band centered at 6000ÅFor this preliminary report we have studied two digitized subsections, a 40 × 40 arc second quiet sun region, and a 60 × 60 arc second pore region. The pores are part of AR 4682 at approximately S15, W31 ($\mu = 0.83$). Because of limitations of the processing computer and our image display system, all digital images are 256 x 256 pixels. This corresponds to 0.161 and 0.234 arc second per pixel for the quiet and pore regions, respectively. The images are separated by 10 seconds in time and cover 1650 seconds. The results reported here are all from orbit 110 (19:10:35 to 19:38:07 GMT on 5 August 1985.)

III. Autocorrelation Measurements

One of the standard methods of determining lifetime of an intensity pattern is from the width of its autocorrelation (AC) function. Here we define the temporal autocorrelations of the intensity function as

$$AC(\tau) = \frac{\langle \delta I(x,y,t_0)\ \delta I(x,y,t_0+\tau) \rangle}{\langle \delta I^2(x,y,t_0) \rangle}$$

where x and y are the spatial coordinates, t_0 is the reference time, and τ the time separation. The brackets indicate an average over space, and

$$\delta I(x,y,t) = I(x,y,t) - \langle I(x,y,t) \rangle$$

where here the brackets indicate an average over space and time.

Previous AC lifetime measurements of granulation have ranged from 3 to 7 minutes with an average of about 6 minutes. Figure 1 shows the autocorrelation function measured in a number of recent studies (Mehltretter, 1978) compared with results from our data. As can be seen from the figure the agreement is good. The lifetime, as measured by the time for the correlation to drop to $1/e$ (.37) is about 5 minutes.

Our data for figure 1 were obtained from an area of about 350 square arc seconds (SAS). When smaller areas are examined the AC functions look quite different. Figure 2 (solid)

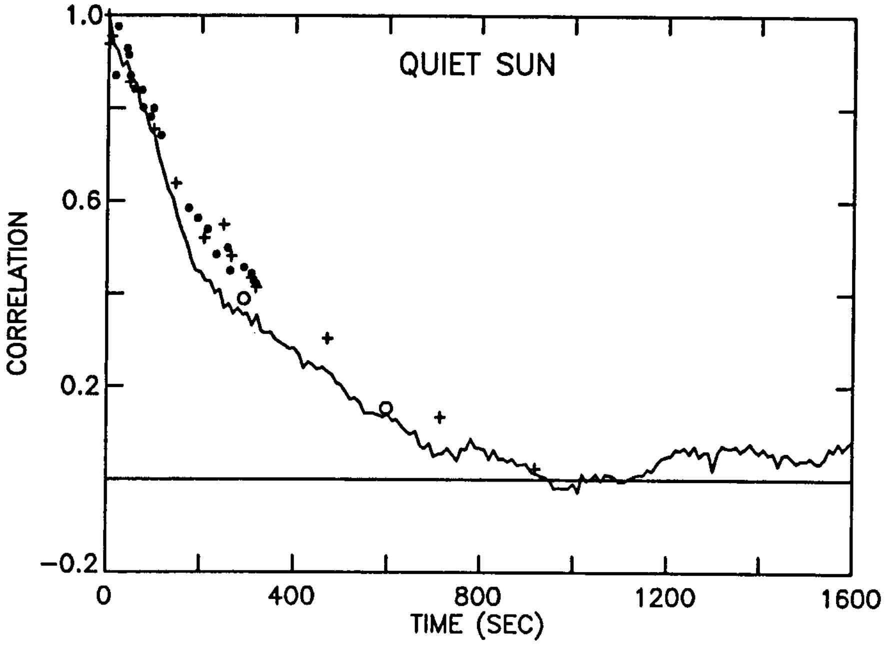

Fig. 1 Comparison of SOUP (solid) autocorrelation measurements with previously published results.

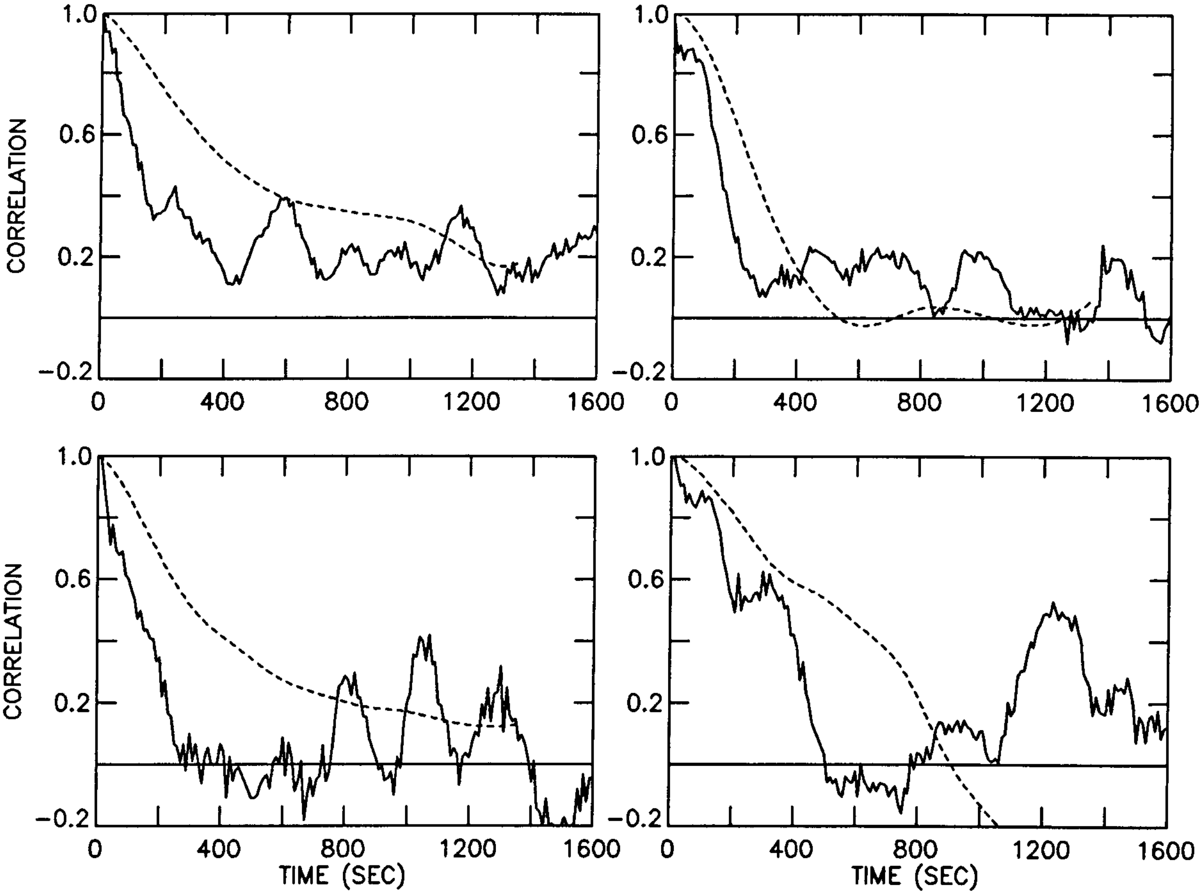

Fig. 2 AC(τ) in four 6 × 6 arc second regions (solid). These exhibit oscillations due to the solar p-modes. Dashed lines show AC(τ) for the same regions after subsonic filtering.

shows the AC functions generated from four 26 SAS areas. In these smaller regions the AC functions do not drop monotonically, but rather exhibit oscillations with periods of 3 to 6 minutes (depending on the region). This suggests that the five minute oscillation is affecting the correlation lifetime, which is not too surprising as it is strongly present in the granulation movies. The average AC over a sufficiently large region does not oscillate because a range of periods is present.

To remove the effect of the five minute oscillation we have applied what we call a subsonic fourier filter to the time sequence of quiet sun images. The original sequence of images is fourier transformed from a function of x, y, and t into a transformed function of k_x, k_y, and ω. The subsonic filter is defined by a cone

$$\omega = v \times k$$

in $k - \omega$ space, where k and ω are spatial and temporal angular frequencies and v is a velocity. All fourier components inside the cone (i.e., with phase velocities less than v) are retained, while all those outside are set to zero. A value of $v = 3$ km/s, well below the sound speed, 7 km/s, is used. For this value of v, the velocity cone is totally inside the fundamental and, of course, all of the overtones of the five minute oscillation. That is, it lies below the p-mode ridges in the well known $k - \omega$ diagram of the power spectrum of the solar velocity field. Therefore, it should include virtually all local phenomena, but exclude any waves with phase velocities greater than 3 km/sec.

Figure 3 shows a $k - \omega$ power spectrum for this data with the ridge pattern and the 3 km/s line overlayed. Clearly this filter excludes the power in the ridge pattern.

A subsonic filtered movie exhibits very little five minute oscillation. As seen from figure 2 (dashed) the AC functions created from subsonic filtered data for the individual regions have the oscillations strongly suppressed. Figure 4 shows the AC of 350 SAS for original (solid) and subsonic filtered (dashed) images. The AC lifetime of the subsonic data is greater by 50 percent than the original – a lifetime of 410 versus 270 seconds.

In order to observe the effect of magnetic field on the granulation pattern the SOUP images have been aligned with National Solar Observatory (Tucson) magnetograms taken just before and just after the SOUP data. Registration was accomplished by visual blink comparison of NSO continuum images and SOUP images. By registering the small pores and the spot present in both images, alignment to about 2 arc second accuracy was possible. The NSO continuum images and magnetograms are themselvesy registered to better than one arc second. Figure 5 shows the magnetogram contours (white) overlayed on the pore region. The boxes (black) in the figure are the regions selected for AC function analysis.

Twelve 36 SAS regions were selected to be inside the 70 gauss contour of the magnetograms, but well outside of pores. Shown in figure 6 are the AC functions for the original (solid) and the subsonic filtered (dashed) data for four of these regions. Figure 7 shows the sum

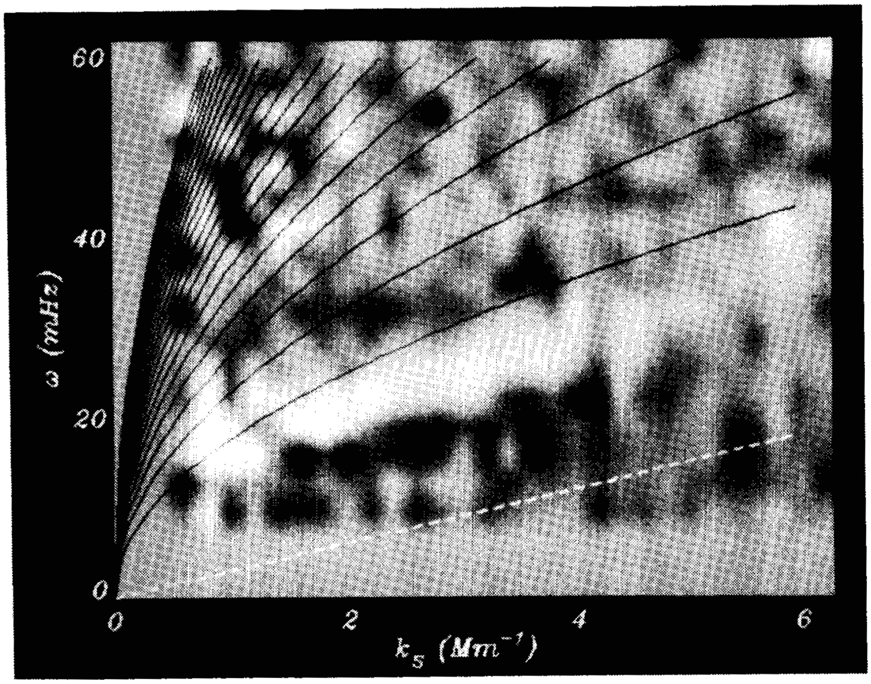

Fig. 3 $k - \omega$ diagram showing power in this data and the position of ridge pattern from other measurements (solid), and the line $\omega = 3k$ (dashed).

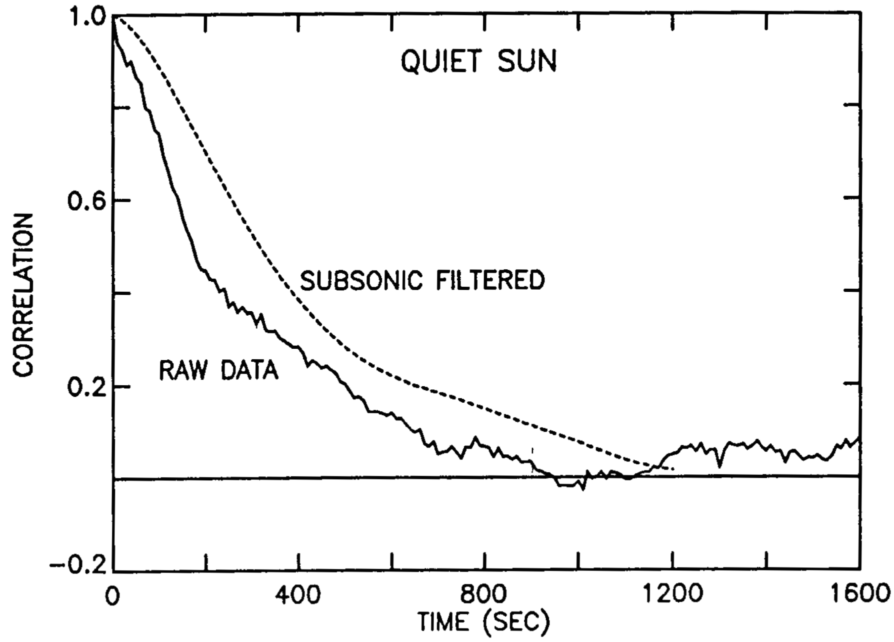

Fig. 4 AC functions for 350 SAS of quiet sun for original data (solid) and subsonic filtered data (dashed).

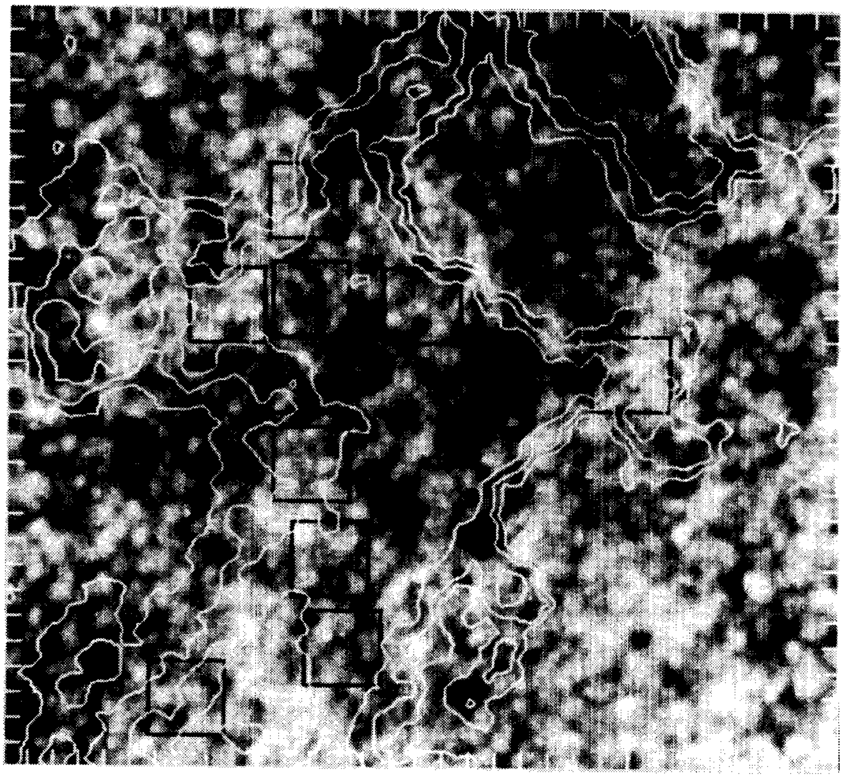

Fig. 5 Image of the pore region with magnetic contours overlayed. The contour levels are −75 and −270 gauss. The black boxes indicate regions used for constructing autocorrelation functions. Ticks are separated by one arc second.

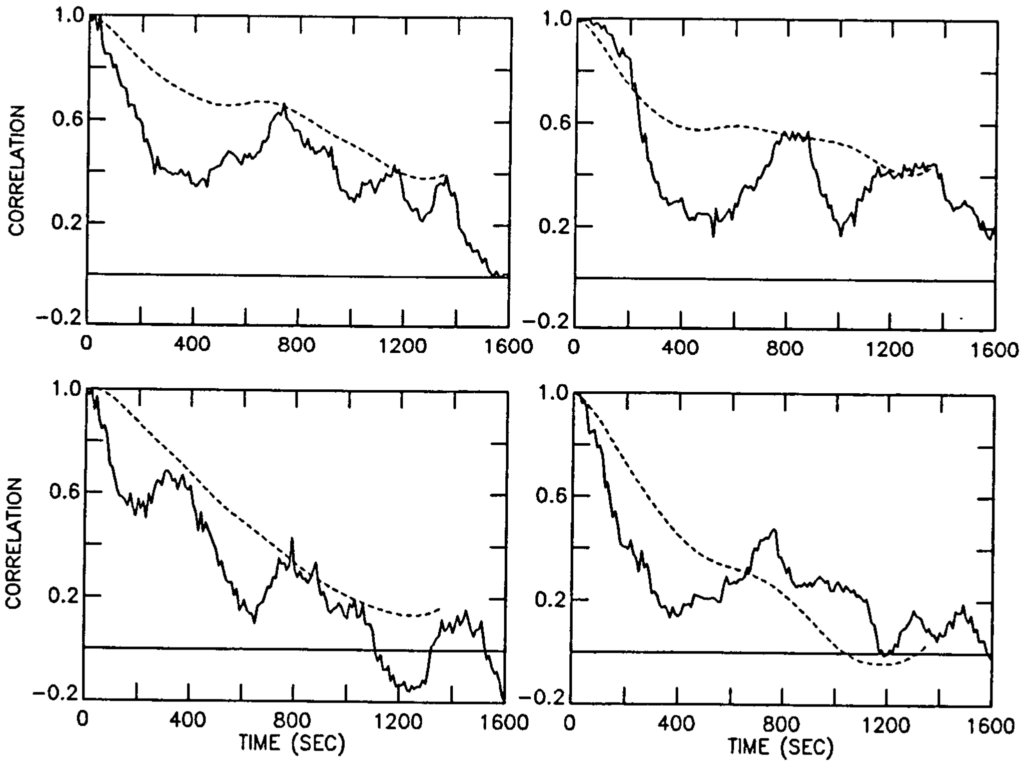

Fig. 6 AC functions for four magnetic regions using original (solid) and subsonic data (dashed).

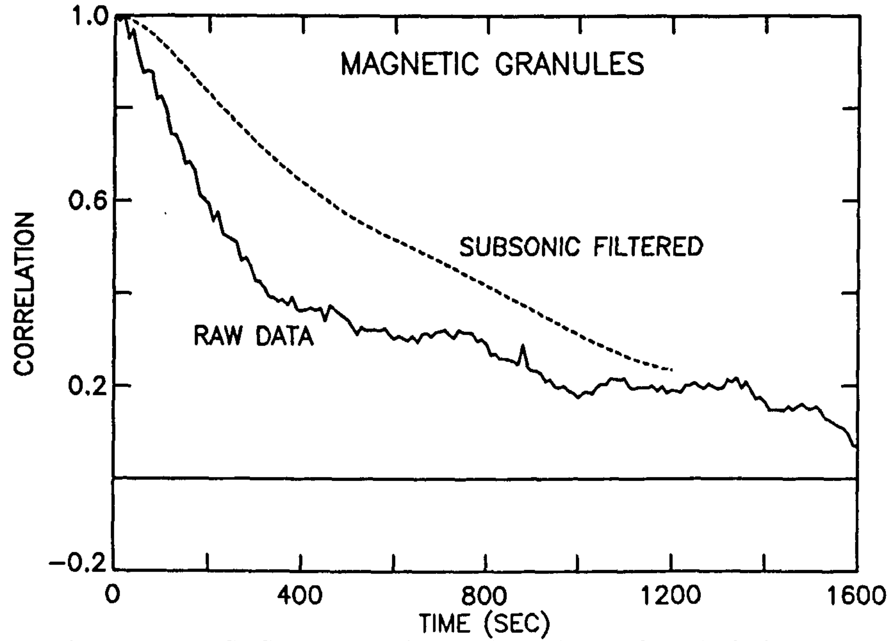

Fig. 7 AC functions for 350 SAS of magnetic sun for original data (solid) and subsonic filtered data (dashed).

of the AC's for the twelve regions for original (solid) and subsonic filtered (dashed) data. The lifetime from the subsonic data is a factor of two greater than the original data – 890 versus 420 seconds.

In magnetic regions the AC lifetime is dominated by the five minute oscillation and when this oscillation is removed the AC lifetime increases by about a factor of two. In quiet sun the effect of the subsonic filtering is much less. The removal of the effects of the five minute oscillation allows the autocorrelation technique to demonstrate that the convective pattern is significantly more stable in magnetic field regions than in quiet sun.

The temporal autocorrelation functions discussed above compare sets of spatially aligned images as a function of time and yield information related to feature lifetime. Spatial autocorrelation functions compare the same image with different spatial offsets and yield information on the spatial scale of the image. Here we define the spatial AC function as

$$AC(\Delta) = \frac{\langle \delta I(x,y,t)\ \delta I(x+\Delta,y,t)\rangle}{\langle \delta I^2(x,y,t)\rangle}$$

where Δ is the spatial offset. Figures 8a and 8b show (solid) the spatial AC's for quiet and magnetic sun, respectively. For a wide variety of patterns the half width at half maximum (HWHM) of the correlation function is related to the pattern size, r_o, by (Mosher,1977)

$$r_o = 1.2 \times \text{HWHM}.$$

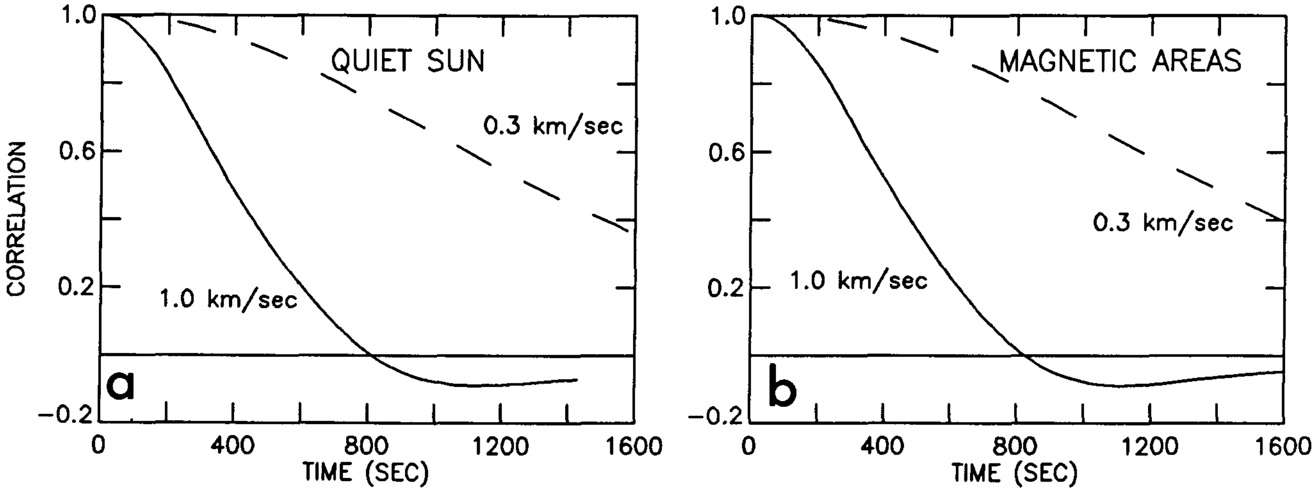

Fig. 8 Spatial autocorrelation functions for quiet (a) and magnetic sun (b). Solid curves curves are labeled 1 km/s to represent the fact that this curve would be generated by an infinite lifetime structure moving at 1 km/s. Dashed curves show the spatial AC functions for unchanging images displaced at 0.3 km/s.

The radius of the average structure in the quiet and magnetic regions is 450 and 500 km (diameters of 1.25 and 1.4 arc seconds), respectively. This suggests that on average the structures in the quiet and magnetic regions are about the same size.

The spatial AC functions can also be used to understand the effect of flows on the lifetime data because the displacement field can be interpreted as the result of a flow field. That is,

$$\Delta = v \times t.$$

The solid curves in figure 8 are labeled 1 km/s and can be interpreted as the temporal AC function of an intensity field of infinite lifetime that is moving at a constant velocity of 1 km/sec. Shown dashed in the same figure are curves corresponding to a displacement rate of 0.3 km/sec. The flow lifetime T_f, the time required for the flow to cause the spatial AC to drop to $1/e$, is just

$$T_f = \frac{AC_{1/e}}{v_f},$$

where v_f is the flow velocity. The value of $AC_{1/e}$ is 450 km for quiet sun and 500 km for magnetic.

The presence of a flow field will cause the measured lifetime from the temporal AC function to underestimate the lifetime of the granulation. Roughly the lifetimes as measured by the temporal AC functions, the actual lifetime, and the flow lifetime from the spatial AC functions are related by

$$1/T_m = \sqrt{(1/T_a)^2 + (1/T_f)^2},$$

or

$$T_a = \frac{T_m \times T_f}{\sqrt{T_f^2 - T_m^2}},$$

where T_a is the actual lifetime of the granules and T_m is the measured lifetime from the temporal AC function. This equation limits the flow lifetime to the measured lifetime, and therefore sets an upper limit on the average flow velocity. For quiet and magnetic sun the maximum flow velocities permitted by the observations are 1.1 and 0.5 km/s, respectively.

Using local correlation techniques (described below), we have measured the average flow velocities for quiet and magnetic sun to be 400 and 200 m/s, respectively. Correcting for the flow field yields "corrected" quiet and magnetic granule lifetimes of 440 and 950 seconds, respectively. Measurements of the velocity of individual granules has been done for the quiet sun (described below) and an average velocity of 0.9 km/s has been found. This corrects the AC lifetime to 710 seconds in quiet sun. The AC lifetime data is summarized in Table 1.

Table 1.

	Original	Subsonic	Steady Flow Correlation	Feature Flow Correlation
Quiet	270s	410s	440s	710s
Magnetic	420s	890s	950s	–

IV. Intensity Fluctuations

It is clear from the movies of the pore region that the oscillations and other intensity fluctuations are reduced in the magnetic field areas. (Reduced amplitude Doppler velocities in magnetic regions have long been observed.) Figures 9a and 9b show the mean intensity and the RMS intensity fluctuation as a function of position averaged over the entire movie. Brighter areas correspond to higher average intensities and higher RMS fluctuations respectively. Comparison of 9b, the RMS fluctuation map, and figure 5, the magnetic contour map overlaped on the pore image, shows that the RMS fluctuation tends to be lower in magnetic field regions. Figure 10 shows the mean RMS fluctuation versus

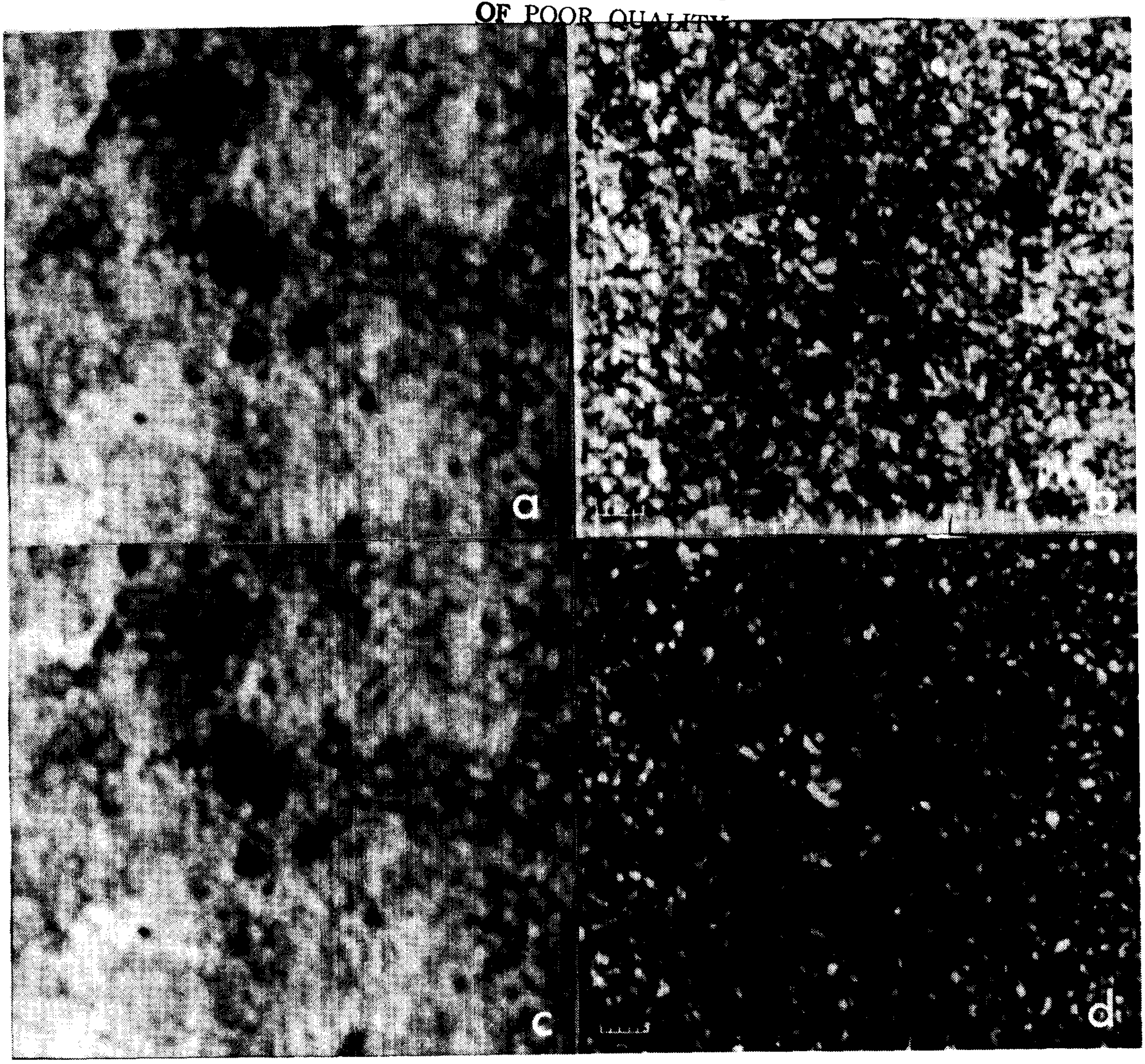

Fig. 9 A and B show the mean intensity and the RMS intensity fluctuation, respectively, for the original data in the pore region. C and D are similar images for the subsonic data for the pore region. The scale is marked in arc seconds.

magnetic field strength. Although the data is matched pixel by pixel, there is probably an offset error of several arc seconds and the resolution of the two images differ by a factor of at least four, so this good relationship suggests that the presence of a magnetic field affects a reasonable area of the granulation pattern.

Figures 9c and 9d show the mean and RMS fluctuations formed from the subsonic data set. Figures 9a and 9c are visually identical which shows that the removal of the periodic variations has almost no effect on the mean. Figures 9b and 9d, however, differ significantly.

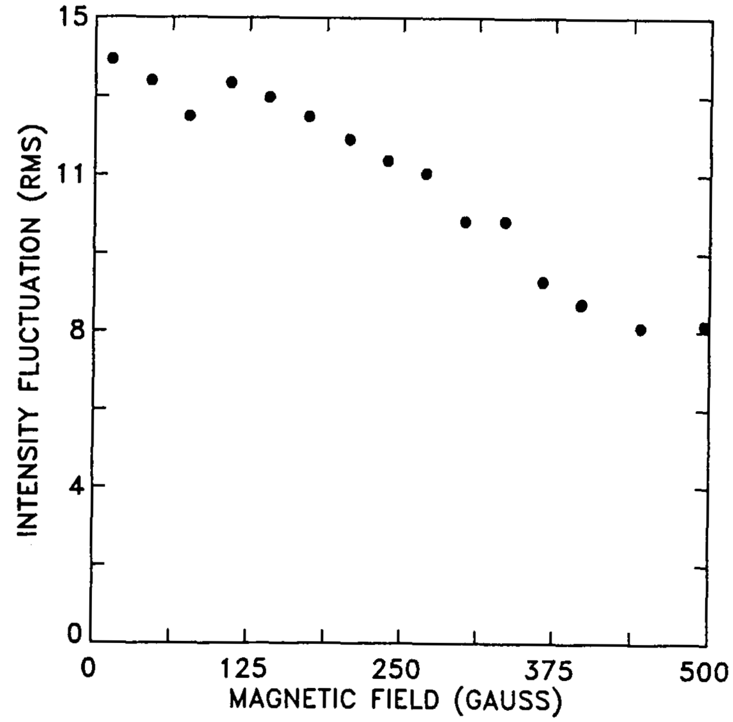

Fig. 10 Plot of the mean of the RMS intensity fluctuation at a particular value of the field versus magnetic field.

Most of the bright areas in RMS from the original data are considerably reduced in intensity in the subsonic RMS image. This refects the efficient removal of the five minute oscillation by the subsonic filter.

The higher average intensity and lower RMS fluctuation in magnetic regions are exactly what should be expected given the AC measurements described above and again strongly suggests that the magnetic field significantly changes the convective pattern.

V. Granule Tracking

Because granules move and change shape the autocorrelation method underestimates granule lifetimes. Another technique for determining lifetime is to track individual granules. The standard approach has been to find a granule on a master frame and then to track it as long as possible on following and preceding images. The weakness of such procedures is the biased selection of the tracked granules. Since our data are free of seeing we have tried to develop unbiased computer procedures for following granules.

The first step toward tracking granules is to identify them in all the images of a movie. We have tried two families of approaches. One is based on finding locally brightest points, and the other on finding borders which surround locally brighter areas. Or to put it another way, we have explored techniques to find granule centers directly by identification, and indirectly by finding their boundaries and inferring a center in the middle of an enclosed area.

All center finding algorithms are based on exploring a local neighborhood and finding the brightest point in that area. Centers are located by subjecting every point in the image to the common test. Shown in figures 11a and 11b are a typical granulation frame and the same frame marked with the centers located by a center finding process. The average number of granules identified by center finders is 500 in a 1600 SAS area of quiet sun, or 31 granules per 100 SAS. This result for the granule density is about the mean of the value found by previous observers (Wittmann, 1979).

The lane finding procedure is much more sophisticated. It isolates local bright areas by surrounding them with a boundary lane. Granule centers are located at the center of gravity of the individual holes in the lane net. Figure 11c shows the quiet sun frame (figure 11a) overlaid by the lane net and its implied centers. About 1000 centers were found by the lane finding procedure, or 63 granules per 100 SAS.

A comparison of the center and lane finding results is shown in figure 11d, where the granulation mesh is shown shaded wherever a granule center was not found in the mesh cell. The shaded region in figure 11d covers 22 percent of the area of the image, but it contains as many cells as the other 78 percent of the image. (With very few exceptions mesh cells have no more than one "center found" granule in them.)

If we adjust the number of granules from the center finding process for the fact that they occupy only 78 percent of the area, then the granule density becomes 40 per 100 SAS. The granule density obtained from the center finding process and the area-corrected center finding process bracket the published values of the granule density. Mesh fragments in shaded areas have a density of 140 per 100 square arc seconds. With the assumption that granules are in a roughly hexagonal close packed pattern, the granule center-to-center distance is 1.9, 1.7, and 0.9 arc seconds for densities of 32, 40, and 140 granules per 100 SAS.

The agreement in the granule density gives us some confidence that the granule center finding procedure is a reasonable approach to finding granules. The factor of two higher densities found by the lane finder algorithm suggests that, in addition to finding granules, it also finds smaller granule "fragments".

Given a set of images with granule centers marked, it should be straightforward to identify the center of the same granule on sequential movie frames. We make this identification if two granule centers are within M arc seconds of each other on frames separated by 30 seconds in time. Proceeding this way through a time series of frames, we obtain a set of granule centers marked in three dimensional space-time. Each granule corresponds to a connected path in space-time, which we call a "string"; a string has a well-defined duration in time and an average slope (transverse velocity) may also be computed. Figure 12 contains plots of the number of granules with string duration t as a function of t, for M's of 0.5 and 1 arc second for center and lane found granules in original and subsonic

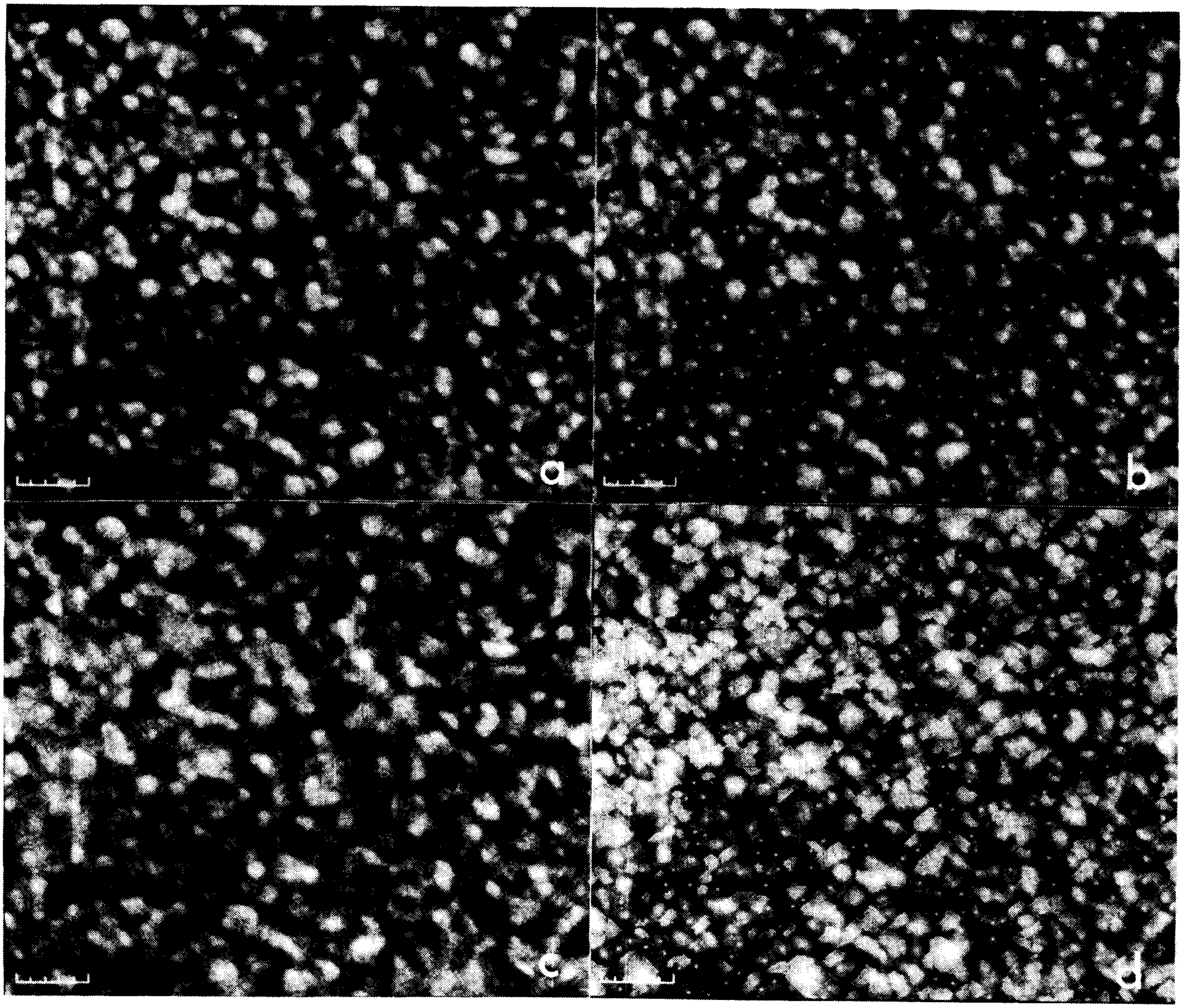

Fig. 11 Granule finding in quiet sun image (a), image with granule centers marked (b), image with lanes marked (c), and lane mesh shaded wherever a cell does not contain a center (d). The scale is marked in arc seconds.

data. All of the plots are well fitted by an exponential decay,

$$N(t) = N_0 e^{-t/T},$$

where $N(t)$ is the number of granule strings of duration t, and T is the mean string lifetime. When $N(t) = 1/e,\ t = T$.

The center found granules yield a mean string lifetime of about five minutes, and the lane found granule strings have a somewhat shorter life. Increasing the value of M does not increase the apparent lifetime.

It was disapointing that the string finding procedures did not yield granule lifetimes longer that those measured by autocorrelation techniques; however, it was not suprising after viewing the movies which show many exploding granules and granules with apparent internal structure. The string lifetime result probably suggests that a significant fraction of granules fragment and then perhaps reform during a lifetime, and the simple procedure of following a center is not a sufficiently sophisticated algorthim for defining a granule history. It also suggests that granule evolution is not a simple central upwelling and boundary downflow. In the sections below we will discuss exploding granules and elongated granules which may offer some explanation of the lack of success of string finding, and give some insight into the evolutionary processes.

Although string finding has not been successful in finding a better measure of granule lifetimes, it has been very useful for measuring granule velocities. Each string connects the center of a granule or granule fragment as a function of time. We have fitted a straight line to the granule string paths and measured the slopes of these lines in space-time, and hence the velocity of the granule centers. Shown in figure 13 is the velocity, the $\pm 1\sigma$ velocity error, and the error of the mean as a function of string length-lifetime. There is some indication that short lived granules or granule fragments move faster than 1 km/s, but the error is rather large. However, it is hard to escape the fact that, on average, granules have a random velocity of 750 to 850 m/s.

The measurement of granulation size and evolution using tracking methods has not yet been done for magnetic sun. The original digitization operation in the pore region used 0.234 arc second pixels (quiet sun pixels are .161 arc seconds), which is not sufficent to reliably find granules using the techniques described here. We plan to redigitize the pore region data and carry out the analysis in the near future.

VI. Local Correlation Tracking

When unfiltered quiet sun movies are viewed, there are local centers that appear to be bubbling or upwelling. We took this appearance as visual evidence for the existence of local flows rather than some chance pattern in the p-mode oscillations. To study these flows we compared local regions in images separated in time by 60 seconds. A local region

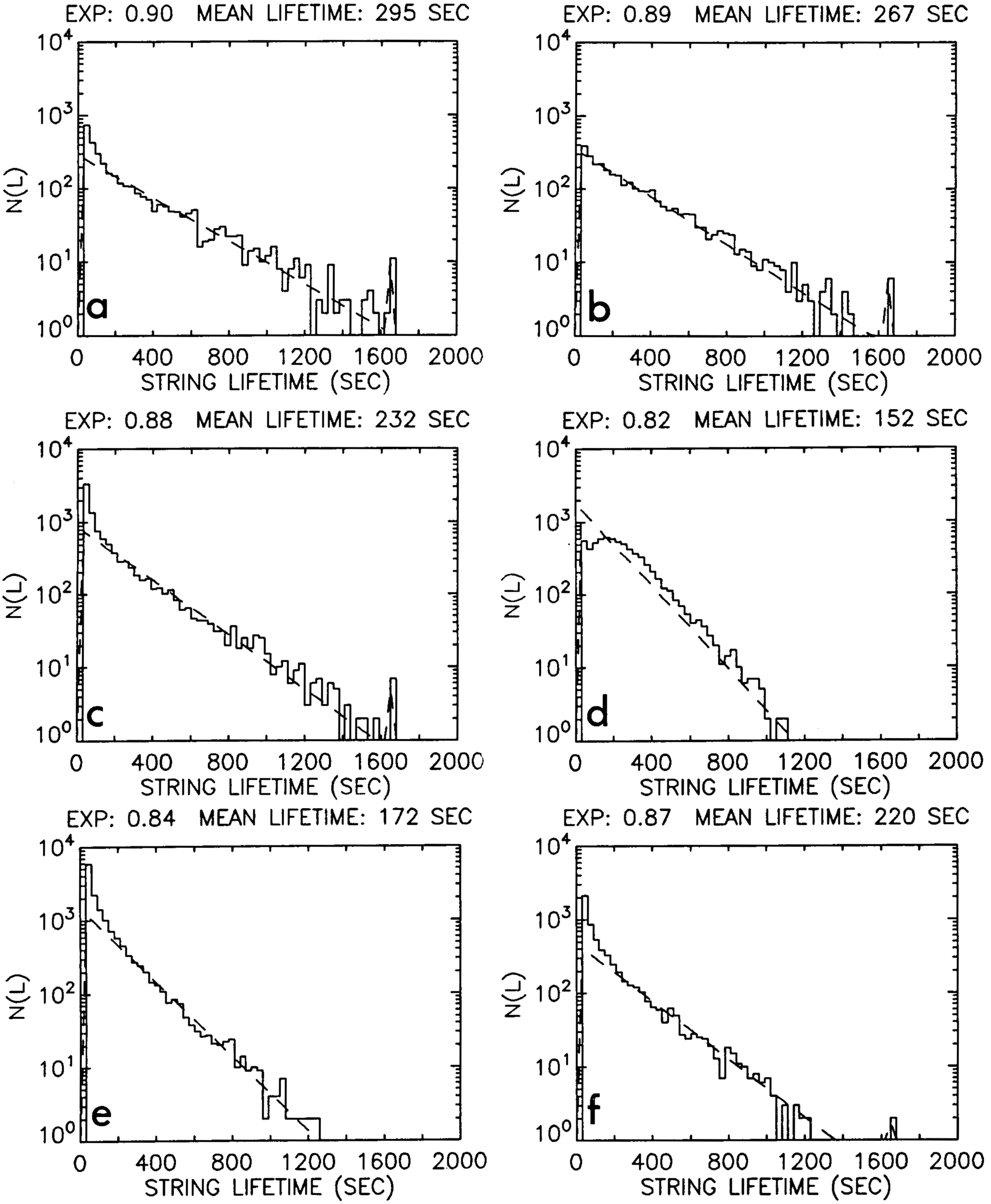

Fig. 12 Histograms of string lifetimes for subsonic data using center finding with M=0.5 arc second (a) and M=1 arc second (b); using lane finding (c) and (d); and for raw data using center finding (e) and string finding (f) with M=0.5 arc second.

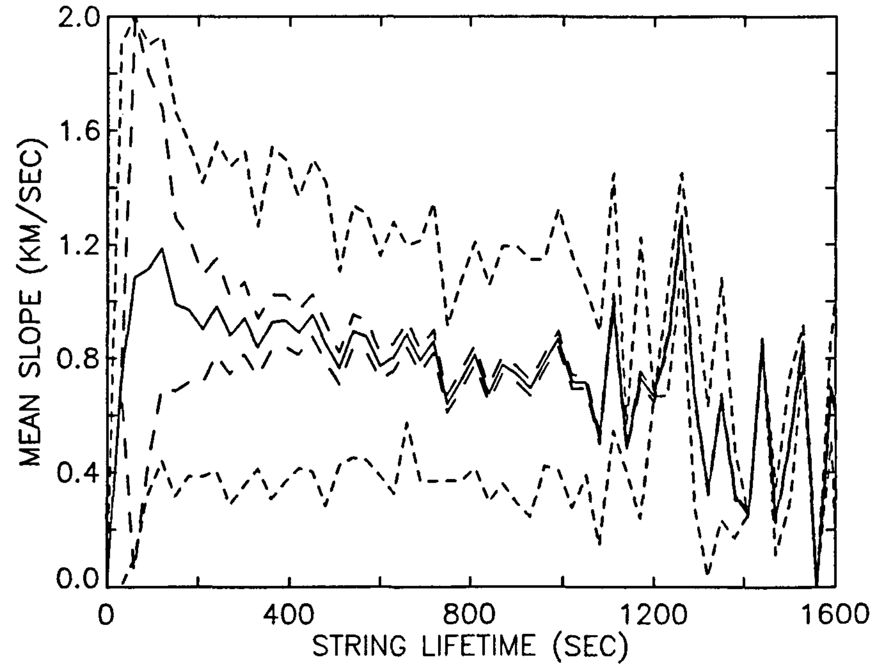

Fig. 13 Velocities from string slopes (solid), error of the mean (short dashes), and 1σ (long dashes).

was defined at a given image point by a mask centered at that point with a gaussian shape of 4 arc seconds diameter (FWHM). The mask function was set to zero outside an 8 arc second box. Before comparing locally, the full frames of each pair were aligned using a correlation algorithm. The mask was applied successively to a square grid with 2.5 arc second spacing (a 16 × 16 array) on the first image of a pair and then correlated with the second image to obtain the best fit. If the images had been identical a square grid of points with 2.5 arc second spacing on the second frame of the pair would have been found. Motions in the second image would cause the grid of best fit points to be distorted with respect to the first, and a displacement vector could be defined for each grid point.

The relative displacement field was obtained for 165 interleaved pairs of images each with 60 second spacing, and the average displacement field was computed. The largest displacements correspond to velocities of 1000 m/s and the average flow was 400 m/s. Figure 14a shows this displacement field overlayed on the average quiet sun image. The right hand side of the image appears to contain half of a supergranulation cell. In addition the image seems to be covered with smaller cells of size 10 to 15 arc seconds. The apparent cellular structure is accentuated when the mathematical divergence of the flow field is taken. (This is not the divergence of the solar flow because only the horizontal component is used.) Figure 14b shows the divergence field overlayed by the arrows.

We have used the flow maps to construct a synthetic time evolution of the surface flow. This was done by starting with a rectangular grid of tracers, "corks," at our grid intersections, and then subjecting the corks to the measured flow field. Initially the corks move in the direction of the arrows at their respective grid points, but as they displace they are moved by the flow field at their new positions. Cork frames at times of 0, 2.5, 5, and 7.5 hours

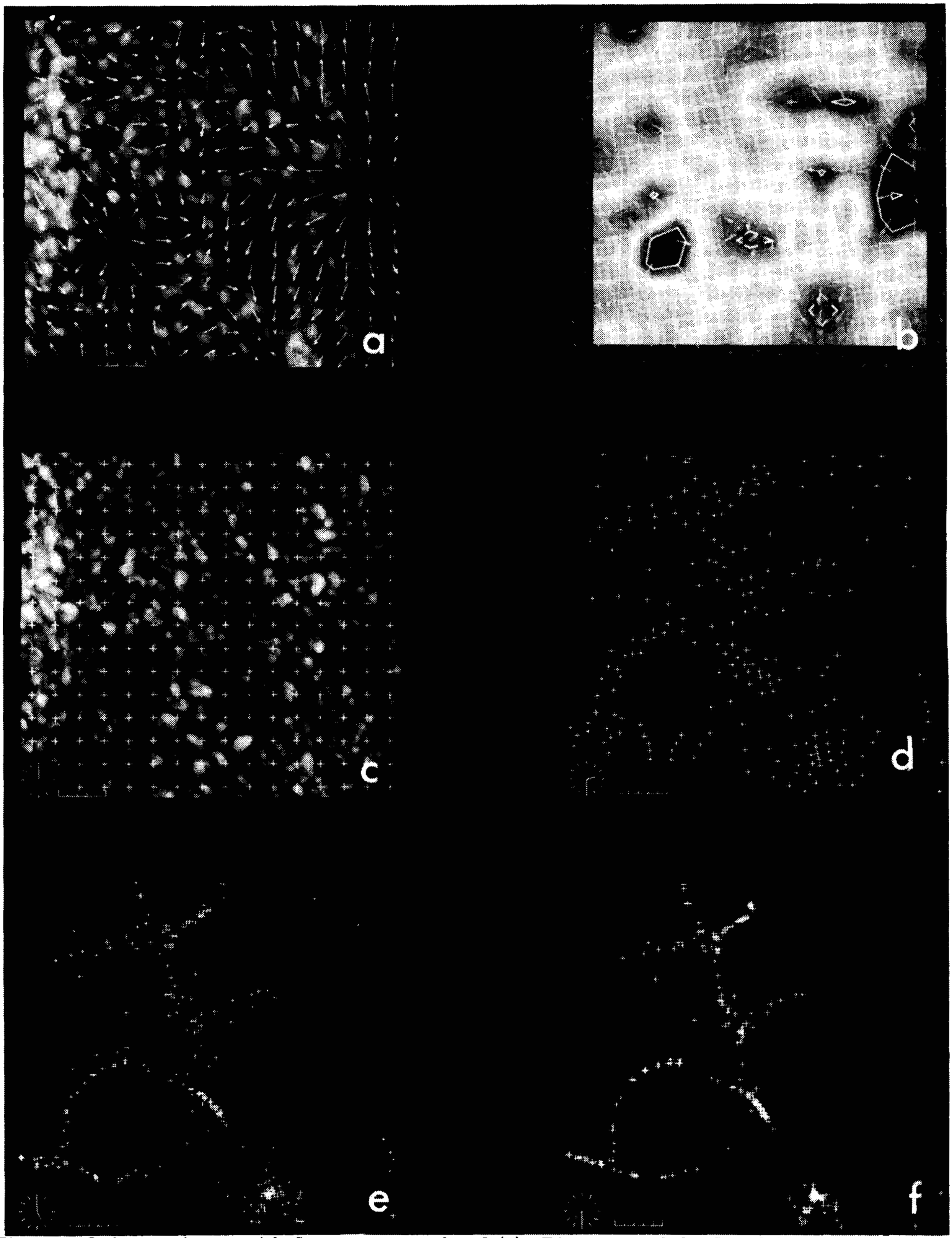

Fig. 14 Quiet sun image with flow arrows overlayed (a). Divergence of the flow field with flow arrows overlayed (b). Red areas are positive and blue areas are negative divergence. Quiet sun image overlayed by corks on a 2.5 arc second grid (c). Corks after 2.5 (d), 5 (e), and 7.5 (f) hours of being subject to the flow field.

after release are shown in figures 14c, d, e, and f. The cork movie illustrates that the measured flows would create a "network" pattern, if they persisted for 6 to 10 hours. A current priority project is to measure how the actual flow pattern changes with time over the 16 hour interval for which we have SOUP data.

In the vicinity of the pores, the average flow field is significantly less than in the quiet sun. Figures 15a and b show the distribution of velocities for the quiet and pore regions. The area average velocity is 40 percent less in the pore region than quiet sun – 222 versus 368 m/s. Figure 16 shows a scatterplot of flow speed versus line of sight magnetic field. From the figure the flow averages about 100 m/s where the field is greater in magnitude than 100 gauss. Figures 17a and b show the velocity distribution functions in regions where the field is greater and less in magnitude than 100 gauss.

VII. Exploding Granules

Granules that appear to expand radially at the end of their lifetimes have been called exploding granules. A prototypical example is shown in figure 18. They are rather rare in groundbased granulation movies, but in SOUP data it is hard to find areas of quiet sun without them. Usually the ring is not a complete symmetrical structure, but rather an ensemble of local brightenings which are all traveling outward from a center. We have studied the 40×40 arc second quiet sun region intensively, and in it 44 (relatively isolated) examples of exploders can be recognized in the 1360 second movie.

Because the average diameter of the cells at maximum expansion is about 4 arc seconds, events which occur within 1.5 arc seconds of the edge of the frame are probably missed. In addition because it is hard to recognize an event unless the initial center or the final ring can be seen, a total of about 360 seconds at the beginning and end of the movie are lost for detection. Together these two effects amount to a correction factor of $(37/40)^2 \times (1000/1360) = .63$, which suggests that the movie most probably has about 70 exploders. Also, due to the relatively high density of exploders, some events will not be recognized because of overlap and interference. Using 70 events in 1360 seconds, at least one exploder is born in a 10×10 arc second area every 310 seconds.

The mean area of maximum expansion is 14.5 SAS, so that 1000 SAS, or 63 percent of the movie region are affected by exploders. When a granule explodes it "removes" $32 \times .145 = 4.7$ average granules. Thus, if the real granule lifetime is on the order of 10 minutes, about 1000 will have died in the duration of the movie, and 325, or 32 percent, may die because they were in the vicinity of "exploders." The exploding granule counts were based on a measurements of a movie smoothed by a 5 minute running average. When the subsonic filtered movie is observed, it is hard to find a granule that does not either explode or is not in the near vicinity of an exploder. In short, explosions are a major factor in determining the lifetime of granules in quiet sun.

We are using "time-slice" images to measure and quantify the behavior of individual granules. Imagine that all of the frames of the movie were glued together to make an (x, y, t) image cube. An individual granule in this cube would be a bright tube of some length and

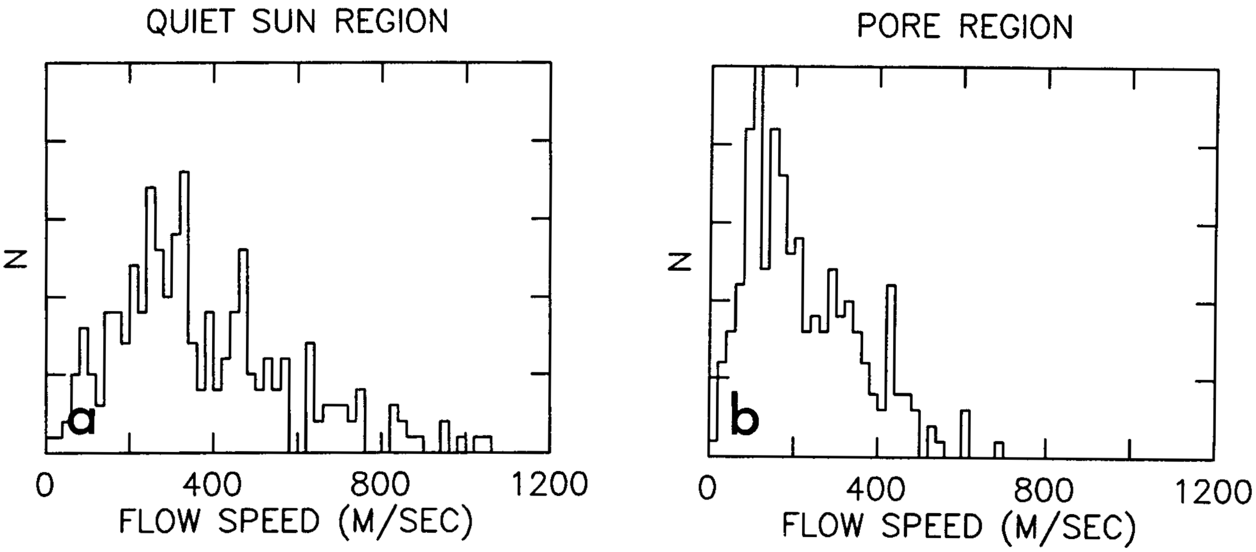

Fig. 15 Histogram of number (area) versus velocity in quiet (a) and pore (b) region.

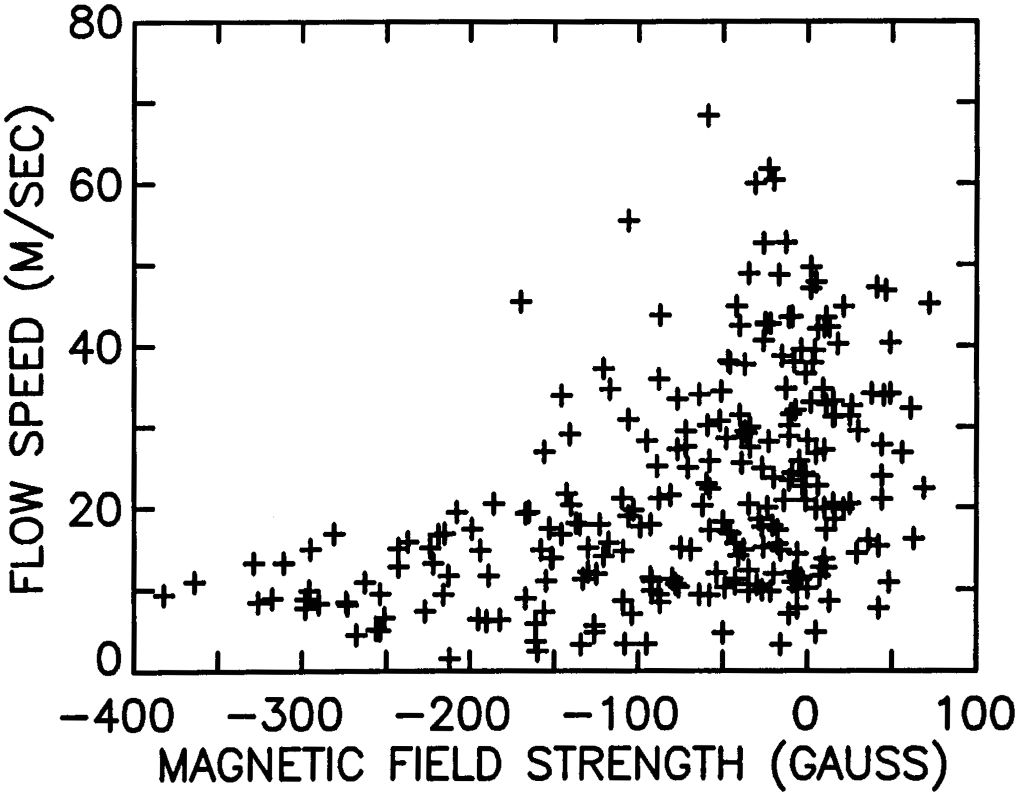

Fig. 16 Scatter plot of flow speed versus magnetic field strength.

ORIGINAL PAGE IS
OF POOR QUALITY

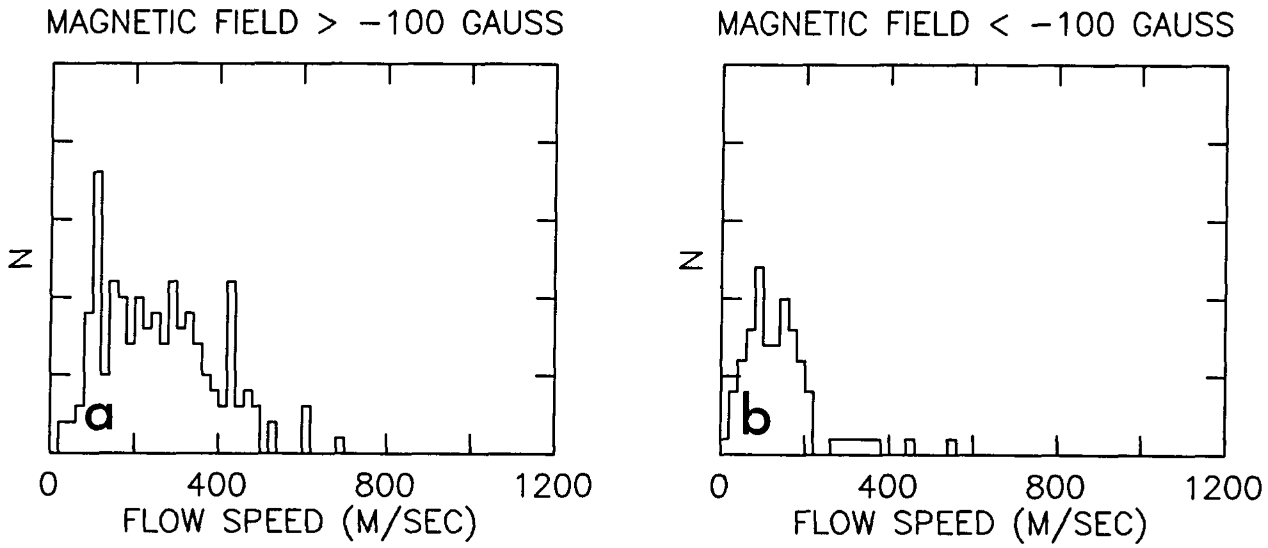

Fig. 17 Histograms of number (area) versus velocity in areas where the field strength is below (a) and above (b) |100| gauss.

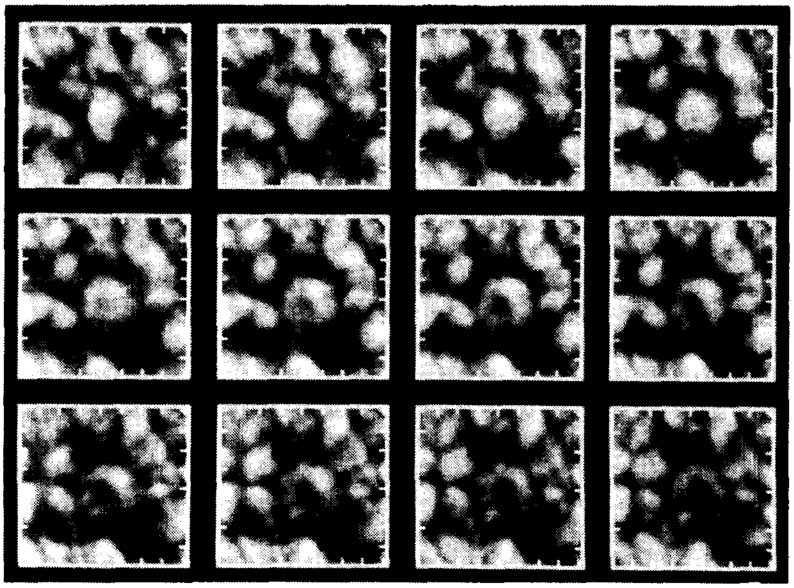

Fig. 18 Prototypical exploding granule time history. Tick marks are at arc second intervals and the time between frames is one minute.

inclination to the edges of the cube. An exploding granule would form a conical shell in the image cube. Imagine that the cube was placed on a slicing machine and was pushed into the slicer blade along the y spatial axis. As the slicer operated (x,t) slices at fresh values of y would be exposed. In the case of an exploding granule the slicer would expose a series of "V" shapes, and at the spatial center of the exploder the "V" would have its maximum opening angle. The tilt of the arms of the "V" is the radial expansion velocity of the exploder. Typical tilts correspond to velocities of about 1 km/s. Figure 19 shows slices through the center of five exploding granules.

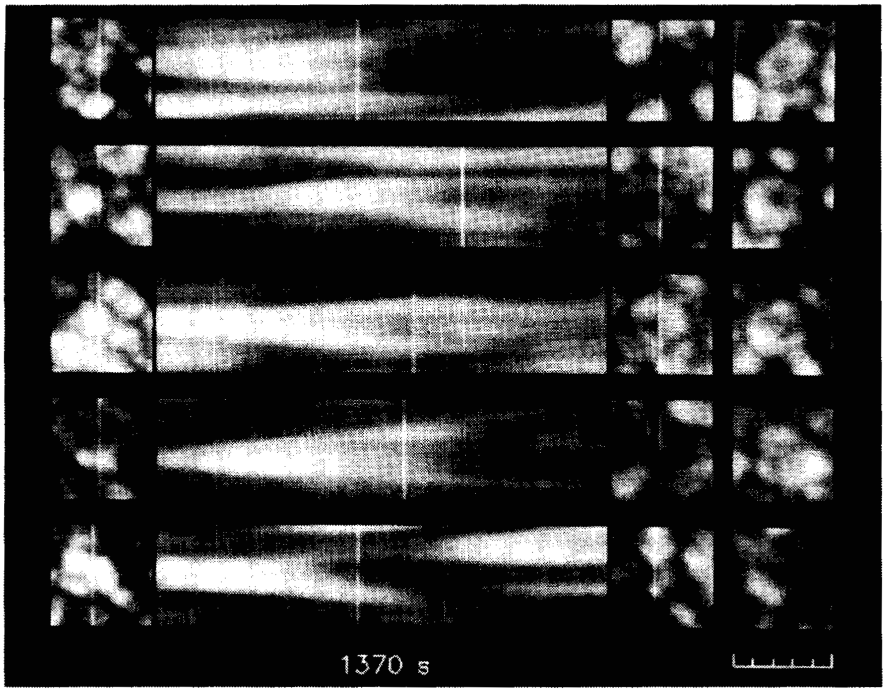

Fig. 19 Time slice images of five exploding granules.

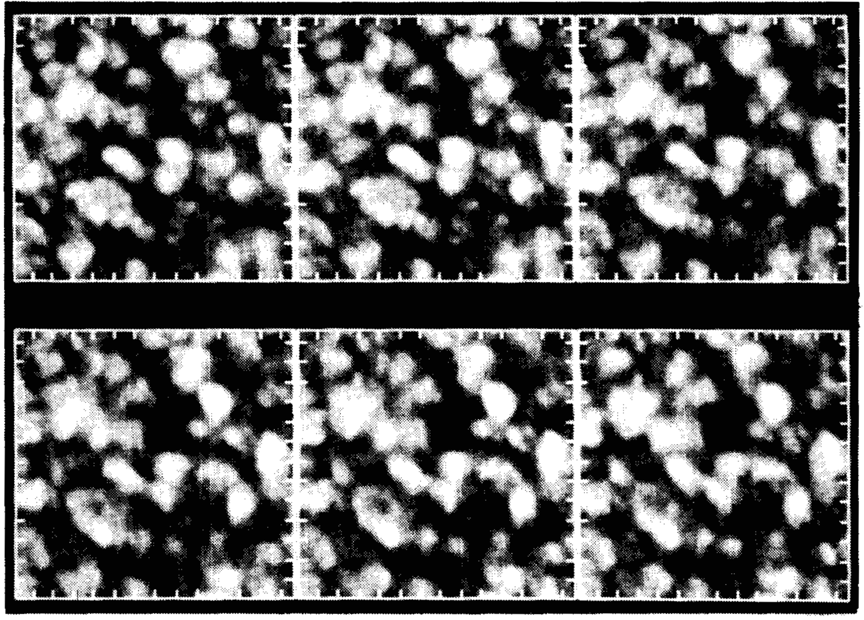

Fig. 20 Time sequence of images of region of elongated granules. Tick marks are at arc second intervals.

VIII. Elongated Granules

Figure 20 shows a sequence of frames with a number of granules that are elongated. Typical elongated granules are 0.5 × 1.5 arc seconds and appear in groups with their long axes parallel. From the illustration one gets the impression that the striations occur over an area much larger than a single granule. In at least one case we have observed a group of three elongated granules that turned into a single bright granule, and later dissolved back into a group of elongated granules. Our subjective impression is that the elongated granules are caused by a relatively stationary surface wave field in the photosphere. In rare cases striations appear to travel. These striations and their time evolution undoubtably play a significant role in complicating the definition of granules by an automated process.

Acknowledgements

Special thanks are extended to the crew of Spacelab 2 and the controllers and planners on the ground who worked so hard to get the observations . The SOUP experiment was supported by NASA under contract NAS8-23805. The image processing developments using laser optical disks has been supported by Lockheed Independent Research funds.

REFERENCES

Bray, R.J., Loughhead, R.E., and Durrant, C.J, 1984: *"The Solar Granulation,"* Cambridge University Press.

Mehltretter, J.P., 1978: *Astr. Astrophy.*, **62**, 311.

Mosher, J.M., 1977: PhD. Thesis, California Institute of Technology.

Namba, O., 1986: *Astr. Astrophy.*, **161**, 31.

Title, A.M., Tarbell, T.D., Simon, G.W., and the SOUP Team, 1986: *Advances in Space Res.*, in press.

Wittmann, A., 1979: *"Small Scale Motions on the Sun,"* Kiepenheuer-Institut für Sonnenphysik.

N88-11614

High-Resolution Continuum Observations of the Sun

Harold Zirin
Big Bear Solar Observatory

When I first came to this city in 1954 the focus of the new wave in solar physics was on the study of the chromosphere and corona. While astronomers of the Unsold school were still pursuing the problems of limb darkening and models of the photosphere, the exciting problems seemed to be in the tenuous atmosphere where so many remarkable phenomena occur. One reason, at least for me, for the lack of interest was the small scale of photospheric fine structure. The mean free path of radiation and particles is short, and the structures were below the level at which we could study them with the resources then available. Today the situation has changed. The Lockheed results from Spacelab have shown how much complex and interesting structure there is in the photosphere. Our videomagnetograph movies have revealed the fascinating details of magnetic field evolution in the photosphere. And the development of helioseismology has brought renewed interest to the subsurface region.

Another reason the photosphere was neglected is that the phenomena seemed quite straightforward. But the discovery of exploding granules at Pic du Midi showed that there were unexpected hydrodynamic phenomena present, and the Spacelab observations have shown how this structural phenomenon affects the velocity and brightness pattern of the photosphere.

It is important for the HRSO project to learn as much as we can about the solar granulation in different wavelengths. Of course a major step forward has been made in the Spacelab observations. But since Spacelab cannot fly very often and the wavelength range and other factors are limited, it behooves us to do the best we can from the ground. At Big Bear we have done this by videotape recording of the granulation image. This makes it possible to take many frames and pick out the best ones. The movie that I will show you was made by some Caltech students this summer, Haimin Wang, Matt Penn, and Mark Looper, as well as Bill Marquette of our observing staff. From each videotape the best image in a 10 second range was chosen and digitized with our image processor. The image processor was then used to register the frame with the time zero frame. In this way a movie lasting about an hour was produced; however there is a 15 minute break in the middle. I believe this technique gives us a powerful way to reconnoiter the range of HRSO; it can be applied to all solar observations where video may be used. Although it does not improve individual frames, it makes possible evolutionary studies with sustained high resolution. Further improvement will include smoothing with various algorithms and summing of frames. Unfortunately it cannot be applied to videomagnetograms, where we already are summing.

The evidence from our granulation film is most interesting. We find that the typical granular lifetime is about 15 minutes. Why is this so much longer than the canonical value of 8 minutes? Because it takes 8 minutes for the granule to form and 8 minutes for it to explode or fade. We quickly see the importance of the "explosion" phenomenon on granular structures. And we begin to see how sunspots form. We already have other, better videotapes which will be processed this winter, and we expect to explore the other aspects of this work, in particular the variation of granule appearance in other wavelengths and near the limb, as well as the behavior in strong magnetic fields.

The aim of the PFI or photometric filtergraph instrument is to observe the sun in the continuum with as high resolution as possible and utilizing the widest range of wavelengths. In the original proposal we combined the high resolution and high data accuracy of film with the high photometric capacity and wavelength range of a CCD. Those observations were to cover the range from 1100 to 7000Å. Because of financial and political problems the CCD has been eliminated so that the highest photometric accuracy is only obtainable by comparison with the CFS images; furthermore we are presently limited to wavelengths above 2200Å due to the lack of sensitivity of untreated film below 2200Å. Therefore the experiment at present consists of a film camera with 1000 feet of film (16000 exposures) and 12 filters. To picture what can be accomplished with even that limited instrument, one should consider what the Lockheed Spacelab data would look like with HRSO resolution, twelve wavelengths and many targets.

It is commonly thought that HRSO has no ultraviolet capability. That statement is wrong, unless the ultraviolet range has been redefined. The PFI reaches to 2200Å and can go further if someone will find money for it. We expect to do significant science in that region.

Why is it valuable to observe the continuum? First, continuum is easy to understand, or at least easier than lines which suffer from non-LTE effects and can be hard to interpret. Second, Lyot filters are not very effective in the blue, so a wider spectral range is available, particularly the UV. Third, the short exposures and lack of possible image degradation by the Lyot filter appear to permit higher resolution observations in the continuum. Our observations of continuum features suggest that the features low in the atmosphere that are observed are smaller than those observed higher up in the Lines. Broad-band filter observations will outline elements of the magnetic field rather well. Finally, the potential resolution of the telescope is doubled in the near UV, a fact of increased importance as we face utilization of a 1 meter aperture. This makes the mirror figure of critical importance; with a proper mirror we can resolve 0.07 arc sec at 2200Å.

The Lockheed results from Spacelab have shown how much one can learn from even a brief sequence of continuum images. Although the granulation appears relatively featureless superficially, high resolution observations show it full of the most remarkable structure; and that structure is fundamental to an understanding of the photosphere.

Unfortunately granulation studies can only occur from the ground over very brief intervals and are quite limited in what they can tell us. Our knowledge of the dependence of granular contrast on wavelength or on distance from sun center is sketchy at best. Although the removal of the CCD makes it difficult for us to carry out the best photometry, the steadiness of the HRSO images should make it possible for us to determine at least relative contrast to a reasonable degree of accuracy. Some calibration information will come from comparison with the CFS. Furthermore, steady images of the same field will allow us to carry out measurements of the oscillatory component which will enable us to extend the power versus frequency diagram of the 5 minute oscillation to still higher values. One advantage of film is that it covers a large field with high resolution. This will enable us to obtain a relatively large sample of granulation with a relatively small number of sequences.

Observation with filters in the blue clearly reveals the network magnetic elements. We have found this works best with a 10 Angstrom filter centered on the K-line, but we may also see it with a filter at 2000Å, for example. We expect that with the resolution of HRSO the contrast of such images should be even better. The appearance of the granulation in the blue is quite different from that in the visible, partly because of the many lines and partly because we are looking at a different height. We hope for the first time to quantify this difference. As I mentioned, we can easily see the small elements of magnetic flux on the surface, where the chromospheric heating is taking place. By combining the highest resolution granulation and magnetic observations with one instrument, we should be able to say more about the detailed relation of granulation changes to magnetic field changes. Only the strongest intranetwork magnetic elements are presently visible with the broadband K-line filter, so we will have to rely on the CFS magnetograms to determine the correlation between granular motion and the intranetwork fields. The evidence is that the intranetwork field generation brings about 100 times more flux to the surface of the sun than the ephemeral regions which in turn bring more than 100 times more flux to the surface than the sunspots. I would guess that the intranetwork fields are generated by granular motion, but we cannot tell without detailed observation.

The PFI experiments are outlined in Fig. 1 and Fig. 2. These experiments were developed when we had two cameras. Reduction of our experiment means we will have to cut out some of these; we are facing those decisions now. I discuss some of the problems we will address:

Surface Flows

As soon as one has mileposts one can look for surface flows. In the weak magnetic fields we can detect flows on the order of 0.1 kilometers per second. The granulation lifetimes are unfortunately limited, but there is a certain continuity in the pattern that may make it possible for us to follow granular structures for longer than that. Of course, small pores and sunspots will be even better for this purpose. We will search for flows, with the particular goals of looking for velocity field and supergranular cells, the moving magnetic elements near sunspots, and other features. A particularly striking example of this fluctuation are the very small points which one observe to oscillate in the K-line and in the blue. The relationship of these points to the magnetic field is not clear.

Magnetic Fields

Besides the questions of the interaction of magnetic fields with granulation and other flows, one of the most important problems that HRSO will address will be the size of the magnetic field elements. Stenflo and others have presented arguments that the elements of flux must be quite strong, of the order of 1000 Gauss. To match the measurements of total flux in the magnetic elements we see, this means that they must be of the order of

50 kilometers across, approximately .07 arcseconds. There is no better way to resolve this question than to look at the elements and see what is the best thing we can resolve. Now so far as we know most of the magnetic elements in the low chromosphere/upper photosphere reveal their presence by local brightening. These are observed as bright points in the continuum, particularly on the edges of the network. In a recent study, we found that the contrast of these elements increases to the limb, but the maximum contrast of a 1 arcsecond magnetic element is about 30%. It is a curious contradiction of solar physics that we can only understand the equilibrium of a small and strong magnetic field element if there is a sunspot or pore present. Then we get an equilibrium of pressure inside and outside the magnetic element. But rather than a darkening, one in fact finds a brightening in these magnetic elements so long as the flux is not great enough to produce a sunspot. Spruit has attributed this to our seeing the bright hot walls of depressed invisible sunspots, but he has also shown that the curve of visibility of these bright elements would not follow the observed curve of facular visibility. There is an additional problem in that we observe a 30% brightening in a 1 arcsecond element. If the magnetic element only filled 1/10 of that area, it would have to be 3 times as bright as the photosphere, which would make it spectacular indeed. If it in fact matched the area supposed for 1000 Gauss fields, it would have to be 30 times brighter than the photosphere. This means that at the smallest scales there is a decoupling between the brightening in the upper photosphere and the magnetic field or else Stenflo is wrong and the fields are not 1000 Gauss. Whatever the truth is, we probably will get at it by making the highest resolution observations of faculae both in disk center and near the limb in a number of wavelengths. While you may think that .07 arcseconds is beneath the resolution of HRSO, I should point out that the resolution of a diffraction limited 1 meter telescope at 2000Å is in fact .04 arcseconds, and there is no reason why the HRSO mirror could not be figured to deliver this resolution. Even if the mirror is only figured to the diffraction limit at 5000Å the resolution at the shorter wavelengths will be always better. While I know that there is some cost involved to obtaining a mirror of better figure, the HRSO mirror is well within the state of the art and it would make sense to make a strong effort to provide the very best optical figuring which would make it capable of observation in this range. The mirror would have to be figured to lambda by 50RMS at 6328Å.

Impulsive Events

At one time HRSO was a quiet sun instrument and somebody told us we would not be allowed to take pictures of flares. Then it became a solar maximum instrument and we are going to look at flares. Now it is receding into the next sunspot minimum and we don't know what we will see. There are two extremely important observations of flares that can be made with the PFI: a spectrum of white light flares and the smallest element of flare kernels.

Spectrum of White Light Flares

White light or continuum flares present two extraordinarily difficult contradictions: first, they show a strong brightening in the blue and second, we don't know how the flare energy gets down to the photosphere where we observe them in the continuum. With the PFI we should at least be able to shed light on the first. The continuum intensity of a white light flare sharply increases below 4000Å. There is some evidence from the one weak flare observed by the LPSP rocket experiment that this brightening continues into the violet. Various explanations for the blue continuum have been advanced. One reasonable explanation is that a flare consists of a number of hot elements with spectrum peaking far in the blue; one example would be a 10,000 degree black body with a peak emissivity at 2500Å. With the PFI we hope to take rapid exposures on white light flares in a wide range of wavelengths down to 2100Å. This should enable us to construct a black body curve for the emitting elements to see if they might follow this example. The problem is not so simple because the continuum brightness is occasionally 2 or 3 times the photosphere and this may be hard to explain by a simple increase in temperature. However there is no data below 3300Åat present, and we should be able to pick up some sort of peak in the emissivity if it is a Planck function effect.

You may ask how I expect to observe so many white light flares in a 7-day flight. The answer is that the number of white light flares increases quite sharply with resolution. The LPSP observation showed that almost any little old flare will show continuum brightening at 2100Å. It should be remembered that the greatest activity in the last cycle took place in 1982 and 1984 and the greatest activity in the preceding cycle in 1972 and 1974. If we are lucky, we too may see great activity on the launch of HRSO in 2004.

The Scale of Continuum Flare Kernels

We know from our original observations of the August 2, 1972 flare that kernels of the order of 1/2 to 1 arcsecond are responsible for much of the continuum emission in impulsive white light flares. We hope the PFI will either resolve these and show they are no smaller or tell us how small they really are. These kernels of emission are closely correlated with X-ray bursts. While we hope that the HESP spacecraft is still active when HRSO flies, we can also use microwave observations to get an idea of the high energy aspects of these events. Determination of the scale of the flare footpoint kernels should give us another limit on the density and total energy in the hard electron flux producing these events.

Another target for the high resolution of the PFI will be growing sunspots. We have watched EFR's form from the ground and seen the small pores emerge from dark granule lanes. But the images are still too blurry to detect what actually happens. Further, we do not know what happens to the magnetic field. Coordination of continuum observations of forming sunspots with magnetograms from the CFS should yield important new results in this regard. Observation of the contrast of the new pores in a wide range of wavelengths will determine the change in temperature of same and show us how the cooling process proceeds as the pore forms.

High-Resolution Ground-Based Observations

Right now most of the proposed experiments for both groups do not take advantage of all we know or can learn about the small-scale structure of the photosphere. It is most important that we learn as much as we can from the ground to direct our observations; we have only a little time for observing with HRSO and must use it wisely. The next film shows the evolution of the weak fields on the surface of the sun; Sara Martin will discuss later the details of magnetic interaction and reconnection among the magnetic elements. We have already found that the flux emerging in the intranetwork fields is two or three orders of magnitude above the flux in the ephemeral regions. I believe it crucial to push forward the high-resolution boundaries to better understand what we can get out of HRSO.

Some people have said to me we will be out of business in ground-based work after HRSO flies. That is nonsense. Our work will be strengthened because we will better understand what we are seeing, just as the Spacelab granulation data helps us understand and carry forward our granulation studies. Similarly, the idea that "rubber" mirrors and such will do the job of HRSO is also a fairy story because of the complexity of the atmospheric wave front distortion. Ask them for the high resolution pictures before you believe such tales.

PFI EXPERIMENTS

- ACTIVE REGIONS

A1. Development of Active Regions

A2. Emerging Flux Regions and Sunspot Creation and Growth

A3. Sunspot Structure and Dynamics

- SURFACE FLOWS

F1. Supergranular Flow

F2. Outflow in Sunspot Moats

- GRANULATION

G1. Temperature Structure and Evolution of Granule

G2. Search for Granulation Distortion by Large-scale Flows

G3. Height Variation of Granule Convective Overshoot

G4. Search for Latitude Dependence of Surface Convection

- HIGH SPEED PHENOMENA

H1. Flare Observation

H2. Eruptive Prominences

Figure 1.

PFI EXPERIMENTS

- MAGNETIC FINE STRUCTURE

M1. Interaction of Filigree and Granulation

M2. Diffusion of Magnetic Flux

M3. Photospheric Magnetic Structure at Neutral Lines

M4. Fine-Scale Magnetic Activity and Structure, Active Regions

M5. Fine-Scale Magnetic Activity and Structure, Quiet Regions

- ATMOSPHERIC STRUCTURE

S1. Limb darkening at extreme limb in all wavelengths

S2. Plage and facular brightness across the disk

Figure 2.

Mag Field Hierarchy

	Size	Life	Rate
AR's	10^{22} Mx	27 da.	10^{22} Mx/day
ER's	10^{20} Mx	1 da.	10^{23} Mx/day
Network	$10^{18\text{-}20}$ Mx	1-3 da.	10^{23} Mx/day
Intra-Network	10^{16} Mx	1 hr.	10^{26} Mx/day

In Parameters

Flux: 10^{16} Mx Vel. 0.3-0.5 Km/sec. Lifetime 1-2 hrs.

Figure 3.

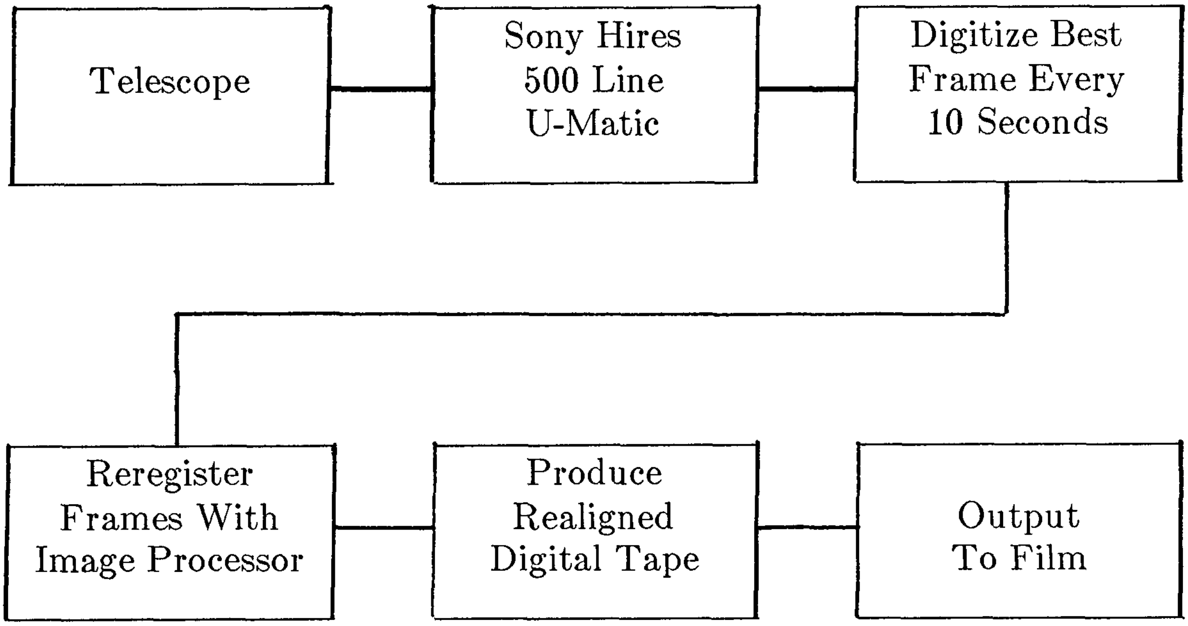

This process produces

1. Acceleration (visualize motions)

2. Continuity

Figure 4.

SMALL-SCALE ENERGY STORAGE AND RELEASE AS THE CAUSE OF THE STELLAR X-RAY CORONA

E.N. Parker
Enrico Fermi Institute
University of Chicago
Chicago, Illinois

Abstract. It has yet to be established why ordinary stars possess X-ray coronas. Detailed observations of the sun make it doubtful that the X-ray corona is produced by the dissipation of Alfven waves. The uniform X-ray brightness over all scales from 10^4 to 10^5 km simply does not look like a resonance phenomenon.

It is demonstrated that the arbitrary winding patterns introduced into the bipolar magnetic fields of the X-ray corona produce discontinuities within the field. It is suggested that the random motions of the footpoints of the field cause the accumulation of internal strains in the field, which dissipate through neutral point reconnection across the associated discontinuities to provide the primary heat source for the X-ray corona. It is emphasized, however, that the essential high resolution observations of the sun have yet to be carried out, and until the theory is firmly established for the sun, we cannot know how to interpret the X-ray emission of the sun or of other stars.

1. INTRODUCTION

The emission of X-rays is a universal property of stars, and a variety of ideas have been invented to explain the phenomenon. The more intense X-ray sources require matter falling on to massive compact objects to provide the basic source of energy. However, the ordinary star is more subtle. The energy source can only be the convective zone, operating as a turbulent heat engine (Alfven, 1947; Schwarzschild, 1948; Biermann, 1948) but the means by which the energy is transported to the outer atmosphere has proved elusive. It is obvious that the question can be resolved only be detailed and quantitative study. It is not sufficient to <u>detect</u> the phenomenon of stellar X-ray emission. It is necessary to <u>see</u> the phenomenon in action, to study its detailed working. The essential effects occur on scales as small as 10^2 km or less. So the sun is the essential laboratory for studying stellar X-ray emission.

It is clear from the observations of the solar corona that there are two distinct states of the stellar corona, depending upon the connectivity of the magnetic field. The open magnetic regions, in which the lines of force extend to infinity, occur where the field is relatively weak (~ 10 gauss) and the gas density is low ($\sim 10^8$ atoms/cm^3) so that there is little emitted radiation in spite of the temperatures of 1.5-2x10 °K. These "coronal holes" continually expand outward into space, producing the fast streams--and perhaps the entirety--of the solar wind, requiring an energy input of nearly 10^6 ergs/cm^2 sec (Withbroe and Noyes, 1977). The only known mechanism for supplying this energy is the emission of Alfven waves by the photospheric motions and the dissipation of the waves through phase mixing, etc. (cf. Hayvaerts and Priest, 1983; Abdelatif, 1987) over characteristic lengths of the order of 10 $R_\odot$ or more. This idea needs to be tested quantitatively of course, beginning with the measurement of the wave spectrum emitted at the photosphere.

In contrast to the open magnetic regions, the closed magnetic regions, in which the re-entrant bipolar magnetic field may be 10^2 gauss, are copious emitters of X-rays. The gas is trapped in the magnetic field and cannot escape, with the result that the temperature rises to 2-3x10^6 °K, and the density (from the photosphere) builds up to 10^{10} atoms/cm so that the principal energy loss is electromagnetic emission at X-ray frequencies. The energy consumption is approximately 10^7 ergs/cm^2 sec (Withbroe and Noyes 1977). Rosner, Tucker, and Vaiana (1978) have emphasized, from their analysis of the detailed observations of the structure of the closed magnetic regions - the X-ray corona - of the sun, that there is a direct connection between the strength of the magnetic field and the energy output. That is to say, as with all other aspects of stellar activity, the X-ray emission is a magnetic phenomena. The magnetic energy density in the corona is 20 or 30 times the thermal energy density.

Fortunately the observations of the sun go on to define the problem rather closely. Studies of the widths of coronal lines (Beckers and Schneeberger, 1977; Bruner, 1978; Cheng, Doschek, and Feldman, 1979) place an upper limit of about 20 km/sec on the rms fluid velocities in the line of sight in the X-ray corona, severely limiting the energy that can be transported by Alfven waves. The observations also disclose the remarkable fact (cf. Rosner, Tucker and Vaiana, 1978) that the intensity of the X-ray emission is essentially independent of the scale of the bipolar magnetic region in which it occurs, from the small X-ray bright points (10^4 km) to the normal active regions (10^5 km). These two constraints restrict the theoretical possibilities for producing (i.e. heating) the X-ray corona.

The obvious mechanism is the coronal dissipation of Alfven waves generated in the photosphere, much as in the coronal hole. The difficulty with this idea is that we expect waves with periods of the order of 10^2 sec, which have wavelengths of 2x10^5 km in the corona. Yet these waves must dissipate equally and substantially over scales of 10^4 km in the X-ray bright points and over scales of 10^5 km in the normal active regions. Some authors appeal to resonance effects (cf. Davila, 1985) and to turbulent energy cascade (Hollweg, 1984), which all requires a broad input wave spectrum, from periods of 10^2 sec down to 10 sec, in order to function equally over all scales from 10^4 to 10^5 km.

Our own view is that the scale independence of the X-ray coronal features does not look like a resonance phenomenon. Wave heating as the principal cause of the corona requires too many special circumstances. It is time to look for alternatives.

2. SMALL-SCALE STORAGE OF MAGNETIC ENERGY

Energy is continually introduced into the bipolar magnetic fields above the surface of the sun by the random wandering of the footpoints of the field (Parker, 1983b). The individual magnetic fibrils at the photosphere are kicked about by the granules at velocities of some fraction of a km/sec. The motions cannot be well ordered, with the result that any given fibril spends its time wandering among the neighboring fibrils, say with a velocity u. The flux bundle in the corona trails out behind its wandering photospheric footpoint and meanders among the neighboring flux bundles along the random path of the footpoint. The length of the path traversed by the footpoint at the photosphere after a time t is ut.

Then consider the idealized situation illustrated in Fig. 1, wherein there is a vertical uniform field e_zB_o, except for one wandering flux bundle whose upper end is anchored at a horizontal plane z=L above the surface z=0 on which the footpoint wanders at random. The region is filled with a tenuous infinitely conducting fluid. The vertical component B_o of the field in the wandering flux

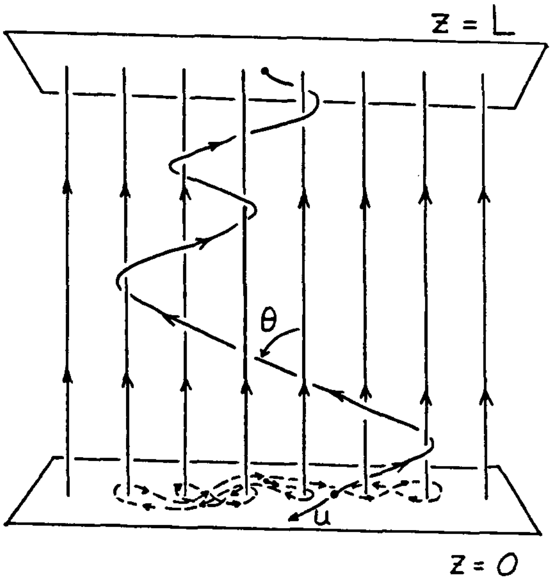

FIG. 1 A sketch of a flux bundle whose footpoint has been displaced a distance ut along a random path among the other flux bundles. The dashed line on the plane z=0 indicates the track of the footpoint.

bundle is essentially unaffected by the inclination θ of the bundle to the vertical, where

$$\tan\theta = ut/L \tag{1}$$

The horizontal component of the field is

$$\begin{aligned} B_\perp &= B_0 \tan\theta \\ &= B_0\, ut/L \end{aligned} \tag{2}$$

The tension in the inclined bundle, trailing out behind the footpoint, opposes the random walk velocity u of the footpoint with the Maxwell stress $B_\perp B_z/4\pi$, so that the motion of the footpoint does work on the field at a rate

$$\begin{aligned} W &= uB_\perp B_0/4\pi \\ &= \frac{B_0^2 u^2 t}{4\pi L} \quad \text{ergs/cm}^2\ \text{sec} \end{aligned} \tag{3}$$

This energy accumulates in the field, of course. Every footpoint (i.e. every individual fibril) is undergoing a statistically similar random walk, with the result that W is an estimate of the average rate of energy input over the magnetic field.

Note that, beginning with a uniform vertical field at time t=0, the rate of energy input increases linearly with the passage of time, as the magnetic stresses opposing the motion of the footpoint become larger. The accumulated energy in the field is

C - 2

$$U(t) = \int_0^t dt\, W(t)$$

$$= \frac{B^2 u^2 t^2}{8\pi L} \text{ ergs/cm} \qquad (4)$$

and increases quadratically with time. For a normal active region with $B_0 = 10^2$ gauss and $L = 10^5$ cm, a random motion $u = 0.5$ km/sec yields

$$ut/L = 0.5\text{x}10^{-5}t, \qquad (5)$$
$$W = 2\text{x}10^2 t \text{ ergs/cm sec} \qquad (6)$$
$$U = 1\text{x}10^2 t^2 \text{ ergs/cm} \qquad (7)$$

We presume that the accumulation of energy in the small-scale strains goes on until either the magnetic stress opposing the footpoint motions becomes so strong as to halt the motions, or, as seems more likely, some form of dissipation appears that destroys the accumulating small scale strains in the field as rapidly as the strains can be produced by the motion of the footpoints.

This, then, is the state of the bipolar magnetic fields in the sun. There is a substantial energy stored in small-scale strains, on scales less than 10^3 km, as a consequence of the convective motions at the photosphere.

3. SPONTANEOUS APPEARANCE OF DISCONTINUITIES

Consider how the small-scale distortions introduced in a large scale bipolar magnetic field B by the small scale ($\ell \cong 10^3$ km) motions u of the footpoints can be dissipated in a plasma at 2-3x10^6 °K. The resistive diffusion coefficient η is only 10^3 cm /sec ($\sigma \cong 10^{17}$/sec). The characteristic dissipation time over a scale of 10^3 km is 10^5 years. There can be significant dissipation only if the characteristic gradients (curl) within the field are enormously increased above the characteristic value B/ℓ.

We are familiar with the potential fields of electrostatics and magnetostatics in nonconducting media, in which the field is described by the single scalar equation

$$\nabla^2 \phi = 0$$

There is a unique solution for any given distribution of ϕ (or $\partial\phi/\partial n$) over the boundaries, and that solution is as well behaved as the boundary conditions. The inhomogeneities introduced at the boundary decline exponentially inward from the boundary, so that gradients B/ℓ introduced at the boundaries diminish into the field.

On the other hand, a magnetic field in a highly conducting fluid of negligible pressure p satisfies the familiar force-free equation $(\nabla \times \mathbf{B}) \times \mathbf{B} = 0$, so that

$$\nabla \times \mathbf{B} = \alpha(r)\mathbf{B}, \qquad (8)$$

and, with $\nabla \cdot \mathbf{B} = 0$, it follows that

$$\mathbf{B} \cdot \nabla\alpha = 0 \,. \qquad (9)$$

These nonlinear equations have quite different properties from the linear Laplace equation. In particular they are vector equations, so that the connectivity or topology of the frozen-in field plays an essential role. The result is tangential discontinuities in a field with any but the most special topologies. The tangential discontinuity is a surface across which $|\mathbf{B}|$ is continuous but the direction of $\mathbf{B}$ is discontinuous. The curl of the field is essentially a Dirac-delta function at the discontinuity, providing a current sheet.

The formation of current sheets in complicated field topologies has been developed from several directions. Syrovatsky (1966, 1978, 1981; Bobrova and Syrovatski, 1979; Low and Hu, 1983) pointed out that a current sheet is formed when an X-type neutral point is squashed in one direction or another. The circumstances under which the strains introduced into the field may accomplish this feat emerge from the treatment of the simple problem of a magnetic field $e_z B_O$, initially uniform, extending between the boundary planes z=0 and z=L. The footpoints at z=0 are then moved about and mixed among each other by some bounded continuous mapping with characteristic scale $\imath$ ($\ll$L) so that the lines of force are wound and interwoven among each other in their extension from z=0 to z=L. The elementary perturbation expansion about the initial field (Parker, 1972, 1979; see also Tsinganos, 1982) produces only those solutions that are invariant along the initial field ($\partial/\partial z = 0$). Van Ballegooijen (1985) has shown recently that there is a more general perturbation solution in which a variation with z is permitted of the special form

$$\frac{\partial\alpha}{\partial z} = \frac{\partial\alpha}{\partial y}\frac{\partial A}{\partial x} - \frac{\partial\alpha}{\partial x}\frac{\partial A}{\partial y} \qquad (10)$$

where α is the torsion coefficient appearing in eqns. (8) and (9), and the transverse components of the field, produced by the winding of the lines of force, are expressed in terms of the vector potential A by

$$B_x = +B_0\,\partial A/\partial y,\; B_y = -B_0\partial A/\partial x$$

so that

$$\alpha = -\,(\partial^2 A/\partial x^2 + \partial^2 A/\partial y^2)$$

Van Ballegooijen points out that equation (10) is exactly analogous to the two dimensional vorticity equation for the motion of an ideal inviscid fluid described by the stream function ψ, so that

$$v_x = +\partial\psi/\partial y,\; v_y = -\partial\psi/\partial x$$

The vorticity is then

$$\omega = -\,(\partial^2\psi/\partial x^2 + \partial^2\psi/\partial y^2)$$

and the vorticity equation is

$$\frac{\partial\omega}{\partial t} = \frac{\partial\omega}{\partial y}\frac{\partial\psi}{\partial x} - \frac{\partial\omega}{\partial x}\frac{\partial\psi}{\partial y} \qquad (11)$$

It follows that the magnetic field varies with z in the same way that the vorticity varies with the passage of time. There is considerable knowledge of the properties of two dimensional vortex flows of inviscid fluids (cf. Batchelor, 1967). In particular, it follows that there is a well behaved continuous solution to (10) for any bounded continuous smooth vector potential A specified on z=0. From this fact Van Ballegooijen asserted that the bounded continuous mapping of the footpoints of the field cannot produce discontinuities in the field. This overlooks the fact that the winding and interweaving of the vortex lines is restricted to the special form described by the vorticity equation (11) which, for instance, does not allow braiding of three vortex filaments), whereas we are free to introduce <u>any</u> arbitrary winding pattern through continuous motion of the footpoints of the field. It can be shown by formal development of the force-free equations (8) and (9) (Parker, 1986a,b) that discontinuities occur in α and $\mathbf{B}$ unless the mapping of the footpoints is especially restricted to the vorticity equation. The recent papers by Moffat (1985,1986) discuss the ubiquitous discontinuities (vortex sheets) as a general property of the Euler equations for the ideal inviscid fluid. Tsinganos, Distler, and Rosner (1984) develop the analogy between the lines of force and the trajectory of a Hamiltonian system in phase space.

In the present exposition we illustrate the spontaneous formation of a tangential discontinuity with a simple example (Parker, 1987). Consider a twisted flux bundle extending uniformly ($\partial/\partial z=0$) from $z=0$ to $+L$ (sketched in Fig. 2) and fitting <u>smoothly</u> into the ambient uniform field $e_z B_0$ that surrounds it. That is to say, the helicity of the magnetic field declines to zero at the surface of the bundle. Indeed, we may define the surface of the bundle by the vanishing of the helicity. The twisted flux bundle is in force-free equilibrium, so that the helical field within the twisted flux bundle can be expressed in terms of a generating function $f(\varpi)$, where $\varpi = (x^2+y^2)^{\frac{1}{2}}$ represents distance from the axis of the bundle. Then (Lüst and Schlüter, 1954a,b)

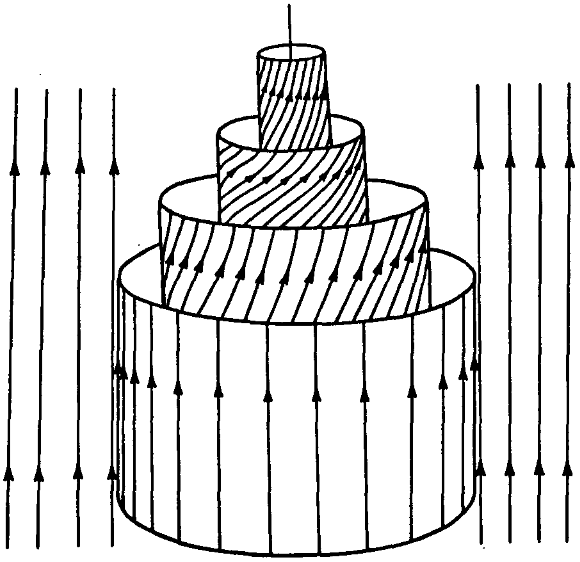

FIG. 2 A sketch of a twisted flux bundle extending uniformly from z=0 to z=L whose field fits smoothly and continuously onto the surrounding uniform field B_α.

$$B_z = f(\varpi) + \tfrac{1}{2}\varpi f'(\varpi), \quad B_\varphi = -\tfrac{1}{2}\varpi f'(\varpi)$$

with B falling to zero at the surface of the bundle, where $f=B_0^2$. The equilibrium field can also be described by

$$B_x = +\partial A/\partial y,\ B_y = -\,\partial A/\partial x,\ B_z = B_z(A)$$

with

$$\alpha = B_z'(A)$$

and

$$\frac{\partial^2 A}{\partial x^2} + \frac{\partial^2 A}{\partial y^2} + B_z(A)B_z'(A)=0$$

Formal examples of twisted flux tubes formed by bounded continuous rotation of the footpoints may be found in the literature (cf. Parker, 1987)

We consider here the case where the twisted bundle is pressed between two planes $y = \pm h$ (or two other similar twisted flux bundles) so that it is squashed into a flattened cross section, with thickness 2h and width 2w, in the manner sketched in Fig. 3. The twisted bundle resists the squashing, of course, so that some finite incremental pressure $\Delta P = \beta B_0^2/8\pi$ (where β is a number of the order of unity) must be applied by the confining planes $y = \pm h$ to squash a strongly twisted bundle. Thus, whereas the ambient pressure is $P = B_0/8\pi$, the local magnetic pressure along the midline $x=0$, $y = \pm h$ of the flattened surface of the flux tube is larger, $P + \Delta P = P(1+\beta)$. In moving in the x-direction away from the midline of the flattened side, the magnetic pressure declines by ΔP. Equilibrium requires that some force balance the outward thrust of this locally enhanced pressure.

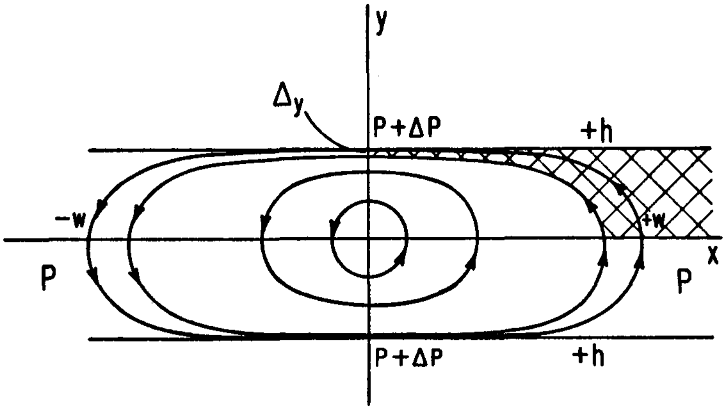

FIG. 3 A sketch of the cross section of the flux bundle in Fig. 2 after being squashed between the two planes $y = \pm h$, so that the width becomes 2w. The cross hatched region represents the thin layer of flux at the surface of the bundle, extending from the midline $x=0$ to $x= +\infty$.

Only the tension in the lines of force is available, in the amount $B_\perp^2/4\pi$ where $B_\perp$ is the transverse component of the field at the surface of the flux tube. Then the total pressure at the surface is $(B_z^2 + B_\perp^2)/8$ where B_z is the longitudinal component, from which it follows that

$$B_z^2 + B_\perp^2 = B_0^2(1+\beta) \tag{12}$$

Consider then a thin layer of flux on the surface of the twisted flux tube. The layer is indicated by the cross hatched area in Fig. 3. The thickness of the layer at the midline of the flattened side (at $x=0$, $y = +h$) is Δy, so that the tension exerted on the layer there is $\Delta y B^2/4\pi$. The enhanced pressure is ΔP, of course, so that the net force in the positive x-direction exerted on the thin layer at $x=0$ is

$$\Delta y(B^2/4\pi - \Delta P).$$

There is no net force in the x-direction exerted on the upper surface $y=h$, nor on $y=0$ throughout $x>w$, nor at $x = +\infty$ where the enhance pressure falls to zero. The only place that ΔP makes itself felt is along the lower surface of the layer. Hence the total force in the x-direction exerted on the layer is

$$F_x = \Delta y[\Delta P(0,h) - B^2\,(0,h)/4\pi] + \int_0^{h-\Delta y} dy\,\Delta P(x,y)$$

where the integral is along the lower surface of the layer from where it crosses the x-axis at $x=w$ to where it crosses the y-axis at $y = h-\Delta y$. Since $F_x=0$ for equilibrium, it follows that

$$\frac{B^2(0,h)}{4\pi} = \Delta P(0,h) + \frac{1}{\Delta y}\int^{h-\Delta y} dy\,\Delta P(x,y) \qquad (13)$$

To estimate a lower limit on B (0,h) note that $\Delta P(x,y)>0$, so that both terms on the right hand side are positive. Hence, dropping the integral on the right hand side it follows that

$$\begin{aligned} B^2(0,h) &> 4\pi\Delta P(0,h) \\ &= \tfrac{1}{2}\beta B_0^2 \end{aligned} \qquad (14)$$

Substituting this result into (12) yields

$$B_z^2 < B_0^2\,(1+\tfrac{1}{2}\beta) \qquad (15)$$

from which it follows that

$$B_\perp/B_z > [\beta/(2+\beta)]^{\frac{1}{2}} \qquad (16)$$

The point of this inequality is that $B_\perp/B_z$ is of the order of unity, i.e. of the order of $(\beta/2)^{\frac{1}{2}}$. The field at the surface of the twisted flux bundle is inclined to the z-direction by an angle ϑ where

$$\begin{aligned} \tan\vartheta &= B\ /B_z \\ &> [\beta/(2+\beta)]^{\frac{1}{2}} \end{aligned} \qquad (17)$$

Note that the field at the surface of the flux bundle was parallel to the axis of the bundle ($B_\psi \to 0$) prior to squashing the bundle. The subsequent inclination ϑ of the surface field to the ambient field direction depends only upon the enhanced pressure $\Delta P = \beta B_0^2/8\pi$ applied to squash the tube. It is independent of the initial state of twisting of the tube. Only the sign of the inclination is obedient to the original twisting. And that is how the spontaneous tangential discontinuity is created.

Wherever a localized enhanced pressure is applied to a twisted flux bundle, the field at the surface of the bundle is strongly rotated relative to the local direction of the flux bundle . Unless the flux bundle exerting the enhanced pressure is the mirror image of the bundle being squashed, and the two bundles are precisely parallel wher they are in contact, the fields on either side of their common surface take up different directions. If, then, we shuffle and intermix the footpoints of the magnetic field in some arbitrary bounded continuous manner, the flux bundles that make up the resulting field are twisted, wound, and interwoven in arbitrary patterns that produce spontaneous misalignment of the fields across the boundaries of the local topological patterns in the winding and wrapping. The continuous fields become discontinuous because the topology becomes discontinuous where one twisted flux bundle is pressed against, or pulled around, another. The discontinuity in the topology (created when twisted tubes are pressed together) creates the discontinuity in the field direction through the rotation described by the above example[1].

This identifies, then, where the X-type neutral points may be flattened by the global magnetic stresses to form current sheets. The phenomenon arises spontaneously and unavoidably throughout any magnetic field subject to internal winding and interweaving that does not adhere exactly to the strictures of the "vorticity" equation. The interested reader is refered to the more formal treatment of the spontaneous formation of tangential discontinuities in the field (Parker, 1981a,b, 1982, 1983a,c,d, 1986a,b, 1987).

4. FORMATION OF THE STELLAR X-RAY CORONA

We suggest that the small-scale strains introduced in the bipolar magnetic fields above the surface of the sun (§II) are relieved by the dissipation that arises at the tangential discontiuities that are an essential part of the force-free equilibrium (§III). It remains for observations to establish the velocity u with which the footpoints of the field are shuffled among each other. In view of the observed horizontal motions of 1-3 km/sec at the visible surface of the sun we would imagine that u is a substantial fraction of 1 km/sec, perhaps $u=0.5$ km/sec.

Consider, then, the requirements for heating the X-ray corona by the dissipation at the discontinuities, presumably by neutral point reconnection in one form or another. We imagine a mean strain level in which the motion of the footpoints does work on the field at the necessary rate $W = 10^7$ ergs/cm^2 sec, and the dissipation relieves the strains as rapidly as they are introduced. Starting from an initial uniform field, it follows from eqn. (6) that W reaches 10^7 ergs/cm sec after a time $t=0.5\times10^5$ sec for the characteristic dimensions ($L=10^5$ km) of a normal active region. At this point eqn. (5) gives $ut/L = 1/4$. The local strains in the field involve inclinations to the mean field direction by a characteristic value of 14°. This same state is reached in an X-ray bright point ($L=10^4$ km) after a time $t=0.5\times10^4$ sec.

We suggest that the X-ray corona of the sun is produced primarily by this effect (Parker, 1983b). It is not possible to compute the reconnection rates associated with the power input $W = 10^7$ ergs/cm sec. We note that the rate lies between the theoretical lower and upper limits for reconnection (Parker, 1983b). It must be appreciated that the slower the reconnection rate, the more intense are the small-scale strains in the field when dissipation finally rises to the input level, and the more work is done on the field by the motions of the footpoints.

---

[1] It is well known that a twisted flux bundle is subject to a kink instability which serves only to produce additional tangential discontinuities at the surface (Rosenbluth, Dagazian, and Rutherford, 1973).

The result is a higher level of energy input to the corona. Evidently a balance is struck when the coronal gas density rises to 10^{10} atoms/cm. and the Alfven speed (which characterizes the reconnection rate) falls to 2000 km/sec. In any case the dissipation is probably sporadic and bursty on the small-scale of the individual discontinuities (current sheets) with widths of 10^7-10^8 cm. The observed quasi-steady X-ray corona is expected to be highly active in the small.

It is obvious from this brief description of the dissipation at magnetic discontinuities that the theory of coronal heating calls upon the smallest known magnetic structures in the sun. Therefore, the theory cannot be regarded as established until observations at high spatial and spectral resolution can establish the random motions of the magnetic fibrils at the photosphere and provide direct evidence for the small-scale dissipation in the X-ray corona. Until the observations have accomplished these tasks to some satisfactory degree, the accumulating observations of stellar X-ray emission can be treated only at the phenomenological level. I hope that it will not be too many years before the theory can be established, or refuted, by observations of the sun, so that we can get on with the scientific interpretation of the fascinating stellar X-ray observations.

This work was supported in part by the National Aeronautics and Space Administration under NASA grant NGL 14-001-001.

REFERENCES

Abdelatif, T.E. 1987, *Ap. J.* (submitted).
Alfven, H. 1947, *Mon. Not. Roy. Astron. Soc.* *107*, 211.
Batchelor, G.K. 1967, *An Introduction to Fluid Dynamics* Cambridge, Cambridge University Press.
Beckers, J.M. and Schneeberger, T.J. 1977, *Ap. J.* *215*, 356.
Biermann, L. 1948 *Z. Ap.* *25*, 161.
Bobrova, N.A. and Syrovatski, S.I. 1979, *Solar Phys.* *61*, 379.
Bruner, E.C. 1978, *Ap. J.* *226*, 1140.
Cheng, C.C., Doschek, G.A. and Feldman, U. 1979, *Ap. J.* *227*, 1037.
Davila, J.M. 1986, Proc. NASA Workshop on Coronal Prominences and Plasmas, ed. A. Poland. Berkeley Springs, W. VA, 7-10 April.
Hayvaerts, J. and Priest, E.R. 1983, *Astron. Ap.* *117*, 220.
Hollweg, J.V. 1984, *Ap. J.* *277*, 392.
Low, B.C. and Hu, Y.Q. 1983, *Solar Phys.* *84*, 83.
Lüst, R. and Schlüter, A. 1954a, *Z. Ap.* *34*, 263.
Lüst, R. and Schlüter, A. 1954b, *Z. Ap.* *34*, 365.
Moffatt, H.K. 1985, *J. Fluid Mech.* *159*, 359.
Moffatt, H.K. 1986, *J. Fluid Mech.* *166*, 359.
Parker, E.N. 1972, *Ap. J.* *174*, 499.
Parker, E.N. 1979, *Cosmical Magnetic Fields*, Oxford, Clarendon Press, pp. 359-391.
Parker, E.N. 1981a, *Ap. J.* *244*, 631.
Parker, E.N. 1981b, *Ap. J.* *244*, 644.
Parker, E.N. 1982, *Geophys. Ap. Fluid Dyn.* *22*, 195.
Parker, E.N. 1983a, *Ap. J.* *264*, 635.
Parker, E.N. 1983b, *Ap. J.* *264*, 642.
Parker, E.N. 1983c, *Geophys. Ap. Fluid Dyn.* *23*, 85.
Parker, E.N. 1983d, *Geophys. Ap. Fluid Dyn.* *24*, 79.
Parker, E.N. 1986a, *Geophys. Ap. Fluid Dyn.* *34*, 243.
Parker, E.N. 1986b, *Geophys. Ap. Fluid Dyn.* *35*, 277.
Parker, E.N. 1987, *Ap. J.* (submitted).

Rosenbluth, M.N., Dagazian, R.Y. and Rutherford, P.H. 1973, Phys. Fluids 16, 1894.

Rosner, R., Turner, W.H. and Vaiana, G.S. 1978, Ap. J. 220, 643.

Schwarzschild, M. 1948, Ap. J. 107, 1.

Syrovatski, S.I. 1966, Sov. Phys. JETP 23, 754.

Syrovatski, S.I. 1978, Solar Phys. 58, 89.

Syrovatski, S.I. 1981, Ann. Rev. Astron. Ap. 19, 163.

Tsinganos, K.C. 1982, Ap. J. 259, 832.

Tsinganos, K.C., Distler, J. and Rosner, R. 1984, Ap. J. 278, 409.

Van Ballegooijen, A. 1985, Ap. J. 298, 421.

Withbroe, G.L. and Noyes, R.W. 1977, Annual Rev. Astron. Astrophys. 15, 363.

N88-11616

MAGNETIC FIELDS IN THE OVERSHOOT ZONE: THE GREAT ESCAPE

F. Cattaneo and D. W. Hughes
Joint Institute for Laboratory Astrophysics
University of Colorado, Boulder, CO 80309, U.S.A.

ABSTRACT

In order that magnetic flux be confined within the solar interior for times comparable to the solar cycle period it has been suggested that the bulk of the solar toroidal field is stored in the convectively stable overshoot region situated beneath the convection zone proper. Such a magnetic field though is still buoyant and is therefore subject to Rayleigh-Taylor type instabilities. In this paper we consider the model problem of an isolated region of magnetic field embedded in a convectively stable atmosphere. The fully nonlinear evolution of the two-dimensional interchange modes is studied, thereby shedding some light on one of the processes responsible for the escape of flux from the solar interior.

1. INTRODUCTION

Despite considerable strides in recent years in both dynamo theory and the study of magnetoconvection, several problems remain regarding certain key features of the sun's magnetic cycle. One of these concerns the location of the sun's primary toroidal field and the means by which this can escape from the interior, eventually to appear at the surface to form sunspots or smaller bipolar active regions. The inherent buoyancy of isolated magnetic flux tubes, together with the unstable convective motions, will carry tubes of equipartition strength through the entire convection zone on a timescale of about a month (see, for example, Parker, 1975; Moreno-Insertis, 1983). This presents certain difficulties for keeping the requisite amount of magnetic flux within the convection zone for timescales comparable to that of the solar cycle. To overcome this difficulty it has been suggested (Spiegel and Weiss, 1980) that the bulk of the toroidal field is contained in the convectively stable overshoot region situated beneath the convection zone proper. Of course such a field alters the density stratification, causing the atmosphere to become top-heavy — in consequence, Rayleigh-Taylor instabilities can ensue.

In this paper we consider the instabilities which can result when an isolated region of magnetic field is embedded in a convectively stable atmosphere. It should be noted that this is a very different situation to that of an isolated flux tube in a field-free gas. In particular, our initial static state possesses a continuous temperature distribution and is a *bona fide* solution of the hydrostatic equation (see Section 2) — for an isolated flux tube in thermal equilibrium with its surroundings, on the other hand, there is *no* static state and the tube is forced to rise. Our calculation is both fully compressible and nonlinear but, for simplicity, we shall here only consider the two-dimensional interchange modes (no bending of the field lines) and shall ignore the effects of rotation. The account given is, of necessity, rather brief — a much more detailed version, which also treats rotational effects, is currently in preparation.

2. MATHEMATICAL FORMULATION

We consider a plane parallel layer of conducting fluid of thickness *d*. Within the layer the magnetic field **B** and gravity **g** are constrained to be mutually orthogonal for all times. The fluid flow is in the xz plane only, perpendicular to the magnetic field. The computational domain can be thought of as a section of a meridional cut near the equator. The field is then toroidal and the flows are axisymmetric. To simplify the problem the thermal conductivity K, the shear viscosity μ and the magnetic diffusivity η are assumed to be constants; furthermore the plasma obeys the perfect gas law with constant specific heats. By choosing the layer depth d and the sound crossing time $d/\sqrt{p/\rho}$ as the units of length and time respectively the evolution equations can be expressed in dimensionless form as follows:

$$p = \rho T, \tag{1}$$

$$\partial_t \rho + \nabla \cdot \rho \mathbf{u} = 0, \tag{2}$$

$$\partial_t B + \nabla \cdot (B\mathbf{u}) = \tau C_k \nabla^2 B, \tag{3}$$

$$\partial_t \rho \mathbf{u} + \nabla \cdot \rho \mathbf{u}\mathbf{u} = -\nabla(p + \frac{B^2}{2\beta}) + \theta(m+1)\rho \hat{\mathbf{z}} + C_k \sigma(\nabla^2 \mathbf{u} + \frac{1}{3}\nabla(\nabla \cdot \mathbf{u})), \tag{4}$$

$$\rho(\partial_t T + \mathbf{u} \cdot \nabla T) + (\gamma - 1)p\nabla \cdot \mathbf{u} = \gamma C_k \nabla^2 T + (\gamma - 1)C_k(\sigma \partial_i u_j \phi_{ij} + \tau(\nabla B)^2/\beta), \tag{5}$$

where $\phi_{ij} = \partial_i u_j + \partial_j u_i - \frac{2}{3}\delta_{ij}\nabla \cdot \mathbf{u}$.
The six dimensionless parameters which appear explicitly are defined by:

$$\sigma = \frac{\mu C_p}{K}, \qquad \tau = \frac{\eta \rho_0 C_p}{K}, \qquad \beta = \frac{\mu_0 p_0}{B_0^2},$$
$$m = (\frac{gd}{R\Delta} - 1), \qquad \theta = \frac{\Delta d}{T_0}, \qquad C_k = \frac{K}{\rho_0 C_p d\sqrt{RT_0}},$$

where Δ is the initial temperature gradient.

The formulation of the problem is completed by imposing boundary conditions at the top and bottom and by requiring that all variables be periodic in the horizontal direction. The boundary conditions at $z = 0$ (top) and $z = 1$ (bottom) are chosen so as to minimise their effects in the interior; they are:

$$T = 1 \quad \text{at} \quad z = 0 \quad \text{and} \quad T = 1 + \theta \quad \text{at} \quad z = 1,$$

$$\rho w = \partial_z u = \partial_z B = 0 \qquad \text{at} \quad z = 0, 1.$$

If the magnetic field has a top hat profile then the equations admit a piecewise-polytropic static solution. Small random disturbances (typically about 1%) of this equilibrium are used as initial conditions for the fully nonlinear calculations. The stability of the static solution to infinitesimal disturbances is determined by linear theory.

3. THE LINEAR REGIME

The linearised versions of Eqs. (1) to (5) are separable in x and t with solutions of the form $f(x,z,t) = \hat{f}(z)e^{st}\cos \ell x$ (or $\sin \ell x$). We are then left with a set of coupled ordinary differential equations (involving only z) with the growth rate s as the eigenvalue. For small values of τ instability always occurs via an exchange of stabilities. We find that there is always one dominant unstable mode and that this has grown appreciably before any of the harmonics lose stability.

As expected, increasing the strength of the magnetic field (reducing β) leads to the instability becoming more vigorous (see figure 1). The figure also shows that as the field is increased then the mode of maximum growth rate moves to larger wavenumbers (smaller cell widths). In the absence of all diffusion the growth rate is maximised for infinitesimally thin cells ($\ell \rightarrow \infty$); however, dissipation acts most effectively on such cells and therefore a balance is struck at a finite cell size. For small β the instability is sufficiently strong that fairly small cells can overcome the dissipative effects and grow most rapidly. This behaviour is analogous to that which occurs in the standard Rayleigh-Taylor instability of two superposed viscous fluids (Chandrasekhar, 1961, p.446). A more surprising feature is that the dependence of the mode of maximum growth rate on the depth of the magnetic layer is very weak (see figure 2). This would appear to be because the instability occurs primarily at the upper interface of the magnetic field and that the depth of the field below that is not of fundamental importance.

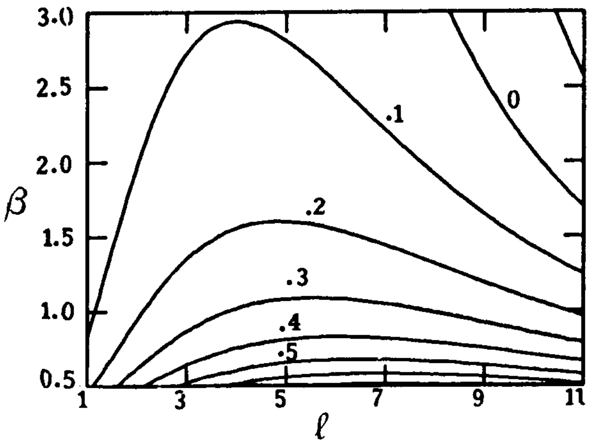

Figure 1 Contours of the growth rate for β versus ℓ. $\sigma = .1$, $\tau = .05$, $C_k = .05$, $m = 1.6$, $\theta = .1$

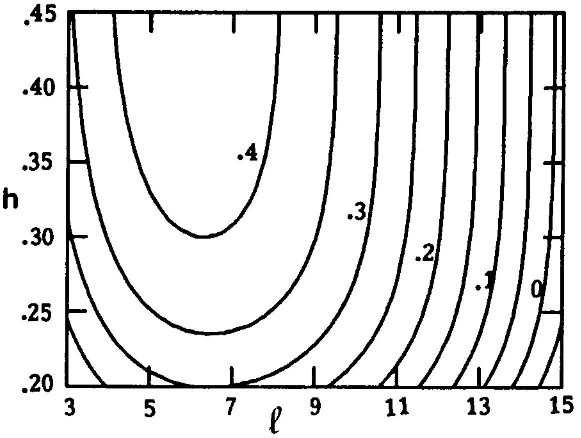

Figure 2 Contours of the growth rate for h, the depth of the magnetic region, versus ℓ. $\sigma = \tau = .1$, $C_k = .05$, $m = 1.6$, $\theta = 1$

4. THE NONLINEAR REGIME

The evolution of a uniform magnetic field confined initially to the region $0.6 < z < 0.8$ is shown in figure 3. The instability due to magnetic buoyancy leads to an initial break-up of the layer and, eventually, to the spreading of magnetic field over the entire domain in a time (a few Alfvén crossing times) short compared to the diffusion time.

In the initial phases of the instability the magnetic layer's upper interface forms the familiar mushroom-shaped structures associated with Rayleigh-Taylor instabilities (see, for instance, Daly, 1967). In all cases considered the density difference between the magnetic and field-free regions was such that mushrooms were formed rather than bubbles and spikes. Associated with the wings of the mushrooms are regions of intense vorticity which, once most of the available potential energy has been released, play a key rôle in the subsequent evolution of the layer. The characteristic wrap-around structures visible in figures 3(c) to 3(f) are typical of flows generated by random distributions of vortex pairs. Some of the vortex-vortex interactions are strong enough to do, albeit locally, negative buoyancy work and to produce the downward displacement of regions of high magnetic field even though these regions are lighter than their surroundings and would have, in the absence of any other flow, risen upwards.

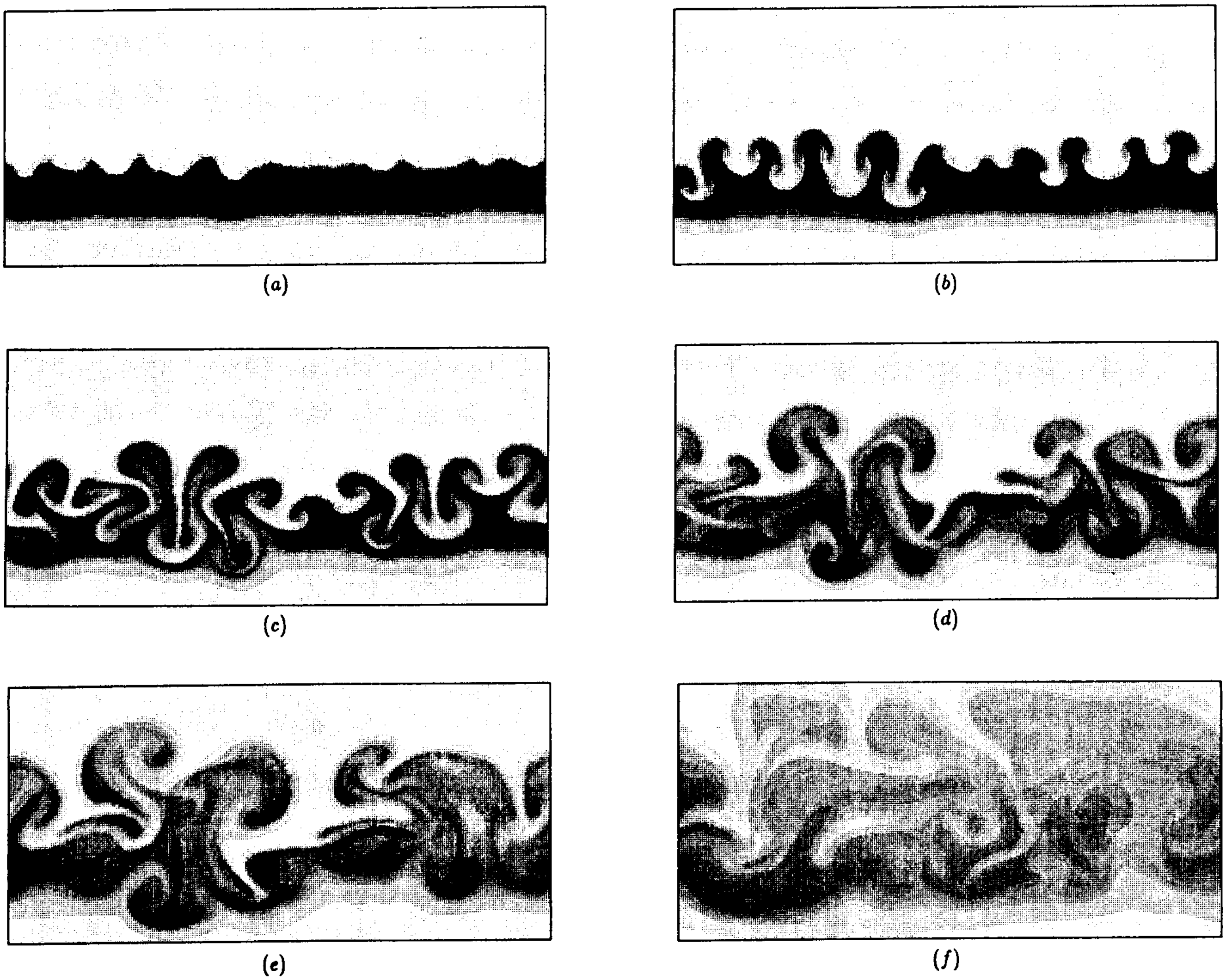
(a) (b) (c) (d) (e) (f)

Figure 3 Time evolution of an unstable magnetic layer. $\sigma = .1$, $\tau = .01$, $C_k = .01$, $m = 1.6$, $\theta = 2$, $\beta = 1$. The simulation times for the frames are respectively: (a) 1.9, (b) 3.5, (c) 5.1, (d) 6.7, (e) 8.3 and (f) 13.1.

ACKNOWLEDGEMENTS

We are grateful to Prof. Juri Toomre for many helpful discussions. This work was supported by the National Aeronautics and Space Administration through grants NSG-7511, NAGW-91 and NAG5-513 and contract NAS8-31958.

REFERENCES

Chandrasekhar, S., *Hydrodynamic and Hydromagnetic Stability*, Clarendon Press, Oxford (1961).
Daly, B.J., *Phys. Fluids* **10**, 297 (1967).
Moreno-Insertis, F., *Astron. & Astrophys.* **122**, 241 (1983).
Parker, E.N., *Astrophys. J.* **198**, 205 (1975).
Spiegel, E.A. and Weiss, N.O., *Nature* **287**, 616 (1980).

N88-11617

THEORETICAL MODELLING OF THE FINE STRUCTURES IN SUNSPOTS

Arnab Rai Choudhuri
High Altitude Observatory
National Center for Atmospheric Research[1]

Until a decade ago most solar physicists thought of a sunspot as the upper end of a giant flux tube floating vertically. Parker (1979a) provided an alternative scenario in his spaghetti model and showed that many properties of sunspots can be understood better if sunspots are regarded as loose collections of fibril flux tubes. In spite of the many attractive features of this model, it is probably fair to say that we are still unable to give an unequivocal verdict in favor of one of the two models on the basis of current observations. Since we cannot hope to observe the subphotospheric magnetic structures directly, the wisest strategy seems to be to work out systematically those consequences of both models which should be distinguishable from high resolution photospheric observations. One approach to this problem discussed here is to do detailed theoretical modelling of sunspot fine structures within the frameworks of both the rival models, in order to provide a basis for future crucial observations from space. Another approach currently under investigation by Bogdan (1986) is to study the scattering of p-modes both from single flux tubes and from collections of fibrils, and then to compare theoretical results with observations.

The existence of umbral dots and penumbral grains has been known for several decades. However, their individual sizes are smaller than the limit set by atmospheric seeing, and consequently their properties cannot be studied with sufficient reliability from gound-based observations. On the basis of available observations, they seem to be regions of photospheric intensity with upflowing gas motion and magnetic fields much weaker than in the surrounding sunspot surface. References to the relevant observational papers are given in Choudhuri (1986). It is not even clear whether umbral dots and penumbral grains can be regarded as convective cells within the sunspots. Claims have been made both for (Bumba and Suda 1980) and against (Loughhead, Bray and Tappere 1979) this hypothesis by different observers.

On the theoretical side also, a magnetoconvective theory of umbral dots has been considered by Knobloch and Weiss (1984) that can be fitted with the single-flux-tube model of sunspots. They suggested that the differences in the appearances of umbral dots and granular cells are caused by the highly nonlinear nature of the convection problem in the presence of strong magnetic fields. Full calculations to substantiate these ideas have not been carried out yet. On the other hand, Parker (1979a,b) explained umbral dots within the framework of his spaghetti model as regions where field-free gas intrudes through the clustered flux tubes from underneath the surface. Elaborating on these ideas, Choudhuri (1986) investigated how the surrounding magnetic field may try to close on the field-free gas from the top and control the dynamic behavior of the system. Here we merely present the main ideas without any equations. Readers are referred to the original paper for the details of calculations.

It can be shown that a pocket of field-free gas surrounded by a vertical magnetic field in the presence of gravity takes up the shape of a tapering column ending at a vertex at the top, as shown in Figure 1a. Choudhuri (1986) first studied the static equilibrium of such a system. Regions away from the apex can be treated by slender flux tube approximation. However, special care is needed to treat the region around the apex. An exact solution for that region in two dimensions and an approximate solution in three dimensions were presented. It was found that, just below the apex, the radius of the tapering column opens up with a 3/2 power dependence on the depth below the apex. When the analytical solutions for the two different regions are

---

[1] The National Center for Atmospheric Research is sponsored by the National Science Foundation.

combined together, it agrees quite well with numerical calculations. The vertical position of the apex depends on the internal pressure of the field-free gas. If the internal pressure is increased, the whole tapering column rises.

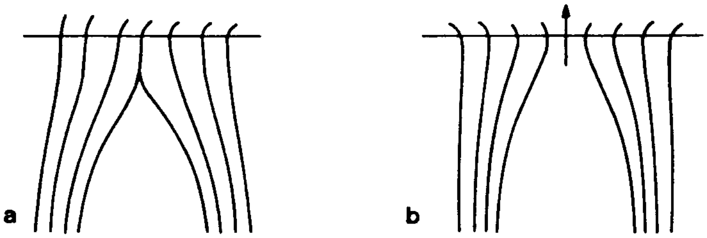

FIG. 1

We expect some convection to take place in the trapped field-free gas, whereas the magnetic field around it makes those regions stable against convection. Hence heat can be transported convectively upward into the trapped field-free gas, but no further convective transport is possible to allow that heat to reach the surface. Since radiative diffusion is rather inefficient once we go some distance below the photosphere, we expect to have a situation where the temperature and pressure of the trapped gas keep growing, causing the whole tapering column to rise. Plugging in typical values of different quantities shows that the velocity of rise is small compared to sound speed. Hence the system can be thought to evolve through a succession of quasi-static states in mechanical equilibrium.

Eventually the apex of the tapering column reaches the photospheric surface where the bulging of the magnetic field makes the field no longer able to close on the field-free gas and trap it underneath. A flow path is thus established as shown in Figure 1b. An analysis of the steady flow problem shows that the velocity of the upcoming gas at the mouth of the flow path should be of the order of Alfvén speed in the surrounding magnetic field. After a sufficient amount of field-free gas has escaped, thereby reducing its internal pressure, it may no longer be possible to maintain a flow path and the field may again close up, stopping any further escape of the field-free gas. Thus the field geometry effectively acts as a magnetic valve. When there is sufficient pressure under it, the magnetic valve opens and allows the trapped gas to come out. But after enough gas has escaped to reduce the pressure sufficiently, the magnetic valve closes and chokes off the flow. An umbral dot can simply be regarded as an open magnetic valve through which field-free gas from below is coming out. Since magnetic field in the penumbra is inclined to the vertical, we expect the flow path also to be inclined, and a simple projection effect can explain the elongated shape of the penumbral grains.

It seems that this model is consistent with most of the current observations. However, the ultimate fate of the model will certainly depend on whether it will be able to explain the future high-resolution observations from space.

I thank Peter Gilman for a critical reading of the manuscript.

Bogdan, T.J. 1986, in preparation.

Bumba, V., and Suda, J. 1980, *Bull. Astr. Inst. Czechoslovakia,* **26,** 315.

Choudhuri, A.R. 1986, *Ap. J.,* **302,** 809.

Knobloch, E., and Weiss, N.O. 1984, *M.N.R.A.S.,* **207,** 203.

Loughhead, R.E., Bray, R.J., and Tappere, E.J. 1979, *Astr. Ap.,* **79,** 128.

Parker, E.N. 1979a, *Ap. J.,* **230,** 905.

_____. 1979b, *Ap. J.,* **234,** 333.

N88-11618

Pressure Structure of Solar Coronal Loops

V KRISHAN

INDIAN INSTITUTE OF ASTROPHYSICS

BANGALORE - 560034, INDIA

Abstract

The steady state pressure structure of a coronal loop is discussed in terms of the MHD global invariants of an incompressible plasma. The steady state is represented by the superposition of two Chandrasekhar-Kendall functions corresponding to (n=m=0) and n=m=1) modes. The relative contribution of the two modes (ϵ) is found to depend on the surface pressure of the coronal loop which is also the pressure of the external medium. The mixed mode state does not exist for high values of the external pressure because ϵ becomes complex.

Steady State Model of Coronal Loops

The coronal loop is represented by a cylindrical column of plasma with periodic boundary conditions at the ends of the cylinder (z=0,L). The pressure (p) profile of an incompressible MHD plasma is given by

$$\nabla^2 p = \vec{\nabla}.[(\vec{\nabla} \times \vec{B}) \times \vec{B}] - \vec{\nabla}.[(\vec{V}.\vec{\nabla})\vec{V}] \qquad (1)$$

where $\vec{V}$, $\vec{B}$ are respectively the velocity and the magnetic field. The magnetic field B is defined in Alfven speed units i.e. $B \equiv B/\sqrt{4\pi\rho}$. The Chandrasekhar-Kendall representation of the velocity and magnetic fields is given in terms of B_{nm} where m is the azimuthal mode number and n is the axial mode number.

$$\vec{B}_{00} = \xi_0 \lambda_0 c_0 [\hat{e}_\theta \lambda_0 J_1(\gamma_0 r) + \hat{e}_z \lambda_0 J_0(\gamma_0 r)] \qquad (2)$$

$$\begin{aligned}\vec{B}_{11} = & -\xi_1 c_1 \gamma_1 [k_1 J_0(\gamma_1 r) + \frac{J_1(\gamma_1 r)}{\gamma_1 r} (\lambda_1 - k_1)] \sin(\theta + k_1 z) \hat{e}_r \\ & -\xi_1 c_1 \gamma_1 [\lambda_1 J_0(\gamma_1 r) - \frac{J_1(\gamma_1 r)}{\gamma_1 r} (\lambda_1 - k_1)] \cos(\theta + k_1 z) \hat{e}_\theta \\ & +\xi_1 c_1 \gamma_1^2 J_1(\gamma_1 r) \cos(\theta + k_1 z) \hat{e}_z \end{aligned} \qquad (3)$$

$$\vec{V}_{00} = \frac{\eta_0}{\xi_0}\vec{B}_{00} \text{ etc } ; \; K_1 = \frac{2\pi}{L} , \; \lambda_{nm} = \pm (\gamma_{nm}^2 + k_n^2)^{\frac{1}{2}}$$

Substituting these fields in equation (1), one can solve for the pressure profile in various cases. λ_0 is determined from the constancy of the ratio of the toroidal invariant ψ_t to the poloidal one ψ_p as

$$\frac{\psi_t}{\psi_p} = + \frac{R}{L} \frac{J_1(\gamma_0 R)}{J_0(\gamma_0 R)} \qquad (4)$$

where R is the radius of the loop. γ_1 is determined from the boundary conditions $B_r = 0$ at $r=R$. For a rigid perfectly conducting wall at $r = R$;

$$Rk_n \gamma_{nm} J_m'(\gamma_{nm}R) + M\lambda_{nm} J_m(\gamma_{nm}R) = 0 \qquad (5)$$

The pressure profile in the state (00 + 11) is given as:

$$\frac{p - p_0}{p_t} = g_0 + 6 \epsilon g_1 \cos(\theta+k_1z) - 2\epsilon^2[g_2\cos^2(\theta+k_1z)$$

$$+ g_3 \cos(2\theta+2k_1z) \quad + g_4 \sin^2(\theta+k_1z) - g_5] \qquad (8)$$

$$p_t = \frac{\gamma_0^2 R^2}{8\pi^2 J_1^2(\gamma_0 R)R^4} , \qquad \epsilon = \frac{c_1 \xi_1 \gamma_1^2}{c_0 \xi_0 \gamma_0^2}$$

$$\gamma_1 r = x_1 \quad , \quad \gamma_0 r = x_0$$

$$g_1(x_1) = \Big[\frac{\lambda_1}{\gamma_1} J_0(x_1)J_1(x_0) - \frac{\lambda_1 - k_1}{\gamma_1} \frac{J_1(x_1)J_1(x_0)}{x_1} - J_0(x_0)J_1(x_1)\Big]$$

$$g_2(x_1) = \Big[\frac{(\lambda_1 - k_1)^2}{\gamma_1^2} \frac{J_1^2(x_1)}{x_1^2} + \Big\{\frac{k_1\lambda_1}{2\gamma_1^2} + \frac{(\lambda_1 - k_1)(3\lambda_1 + k_1)}{8\gamma_1^2} + \frac{1}{2}\frac{\lambda_1^2}{\gamma_1^2}$$

$$+ \frac{(\lambda_1 - k_1)^2}{8\gamma_1^2} \Big] J_0^2 (x_1) + \Big\{\frac{1}{2} + \frac{k_1(\lambda_1 - k_1)}{2\gamma_1^2} + \frac{(\lambda_1 - k_1)(3\lambda_1 + k_1)}{8\gamma_1^2}$$

$$+ \frac{(\lambda_1 - k_1)^2}{8\gamma_1^2} \Big] J_1^2 (x_1) - \Big\{\frac{(\lambda_1 - k_1)(3\lambda_1 + k_1)}{4\gamma_1^2} + \frac{\lambda_1(\lambda_1 - k_1)}{\gamma_1^2} + \frac{(\lambda_1 - k_1)^2}{4\gamma_1^2} \Big\}$$

$$\frac{J_0(x_1)J_1(x_1)}{x_1} \Big]$$

$$g_3(x_1) = \left[\left\{\frac{1}{4} - \frac{k_1^2}{4\gamma_1^2}\right\}J_0^2(x_1) + \left\{\frac{\lambda_1^2 - k_1^2}{4\gamma_1^2}\right\}J_1^2(x_1) - \left\{\frac{1}{2} + \frac{k_1(\lambda_1 - k_1)}{2\gamma_1^2}\right\}\right.$$

$$\left.\frac{J_0(x_1)J_1(x_1)}{x_1} - \frac{(\lambda_1 - k_1)^2}{4\gamma_1^2}\,\frac{J_1^2(x_1)}{x_1^2}\right]$$

$$g_4(x_1) = \frac{1}{2}\left[\frac{k_1}{\gamma_1}J_0(x_1) + \frac{(\lambda_1 - k_1)}{\gamma_1}\,\frac{J_1(x_1)}{x_1}\right]^2$$

$$g_5 = \frac{(\lambda_1 - k_1)^2}{16\gamma_1^2} + \frac{(\lambda_1 + k_1)^2}{8\gamma_1^2} + \frac{\lambda_1 k_1}{4\gamma_1^2}\ .$$

Here $p = p_0$ at $r = 0$, $z = 0$; c's are normalization constants.

An example

$$\frac{L}{R} = 5,\ \frac{\psi_t}{\psi_p} = 1 \quad \text{gives } \gamma_0 R = 1$$

and

$$\lambda_1 R = 3.11,\ \gamma_1 R = 2.85,\ k_1 R = 1.25,$$

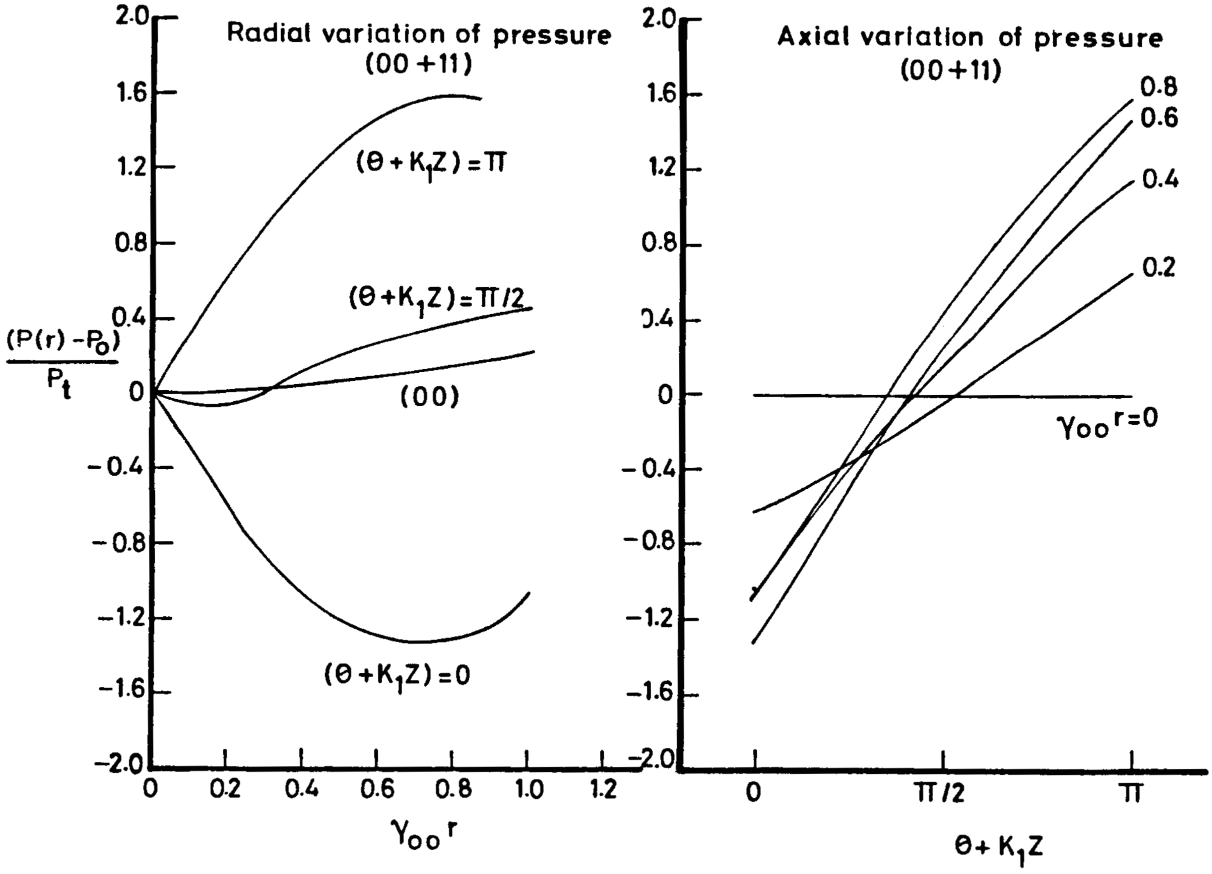

Total Energy, Magnetic Helicity and determination of ϵ.

The total energy $\tilde{W}$ for (00 + 11) state per unit length is

$$\tilde{W} = \frac{2(\gamma_0 R)\,(F_0 + \epsilon^2 \frac{\lambda_1}{\lambda_0}\; F_1)}{(F_0 + \epsilon^2 F_1)^2} \; \frac{\tilde{Hm}^2}{\psi_t^2},$$

The magnetic helicity per unit length $\tilde{Hm}$ is

$$\frac{\tilde{Hm}R}{\psi_t^2} = F_0 + \epsilon^2 F_1$$

And the quantity,

$$I = \frac{(p_e(R) - p_0)\quad \psi_t^8}{\tilde{Hm}^4} = \frac{G_0 + \epsilon G_1 + \epsilon^2 G_2}{(F_0 + \epsilon^2 F_1)^4} \quad .$$

For a fixed $\frac{R}{L}$, ψ_t/ψ_p, n, m. G_0, G_1, G_2, F_0 and F_1 are functions of $\gamma_0 R$ and $\gamma_1 R$ and completely determined. Therefore I is a function only of ϵ. ϵ can be determined from the following (approximate) equation:

$$\epsilon^2 = - \frac{(4F_1 F_0^3 I - G_2) \pm [(4F_1 F_0^3 I - G_2)^2 - H(F_0^4 I - G_0)\; 6F_1^2 F_0^2 I]^{\frac{1}{2}}}{12 I F_1^2 F_0^2}$$

where

$$F_0 = \frac{\gamma_0^3 R^3}{2\pi J_1^2(\gamma_0 R)} \left[J_0^2(\gamma_0 R) + J_1^2(\gamma_0 R) - \frac{J_0(\gamma_0 R) J_1(\gamma_0 R)}{\gamma_0 R} \right]$$

$$F_1 = \frac{1}{4\pi^2 \gamma_0 R\; J_1^2(\gamma_0 R)} \; \frac{\lambda_1}{\lambda_0} \; \frac{\gamma_0^4}{\gamma_1^4} \; \frac{1}{c_1^2}$$

$$G_0 = \frac{\gamma_0^2 R^2}{8\pi^2 J_1^2(\gamma_0 R)} \left(1 - J_0^2(\gamma_0 R) - J_1^2(\gamma_0 R)\right)$$

$$G_1 = \frac{3\gamma_0^2}{\gamma_1^2} \; \frac{\gamma_1^2 R^2}{4\pi^2 J_1^2(\gamma_0 R)} \left[\frac{\lambda_1}{\gamma_1} J_0(\gamma_1 R) J_1(\gamma_0 R) - \frac{\lambda_1 - k_1}{\gamma_1} \; \frac{J_1(\gamma_1 R) J_1(\gamma_0 R)}{\gamma_1 R} - J_0(\gamma_0 R) J_1(\gamma_1 R) \right]$$

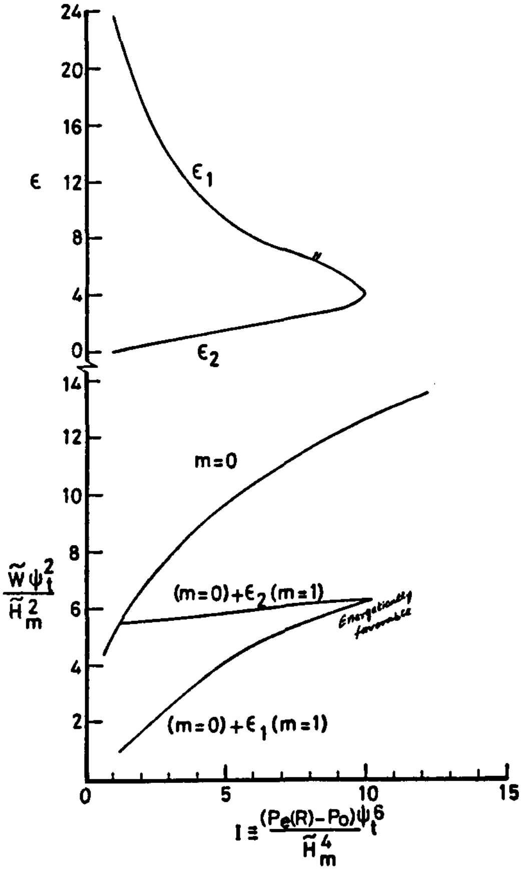

A plot I vs ϵ is shown which shows that as the external pressure decreases, ϵ increases. For $I \geqslant 9.9$, ϵ becomes complex.

$\frac{\tilde{w}\psi_t^2}{\tilde{H}m^2}$ is also plotted against I for the axisymmetric and the mixed mode state.

The m=0 curve is obtained by varying the ratio R/L and keeping ψ_t/ψ_p fixed. $\gamma_0 R$ increases as L/R increases and I also increases. For fixed L, I increases as R decreases, in other words smaller loops are in a medium of higher external pressure, which is as it should be. At a certain value of the external pressure the mixed mode state is energetically more favourable than the m=0 state. Thus there is a transition from m=0 state to (m=0 + m=1) state as the loop moves outwards in the corona in a medium of decreasing external pressure. The inner presure variation conforms to an increase of temperature along the axis from z=0, to z=L. The radial variation of temperature at the top of the loop confirms to the cool core and hot sheath model. Thus depending upon the position of the loops in the corona, one may observe them to be either in the m=0 state or (m=n=1) + (m=n=0) state and therefore the corresponding temperature variations are observed.

N88-11619

A NUMERICAL STUDY OF THE THERMAL STABILITY OF SOLAR LOOPS

J. A. Klimchuk*, S. K. Antiochos, J. T. Mariska
E. O. Hulburt Center for Space Research
Naval Research Laboratory

Background

It has recently been shown that low-lying solar loops with apex heights $< 5 \times 10^3$ km admit a "cool" solution to the static energy and force balance equations, in addition to the familiar "hot" solution (Antiochos and Noci 1986). This cool solution reaches a maximum temperature of less than about 10^5 K, far below the million or so degrees of the hot solution. Both solutions are possible for a given amount of energy input to the loop. In hot loops much of the energy is conducted down to a thin transition region, where it is more easily radiated away, but in cool loops there is a much closer local balance between radiation and energy input, and conduction is relatively small.

With the exception of chromospheric features such as fibrils and filaments, the importance of cool loops on the Sun has yet to be established. Foukal (1975) discussed observations of loops cooler than 10^6 K, but such loops are not very common and are generally much hotter than 10^5 K. The possibility of cool loops in the range between 10^4 and 10^5 K has nonetheless stirred considerable interest, since an adequately large number of these loops could perhaps explain the well-known but not well-understood rise in emission measure for decreasing temperature below 10^5 K (Antiochos and Noci 1986; Dowdy, Rabin, and Moore 1986). Hot loops can satisfactorily reproduce the upper part of the observed emission measure curve, but they fail in the lower part where cool loops would be significant.

An important property of all loops is their thermal stability. If low-lying hot loops were thermally unstable, for example, we might expect a great majority of the low loops on the Sun to be cool. Indeed, theoretical studies suggest that very low-lying ($< 10^3$ km) hot loops are unstable to infinitely small perturbations (e.g., Antiochos et al. 1985). These studies fail to describe how the perturbations will behave in the nonlinear, physically observable regime, however. If the perturbations quickly saturate, then the loops are effectively stable.

The purpose of the work reported here is, first, to determine how small perturbations evolve in low-lying, linearly unstable hot loops, and second, to examine how high-lying, linearly stable hot loops respond to large amplitude disturbances such as might be expected on the Sun. Only general descriptions and results are given here. Details will be provided in a forthcoming paper (Klimchuk, Antiochos, and Mariska 1986).

---

* NRC-NRL Cooperative Research Associate

PRECEDING PAGE BLANK NOT FILMED

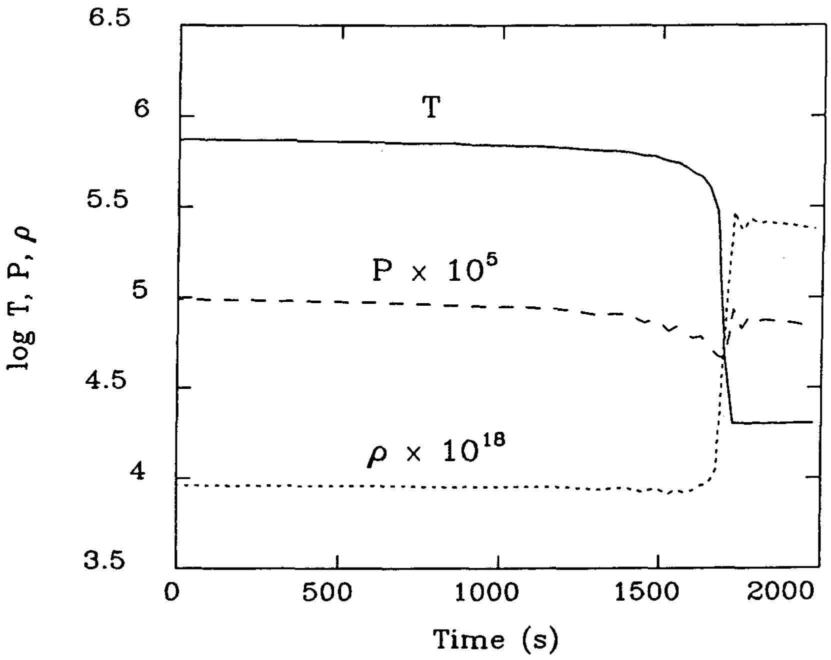

Figure 1. The evolution of temperature, pressure, and density at the top of the low-lying loop. Units are in the cgs system. Note that the vertical scale is logarithmic.

Numerical Simulations

The computer model we use to address these issues solves the time-dependent equations of mass, momentum, and energy transport for a fully ionized solar plasma confined to a rigid magnetic flux tube. The tube consists of a semi-circular coronal loop which extends deep into a $2x10^4$ K chromosphere. We assume uniform energy input per unit volume, constant cross-sectional area, and the radiation law of Raymond modified by a T^3 dependence below 10^5 K. If anything, these assumptions should have a stabilizing influence on the atmosphere. The spatial resolution of the finite difference grid ranges from 1 km in the transition region to 100 km in the upper corona.

We first consider a low-lying loop with an apex height of 500 km above the chromosphere (in the regime of linear instability). Small imperfections in the initial static "equilibrium" are allowed to evolve. Figure 1 shows the variation of temperature, pressure, and density at the top of the loop. A very slow cooling takes place during the first 1650 s, but then the temperature plummets dramatically from $4x10^5$ to $2x10^4$ K in matter of less than a minute. Densities increase by a comparable amount during this time, so the pressure is approximately constant. Eventually the transient flows which are created die down and the atmosphere settles into a new static equilibrium. It is a cool equilibrium of the type discussed by Antiochos and Noci (1986). Because of the very low temperatures, however, the state of the loop is best described as an "extended chromosphere."

Closer examination of the calculations reveals that the rapid cooling phase seen in Figure 1 occurs throughout the simulation, but at progressively higher locations within the loop. At all times the plasma at lower transition zone temperatures cools very quickly and condenses onto the chromospheric interface. This interface moves upward, partially from the accumulation of new material, but mostly because the chromosphere expands in response to gradually decreasing pressures in the overlying corona. The expansion finally reaches the top of the loop at a time of about 1700 s into the simulation. In some sense the chromosphere appears to "eat away" at the slowly cooling corona from below. We can understand this evolution in terms of a succession of quasi-static equilibria, each of which is destroyed by the nonlinear growth of its fundamental eigenmode (Klimchuk, Antiochos, and Mariska 1986). These eigenmodes are sharply peaked near 4×10^4 K, where most of the evolution takes place.

We next consider a much larger loop with an apex height of 10^4 km. Linear theory predicts it to be stable. In agreement with this theory, the loop does not respond to imperfections in the initial equilibrium other than by adjusting very slightly to achieve the true equilibrium. We have simulated the response of this loop to perturbations as large as 20 %. Both short and long wavelength disturbances were considered. The short wavelength disturbance has the form of the least stable (fundamental) eigenmode, and the long wavelength disturbances have the form of quarter sine waves extending from the top of the loop through most of the corona. The latter are characterized by either constant pressure or constant density. In each case the loop atmosphere appears to be returning to its original hot state after the perturbation is applied. There is no evidence for evolution to a new cool state or a highly dynamic hot state.

Discussion

The outcomes of our numerical simulations suggest two important results concerning the stability of hot coronal loops: 1) low-lying loops with apex heights less than about 10^3 km are nonlinearly unstable to small amplitude perturbations; and 2) high-lying loops with apex heights greater than about 5×10^3 km are stable to all reasonable perturbations, including those of large amplitude and long wavelength. The latter conclusion was reached independently by other investigators (e.g., Peres et al. 1982). These results are fully consistent with the most recent linear theory (Antiochos and An 1987). By showing that unstable linear perturbations are able to grow without saturation, we have extended the theory into the realm of physical observation.

The potential implications of these results are severalfold. First, high-lying hot loops can be in a static or nearly static state if the applied perturbations are of small enough amplitude; dynamical motions need not be a fundamental property of all loops. The motions that have been observed (e.g., Brueckner 1980) seem to imply large amplitude disturbances of the type discussed above, or, more likely, large changes in the heating rate as discussed elsewhere in these Proceedings by Mariska.

A second implication is that the hot state should not occur frequently in very low-lying loops on the Sun. Since low-lying magnetic fields are known to be common (e.g., Giovanelli 1980), we might therefore expect cool loops to be very abundant. This could perhaps explain the emission measure puzzle discussed above. A difficulty with this picture, however, is that the hot loops which are linearly unstable are so low-lying ($<10^3$ km) and their cool state may be not much more than an extended chromosphere. The more interesting cool states with temperatures approaching 10^5 K would then occur only in loops of greater height.

For a roughly uniform heating, cool loops are possible up to a height of a few thousand kilometers. We can therefore identify an intermediate height range in which cool states exist and the corresponding hot states are linearly stable. The mere existence of an alternate state suggests that the hot state in these loops might be unstable to large amplitude disturbances. We have tested this hypothesis on a 2×10^3 km loop and find that the hot state is, in fact, stable to such disturbances. Thus, if 10^5 K cool loops exist on the Sun, they must be formed in that state initially; apparently then cannot easily evolve from preexisting hot loops.

This work was sponsored by the Solar Terrestrial Theory Program and the Office of Solar and Heliospheric Physics of the National Aeronautics and Space Administration and by the Office of Naval Research.

References

Antiochos, S. K., Shoub, E. C., An, C.-H., and Emslie, A. G. 1985, Ap. J., **298**, 876.

Antiochos, S. K., and Noci, G. 1986, Ap. J., **301**, 440.

Antiochos, S. K., and An, C.-H. 1987, in preparation.

Brueckner, G. E. 1980, in Highlights of Astronomy, vol. 5, ed. P. A. Wayman (Dordrecht: D. Reidel), p. 557.

Dowdy, J. F., Jr., Rabin, D., and Moore, R. L. 1986, Solar Phys., **105**, 35.

Foukal, P. V. 1975, Solar Phys., **43**, 327.

Giovanelli, R. G. 1980, Solar Phys., **68**, 49.

Klimchuk, J. A., Antiochos, S. K., and Mariska, J. T. 1986, submitted to Ap. J.

Peres, G., Rosner, R., Serio, S., and Vaiana, G. S. 1982, Ap. J., **252**, 791.

N88-11620

SOLAR TRANSITION REGION AND CORONAL RESPONSE TO HEATING RATE PERTURBATIONS

John T. Mariska
E. O. Hulburt Center for Space Research
Naval Research Laboratory, Washington, DC

I. OVERVIEW

The solar transition region is in a dynamic state characterized by impulsively upflowing plasma and continually downflowing plasma. Using numerical simulations, I examine the conjecture that the areas of downflowing plasma are simply the base regions of coronal loops in which the heating rate is gradually decreasing and the areas of upflowing plasma are the base regions of coronal loops in which the heating rate is gradually increasing.

Only when the heating in a coronal loop is reduced to 1% of the initial value required to maintain the loop do appreciable downflow velocities develop at 10^5 K. The time scale over which the heating is reduced is not of great importance. Moreover, maximum downflow velocities are present only after the loop has cooled to the point where the emission measure at 10^5 K is very small, making them difficult to observe.

Appreciable upflow velocities are only present in the case in which the loop that has been cooled by reducing the heating rate to 1% of the initial rate is reheated. These upflow velocities at 10^5 K are much smaller than those observed at high spatial resolution in impulsive events. Larger velocities are present in the higher temperature plasma in the loop early in the heating. At this stage, however, the emission measure at high temperatures is small, making it unlikely that the plasma could be observed.

The calculations suggest that gradually reducing or increasing the heating in a magnetic flux tube will not result in plasma motions that are similar to those that are observed at high spatial resolution in the UV. A more detailed description of the calculations is presented in Mariska (1986).

II. COOLING

The initial model consists of a static atmosphere in a loop with a half-length of 21,000 km. At the base of the model is a 1050 km thick chromospheric region in hydrostatic equilibrium at 10^4 K. Above this region are a transition region and corona whose properties are determined by solving the static force and energy balance equations. The base pressure here is 0.25 dynes cm^{-2}, a value typical for the quiet sun. The background heating rate required for this initial model is 2.71×10^{-4} ergs cm^{-3} s^{-1}. This results in a peak temperature for the initial half loop of 1.06×10^6 K.

Beginning with this initial model, I reduce the heating everywhere to 10% and 1% of the initial rate on time scales of 100, 1000, and 2000 s. Figure 1 shows the evolution of the volume emission measure and the velocity at 10^5 K. The emission measure plot is for the calculation in which the heating was reduced to 1% of the initial rate with a time scale of 100 s. The velocity plot shows the velocity evolution for the 1% case for all three time scales.

Early in the cooling the shape of the emission measure curve remains relatively unchanged. The high-temperature turnover simple moves to lower temperatures accompanied by a gradual decrease in the slope near 10^5 K. As the cooling continues, the slope above 10^5

K changes from positive to negative. This negative slope continues to the final quasisteady equilibrium at then end of the simulation.

As the loop cools, appreciable velocities develop at 10^5 K. The maximum downflow velocity for all three time scales is near 15 km s^{-1}. Note, however, that the downflow velocity is only large for a time interval of less than 500 s. Moreover, comparison with the emission measure plot shows that the maximum downflow velocities are present only when the emission measure has fallen to very small values at 10^5 K. Thus the maximum downflow velocities are present only when it is becoming increasingly difficult to observe them.

III. HEATING

Beginning with the atmospheric structures at the end of the cooling calculations, I increase the heating everywhere back to the initial value on time scales of 100, 1000, and 2000 s. Figure 2 shows the evolution of the volume emission measure and the velocity at 10^5 K. The emission measure plot is for the calculation in which the model which has been cooled by reducing the heating rate to 1% of the initial value is reheated on a 100 s time scale. The velocity plot shows the velocity behavior for all three time scales for the restoration of heating to the 1% model.

When the heating is restored, the temperature in the coronal portions of the loop increases very rapidly while the density remains relatively unchanged. This causes the emission measure curve to shift to the right, with some increase in absolute value. Once the mass motions have begun to redistribute plasma in the loop the slope of the emission measure also begins to change. The shape of the emission measure curve reaches its final configuration within just a few hundred seconds. For the remainder of the evolution, the loop simply fills with plasma which increases that absolute value of the emission measure at all temperatures.

The initial response of the velocity at 10^5 K to the restoration of heating is a brief downflow. This is due to the sudden rise in the pressure in the coronal portions of the model pushing the entire transition region downward. The upflow velocities from evaporation for all three time scales are small and last for only a short time. Comparison of the velocity and emission measure plots shows that these upflows are largest when the emission measure at 10^5 K is still small compared with its final value. Thus the velocities would be difficult to observe.

IV. DISCUSSION

These heating and cooling calculations suggest that simple changes in the heating rate in a loop will not reproduce the mass motions observed in the quiet solar transition region. The calculations are unable to reproduce the large downflows seen at 10^5 K, the shape of the emission measure curve below about 10^5 K, or the formation of cool spicular upflows. It appears that instead some kind of steady driving mechanism, such as a heating rate asymmetry (e.g., Boris and Mariska 1982; McClymont and Craig 1986), is required.

This work was sponsored by the NASA Solar Terrestrial Theory Program and by the Office of Naval Research.

REFERENCES

Boris, J. P., and Mariska, J. T. 1982, *Ap. J. (Letters)*, **258**, L49.
Mariska, J. T. 1986, *Ap. J.*, submitted.
McClymont, A. N., and Craig, I. J. D. 1986, *Nature*, **324**, 128.

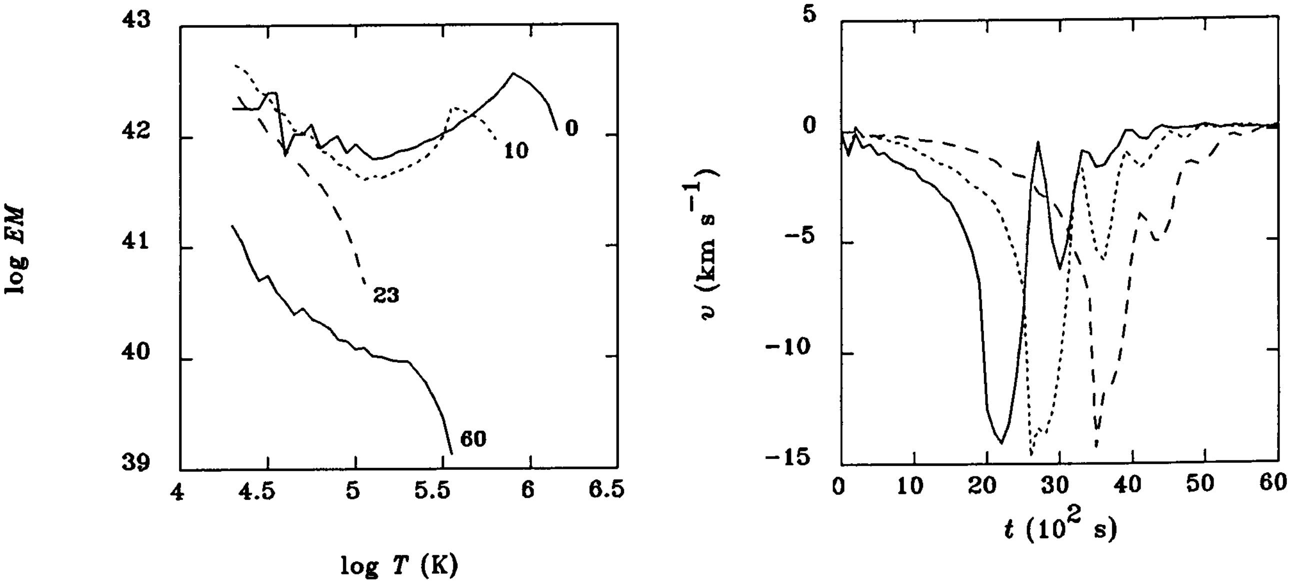

Fig. 1.—The evolution of the volume emission measure and the velocity at 10^5 K for the cooling calculation in which the heating was reduced to 1% of the initial rate. The times in the emission measure plot are in units of 100 s. In the velocity plot the solid line is for the 100 s time scale for the reduction in the heating, the short dashed line is for the 1000 s time scale, and the long dashed line is for the 2000 s time scale.

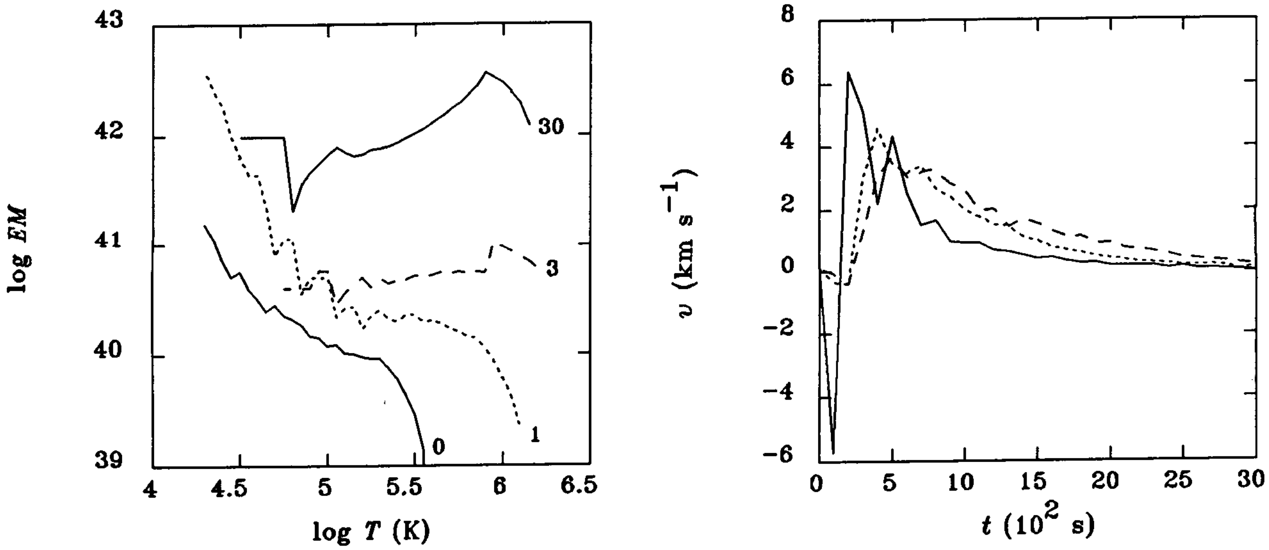

Fig. 2.—The evolution of the volume emission measure and the velocity at 10^5 K for the calculation in which the heating was restored to the atmosphere that had been cooled by reducing the heating rate to 1% of the initial rate. The labeling on the plots follows the same conventions as in Figure 1.

N88-11621

LARGE-SCALE HORIZONTAL FLOWS FROM SOUP OBSERVATIONS OF SOLAR GRANULATION

L.J. November (NSO/SP), G.W. Simon (AFGL/SP), T.D. Tarbell,
A.M. Title, and S.H. Ferguson (LPARL)

ABSTRACT

Using high-resolution time-sequence photographs of solar granulation from the SOUP experiment on Spacelab 2, we have observed large-scale horizontal flows in the solar surface. Our measurement method is based upon a local spatial cross correlation analysis. The horizontal motions have amplitudes in the range 300 to 1000 m/s. Radial outflow of granulation from a sunspot penumbra into surrounding photosphere is a striking new discovery. We see both the supergranulation pattern and cellular structures having the scale of mesogranulation. The vertical flows that are inferred by continuity of mass from these observed horizontal flows have larger upflow amplitudes in cell centers than downflow amplitudes at cell boundaries.

1. Introduction

Since the Doppler effect measures line-of-sight velocities it cannot be used to determine horizontal motions at disk center. The only way to observe such flows is through proper motion studies using solar features as tracers. Granules are the obvious choice as tracers of photospheric flows, but because of their small size, coupled with the blurring and geometric distortion due to atmospheric turbulence, they have proven to be difficult to use in ground-based observations (Simon 1967). During its 10 minute lifetime, a typical granule might move only a few hundred kilometers, about one-third of an arcsec, which is much less than the size of the random fluctuations caused by atmospheric seeing, even under the best conditions.

Now, however, with the high-quality distortion-free movie sequences from SOUP, we can measure granulation proper motions with high accuracy. The SOUP image quality was so good (pointing jitter was about 0.003 arcsec, or 2 km on the sun) that we can measure flow speeds to an accuracy of 15 - 20 m/s rms. This is much less than errors in the flow measurements due to random motions and evolution of individual granules and the residual effects of the large-scale five-minute oscillations. Analysis of these various "solar noise" contributors indicates an overall error of about 80 m/s per independent spatial sample in the results to be discussed below. This is far smaller than the 300 - 1000 m/s signals which we report.

Some of the preliminary results have already been reported (Title et.al. 1986, November et.al. 1986b).

2. Technique

Proper motion is determined from these data by computing the displacement that maximizes the cross-correlation between two image fields separated by a time Δt. In our analysis we have used values of Δt from 10 to 60 s. The images are first filtered to remove some photographic grain noise and any large- scale intensity gradients so that the remaining signal is mainly the solar granulation. Then the cross-correlation function is computed at each "locale" on the images. The locale around each image point is defined as the product of the intensity field and a gaussian window centered on that point. The gaussian window used in this analysis had a full width at half maximum (FWHM) of 4.2 arcsec. The vector displacement and transverse flow velocity of the features within the window during the interval Δt are then found by locating the cross-correlation maximum. The window is moved from pixel to pixel over the entire image to give the vector displacement at every pixel locale. This computational method is described by November (1986a). The 4.2 arcsec size of the gaussian was found to be a reasonable compromise between sensitivity and resolution in the final map of transverse flow velocities. We have developed a similar algorithm at Lockheed that uses the minimum of a squared residual function. The agreement in displacements measured by the two techniques is excellent.

Figure 1 is an example of a vector displacement map formed by averaging 160 original vector maps spanning 1600s of time. The window size is plotted in the lower left of each figure; this represents the actual spatial resolution of the displacement measurements. Note that we considerably oversample this resolution in the analysis and display vectors formed from overlapping granulation fields.

We have calibrated this technique by cross-correlating a digitized photographic image with itself after applying a known spatial shift in the microdensitometer digitizing stage. The precision depends very sensitively upon the method used for interpolation in the cross-correlation. With the data sampled at or exceeding the diffraction limit of the telescope, a 2–D quadratic interpolation to

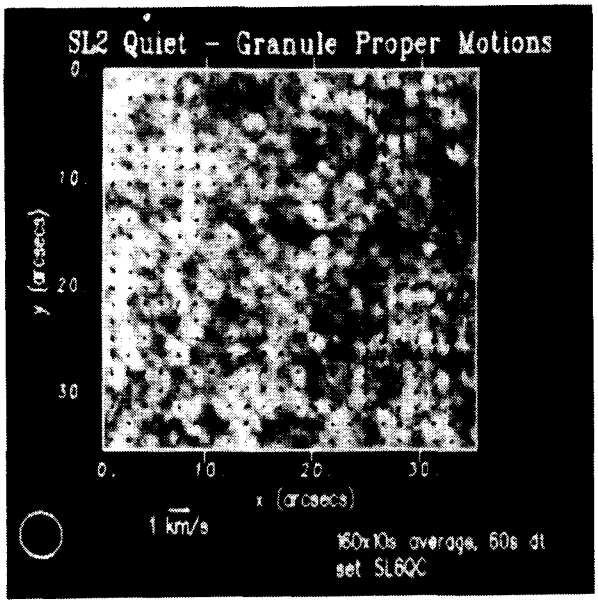

Figure 1. Average proper motion vector map – quiet region. The proper motion at each spatial locale has been defined by spatial cross-correlation analysis within a sliding gaussian window. The granulation is shown with superposed vectors having lengths proportional to the amplitude of the local flows. The scale of the vectors is given by the arrow shown below these figures. The gaussian window size of 4.2 arcsecs FWHM is indicated by the size of the circle in the lower left. This vector map is formed from the average of 160 original vector maps and spans 1600s in time.

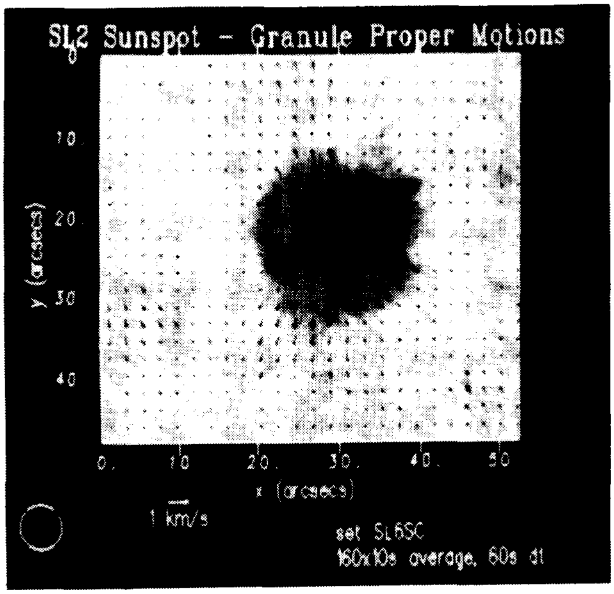

Figure 2. Average proper motion vector map – sunspot region. A large isolated spot was photographed by SOUP, and shows radial outflow from the penumbra and nearby photosphere. No vectors are shown in the umbra of the sunspot as there was inadequate signal there for the cross-correlation.

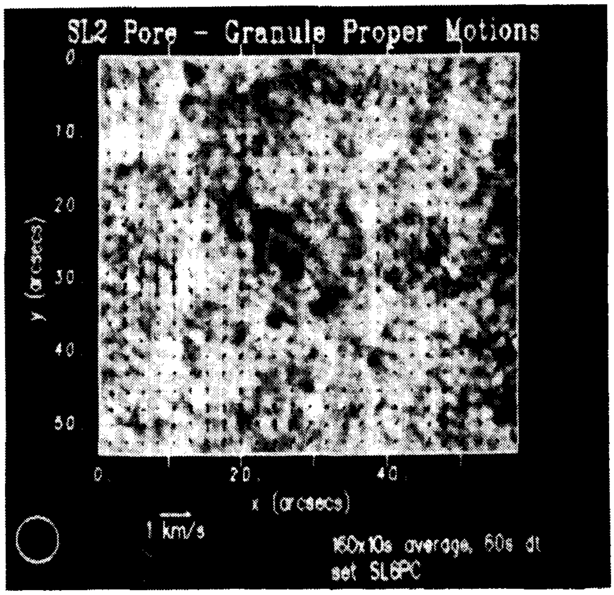

Figure 3. Average proper motion vector map – pore region. This is a region containing numerous pores. Notice that the amplitude of the flows is considerably reduced in the vicinity of the pores. Away from the pores cellular flows characteristic of those seen in the quiet sun image are again apparent.

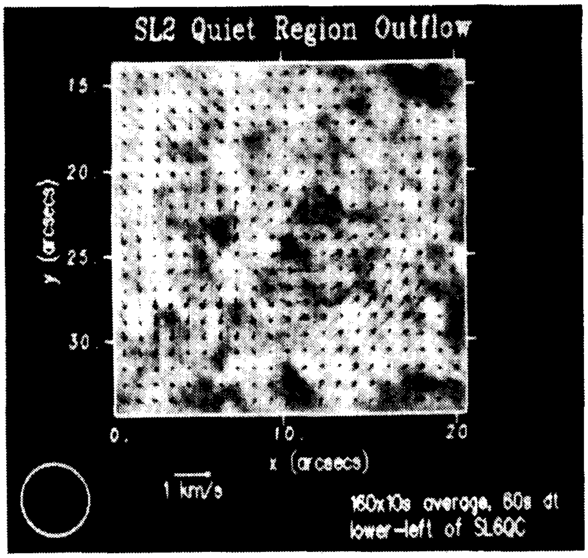

Figure 4. A magnified portion of the quiet proper-motion map from Figure 1 is magnified and more vectors are displayed. This demonstrates the cellular nature that is characteristic of the large-scale proper-motion flows.

the cross-correlation gives a measurement of the image shift having a bias error of less than 3 percent for displacements in the range 0.005 pixel (0.6 km on the sun) to 0.5 pixel.

The error in the measurement is estimated by examining the evolution of the vector displacement in time. We compute a time-averaged vector displacement map as in Figure 1; the fluctuations about this average give an upper estimate of the noise in the measurement. The Fourier power spectrum of this temporal variation shows two components: a low-frequency feature and a smaller high-frequency white-noise tail. The tail reflects the statistical uncertainty in the measured displacement and is probably due principally to photographic granularity noise. It contributes an rms error of 20 m/s, or 0.01 pixel, to the 160 frame average of vector displacements. The low-frequency component has maximum power at about 200s period and contributes an rms error of 80 m/s to the average. The level of this "solar noise" may vary from quiet sun to plage or sunspot regions.

3. Analysis

Three specific portions of the 166x250 arcsec, 160 frame, 27 minute data set have been analyzed: a region of quiet sun, an isolated sunspot, and a pore region. This data set was obtained between 19:10 and 19:38 UT on 5 August 1985, in the vicinity of NOAA active region 4682. Single frames of these image fields are shown with their overlying average vector proper motions, respectively, in Figures 1, 2, and 3. Each of these images was produced by digitizing positive copies of the original films. Let us look at these figures in some detail.

In the quiet sun photograph (Figure 1) we identify two regions of larger horizontal outflow emanating from centers at (34,17) and (8,25) (that is to say, the coordinates of the outflow center (34,17) are at x=34 arcsec and y=17 arcsec in the figure). We have magnified the area centered at (8,25) and show it in Figure 4. Here we see also a nearby linear sink region around (15,22). Flows which emanate from single points and then flow toward and along a line are fairly characteristic of quiet- region velocity patterns. However, note the nice exception showing convergence to a point at (25,34) in Figure 1. This small region is magnified in Figure 5. The scale of many of the cellular features is typically 10 arcsec; we associate this with mesogranulation (November, et.al. 1981).

The region around (34,17) in Figure 1 is shown enlarged in Figure 6. This feature has the typical supergranule scale of about 30 - 40 arcsec (Simon and Leighton 1964). The outflow in this example appears to show abrupt changes in flow direction partitioned along radial lines approximately 45 degrees apart: note the lines of flow from (34,17) to (25,10), from (34,17) to (25,17), and from (34,17) to (28,24). We can understand this structure by analyzing the divergence of the horizontal flow $\mathbf{u} = (u,v)$, $\nabla\cdot\mathbf{u} = \partial u/\partial x + \partial v/\partial y$. The divergence is shown in Figure 7 as contours superposed on the quiet granulation field from Figure 1. Here we identify the outflow at (34,17) as the large positive divergence that reaches an amplitude of $5.5\cdot10^{-4}$ s^{-1}. This outflow is surrounded by smaller cells. Apparently the superposition of the flows from the smaller cells creates the impression of the radial velocity structure.

One large sunspot was observed in the area photographed by SOUP. Figure 2 shows this region with superposed flow vectors. Radial outflow extends from the edge of the sunspot penumbra into surrounding photosphere with amplitude 300 - 700 m/s. This annulus or "collar" around the penumbra has a width of about five arcsec. This outflow is reduced adjacent to two small sectors of penumbra, one of which is poorly-formed and intermediate in brightness between normal penumbra and photosphere. We show in Figure 8 the sunspot region with superposed contours of flow divergence. Away from the sunspot we find cellular inflows and outflows similar to those seen in the quiet region of Figure 1.

Figure 3 shows a region containing numerous pores with superposed flow vectors. The granule proper motions are much reduced in the pore region, but away from the pores we again find cellular inflows and outflows as in the quiet sun. The lack of flow in the pore region is illustrated by the small amplitude of the divergence signal over the pores shown in Figure 9. The region in the immediate vicinity of the pores is magnified in Figure 10, and here the reduced magnitude of flow vectors can be clearly seen. The flow velocities in the pore region are about 100 m/s, about the size of the "solar noise" in our measurements, and thus difficult to observe.

4. Discussion

In the divergence maps of the cellular quiet sun flows, we find that the places of positive divergence characteristically have larger amplitudes than the places of negative divergence even though in its definition the average divergence over the area of the image is set to zero. Compare, for example, the extremes of divergence in Figure 1 at region (8,25) with $5.5\cdot10^{-4}$ s^{-1} and the region at (24,31) with divergence $-4.5\cdot10^{-4}$ s^{-1}. We quantify the difference between upflow and downflow regions by plotting a histogram of the divergence. It extends to larger amplitudes for the positive divergences. The mean of the positive divergence is $1.29\cdot10^{-4}$ s^{-1} and the mean of the negative divergence is $-1.17\cdot10^{-4}$ s^{-1}; thus the sinks occupy more area than the sources.

The sinks and sources are associated with downflows and upflows through the mass con-

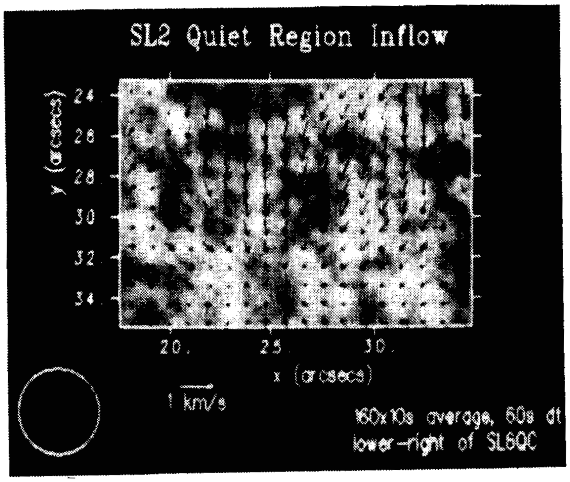

Figure 5. Magnification of another portion of Figure 1 to show a sink point. More typically, however, sources are isolated points, while sinks lie along lines of convergence.

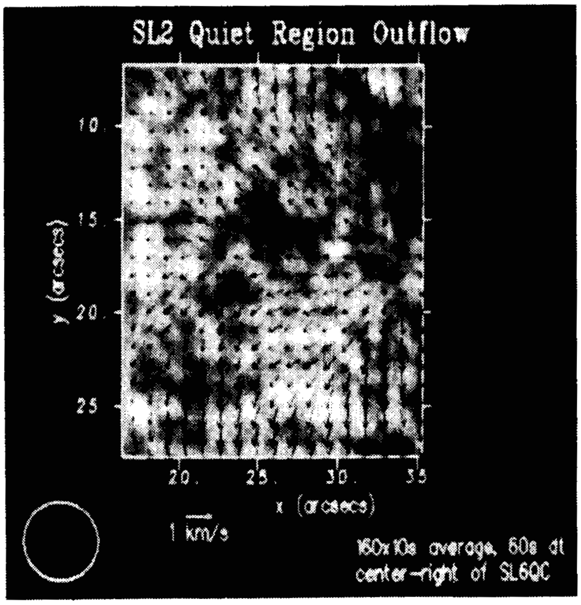

Figure 6. Magnification of a third part of Figure 1 showing a large supergranular cell.

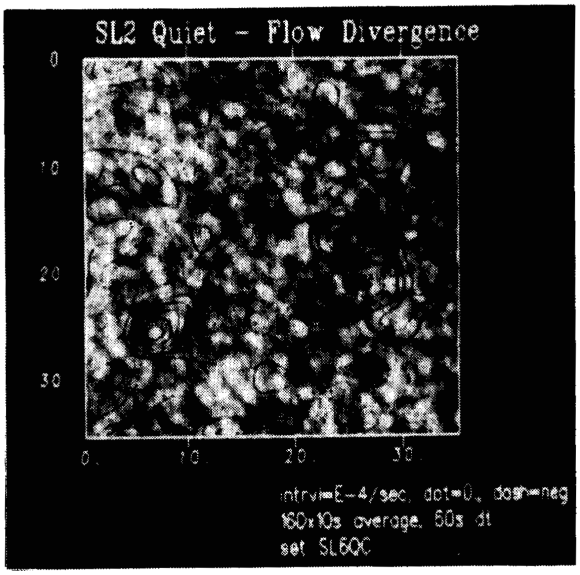

Figure 7. Divergence of quiet-region flows. The contours show the amplitude of the local divergence of the horizontal flows from Figure 1. The contour interval is $1 \cdot 10^{-4}$ s^{-1}. Point source regions are those with positive divergence (solid contours), while the linear sink regions have negative divergence (dashed contours). The zero contour is dotted.

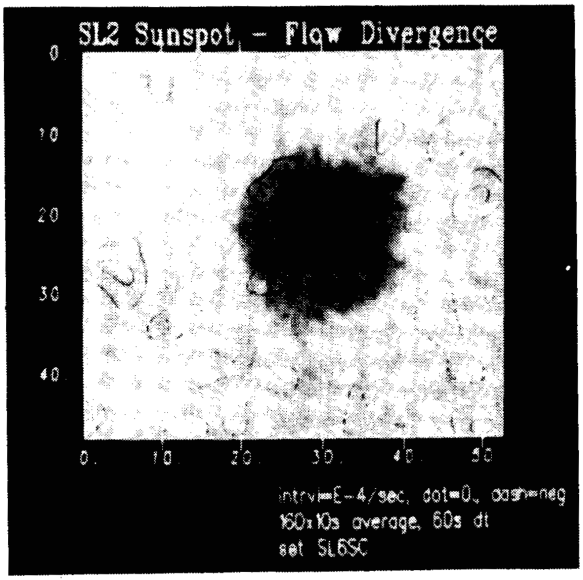

Figure 8. Divergence of sunspot-region flows shown in Figure 2.

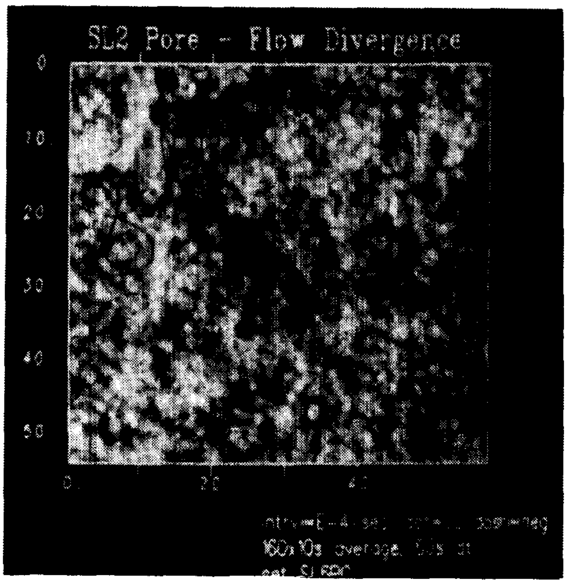

Figure 9. Divergence of pore-region flows from Figure 3.

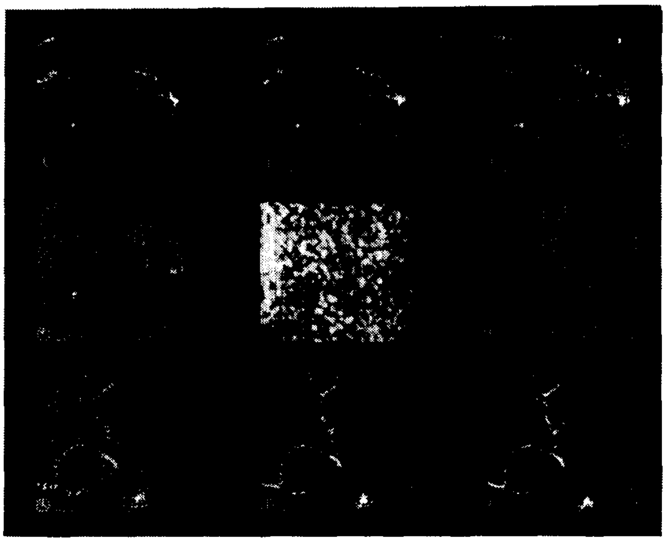

Figure 11. Propagation of long-lived tracers. "Corks" embedded in the flow field of Figure 1 trace out the flow pattern from their emergence in regions of positive divergence until they congregate in sinks and network regions where the divergence is negative. The nine frames proceed from −8 to +8 hours with the actual observation time (hour 0) shown as a superposed uniform grid of corks and granulation intensity in the center frame.

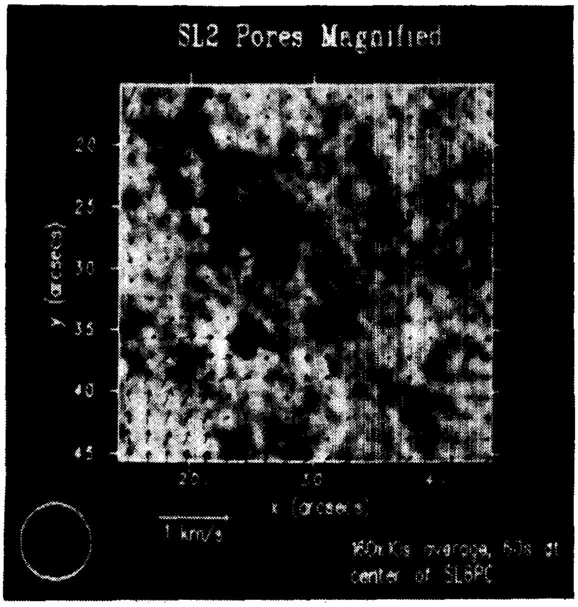

Figure 10. Pore region magnified. This shows the vectors in the immediate vicinity of the pores from Figure 3. The amplitude of the flow is considerably reduced here relative to the quiet sun flows.

tinuity equation: $\partial(\rho w)/\partial z = -\nabla\cdot(\rho \mathbf{u})$, where w is the vertical and $\mathbf{u}$ the vector horizontal velocity. We rewrite this as: $(w/\rho)\cdot(\partial\rho/\partial z) + \partial w/\partial z = -\nabla\cdot\mathbf{u}$. The horizontal density fluctuations at any level must be small because the mean density is defined by the local pressure which is mainly hydrostatic, and by the temperature which is approximately fixed at a given depth. Replacing $1/\rho\cdot\partial p/\partial z$ with $1/h_\rho$, and $\partial w/\partial z$ with w/h_w, where h_ρ and h_w are the density and velocity scale heights, respectively, we obtain $w(1/h_\rho + 1/h_w) = -\nabla\cdot\mathbf{u}$. Letting $(1/h_\rho + 1/h_w) = 1/h_m$ where h_m is the mass flux scale height, then assuming $h_w << h_\rho$ (Schmidt, et.al. 1985), and using a value of h_ρ=200 km for the subphotosphere, $h_m \simeq 200$ km and we obtain w=26m/s as the average of the sources and w=−23m/s as the average of the sinks. These values, smaller than the noise in earlier Doppler measurements, explain why it has been so difficult to detect vertical velocities in supergranulation.

The sense of our flow fields is like that of typical Benard cells that have greater central upflows than downflows at the boundaries (Chandrasekhar 1961). Further, the small amplitudes which we infer are in general agreement with Doppler measurements of the vertical flows in the supergranulation. Simon and Leighton (1964) were unable to detect vertical motions at disk center although their sensitivity was better than 100 m/s. More sensitive Doppler measurements (Frazier 1970, Worden and Simon 1976, Giovanelli 1980, November, et.al. 1982, Küveler 1983) give vertical amplitudes similar to those we infer here. Our proper motion measurements are, however, in qualitative disagreement with the Doppler observations which showed larger amplitude downflows than upflows. Thus they probably reflect another effect. The difference might be explained as a systematic error in the Doppler signal caused by a possible contrast effect in granulation over magnetic elements (Giovanelli 1980). More likely, the Doppler observation could result from a superposition of photospheric flows that are dominated by magnetic rather than convective processes in the network boundaries (Giovanelli 1980, Gebbie, et.al. 1981).

The large-scale flow fields, both as observed visually from the movies, and quantitatively from the calculated vector displacements, have the proper size and appearance of super- and mesogranular convection flows. Therefore we would expect these flows, at subsurface levels in the sun, to move magnetic fields to the cell boundaries, and form the loci of the photospheric and chromospheric networks. The SOUP white-light movies indeed give us the definite impression that lanes of brighter-than average granules occur at these places (converging sinks and line flows) where the divergence is negative, i.e. at the cell boundaries. This bright photospheric network always seems to surround the upwellings, or boiling centers, which mark the darker-appearing super- and mesogranule centers. Unfortunately we have not yet been able to locate from ground-based data any good quality magnetogram or chromospheric spectroheliogram coincident with these SOUP data. These are needed to make a definitive comparison with our flow fields. SOUP data from earlier and later orbits are currently being reduced. Some of these do coincide with National Solar Observatory images of sufficiently high quality to make useful comparisons. We hope to analyze these data in the next few months.

Implicit in our analysis is the assumption that the granules float, like corks, on the supergranular flows, and thus can serve as tracers to define the larger structures. Suppose, then, that we start with a uniform distribution of granule "corks" superposed on and subject to the pattern of arrows which define our average flow fields. As time evolves, the corks move, and as they reach the next pixel point, they are subjected to the slightly different flow field corresponding to that location. We have made a movie of such cork flows in which we extrapolate our measured velocities forward and backward in time assuming that they do not change over the 36 hour length of the movie. It is interesting to note that the corks form into a network pattern in two to three hours; some of the corks, as expected, congregate at the few sink holes in our images. If we run such a cork movie in reverse, the corks quickly concentrate in the upwellings which form the meso- and supergranule centers. We illustrate the cork motions in Figure 11 where we show the movie frames from times −8, −6, −4, −2, 0, 2, 4, 6, and 8 hours relative to the actual time of observation for the quiet sun image of Figure 1. While these cork movies give only an artificial picture of the development of large-scale flows, they do agree well with our intuition. Fortunately there exist, in all, about 16 hours of SOUP data so that it will be possible to make an authentic study of the evolution of these flows.

References

Chandrasekhar, S., *Hydrodynamic and Hydromagnetic Stability*, Oxford University Press, 1961.

Frazier, E.N., "Multi-Channel Magnetograph Observations II. Supergranulation", *Solar Phys.* ***14***, 89-111, 1970.

Gebbie, K.B., Hill, F., Toomre, J., November, L.J., Simon, G.W., Gurman, J.B., Shine, R.A., Woodgate, B.E., Athay, R.G., Bruner, E.C., Rehse, R.A., Tandberg-Hanssen, E.A., "Steady Flows in the Solar Transition Region Observed with SMM", *Astrophys. J.* ***251***, L115-L118, 1981.

Giovanelli, R., "The Supergranule Velocity Field", *Solar Phys.* ***67***, 1980.

Küveler, G., "Velocity Fields of Individual Supergranules", *Solar Phys.* ***88***, 13-29, 1983.

November, L.J., Toomre, J., Gebbie, K.B., Simon, G.W., "The Detection of Mesogranulation on the Sun", *Astrophys. J.* ***245***, L123-L126, 1981.

November, L.J., Toomre, J., Gebbie, K.B., Simon, G.W., "Vertical Flows of Supergranular and Mesogranular Scale Observed on the Sun with OSO−8", *Astrophys. J.* ***258***, 846-859, 1982.

November, L.J. "Measurement of Geometric Distortion in a Turbulent Atmosphere", *Applied Optics* ***25***, 392-397, 1986a.

November, L.J., Simon, G.W., Tarbell, T.D., Title, A.M., and the SOUP Team, "Precise Proper Motion Measurement of the Solar Granulation", *B.A.A.S.*, June 1986b.

Schmidt, H.U., Simon, G.W., Weiss, N.O., "Buoyant Magnetic Flux Tubes II. Three-Dimensional Behavior in Granules and Supergranules", *Astron. Astrophys.* ***148***, 191-206, 1985.

Simon, G.W., "Observations of Horizontal Motions in Solar Granulation: Their Relation to Supergranulation", *Zeitschrift für Astrophysik* ***65***, 345-363, 1967.

Simon, G.W., Leighton, R.B., "Velocity Fields in the Solar Atmosphere III. Large-Scale Motions, the Chromospheric Network, and Magnetic Fields", *Astrophys. J.* ***140***, 1120-1147, 1964.

Title, A.M., Tarbell, T.D., Simon, G.W., and the SOUP Team, "White-Light Movies of the Solar Photosphere from the SOUP Instrument on Spacelab 2", *Proceedings of* COSPAR 26th Plenary Meeting, Toulouse, France, June 1986.

Worden, S.P., Simon, G.W.," A Study of Supergranulation using a Diode Array Magnetograph", *Solar Phys.* ***46***, 73-91, 1976.

N88-11622

LOOP INTERACTION IN THE VISIBLE EMISSION CORONA -- MORPHOLOGICAL DETAILS

Raymond N. Smartt and Zhenda Zhang[1]

National Solar Observatory
National Optical Astronomy Observatories[2]
Sunspot, New Mexico 88349
U.S.A.

ABSTRACT

Coronagraph observations of two post-flare loop systems, recorded photographically in the emissions of Fe XIV (5303Å) and Fe X (6374Å), show occasional enhancements at the intersections of some loops. The brightness of such enhancements in the green-line gradually increases to a maximum value several times greater than that of the legs of the loops and then declines with a typical lifetime ~ 30-60 minutes. In red-line emission the loop systems are usually very faint, but show the same overall type of enhancement, with a lag in maximum brightness relative to that of the green line ~ 10 minutes. The electron density, derived from the cooling time, is ~ $10^{12} cm^{-3}$.

I. INTRODUCTION

We discuss here observations of two flare-associated coronal loop systems, as observed in visible coronal emission lines, with emphasis on characteristics of loop interaction processes during the post-flare phase.

Interacting coronal loops have been investigated in relation to flare studies. Machado (1982) has found that most, if not all, X-ray flares originate in two or more intersecting loop structures. Rust and Somov (1984) showed that 3.5 - 11.5 Kev X-ray brightening started near the intersection of two flare loops. They assumed a thermal energy source at the point of intersection of the two loops, with equal conduction of heat flux into each loop. Transient X-ray brightenings of interconnecting loops have been investigated by Spicer and Svestka (1983). They argue that the fast tearing mode or anomalous Joule heating (following inductive changes in the field) could cause the brightenings, the mechanism depending on the loop history. VLA 6-cm observations have provided evidence of interacting loops that trigger flares and the first direct evidence of the coalescence of coronal loops (Kundu *et al.*, 1984; Kundu, 1983, 1985). These radio observations indicate that in the 20 seconds preceding the impulsive peak ($T_b \sim 1.1 \times 10^9 K$), the arcade of loops (burst source) changed and ultimately developed into two strong bipolar regions or a quadrupole structure whose orientations were such that the field lines were opposed to each other near the loop tops.

The above studies are concerned with the large energies associated with flare production, while the events discussed here represent much smaller energies, since they occur in loop systems in the post-flare phase, often several hours after the flare occurrence. However, the basic processes associated with interacting loops that lead to the release of energy appear to be the same in both the high- and the low-energy cases.

---

[1] Permanent address: Department of Astronomy, Nanjing University, Nanjing, People's Republic of China

[2] Operated by the Association of Universities for Research in Astronomy, Inc., under contract with the National Science Foundation

PRECEDING PAGE BLANK NOT FILMED

II. OBSERVATIONS

Observations were obtained with the National Solar Observatory/Sacramento Peak 20-cm aperture patrol coronagraph. Coronal images in Fe XIV (5303Å), Fe X (6374.5Å) and images in Hα of the disk and of prominences are recorded sequentially on high-resolution (SO-115), 70-mm film (Smartt *et al.*, 1981). In the normal mode of operation, a set of these four images is recorded in an interval $\lesssim$ 30s, and repeated at 1 minute intervals. Here we describe the loop interaction features observed in the post-flare loop systems of April 28, 1980 and November 14, 1980.

a) Flare-associated loops, April 28, 1980

These data cover the period 1343 to 1652 UT and 2145 to 2345 UT. The loops are located at a latitude ~ 22°. At 1531 UT, an obvious bright point in the green-line loops occurs at the projected intersection of two loops. Microdensitometer measurements of this feature reveal that it is equivalent to a coronal brightness ~ 5 times larger than that of the well-defined loop legs. Approximately 15 minutes before, and 15 minutes later, this feature was no brighter than the other parts of the loop tops. At 1531 UT, the same feature can be identified in the red-line image, although far less bright and less extensive than in the green-line image. It reaches maximum brightness at ~ 1541 UT, although still exceedingly faint. Fine, hair-like lines define the point of intersection of the loops. These combined green- and red-line observations suggest that the enhancement is due in part to an increase in temperature, the lag ~ 10 minutes in the red-line maximum relative to that of the green-line being a measure of green- to red-line cooling time. However, since the feature is visible in the red-line image, but with little other associated structure of the whole loop system, it is likely that the integrated path is greater than simply the sum of two loops along the line-of-sight.

At 1931 UT, the green-line loops (Figure 1) have now reached a height ~ 10^5 *km*. At this time, there are fewer loops in the system, and due to the inclination of the plane of the loops relative to the line-of-sight, enhancements that occur at loop intersections are now clearly evident. The large X-point enhancement corresponds to a brightness ~ 3 times larger than unenhanced parts of the loops. This enhancement is not confined to the region of intersection, but clearly extends for considerable distances along the loops. For example, the lower right-hand part of the "X" appears to be enhanced for at least 2.5 x 10^3 km from the point of intersection. This type of observation, together with the measured brightness, confirms that such features arise from localized loop interactions.

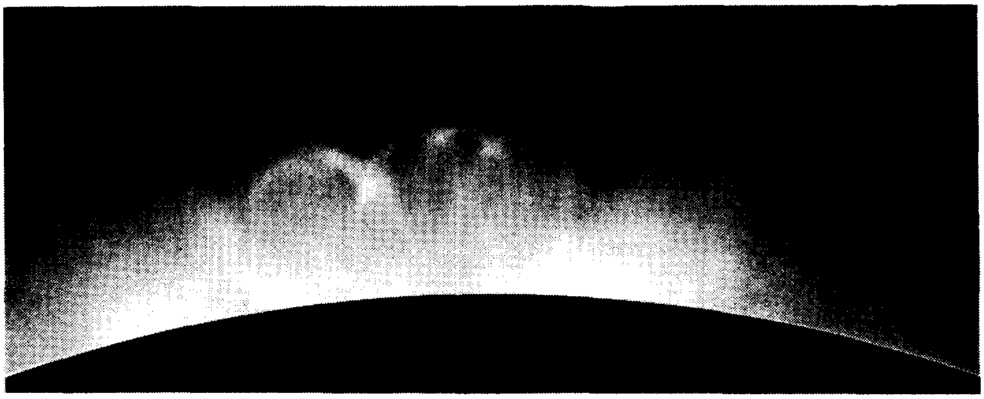

Fig. 1 - Flare associated coronal loops, recorded in Fe XIV (5303Å), on April 28, 1980, at 1932 UT, showing enhancements at loop interactions.

b) Flare-associated loops, November 14, 1980

These loops occurred on the west limb at a latitude of 22 ° N, the data spanning the interval 1633 - 1808 UT. However, due to a fault in the microprocessor control, data were recorded only at intervals of a few minutes. The most obvious general characteristic of the loops as they appear in the green-line image is the suggestion of two systems of loops, as indicated by the obvious discontinuity in the outline of the loop tops. A bright point occurs at this location, maximum at ~ 1732 UT, as shown in Figure 2.

Fig. 2. Flare-associated coronal loops, recorded in Fe XIV (5303Å) on November 14, 1980, at 1732 UT, showing a bright enhancement at the intersections of two loop systems.

The rise time is estimated to be ~ 25 minutes, while the decay time is ~ 30 minutes. As in the cases discussed above, a similar bright point also becomes evident in the red-line record, reaching a maximum value ~ 10 minutes after the green-line maximum. This lag time estimate is less precise than in the previous cases because of the data gaps. The faint red-line "X" enhancement is notable for its narrow dimensions. The green-line enhancement has an area ~ 4.6 x $10^7 km^2$.

III. ANALYSIS

It was noted in Section II that the maximum brightness in a red-line enhancement at the X-point appears to lag the maximum in the green-line enhancements by about 10 minutes, apparently a measure of the cooling time. Moore et al. (1980) find that radiative cooling dominates conductive cooling when $T < 10^7 K$. The radiative cooling time is given by,

$$\tau_c = \frac{3KT}{\Lambda_\gamma N_e} \tag{1}$$

where K is the Boltzman constant, T, the plasma temperature before cooling, Λ_λ, the radiative cooling coefficient and N_e, the electron density. If we assume that cooling from maximum green-line emission to maximum red-line emission is due predominantly to radiative cooling, we can estimate a maximum value for the electron density in the region of the enhancement from equation (1). The radiative cooling coefficient has a value of about $10^{-22} erg\ cm^3 s^{-1}$ (Raymond *et al.*, 1976). Then,

$$Ne \lesssim 4.3 \text{ x } 10^6 \, \mathrm{T}/\tau_c,$$

where the unit of τ_c is in minutes.

The appropriate value for T is uncertain, but since red-line emission can be observed faintly at the X-point at the time of maximum green-line emission, we argue that an average value of T in the enhancement cannot be far in excess of the characteristic temperature of the green-line. We therefore take T = 2 x $10^6 K$; then $Ne \lesssim 10^{12} cm^{-3}$.

IV. DISCUSSION

The question arises concerning the morphology of the loop system that leads to the condition required for an X-point brightening. An arcade of loops spanning a field line contains parallel loops with currents having the same sense. Our observations typically show much more complex structure in which parallel loops appear to be the exception. It therefore seems likely that an encounter between two loops that have intersecting planes occurs when the lower loop develops more rapidly than the higher loop, or simply if photospheric motion moves the loop footpoints such that contact occurs. The reason for the relatively short life-times of the enhancements is not obvious.

In summary, we have presented here the first evidence of coronal loop interaction in the post-flare phase as observed in visible coronal lines. Derived electrons densities are found to be roughly an order of magnitude larger than those that characterize the loop system. A definitive analysis of the phenomenon will probably require spectral data of the visible emisison as well as coordinated observations with X-ray, EUV and radio measurements.

REFERENCES

Kundu, M.R.: 1983, *Solar Phys.* **86,** 205.

Kundu, M.R., Machado, M.E., Erskine, F.T., Rovira, M.G., and Schmahl, E. J.: 1984, *Astron. Atrophys.* **132,** 241.

Kundu, M.R.: 1985, Proc of the IAU Symp. (No. 170) on Unstable Current Systems and Plasma Instabilities in Astrophys., p. 185.

Machado, M.E.: 1982, *Adv. Space Res.* **2,** 115.

Moore, R., *et al.*: 1980, Skylab Solar Workshop II: Solar Flares, P.A. Sturrock (ed.), p. 341.

Nakajima, H., Tajima, T., Brunel, F., and Sakai, J.: 1985, *Bulletin of Faculty of Engineering,* Toyama University, **36**, 39.

Raymond, J.C., Cox, D.P., and Smith, B.W.: 1976, *Ap.J.* **204**, 290.

Rust, D.M., and Somov, B.V.: 1984, *Solar Phys.* **93**, 95.

Smartt, R. N., Dunn, R. B. and Fisher, R. R.: 1981, *S.P.I.E.* **288**, 395.

Spicer, D.S., and Svestka, Z.: 1983, *Solar Phys.* **87**, 271.

N88-11623

SUNSPOT OBSERVATIONS FROM THE SOUP INSTRUMENT ON SPACELAB 2

R.A. Shine, A. Title, T. Tarbell (Lockheed PARL), and the SOUP Team

(L. Acton[1], D. Duncan[1], S. Ferguson[1], M. Finch[1], Z. Frank[1], G. Kelly[1], R. Lindgren[1], M. Morrill[1], T. Pope[1], R. Reeves[1], R. Rehse[1], K. Topka[1], G. Simon[2], J. Harvey[3], J. Leibacher[3], W. Livingston[3], L. November[4], J. Zirker[4])

[1]*Lockheed Palo Alto Research Laboratory, Dept. 91-30,*
Bldg. 256, 3251 Hanover Street, Palo Alto, CA 94304, U.S.A.
[2]*Air Force Geophysics Laboratory, Sunspot, NM 88349, U.S.A.*
[3]*National Solar Observatory, Tucson, AZ 85718 U.S.A.*
[4]*National Solar Observatory, Sunspot, NM 88349, U.S.A.*

ABSTRACT

A series of white light images obtained by the SOUP instrument on Spacelab 2 of active region 4682 on August 5, 1985 have been analyzed in the area containing the sunspot. Although the umbra of the spot is underexposed, the film is well exposed in the penumbral regions. These data have been digitially processed to remove noise and to separate p-mode oscillations from low velocity material motions. The results of this preliminary investigation include: (1) proper motion measurements of a radial outflow in the photospheric granulation pattern just outside the penumbra; (2) discovery of occassional bright structures ("streakers") that appear to be ejected outward from the penumbra; (3) broad dark "clouds" moving outward in the penumbra in addition to the well known bright penumbral grains moving inward; (4) apparent extensions and contractions of penumbral filaments over the photosphere; and (5) observation of a faint bubble or loop-like structure which seems to expand from two bright penumbral filaments into the photosphere.

1. Introduction

Although the Spacelab 2 mission was flown during the sunspot minimum of the solar cycle, we were fortunate enough to have a medium size sunspot and a group of pores on the disk during the week of the mission. The high resolution (approximately 0.5″ or 350 km) and, more importantly, the stability and freedom from variable atmospheric distortion of the SOUP data has provided an unprecedented opportunity to study the dynamics of a sunspot in "white light" by viewing and analyzing movie sequences. Unfortunately, the umbra was underexposed and there we can only set upper limits on the brightness of any structures but the penumbra and the surrounding photosphere show a large variety of interesting phenomena. Many of these have not been previously described. Figure 1 is a cartoon which summarizes and indicates the locations of some of these phenomena.

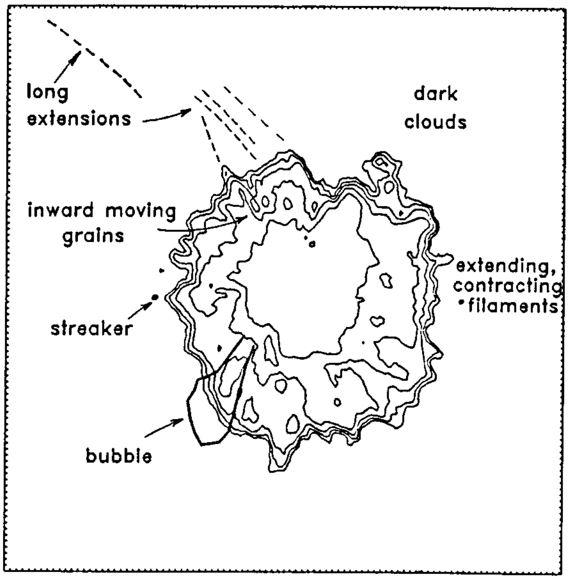

Fig. 1 A cartoon indicating locations of various phenomena. The ticks marks are spaced every arc second.

2. Observations

A description of the SOUP instrument and a summary of the data obtained are given by Title *et al.* (1986). White light film images containing the sunspot in the field of view were obtained during portions of 5 orbits. The longest uninterupted sequence was exposed during Rev 110 and consists of about 28 minutes of data with a frame taken every 2 seconds on August 5, 1985 between 19:10 – 19:38 GMT. Analysis of the guider data indicates that the image was stable with an RMS jitter of about 3 milli arc seconds. All of the analysis reported in this paper has used this particular sequence. We have digitized every fifth frame over the entire interval to give us data with 10 second spacing. Processing every frame will allow us to further reduce the noise and improve the quality of the images in the future.

Our analysis has benefited greatly from use of an interactive video viewing system and from a number of image processing techniques including 3-D fourier filtering. A optical video disk recorder/player allows recording large numbers of computer-generated images which can then be played back interactively as movie loops or single frames. Although most of the phenomena described in this paper can be recognized in the raw digitized data (when one knows what to look for), some may have never been discovered without viewing processed movies. The fourier filtering has allowed us to suppress the effects of the suprisingly strong p-mode oscillations, remove noise in the data, and enhance or suppress motions within any desired velocity range. The work described here and in the preceeding paper (Title, *et al.* 1987) seems to be the first major application of these techniques for processing movies of solar data. They are very useful tools and we expect to see them used extensively in the future in spite of the demands they make on computer time and storage.

Figure 2 shows a series of 12 images spaced two minutes apart which were taken from a sequence

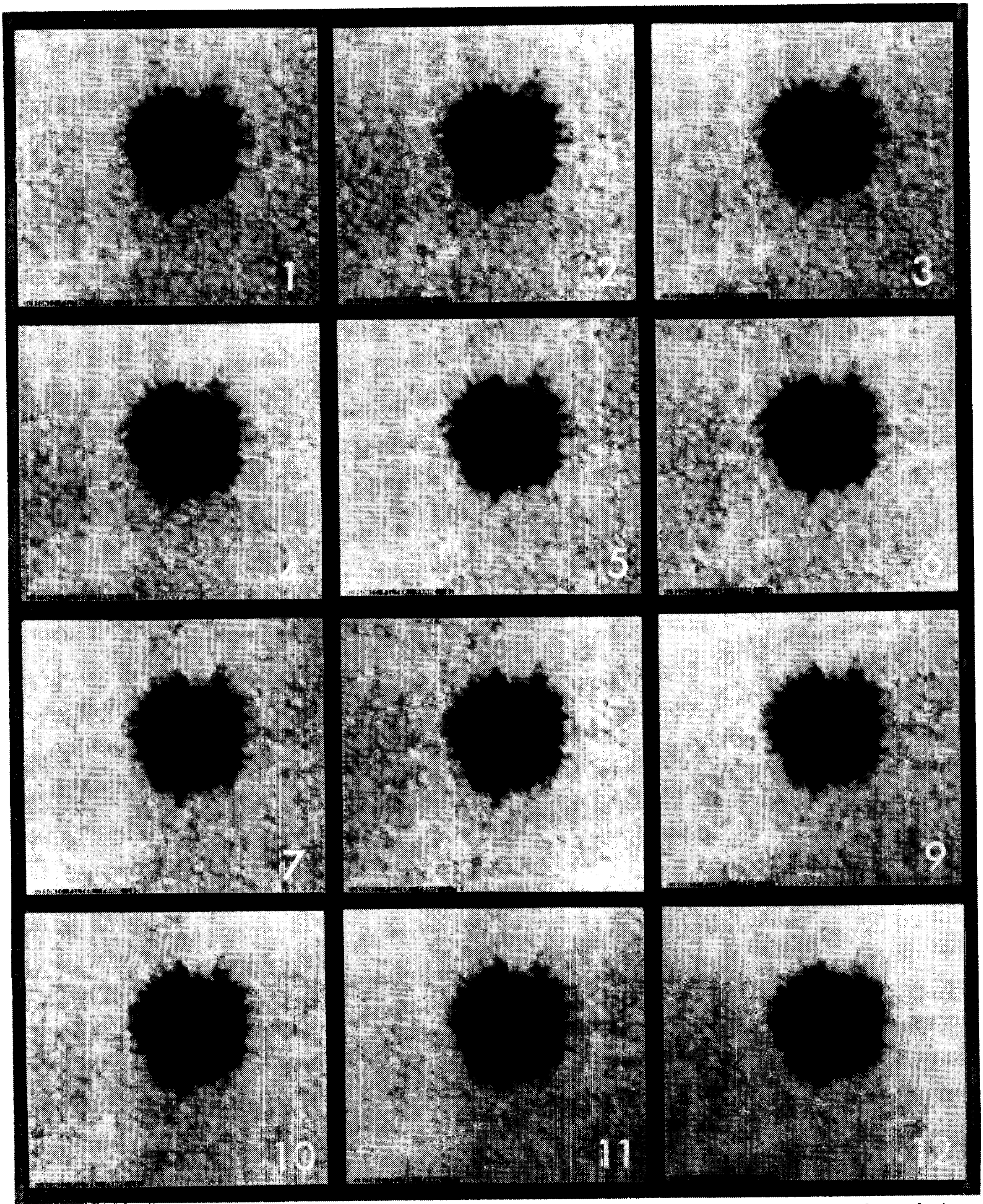

Fig. 2 Twelve images of the sunpot spaced two minutes apart. This is subsonic filtered data with a velocity cutoff of 4 km/s.

processed with a "subsonic" fourier filter. This was done by zeroing all fourier components in (k_x, k_y, ω) space with phase velocities greater than 4 km/s. This is very effective at removing noise and suppressing the p-mode oscillations (Title, *et al.* 1987).

3. Results

3.1 Granulation Outflow

The area immediately surrounding the sunspot penumbra shows a radial outflow that is clearly visible even in the unprocessed movies, especially when run at high speed (60 frames/s which is 600 times real time). The apparent width of this "collar flow" is $\approx 5''$. Movies temporally filtered to suppress the p-mode oscillations show the motion more clearly and allow an estimate of the velocities of individual granules. These range from 0.2 to 1.5 km/s. The radial time slices through the sunspot shown in figure 3 are the most convincing displays of radial flows. The radially advecting granules appear in these images as slanted lines. The radial velocity can be determined from the slope.

This advection of the granules is also clearly seen in the flow maps generated by local correlation tracking as shown in figure 4. The maps represent the transverse flow averaged over the entire 28 minute span available. The technique used to make this flow map is described by November, *et al.* (1987).

These proper motions have apparently not been previously reported although their doppler signature would explain observations of outflows beyond the penumbra in studies by Kinman (1952) and Sheeley and Bhatnagar (1971). Because the flow around the penumbra had lower velocities and because of pattern similarities in their dopplergrams, Sheeley and Bhatnagar suggested that the flows were more closely related to the pattern of supergranulation than the penumbral Evershed effect. This is consistent with the SOUP observations.

The relationship of these motions to the photospheric Evershed effect is unclear although both represent radially outward flows. The moving granules could be upward convention deflected by the slanted magnetic field under the photosphere or part of a large scale convection pattern around the sunspot. It is generally accepted that the Evershed effect is concentrated in dark penumbral lanes (based on observations of Beckers (1968) and Abdusamatov and Krat (1970)) and that the velocities end abruptly at the penumbral boundary (e.g., Wiehr, *et al.*, 1986). These dark penumbral filaments may be elevated relative to the surrounding photosphere (e.g., Moore, 1981). Actually, this granulation advection is probably the source of confusion over whether the Evershed effect actually ends abruptly at the penumbra. The granular motion may or may not show up in an individual spectra but it would clearly be present in any adequate average or under conditions of poor seeing.

3.2 Fast Ejections ("Streakers")

Around the penumbra there are bright granule-like features that seem to be ejected from the sunspot. The most obvious of these bright features, dubbed the "streaker", travels at about

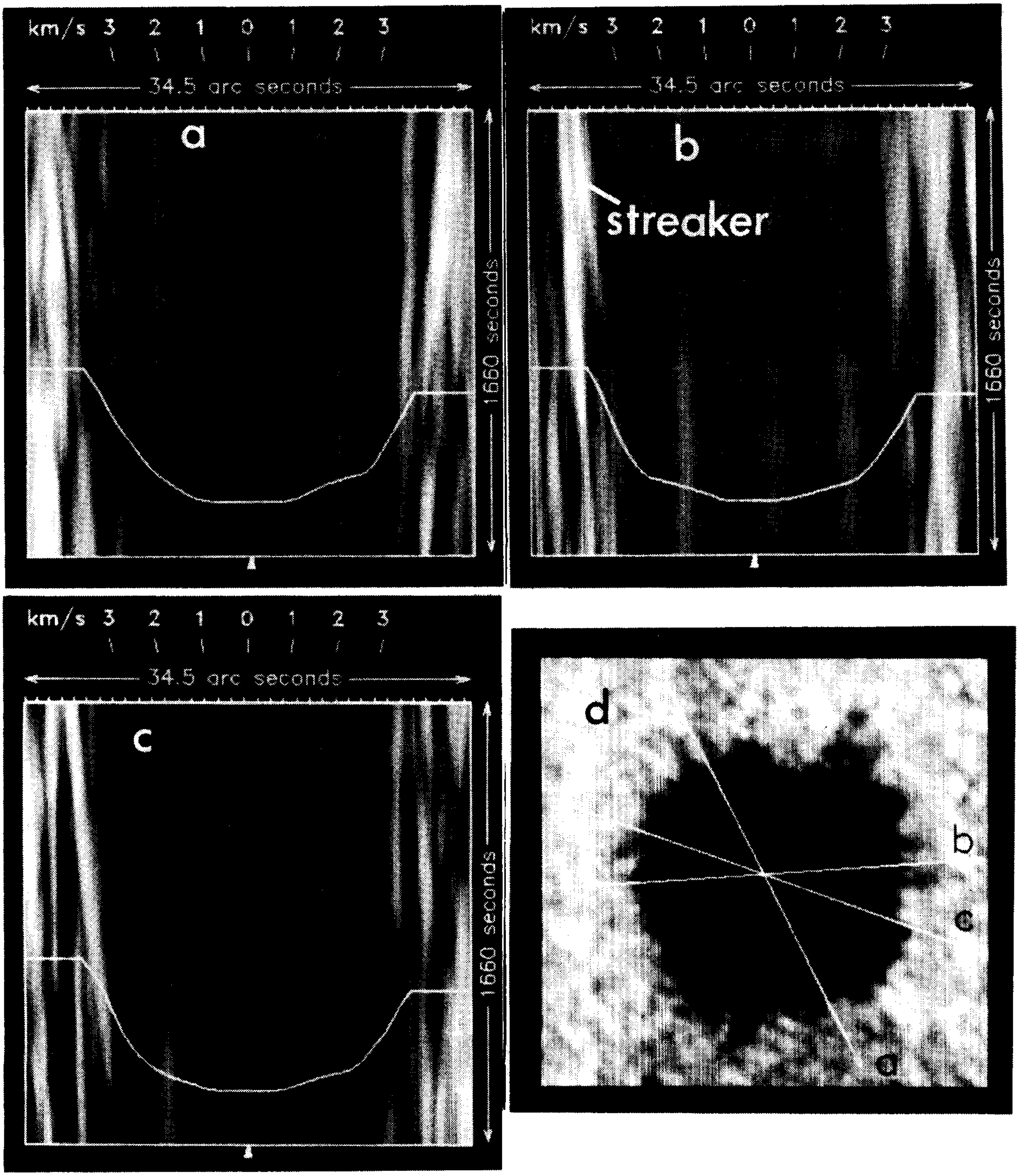

Fig. 3 Parts a, b, and c are space-time slices through the sunspot with the spatial sections indicated in part d which is an image at the center of the time range. These are called radial slices because the spatial sections are along a line passing through the center of the spot.

2.7 km/s. The normal granulation outflow is at $\frac{1}{3}$ to $\frac{1}{2}$ that rate. Thus, the bright moving features move through (perhaps as a wave) or over the granulation.

The radial trajectory of the streaker is clearly shown in figure 3b, one of the time slices through the sunspot. A dark structure appears to originate in conjuction with the streaker and moves in

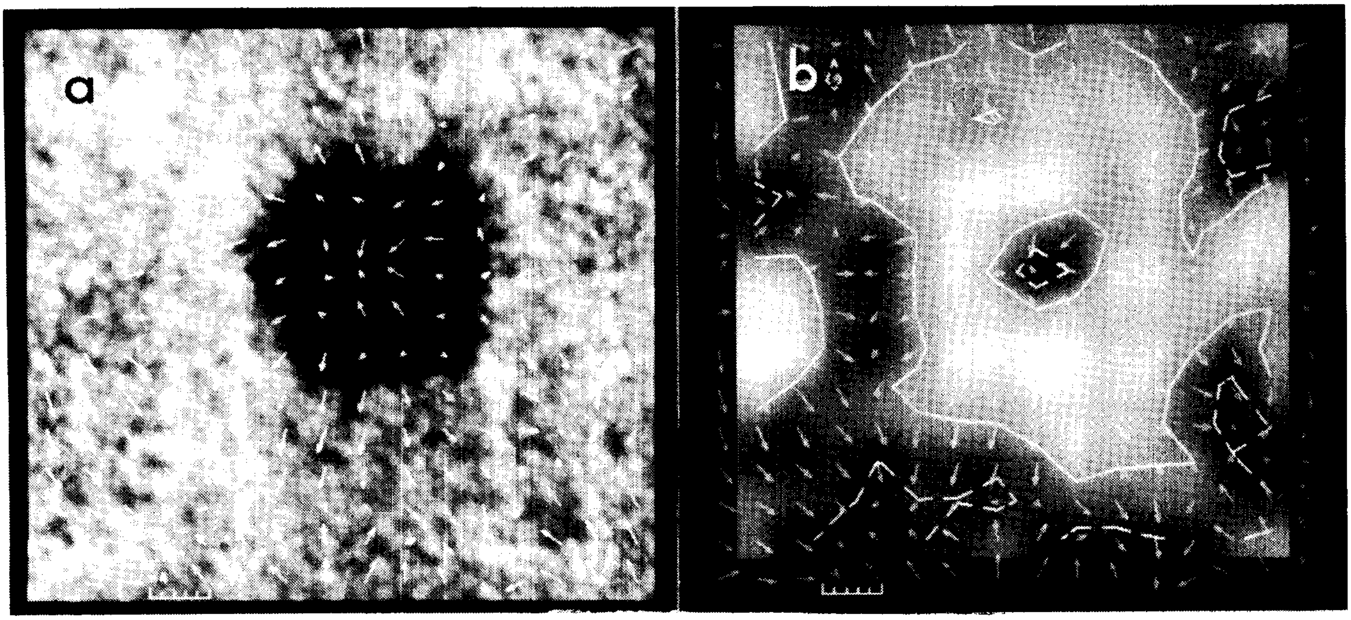

Fig. 4 (a) A map of horizontal flows indicated by the arrows and (b) an image of the computed horizontal divergence of this flow. Bright areas have positive divergence (outflowing material, probably upwelling) and dark areas have negative divergence (inflowing material).

the opposite direction into the penumbra. The streaker approaches another bright photospheric structure which is also moving outward from the spot at 0.95 km/s. Another streaker is seen in figure 3c.

We have not yet made a thorough study of these bright structures. However, they are clearly related to activity of the nearby penumbra. Further understanding will require measurements of the interaction of the penumbral filaments with the photosphere surrounding the sunspot.

3.3 Ejected Loop or Bubble

A very interesting feature was discovered by examining movies of images such as the one in figure 5. This is one frame in a movie which has velocities in the range 2 - 4 km/s enhanced by 3-D fourier filtering. This was accomplished by multiplying the appropiate fourier coefficients by 2. A large loop or bubble is seen which seems to be associated with two bright penumbral filaments. It begins in the penumbra and travels out into the surrounding photosphere. Although much easier to see in figure 5, the same structure can be seen in the corresponding frame in figure 2 (image # 11 which is frame 153 in the movie) and in the raw images. We have no information on the height of this structure in the atmosphere but it may be easier to understand energetically if it represents an ejected mass above the photosphere.

3.4 Penumbral Filaments

Dynamics: It is evident from the movies, and images separated in time by more than five or ten minutes, that some penumbral filaments or groups of filaments extend and contract at rates of 0.1 to 0.5″/minute (1.2 to 6 km/s). These might be actual motions of filaments or possibly waves propagating through the filaments which cause temperature or density changes

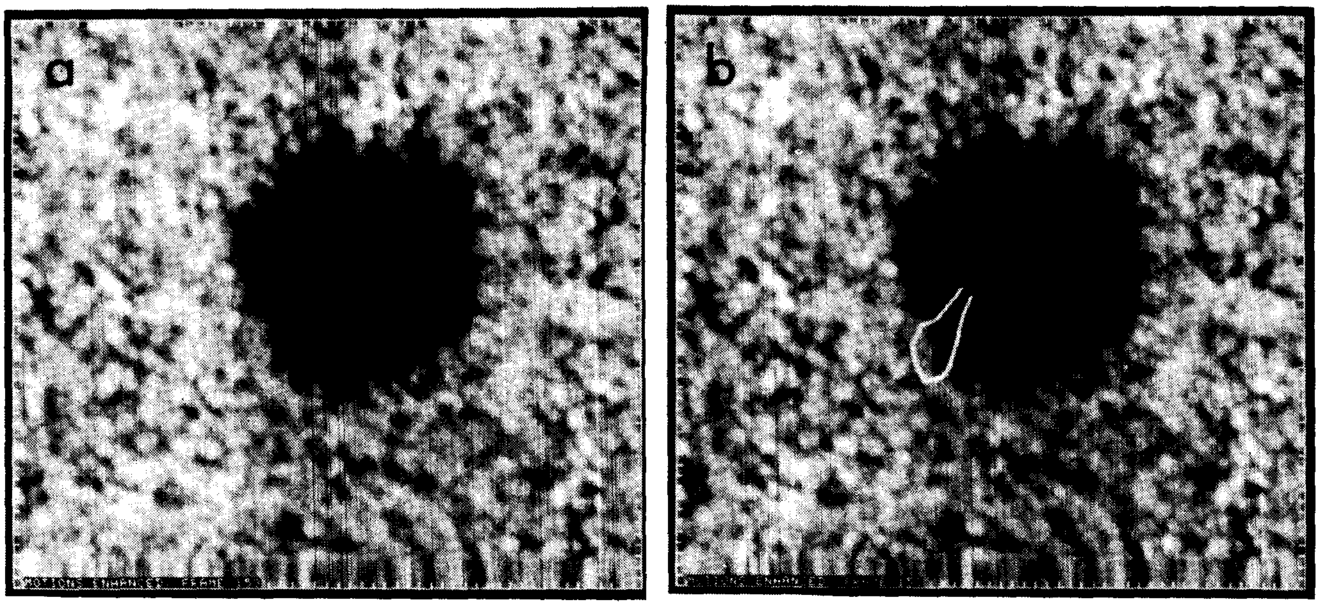

Fig. 5 (a) A single frame from a movie filtered to enhance motions with phase velocities between 2 and 4 km/s. (b) The same image with a white line drawn to show a faint bubble or loop that seemed to be ejected from the penumbra.

that affect the filament's visibility. These waves might be photospheric p-mode oscillations or waves generated from the umbra which then propagate along the filament. The overall impression is that the filaments overlay the surrounding photosphere. The idea of an overlying penumbra seems more consistent with these rapid fluctuations. We plan some modeling to test the viability of this concept. The areas showing the most obvious changes are marked in figure 1 and can be seen in the series of images in figure 2.

Often, as precursors to the filament extensions, there are photospheric brightenings in the boundaries of the regions into which the filaments extend. This is consistent with a wave scenario in which a particularly high amplitude p-mode oscillation (these have a typical spatial coherence of 10″ or more) causes the photosphere to brighten and subsequently causes the density in a nearby overlying filament to increase (thereby increasing its opacity and making it appear darker).

Possible Long Extensions: In addition to the more modest extensions described above, there may be fainter extensions of some filaments of tens of arc seconds. These are indicated in figure 1 and are visible in the later images in figure 2. These are very faint and, as figure 2 and the movies show, variable in visibility. It is unclear if they are above or within the photospheric granulation but we favor the former opinion. Their variable visibility could be the same mechanism for the shorter extensions; i.e., large scale pressure waves. The extensions may be similar to a larger class of variable linear and arc-like structures seen in the data, all of which may be density increases in overlying magnetic flux tubes.

3.5 Penumbral Motions

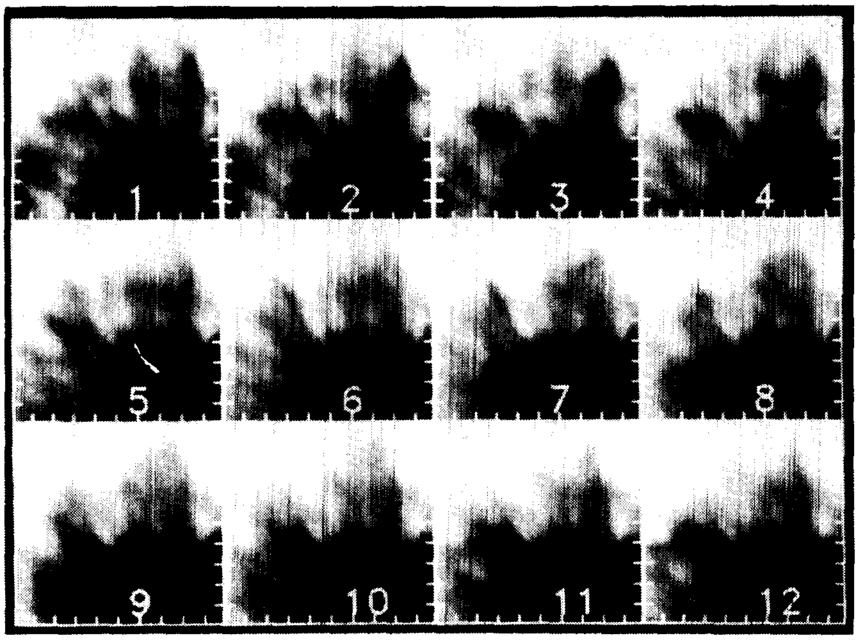

Fig. 6 A series of images showing time variations in a portion of the penumbra. The frames are 2 minutes apart and the tick marks are spaced at 1 arc second intervals.

Flow maps made by local correlation tracking (figure 4) indicate that the entire penumbra flows radially outward with velocities in the range of 100 to 400 meters per second. However, this result, which is smaller than typical doppler measurements of the Evershed flow, is affected by the field-of-view of the correlation tracker algorithm (4″ FWHM). It therefore represents an average over the penumbral structures and is probably also affected by the granulation outflow outside the penumbra. We plan to attempt further feature tracking with smaller aperatures. The preliminary map shows a positive divergence in the region of the penumbra. Not all of the penumbral structures move outward; some bright features (see below) are observed to move inward.

Penumbral Grains: The bright penumbral grains, at least those which are inside 0.75 of the penumbral radius, move inward toward the umbral. The rates are up to 500 m/s and tend to increase as the grain approaches the umbra. This is in agreement with earlier measurements of the motions of bright penumbral grains (Muller, 1981). A mosaic of images showing a $10'' \times 10''$ area of the penumbra and containing some moving penumbral grains is shown in figure 6.

Dark Clouds: Both movies and time slices show dark penumbral clouds which move outward. An area that shows particularly prominent ones in the movies is marked on the cartoon in figure 1. These are broad structures covering a few arc seconds, much larger than the width of the filaments and grains. They might be related to the "dark puffs" seen in the blue wing of H_α (Moore and Tang, 1975) and/or running penumbral waves.

4. Concluding Remarks

These first space-based high resolution white light movies of a sunspot have been remarkably successful in elucidating sunspot phenomena and highlight the severe handicap imposed by atmospheric seeing on visible light solar observations. However, it is clear that these data are only a tantalizing hint of what can be done with a stabilized solar telescope in space. Further space-based observations coupled with image processing systems capable of handling the large amounts of data will revolutionize solar physics and our understanding of stellar atmospheres in general.

There is still significant work remaining on these white light images to quantify the preliminary results better and hopefully discover new phenomena. From this 28 minute observation of a single sunspot, we cannot resolve the possibility that some of these phenomena occur only within a certain epoch of a sunspot's evolution or whether other phenomema occur. However, we can also use the insights we have gained from the SOUP data to re-examine ground based and balloon observations and help separate solar and atmospheric effects in these data.

Acknowledgements

Special thanks are extended to the crew of Spacelab 2 and the controllers and planners on the ground who worked so hard to get the observations. The SOUP experiment was supported by NASA under contract NAS8-32805. The image processing developments using laser optical disks and portions of the image processing software development have been supported by Lockheed Independent Research funds.

REFERENCES

Abdusamatov, H.I., and Krat, V.A.: 1970, *Solar Physics*, **14**, 132.

Beckers, J.M.: 1968, *Solar Physics*, **3**, 258.

Kinman, T.D.: 1952, *Monthly Notices Roy. Astron. Soc.*, **112**, 425.

Moore, R.L.: 1981, in L.E. Cram and J.H. Thomas (eds), *The Physics of Sunspots.*

Moore, R.L. and Tang, F.: 1975, *Solar Physics*, **41**, 81.

Muller, R.: 1981, in L.E. Cram and J.H. Thomas (eds), *The Physics of Sunspots.*

November, L., and the SOUP Team: 1987, these proceedings.

Sheeley, N.R.,Jr. and Bhatnagar, A.: 1971, *Solar Physics*, **19**, 338.

Title, A.M., Tarbell, T.D., Simon, G.W., and the SOUP Team: 1986 *Advances in Space Res.*, in press.

Title, A.M., Tarbell, T.D. and the SOUP Team: 1987, these proceedings.

Wiehr, E., Stellmacher, G., Knölker, M., and Grosser, H.: 1986, *Astr. Astrophy.*, **155**, 402.

N88-11624

IMAGING INTERFEROMETRY WITH NON-REDUNDANT ARRAYS

J. B. Zirker
National Solar Observatory
National Optical Astronomy Observatories[1]

The performance of a set of non-redundant arrays, that convert an existing telescope to an interferometer, has been simulated.

Each array is a perforated mask, placed at an image of the objective. Each pair of holes in a mask transmits a unique spatial frequency that is present in the target; hence the term "non-redundant." Each mask produces a fringe I(f) in the focal plane that is the product of the Fourier transforms of the object and the optical transfer function S(f):

$$I(f) = O(f) \cdot S(f)$$

Seeing disturbs the phase and amplitude of the fringe I(f), but since each spatial frequency (f) corresponds to a unique pair of holes, and since each hole pairs with all the others, it is possible to solve algebraically for the atmospheric phase shift at each hole and thus eliminate seeing. With sufficient S/N the phase and amplitude of the object, O(f), can be recovered at each resolvable spatial frequency in the continuous spatial spectrum, out to the diffraction limit. Inverse Fourier transformation then yields an image of the objective.

We require two masks if the wavefront is parallel to each hole, or three masks if, as is more likely, the wavefront is tilted differently at each hole. In the simulation, I use three one-dimensional masks with spacings (0,1,4,6), (0,2,3,7), and (0,1,3,7), in units of a basic spacing, p. Each mask is non-redundant, but the masks have many spacings in common. In practice the hole diameters should not exceed the Fried parameter, r_0, during a short (~ 8ms), narrow-band (~ 50 Å) exposure. I used 6-cm holes, which correspond to 1.5" seeing. As a target, I chose the limb of the Sun. A field stop, 2.4 arcseconds in diameter, limits the field-of-view.

Figure 1 shows the fringe mask 1 would produce (a) with no atmosphere and (b) with randomly-tilted wavefronts. I added random noise in varying amounts to the fringe and followed Rhodes'[2] procedure (1972) to solve for the target's amplitudes and phases.

Figure 2 shows (a) the original target's intensity profile, (b) the reconstructed image, with fringe noise of 3%, and (c) the image that the telescope would form without the masks. The maximum hole spacing (e.g., spatial resolution) in this simulation corresponds to .25 arcseconds.

---

[1] Operated by the Association of Universities for Research in Astronomy, Inc., under contract with the National Science Foundation

[2] W. T. Rhodes, Dissertation, Stanford University, 1972.

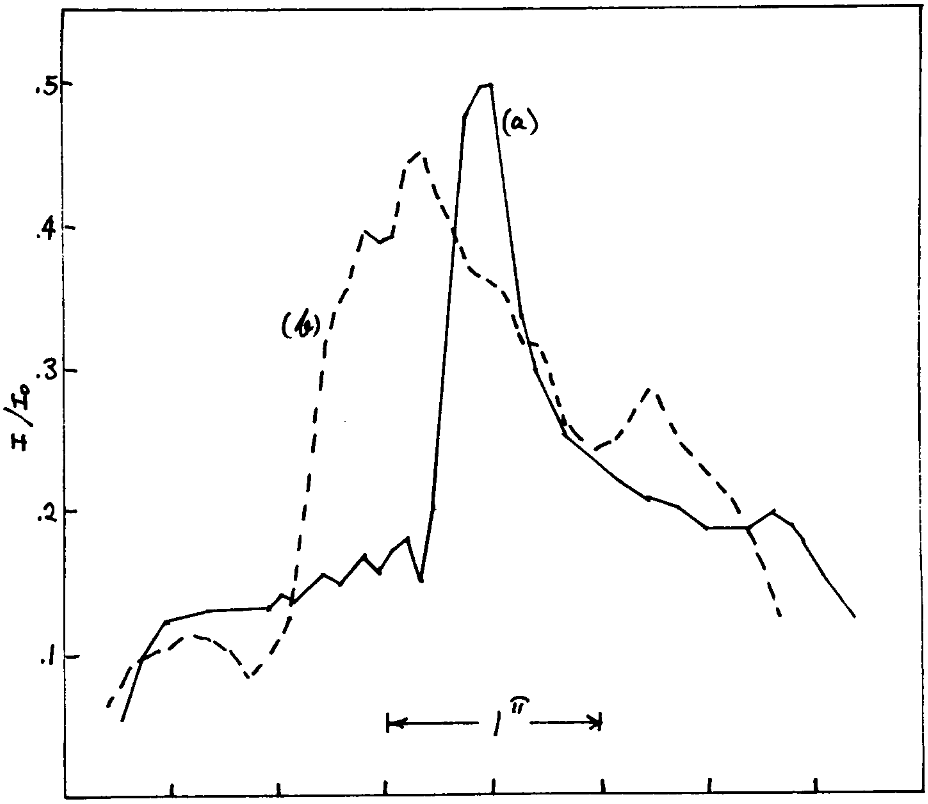

Figure 1

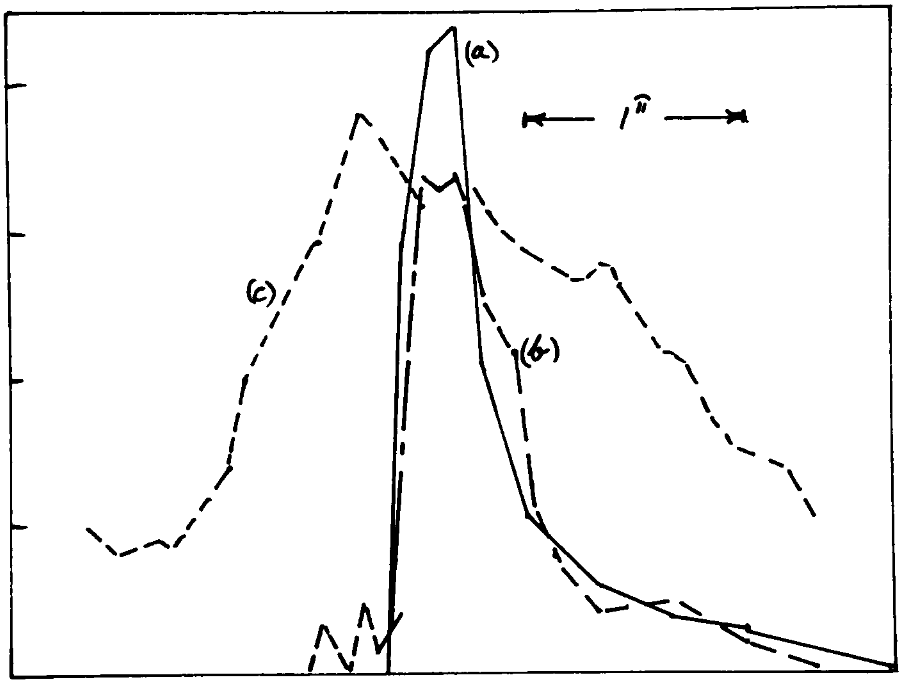

Figure 2

Thus the simulation suggests that diffraction-limited images, at least of high-contrast objects, can be reconstructed from moderately noisy observations in the presence of mediocre (1.5 arcsecond) seeing.

NASA
National Aeronautics and
Space Administration

Report Documentation Page

1. Report No.
NASA CP-2483

2. Government Accession No.

3. Recipient's Catalog No.

4. Title and Subtitle
Theoretical Problems in High Resolution Solar Physics II

5. Report Date
September 1987

6. Performing Organization Code
682.0

7. Author(s)
G. Athay* and D. S. Spicer, Editors

8. Performing Organization Report No.
87B0401

10. Work Unit No.

9. Performing Organization Name and Address
Goddard Space Flight Center
Greenbelt, Maryland 20771

11. Contract or Grant No.

13. Type of Report and Period Covered
Conference Publication

12. Sponsoring Agency Name and Address
National Aeronautics and Space Administration
Washington, D.C. 20546-0001

14. Sponsoring Agency Code

15. Supplementary Notes
* G. Athay is affiliated with the High Altitude Observatory/National Center for Atmospheric Research; Boulder, Colorado.

16. Abstract
The Science Working Group for the High Resolution Solar Observatory (HRSO) laid plans beginning in 1984 for a series of workshops designed to stimulate a broad-based input from the scientific community to the HRSO mission. These workshops have the dual objectives of encouraging an early start on the difficult theoretical problems in radiative transfer, magnetohydrodynamics, and plasma physics that will be posed by the HRSO data, and maintaining current discussions of results in high resolution solar studies. This workshop was the second in the series. The workshop format presented invited review papers during the formal sessions and contributed poster papers for discussions during open periods. Both are presented in this document.

17. Key Words (Suggested by Author(s))
High Resolution Solar Observatory
Solar Physics
Solar Magnetics
Plasma Physics
Radiative Transfer

18. Distribution Statement
Unclassified - Unlimited

Subject Category 92

19. Security Classif. (of this report)	20. Security Classif. (of this page)	21. No. of pages	22. Price
Unclassified	Unclassified	152	A08

NASA FORM 1626 OCT 86

NASA-Langley, 1987